

The Texas Medical Center Library

DigitalCommons@TMC

The University of Texas MD Anderson Cancer
Center UTHealth Graduate School of
Biomedical Sciences Dissertations and Theses
(Open Access)


The University of Texas MD Anderson Cancer
Center UTHealth Graduate School of
Biomedical Sciences

8-2011

IN-VIVO CT DOSIMETRY DURING VIRTUAL COLONOSCOPY

Jonathon W. Mueller

Follow this and additional works at: https://digitalcommons.library.tmc.edu/utgsbs_dissertations

 Part of the [Diagnosis Commons](#), [Gastroenterology Commons](#), [Medical Biophysics Commons](#), [Other Biomedical Engineering and Bioengineering Commons](#), [Other Medical Sciences Commons](#), and the [Radiology Commons](#)

Recommended Citation

Mueller, Jonathon W., "IN-VIVO CT DOSIMETRY DURING VIRTUAL COLONOSCOPY" (2011). *The University of Texas MD Anderson Cancer Center UTHealth Graduate School of Biomedical Sciences Dissertations and Theses (Open Access)*. 172.

https://digitalcommons.library.tmc.edu/utgsbs_dissertations/172

This Thesis (MS) is brought to you for free and open access by the The University of Texas MD Anderson Cancer Center UTHealth Graduate School of Biomedical Sciences at DigitalCommons@TMC. It has been accepted for inclusion in The University of Texas MD Anderson Cancer Center UTHealth Graduate School of Biomedical Sciences Dissertations and Theses (Open Access) by an authorized administrator of DigitalCommons@TMC. For more information, please contact digitalcommons@library.tmc.edu.

The
TMC  **LIBRARY**
Health Sciences Resource Center

IN-VIVO CT DOSIMETRY DURING VIRTUAL COLONOSCOPY

by

Jonathon Wayne Mueller, M.S.

APPROVED:

Dianna D. Cody, Ph.D., Supervisory Professor

David Followill, Ph.D.

Valen Johnson, Ph.D.

A. Kyle Jones, Ph.D.

John Rong, Ph.D.

APPROVED:

Dean, The University of Texas
Health Science Center at Houston
Graduate School of Biomedical Sciences

IN-VIVO CT DOSIMETRY DURING VIRTUAL COLONOSCOPY

A

THESIS

Presented to the Faculty of
The University of Texas
Health Science Center at Houston
and
The University of Texas
M.D. Anderson Cancer Center
Graduate School of Biomedical Sciences
in Partial Fulfillment

of the Requirements

for the Degree of

MASTER OF SCIENCE

by

Jonathon Wayne Mueller, M.S.

Houston, Texas

August, 2011

IN-VIVO CT DOSIMETRY DURING VIRTUAL COLONOSCOPY

Publication Number: _____

Jonathon Wayne Mueller, M.S.

Supervisory Professor: Dianna D. Cody, Ph.D.

Virtual colonoscopy (VC) is a minimally invasive means for identifying colorectal polyps and colorectal lesions by insufflating a patient's bowel, applying contrast agent via rectal catheter, and performing multi-detector computed tomography (MDCT) scans. The technique is recommended for colonic health screening by the American Cancer Society but not funded by the Centers for Medicare and Medicaid Services (CMS) partially because of potential risks from radiation exposure. To date, no in-vivo organ dose measurements have been performed for MDCT scans; thus, the accuracy of any current dose estimates is currently unknown.

In this study, two TLDs were affixed to the inner lumen of standard rectal catheters used in VC, and in-vivo rectal dose measurements were obtained within 6 VC patients. In order to calculate rectal dose, TLD-100 powder response was characterized at diagnostic doses such that appropriate correction factors could be determined for VC. A third-order polynomial regression with a goodness of fit factor of $R^2=0.992$ was constructed from this data.

Rectal dose measurements were acquired with TLDs during simulated VC within a modified anthropomorphic phantom configured to represent three sizes of patients undergoing VC. The measured rectal doses decreased in an exponential manner with increasing phantom effective diameter, with $R^2=0.993$ for the exponential regression model and a maximum percent coefficient of variation (%CoV) of 4.33%. In-vivo measurements yielded rectal doses ranged from that decreased exponentially with increasing patient

effective diameter, in a manner that was also favorably predicted by the size specific dose estimate (SSDE) model for all VC patients that were of similar age, body composition, and TLD placement. The measured rectal dose within a younger patient was favorably predicted by the anthropomorphic phantom dose regression model due to similarities in the percentages of highly attenuating material at the respective measurement locations and in the placement of the TLDs. The in-vivo TLD response did not increase in %CoV with decreasing dose, and the largest %CoV was 10.0%.

TABLE OF CONTENTS

LIST OF FIGURES	xi
LIST OF TABLES	xiv
1.0: INTRODUCTION	1
1.1 Virtual Colonoscopy (VC)	1
1.1.1 VC Background	1
1.1.2 VC Procedure at MD Anderson Cancer Center	2
1.1.3 VC Computed Tomography (CT) Radiation Dose	6
1.2 Thermoluminescent Dosimeters (TLDs)	8
1.2.1 TLD Overview	8
1.2.2 TLD Physics	12
1.2.3 TLD Readout Process	15
1.2.4 TLD Correction Factors	19
1.2.4.1 Fading Correction Factor	19
1.2.4.2 Linearity Correction Factor	19
1.2.4.3 Sensitivity Correction Factor	20
1.2.4.4 Energy Correction Factor	21
1.2.4.5 f-Factor Utilization	21
1.2.5 TLD Dose Calculation	22
1.3 CT Radiation Dose Measurements	23
1.3.1 Background of CT Dose Measurements	23
1.3.2 CT Dose Index (CTDI)	23
1.3.3 Monte Carlo Method	29
1.3.4 CT Point Dose Measurements	30
1.3.5 MD Anderson VC Rectal Dose Estimates	32

1.4 Hypothesis and Specific Aims	36
1.4.1 Hypothesis	36
1.4.2 Specific Aims	36
1.4.2.1 Specific Aim 1: Establish TLD Linearity Correction	
Factors for VC Scan Parameters on a MDCT	37
1.4.2.2 Specific Aim 2: Obtain Rectal Dose Measurements	
in an Anthropomorphic Phantom and In-Vivo in	
Patients Undergoing VC with TLDs	37
1.4.2.3 Specific Aim 3: Compare In-Vivo Rectal Dose	
Measurements to Anthropomorphic Phantom	
Measurements, CTDI-Based Dose Estimates and Point	
Dose Measurements from a Uniform Phantom	38
2.0 Materials	39
2.1 Introduction	39
2.2 GE LightSpeed VCT Scanner	39
2.3 CTDI Body Phantom	41
2.4 CIRS ATOM Adult Anthropomorphic Phantom	43
2.5 PeopleSize Software	46
2.6 Thermoluminescent Dosimeter (TLD) Capsules	48
2.7 Custom-Made PMMA CTDI Insert Rod	51
2.8 Ionization Chambers	54
2.8.1 Farmer Ionization Chamber	57
2.8.2 CTDI Pencil Ionization Chamber	59
2.8.3 Electrometer	61
2.9 Double Contrast Enema Delivery System	63
3.0 Methods	66

3.1 Introduction	66
3.2 Specific Aim 1: Establish TLD Linearity Correction Factors for VC Scan Parameters on a MDCT	66
3.2.1 <i>MDCT Beam Characterization</i>	67
3.2.1.1 HVL and QVL Measurement	68
3.2.1.2 $(CTDI_{100})_{air}$, $CTDI_w$, and $CTDI_{vol}$ Determination	74
3.2.2 <i>Determination of TLD Dose Linearity Correction Coefficients for Virtual Colonoscopy</i>	78
3.2.2.1 TLD Irradiation at Exposures Received by Patients Undergoing Virtual Colonoscopy	78
3.2.2.2 TLD Readout and Dose Linearity Correction Factor Calculation	82
3.3 Specific Aim 2: Obtain Rectal Dose Measurements in an Anthropomorphic Phantom and In-Vivo in Patients Undergoing VC with TLDs	84
3.3.1 <i>Rectal Dose Measurement Simulation in an Anthropomorphic Phantom</i>	85
3.3.1.1 Modifications to the Anthropomorphic Phantom	85
3.3.1.2 Modification to the Rectal Catheter	92
3.3.1.3 Anthropomorphic Phantom Assembly	94
3.3.1.4 Phantom Measurements and Determination of Population Percentages Represented	95
3.3.1.5 Virtual Colonoscopy Simulation in an Anthropomorphic Phantom	103
3.3.1.6 Simulated Virtual Colonoscopy Data Analysis	113
3.3.2 <i>In-Vivo Rectal Dose Measurements during Virtual Colonoscopy</i>	114
3.3.2.1 QC Step 1: Testing TLD Capsules for Leakage	115

3.3.2.2 Attaching TLDs to the Rectal Catheter	116
3.3.2.3 QC Step 2: Testing for Secure TLD Attachment to the Rectal Catheter	123
3.3.2.4 QC Step 3: Disinfection of Rectal Catheter Assembly	124
3.3.2.5 Irradiating TLDs during VC and QC Step 4: Maintenance of Control of TLDs at All Times	125
3.3.2.6 TLD Retrieval and QC Step 5: Disinfection of Rectal Catheter Assembly and TLD Capsules	128
3.3.2.7 Patient Rectal Dose Determination	130
3.4 Specific Aim 3: Compare In-Vivo Rectal Dose Measurements to Anthropomorphic Phantom Measurements, CTDI-Based Dose Estimates and Point Dose Measurements from a Uniform Phantom	131
3.4.1 Introduction	131
3.4.2 Size Specific Dose Estimate (SSDE)	133
3.4.3 Outlier Analysis	134
3.4.4 Statistical Analysis	136
4.0 Results	138
4.1 Introduction	138
4.2 Specific Aim 1: Establish TLD Linearity Correction Factors for VC Scan Parameters on a MDCT	138
4.2.1 MDCT Beam Characterization	139
4.2.1.1 HVL and QVL Measurement	139
4.2.1.2 $(CTDI_{100})_{air}$, $CTDI_w$, and $CTDI_{vol}$ Determination	141
4.2.2 Determination of TLD Dose Linearity Correction Coefficients for Virtual Colonoscopy	146

4.3 Specific Aim 2: Obtain Rectal Dose Measurements in an Anthropomorphic Phantom and In-Vivo in Patients Undergoing VC with TLDs	153
4.3.1 <i>Rectal Dose Measurement Simulation in an Anthropomorphic Phantom</i>	153
4.3.2 <i>In-Vivo Rectal Dose Measurements during Virtual Colonoscopy</i>	156
4.4 Specific Aim 3: Compare In-Vivo Rectal Dose Measurements to Anthropomorphic Phantom Measurements, CTDI-Based Dose Estimates and Point Dose Measurements from a Uniform Phantom	160
4.4.1 <i>Introduction</i>	161
4.4.2 <i>Percent Coefficient of Variation (%CoV)</i>	162
4.4.3 <i>Outlier Analysis</i>	163
4.4.4 <i>Statistical Analysis</i>	167
5.0 Discussion	169
5.1 Introduction	169
5.2 Specific Aim 1: Establish TLD Linearity Correction Factors for VC Scan Parameters on a MDCT	169
5.2.1 <i>MDCT Beam Characterization</i>	170
5.2.1.1 HVL and QVL Measurement	171
5.2.1.2 $(CTDI_{100})_{air}$, $CTDI_w$, and $CTDI_{vol}$ Determination	172
5.2.2 <i>Determination of TLD Dose Linearity Correction Coefficients for Virtual Colonoscopy</i>	174
5.3 Specific Aim 2: Obtain Rectal Dose Measurements in an Anthropomorphic Phantom and In-Vivo in Patients Undergoing VC with TLDs	177
5.3.1 <i>Rectal Dose Measurement Simulation in an Anthropomorphic Phantom</i>	177
5.3.1.1 Modifications to the Anthropomorphic Phantom	178

5.3.1.2 Anthropomorphic Phantom Assembly	183
5.3.1.3 Phantom Measurements and Determination of Population Percentiles Represented	184
5.3.1.4 Virtual Colonoscopy Simulation in an Anthropomorphic Phantom	187
5.3.1.5 Simulated Virtual Colonoscopy Data Analysis	187
5.3.2 <i>In-Vivo Rectal Dose Measurements during Virtual Colonoscopy</i>	189
5.3.2.1 Maintenance of Control of TLDs during VC Procedure	190
5.3.2.2 Patient Rectal Dose Determination	190
5.4 Specific Aim 3: Compare In-Vivo Rectal Dose Measurements to Anthropomorphic Phantom Measurements, CTDI-Based Dose Estimates and Point Dose Measurements from a Uniform Phantom	198
5.5 Potential Future Work	201
5.6 Conclusions	205
REFERENCES	208
VITA	223

LIST OF FIGURES

Figure 1-1: Trans-axial view of VC image	3
Figure 1-2: Rectal catheter and enema bag assembly	4
Figure 1-3: Processed sagittal 3D image generated during a VC exam	4
Figure 1-4: Administration of stool-tagging enema	5
Figure 1-5: Thermoluminescent dosimeter energy band diagram	12
Figure 2-1: GE LightSpeed VCT Scanner	40
Figure 2-2: 32 cm CTDI body phantom with insert rods	42
Figure 2-3: CIRS model 701 ATOM adult male phantom	44
Figure 2-4: CIRS ATOM adult phantom simulated adipose tissue kit	45
Figure 2-5: ATOM phantom pelvis with simulated adipose tissue assembled	45
Figure 2-6: Double chamber TLD capsule obtained from the RPC	49
Figure 2-7: Custom-made CTDI insert rod in varying stages of assembly	53
Figure 2-8: Custom-made CTDI insert rod with TLD in seating	53
Figure 2-9: Radcal 0.6 cm ³ 9060/10x5-0.6 Farmer-style ionization chamber	58
Figure 2-10: Radcal 3 cm ³ 9060/10x5-3CT pencil-style ionization chamber	60
Figure 2-11: Radcal 9010 electrometer and converter unit and 90C5-6 extension cable	62
Figure 2-12: Close up view of E-Z-EM 8925 Miller™ Enema Air Tip rectal catheter	64
Figure 2-13: Interior view of rectal catheter tip	65
Figure 3-1: Pencil ionization chamber at CT isocenter for in-air measurements	71
Figure 3-2: X-ray tube located at 180 degree position of the CT scanner	72
Figure 3-3: Configuration used to measure unattenuated exposure (I_0)	73
Figure 3-4: Configuration used to measure x_1 and x_2 attenuated exposures (I_1 and I_2)	74
Figure 3-5: Configuration used to measure CTDI body phantom center bore exposure	76
Figure 3-6: Configuration used to measure body phantom 12 o'clock bore exposure	77

Figure 3-7: Configuration measuring center bore exposure with Farmer chamber	79
Figure 3-8: Configuration measuring CTDI body phantom center bore TLD dose	81
Figure 3-9: Images of patients with TLDs located in ATOM sections 33, 34, 35	86
Figure 3-10: Maximum rectal diameter measurements at three TLD locations	87
Figure 3-11: Estimation of cross-sectional area of patients and insufflated rectums	88
Figure 3-12: Determination of the location of an insufflated rectum in the axial plane	89
Figure 3-13: ATOM phantom section 34 before insufflated rectum modification	91
Figure 3-14: ATOM phantom section 34 after insufflated rectum modification	92
Figure 3-15: Miller™ enema air tip rectal catheter after modification for phantom	93
Figure 3-16: Assembly of Styrofoam plug and rectal catheter to ATOM phantom	94
Figure 3-17: Circumference measurement locations on the ATOM phantom	97
Figure 3-18: ATOM phantom configuration in simulated VC of 15 th percentile patient	104
Figure 3-19: ATOM phantom alignment via laser with marks on MDCT table	106
Figure 3-20: Assembly of 87 th percentile phantom configuration in simulated VC	108
Figure 3-21: ATOM phantom configuration in simulated VC of 87 th percentile patient	109
Figure 3-22: ATOM phantom configuration in simulated VC of 99 th percentile patient	111
Figure 3-23: Disassembly of 99 th percentile phantom configuration	113
Figure 3-24: QA test #1: Placement of TLDs into water bath for 24 hours	116
Figure 3-25: Cross section diagram of TLD placement within the rectal catheter	117
Figure 3-26: Application of silicone glue to the interior of the rectal catheter	119
Figure 3-27: Correct application of silicone glue to the interior of the rectal catheter	119
Figure 3-28: Two suture strings tied in the first throws of surgeon's knots	120
Figure 3-29: Proper placement of the first TLD to the interior of the rectal catheter tip	120
Figure 3-30: Proper insertion of the second TLD into the rectal catheter tip	121
Figure 3-31: Proper final placement of two TLDs within the rectal catheter	122
Figure 3-32: Illustration of measurement of relative bone density by HUs	135

Figure 3-33: Patient VC image histogram and thresholded VC image	136
Figure 4-1: Plot of linear output of x-ray tube with increasing mAs	143
Figure 4-2: Measured Farmer dose in body phantom versus uncorrected TLD dose	147
Figure 4-3: Regression of $K_{L,120}$ values versus uncorrected TLD dose	151
Figure 4-4: Phantom rectal dose predictions versus effective diameter	156
Figure 4-5: In-vivo and phantom rectal dose measurements versus effective diameter	160
Figure 4-6: Distribution of VC patients participating in the study	163
Figure 4-7: Patient relative bone density as a function of HU measurements	164
Figure 4-8: Percent of highly attenuating voxels at the mean TLD location	165
Figure 4-9: Visual comparison of low and high percents of highly attenuating material	165
Figure 5-1: Comparison between ATOM phantom with and without solid water plug	180
Figure 5-2: Comparison between fat distribution in patients and ATOM phantom	194

LIST OF TABLES

Table 1-1: MD Anderson CT protocol for VC	6
Table 1-2: Potentially negative aspects of TLD-100 and potential prophylactic actions	11
Table 1-3: k values converting DLP estimates to effective dose estimates	27
Table 3-1: ATOM phantom circumference measurements and percentiles represented	97
Table 3-2: Phantom and first adipose layer measurements and percentiles	98
Table 3-3: Amount of supplemental lard to add to phantom with first adipose layer	99
Table 3-4: Phantom and second adipose layer measurements and percentiles	101
Table 3-5: Amount of supplemental lard to add to phantom with second adipose layer	102
Table 4-1: Results of HVL and QVL measurements under VC simulation conditions	141
Table 4-2: Results of in-air exposure measurements and $(CTDI_{100})_{air}$ values	142
Table 4-3: Results of CTDI body phantom exposures, $CTDI_w$, and $CTDI_{vol}$ values	145
Table 4-4: Results of Farmer and TLD dose measurements in $K_{L,120}$ determination	149
Table 4-5: Summary of rectal dose estimates from the uniform CTDI body phantom	152
Table 4-6: Results of TLD rectal dose measurements in the anthropomorphic phantom	154
Table 4-7: Estimated patient rectal doses resulting from scout images	157
Table 4-8: Results of in-vivo TLD rectal dose measurements during VC	159
Table 4-9: In-vivo TLD dose measurements and percent differences from predictions	162
Table 4-10: Mean square error (MSE) assessment of the phantom dose predictions	168

CHAPTER 1.0: INTRODUCTION

1.1 Virtual Colonoscopy (VC)

1.1.1 VC Background

According to the Agency for Healthcare Research and Quality (AHRQ), more than 80 million Americans at average risk for colorectal cancer (CRC) should be screened, but only half have done so by any means (1). As a result, CRC remains the second-leading cause of cancer deaths in the United States. Although optical colonoscopy (OC) is considered to be the gold standard for screening, the number of qualified endoscopists is limited and unable to meet the demands of screening, diagnosis, treatment, and surveillance; thus, additional screening options are needed (2).

Virtual colonoscopy (VC) (also known as CT colonography (CTC)) was first described in 1994 by Dr. David Vining as a minimally invasive means for identifying colorectal polyps and colorectal lesions (3). The majority of patients undergoing OC could avoid the procedure's inherent risks of bowel injury and sedation by undergoing VC instead. The procedure consists of #1) bowel cleansing with cathartic agents, #2) gas insufflation with carbon dioxide, #3) computed tomography (CT) scanning of the abdomen-pelvis in supine and prone positions, and #4) image analysis for identification of lesions.

VC is most appropriate for the following populations: asymptomatic patients at average-risk who are 50 years of age or younger, patients with previously known polyps or neoplasms that have not yet been resected (in some clinical contexts), symptomatic patients requiring diagnosis (in some clinical contexts), patients having undergone incomplete endoscopy and requiring additional structural information, patients with colorectal lesions deemed indeterminate by OC, and patients at high risk for OC.

Contraindications for the use of VC typically include: patients with chronic inflammatory bowel disease, patients at high risk for colorectal polyps or colorectal lesions, patients (in appropriate clinical context) with various colorectal pathologies (colitis, diverticulitis, recent surgery or perforation, or high-grade small bowel obstructions), patients requiring evaluation for disease of the anal canal, patients with a prior history of anaphylactic reactions to contrast agents, and patients who are pregnant (4).

VC has been proven to be an effective first-line screening test in the average-risk population (5). As a result, the American Cancer Society now includes VC in its screening guidelines (6). However, the Centers for Medicare and Medicaid Services (CMS) concluded in 2009 that the evidence was insufficient with respect to VC's performance in the Medicare population and its potential harms, namely radiation risks and management of extracolonic findings; therefore, CMS denied coverage for VC until these issues can be resolved (7).

1.1.2 VC Procedure at MD Anderson Cancer Center

Thorough bowel cleansing and optimal distention of the colon are critical for obtaining accurate VC results, although both are difficult to achieve reliably. As a result, patients often undergo CT scanning in supine and prone positions to evaluate segments of the colon that may be collapsed during one of the scans, as well as to shift residual feces and water that may mask or simulate colonic lesions. MD Anderson VC protocols dictate that all patients receive both prone and supine CT scans.

Stool tagging involves administering an iodine contrast agent to the colon to change the x-ray attenuation of residual feces and water to aid in identification of underlying polyps (Figure 1-1). The contrast enemas are prepared by mixing 120 cc of MD-Gastroview® (Mallinckrodt Imaging Solutions, Hazelwood, MO) with 1000 cc of warm tap water in a

standard double-contrast enema bag. Patients are excluded from VC procedures if they report a prior history of a contrast reaction to iodinated-contrast agents.

The following outlines the steps of the VC procedure at MD Anderson Cancer Center (after initial screening qualifies a patient for this procedure):

1. The patient undergoes bowel cleansing prior to presenting at the clinic in a standard fashion with the oral administration of a polyethylene glycol solution.
2. The patient is placed in a supine position on a 64 channel CT scanner table (typically the “CT9” scanner).
3. The rectal catheter assembly (Figure 1-2) is lubricated with water-soluble jelly and inserted into the patient’s rectum. After insertion, a retention balloon on the end of the rectal catheter is inflated to maintain a seal against the anus and prevent rectal catheter and contrast expulsion (Figure 1-3).



Figure 1-1. Trans-axial view of VC image. Stool tagging aids detection of polyps under water.



Figure 1-2. Rectal catheter and enema bag assembly.

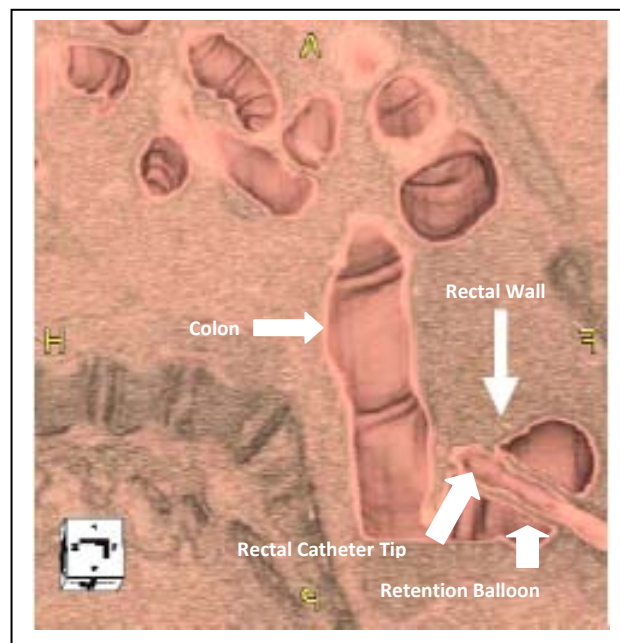


Figure 1-3. Processed sagittal 3D image generated during a VC exam. The rectal catheter is shown within the patient's rectum (with the retention balloon inflated).



Figure 1-4. Administration of stool-tagging enema

4. The patient is placed in a left-lateral decubitus position, and the enema solution is administered under gravity pressure (Figure 1-4). The patient is then rolled to the right to allow the enema to flow into the ascending colon, and the patient is returned to a supine position. This maneuver only takes a few minutes to perform.

5. The rectal enema bag is lowered to a level below the patient to drain excess fluid from the rectum.

6. The enema tubing is clamped.

7. Gas insufflation is performed using a CO₂ insufflator connected to the air insufflation port of the double-contrast rectal catheter. At least 1.5 liters of CO₂ gas delivered at a pressure of 25 mm Hg is administered prior to the start of the supine CT scan. If patients experience excessive discomfort at the 25 mm Hg pressure setting, the pressure is often reduced to 20 mm Hg.

8. The patient is then placed in a supine position, and lateral and anterior-posterior (AP) survey (or “scout”) images are acquired by the CT technologist. After the technologist

verifies patient positioning and specifies the scan length from these scout images, the patient undergoes a supine CT scan according to the standard MD Anderson Cancer Center CT technique described in Table 1-1. Following the supine scan, the patient is rolled to the prone position, the retention balloon is deflated, and the process is repeated by acquiring two CT scouts and a prone CT scan (using the same imaging technique).

Table 1-1. MD Anderson CT protocol for VC.

Series	Description	Scan Type	Rotation Time (s)	Area	Image Thickness (mm)	Table Speed (mm/cycle)	Pitch	Image Interval (mm)	kVp	mA	Delay	Reconstruction
1	SCOUT Supine	AP and Lateral		Mid-Sternum to Trochanter					120	10		
2	Supine	Full Helical	0.5	Diaphragm to Symphysis	1.25	39.37	0.984	0.8	120	100	0	Standard
3	SCOUT Prone	AP and Lateral		Mid-Sternum to Trochanter					120	10		
4	Prone	Full Helical	0.5	Diaphragm to Symphysis	1.25	39.37	0.984	0.8	120	100	0	Standard

9. Upon completion of both CT scans, the rectal catheter is removed.

10. Each VC examination is processed and interpreted by a board certified radiologist using computer software that is routinely used at MD Anderson Cancer Center. Figures 1-1 and 1-3 demonstrate examples of colonic images that result from VC.

1.1.3 VC Computed Tomography (CT) Radiation Dose

One of the perceived harms of VC is the risk of radiation-induced cancer. The radiation dose received by patients while undergoing CT scans of any anatomy (not just VC) has been the subject of recent high-profile media activity (8-12). A standard CT scan of the abdomen and pelvis delivers weighted sum of organ doses (called an effective dose) of 10-15 milliSievert (mSv) (13). This patient risk metric is based on the *linear no threshold* risk model developed from research findings from atomic bomb survivors receiving total body mixed radiation (14). Radiation dose contributions from CT scout images are typically

considered to be negligible compared with the dose administered by the actual CT scans (15).

As a comparison to the dose a patient receives in CT, the average American receives about 3 mSv of annual ubiquitous background radiation (16). Phantom measurement estimates suggest that the average patient undergoing a VC scan with the protocols used by MD Anderson receives an effective dose of 7 mSv and has an absolute increased risk of developing colon cancer by 1 in 2000 (17). In an effort to mitigate radiation risks, several recent VC studies have used low-dose CT techniques yielding effective doses as low as 0.8-2.4 mSv (18, 19). However, each of these estimates of effective dose are based on CT dose index (CTDI) values that are determined from homogeneous acrylic phantom dose measurements and mathematical geometric models of a standard reference person that do not represent the heterogeneous tissues or sizes of patients that undergo VC.

Effective dose is a generic indicator relating to the risk of health detriment to a reference patient. It is more appropriate to base risk estimates on the absorbed doses to the organs receiving the bulk of the radiation when only a limited number of organs are irradiated (20), as is the case in VC where only the abdomen and pelvis are irradiated. In these circumstances, effective dose is diluted by the inclusion of many organs that receive little or no radiation dose. A small effective dose, therefore, does not necessarily indicate a low risk from examinations such as VC. A better alternative for quantification of risk assessment to an individual is provided by organ dose estimates or measurements specific to that individual (20), and such is the method preferred by epidemiologists focused on long term risk assessment.

To date, no in-vivo organ dose measurements have been performed for VC scans; thus, the accuracy of any current dose estimates is currently unknown. Although MD

Anderson VC scanning protocol suggests a 7 mSv average patient effective dose using current methods, many uncertainties exist regarding the risk experienced by MD Anderson patients as a result of undergoing VC exams. Therefore, the need exists to utilize available radiation dose measurement tools to better assess the risk to a patient undergoing VC. In spite of these quoted risk estimates, however, Brenner recently suggested that the potential benefits of VC outweigh its potential radiation risks (17).

1.2 Thermoluminescent Dosimeters (TLDs)

1.2.1 TLD Overview

Solid state dosimeters are those solid materials that provide at least one measurable response to radiation exposure and energy deposition within its active material (21). The use of solid state dosimeters was first published in 1895 (22), and these materials are believed to be the first detectors ever used to evaluate the presence of ionizing radiation (21). Today, the most common solid state dosimeters are thermoluminescent dosimeters (TLDs)—which are classified as solid state dosimeters that emit a light signal when appropriately heated that is proportional to the absorbed radiation dose within the material. Optically stimulated luminescent dosimeters (OSLDs), which emit a light signal proportional to absorbed dose when exposed to a light of specific wavelength, are quickly rising in popularity (23).

Over the years of development that have taken place since the introduction of $\text{CaSO}_4\text{:Mn}$ as a thermoluminescent phosphor in 1895 (22), many TLD materials have been introduced into the marketplace and are used today in medical applications. Lithium fluoride (LiF), first introduced as a TLD material in 1950 by Daniels (24), was revitalized in 1961 by Cameron, et al (25) and has grown in popularity to be the most widely used TLD material (26) because of its advantages over other TLD materials; including: high-

temperature thermoluminescence, inert qualities, insolubility, tissue equivalence, little change in response across a wide range of doses and energies, considerable detection capability across broad energy and dose ranges, low fading, and versatility for several types of radiation (21, 25-29). The Harshaw Chemical Company (Cleveland, Ohio) worked with Cameron to develop “TLD-100” (21, 27), which is the most commercially used variety of LiF (LiF:Mg,Ti) that uses the naturally occurring isotope of Li (7.5% Li-6, 92.5% Li-7) and includes doping with Magnesium and Titanium (26) to act as activators of the material's thermoluminescence (27). Common variations of this material are “TLD-600” (which uses an enriched form of Li-6 (95.6%) to increase sensitivity to neutrons) and “TLD-700” (which uses less than 0.1% of Li-6 such that the material becomes insensitive to neutrons) (26).

As available commercially today, TLD-100 dosimeters provide many advantages to users; most of which are for application in personal and radiotherapeutic dosimetry. They can be manufactured as very small chips or ground into powder to conform to the geometry of its container. They have a very wide useful range for photon dose ranging from 50 μ Gy-1000 Gy (26). They demonstrate little fading (5-10% per year) (21, 26, 27). They are dose rate independent (28), can provide very good precision (as low as 0.22%(30)) and have good accuracy (below 3% with a precision of <1% (26)) with sufficient effort and cost. Finally, the photon effective atomic number ($Z_{\text{TLD-100}}=8.2$) is very close to that of tissue ($Z_{\text{Tissue}}=7.4$); which makes this material substantially tissue equivalent for most applications (31).

In spite of these advantages, proper TLD-100 utilization to obtain optimal results requires consideration of some inherent difficulties and disadvantages that can often be reduced with careful execution. The shortcoming requiring the most consideration is the lack of response uniformity between TLD-100 batches, and even within thermoluminescent material samples taken from the same batch (26). These non-uniformities can be accounted for by determining sensitivity corrections (in units of absorbed dose per charge-

in-air per mass) for each specific batch by using sensitivity correction standards with each reading, by monitoring for drifts in TLD response throughout a reading session via controls, by using well-mixed and characterized TLD-100 powder as opposed to chips, and/or by using more than one dosimeter chip per measurement point. Other difficulties intrinsic to quality TLD measurements, along with appropriate measures to minimize the accompanying negative impacts, are listed in Table 1-2 (26).

Table 1-2: Potentially negative aspects of TLD-100 and potential prophylactic actions

	Negative aspects of TLD-100	Corrective Actions
1	Little uniformity between and within TLD-100 batches	Determine sensitivity corrections for each specific batch at each reading, use controls to monitor for drifts in TLD reader response, use well-mixed and characterized TLD-100 powder (versus chips), use >1 chip per measurement point
2	Over-response of TLD at low energies (<100 keV) (21, 26, 28)	Determine the energy correction coefficient in these low energy ranges, use a more tissue-equivalent TLD such as lithium borate ($\text{Li}_2\text{B}_4\text{O}_7$)
3	Over-response of TLD at high doses (>1000 Gy)	Understand and adhere to the dose range limitations of the TLD material, use a TLD material that can appropriately respond such as $\text{Li}_2\text{B}_4\text{O}_7:\text{Mn}$
4	Spurious thermoluminescence and/or tribothermoluminescence caused by surface trapping states creating background light signals that impact TLD readout (21, 26, 28)	Using nitrogen gas (versus ambient air) in the reader and use a uniform TLD powder size
5	Significantly decreased TLD precision if adequate controls are not taken (often at 10% or more (32))	Use carefully controlled conditions, a high-quality TLD reader, an experienced technician, determine sensitivity corrections with each reading session using standard TLDs, use additional control TLDs when shipping, and monitor TLD response in a reading session with control TLDs
6	Direction of radiation field affecting TLD response	Use symmetrically sized chips or powders
7	TLD response may change with exposure to visible or ultraviolet light	Keep all TLDs in a light- and temperature-safe environment when not in use
8	Heating rate or overall reader instability during read-out affecting TLD response	Use carefully controlled conditions, a high-quality TLD reader, an experienced technician, and monitor TLD response in a reading session with control TLDs
9	Size of TL detector may influence readings	Use consistently sized dosimeters for every reading
10	Thermal history affecting energy response of TLD	Anneal the TLD material, do not store the TLDs longer than 1 week after annealing, maintain a consistent temperature cycle for an entire batch, minimize or eliminate the re-use of TLD material
11	TLD-100 toxicity if ingested	Appropriately train all personnel regarding the risks and proper handling of TLD-100 material
12	Time and cost associated with TLD-100 readout	Budget time and resources appropriately when using TLD-100 for measurements

1.2.2 TLD Physics

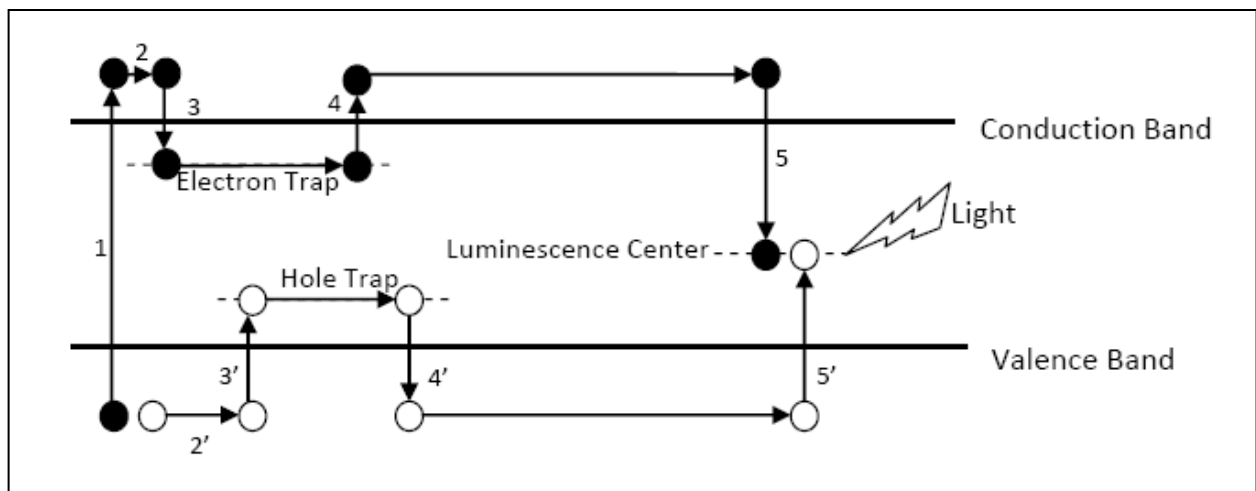


Figure 1-5. Energy band diagram modified from (31) demonstrating measureable light production as a result of exposure to radiation. In an unexcited state, electron-hole pairs exist within the valence band of the crystal matrix. When excited by ionizing radiation, electrons are launched into the conduction band (step 1). In the conduction energy band, electrons may migrate in the crystal lattice (step 2) and positively-charged holes migrate along the valence band (step 2'). Imperfections within the matrix create electron and hole trap levels (steps 3 and 3', respectfully). The excited TL material remains in a metastable state until sufficient heat energy is applied to the system to release these entities back into the conduction and valence bands, respectfully (steps 4 and 4'). These electrons and holes recombine at luminescence centers within the crystal lattice (steps 5 and 5') emitting light.

The theory and physics of thermoluminescence is a very complex subject with intricacies that extend far beyond the scope of this work. On a basic level, however, the theory of thermoluminescence can be explained with the assistance of Figure 1-5, which is an energy band diagram that demonstrates the production of measureable light (visible or ultraviolet) as a result of exposure to radiation. In a normal state unexcited by ionizing radiation or temperature, electron-hole pairs exist within the valence band of the

thermoluminescent crystal matrix. In the presence of ionizing radiation, electrons are freed and move to the conduction band as demonstrated in step 1 of Figure 1-5. In the conduction energy band, electrons may migrate through the crystal lattice as demonstrated in step 2. Accordingly, positively-charged holes may also migrate along the valence band as demonstrated in step 2'. Thermoluminescent materials rely on imperfections within the matrix to create energy trap levels that may encumber both free electrons and holes, as demonstrated in steps 3 and 3' (31). Thus, after excitation the TL material remains in a metastable state with both the holes and electrons unable to move and recombine in a de-excitation process. The doping of LiF with Mg (300 ppm) in TLD-100 accomplishes the creation of such electron traps (26). These electron and hole traps are thermally sensitive, and electrons and holes remain trapped until sufficient energy is applied to the system (in the form of heat) to release these entities back into the conduction and valence bands, respectively. The specific amount of heat required depends on the depth of the traps and the temperature of the TLD material (31). Once released, as demonstrated in steps 4 and 4', these electrons and holes may recombine at luminescence centers within the crystal lattice as shown in steps 5 and 5' and emit measurable light proportional to the excitation received by ionizing radiation. The doping of LiF with Ti (15 ppm) in TLD-100 accomplishes the generation of such luminescence centers (26).

The radiation dose limits of detection are a function of the TLD-100 material, the material set-up and history, irradiation conditions, and TLD readout capabilities. Many of these factors were discussed above and TLD readout specifics will be discussed below. However, with regard to limitations of the TLD-100 material specifically, the upper radiation dose limit is determined by saturation of available traps by electrons, irradiation history, and annealing (21, 26, 31). This phenomenon is observed when TLD readings overestimate the radiation dose due to increased sensitivity, and is known as supralinearity (because the apparent dose response from the TLD material is no longer linear with the actual dose).

The actual dose where this permanent damage to the material is observed is batch dependent (for example, with slightly varying concentrations of Ti), but it is published to be commonly pronounced at 1000 Gy (26) for TLD-100 material. The sensitivity, or linear dose response region, of a batch of TLD-100 material can be increased (sensitized up to a factor of five) or decreased with certain annealing techniques (26, 31, 33).

The lower-limit of the radiation dose detection capabilities of TLD-100 material vary by batch (again, primarily based on batch composition), but is published to be 50 μ Gy (26). Besides composition, the lower radiation dose limits of a batch of TLD-100 material is (similarly to the upper radiation dose limits) observed as supralinearity (over-response). In contrast to the upper radiation dose limit, though, this observed supralinearity is a function of low temperature traps within the lattice (26), spurious signals caused by ambient air being absorbed by the TLD-100 material during with the readout process (21), powder grain size (26), and tribothermoluminescence (21) (defined below).

As a standard feature of a good TLD readout process, the composition variability is overcome by thoroughly mixing the ground TLD powder of a batch and by characterizing and quantifying the material to specific correction factors for every batch and every reading session. Additionally, TLD materials are often preheated to 160°C for 10-20s (34) to eliminate low temperature electron traps; and spurious signals are overcome by minimizing TLD material exposure to air and by using nitrogen gas during TLD readout. Decreasing powder grain size will decrease the relative dose response of TLD-100 material to radiation (26) (which may lead to reduced supralinearity in the low dose region), therefore the grain size of a batch of TLD powder should be as uniform as possible—which emphasizes the need for careful quality control in the manufacturing of TLD-100 materials and distribution of these powders into capsules.

Tribothermoluminescence is defined as unwanted spurious background light signals that are related to the total surface area of the material in the form of friction (21, 26).

These surface trapping state effects (along with ambient air gas absorption) can be partially corrected by sufficient encapsulation of the dosimeter powder (21). Further, the influence of tribothermoluminescence can be characterized by accomplishing TLD-100 radiation dosimetry measurements with TLD-100 powder grains of various sizes (26). These measures are rarely undertaken, however, as the majority of applications for TLD-100 dosimetry measurements are at cancer therapy energies and doses at which this effect is not observed. These effects may, however, impact dose measurements obtained in low energies and dose environments such as those encountered in diagnostic imaging and VC. Additional measures may be required in TLD-100 dosimeter handling and in the quantification of dose linearity and energy correction factors if using TLD-100 dosimetry in such diagnostic applications (which can overrespond by as much as 40%) as opposed to lithium borate ($\text{Li}_2\text{B}_4\text{O}_7\text{:Mn}$), which has better tissue-equivalence properties under these conditions (31).

1.2.3 TLD Readout Process

Although TLD-100 dosimeters can provide very precise and accurate radiation dose measurements for a wide range of doses and energies, a proper TLD readout process requires considerable attention to detail and substantial documentation. The mission of the National Cancer Institute (NCI)-funded Radiologic Physics Center (RPC) at MD Anderson Cancer (Houston, TX) is “to assure National Cancer Institute and the Cooperative Groups that institutions participating in clinical trials deliver prescribed radiation doses that are clinically comparable and consistent.” The RPC fulfills this mission through accurate and consistent radiation measurement capabilities and by conducting quality assurance audits of institutions. More specifically, the RPC’s TLD equipment, policies, and professionals monitor the radiation dose delivered to patients in cancer therapy at sites participating in NCI clinical trials worldwide. Thus, their TLD program is among the very best available and

is designed to minimize and/or eliminate the potential opportunities for the TLD uncertainties and reading errors mentioned above and to optimize measurement precision and accuracy. They publish an overall uncertainty of 2.5% in their TLD measurement process at radiation therapy dose and energy levels (including phantom set-up and beam calibration) (35).

The TLD-100 material used by the RPC is grown as LiF crystals by Thermo Scientific (Waltham, MA) and prepared for the RPC by Quantaflux, LLC (Dayton, OH). Upon purchasing the material from Thermo Scientific, Quantaflux grinds and sifts the crystals into a powder. Such grinding and thorough mixing is necessary to overcome both the small inherent non-uniformities within a single LiF crystal and the non-uniformities between the several LiF crystals contained in a TLD-100 batch sufficiently large to accommodate the quantity of TLDs used by the RPC. Thus, appropriately prepared TLD-100 powder will not have capsule-to-capsule variation in radiation response, as is the case with TLD chips (31).

After mixing, Quantaflux loads specially-designed plastic TLD capsules (designed to maintain a snug fit into the RPC's large inventory of acrylic blocks and anthropomorphic phantom inserts) to the RPC specifications (approximately 22 mg of powdered LiF per aliquot). Upon receipt from Quantaflux, the RPC quantifies the fading, energy, and linearity correction factors for the batch of TLD-100 material (more specific explanations of these and other correction factors are provided below). Once the material's radiation response characteristics have been sufficiently quantified, they are sent (along with phantoms and instructions) to those institutions enlisted by the NCI to conduct clinical trials.

After an institution has irradiated a TLD filled phantom as carefully instructed by the RPC, that institution returns the block and paperwork to the RPC for analysis. When received, analysis begins at the RPC by reading 3 "standards" TLDs (a 4 mm diameter by 15 mm length plastic capsule with a wall thickness of 1 mm containing a single aliquot of

TLD-100 material) that have been irradiated on the Cobalt V2 machine at MD Anderson Cancer Center. This irradiation is conducted at least 14 days prior to the reading of the TLDs received by the institution being assessed (which are also read at least 14 days after irradiation to stabilize the dose response within the TLD-100 material—thus reducing potential time related variability (drift) in the dose measurements).

Irradiation of the standards TLDs is a carefully controlled process conducted by the RPC that includes: inserting 3 TLDs into an acrylic block phantom similar to that sent to the institutions for evaluation, positioning the TLD block on a jig attached at 80 cm source-to-surface distance (SSD) from the cobalt-60 source, and irradiating the block to 3 clicks (4.45181 Gy as calibrated on 10/15/2005) in a 10 x 10 cm field. These standards (which are from the same batch of TLD-100 material as those irradiated by the institution being assessed) are used to establish the sensitivity correction factors used for the calculation of dose to the irradiated TLDs.

Next, 3 “control” TLDs are read, which are also carefully irradiated in a controlled process by the RPC by a different cobalt-60 source than that used to irradiate the standards (MD Anderson’s “Cobalt C” machine). The two irradiation processes are similar, with the primary differences being the fact that the control TLDs are irradiated on a moving carousel attached to a jig and that the control TLDs are irradiated to 5 clicks (4.2924 Gy as calibrated on 10/15/2005). Once the 3 standards and controls are read, the technician begins the reading process on the measurement TLDs irradiated by an institution.

Every TLD is measured in a consistent manner to avoid uncertainties in the readings. After the Harshaw TLD reader (ThermoFisher Scientific Corporation, Santa Fe, NM) has warmed-up for approximately 20 minutes, an independently-certified mass of approximately 20 mg is placed on the scale for calibration purposes. Next, a plastic block fashioned to hold 3 TLD capsules is placed on the scale, the end of a TLD capsule that does not contain the plug is cut and discarded, the TLD is placed in this acrylic block and

on the scale for measurement, and the scale is again zeroed. The TLD-100 material is then placed on the TLD reader planchette, the planchette is inserted back into the reader, and the emptied capsule is returned to the block on the scale and the mass deficit of the removed TLD material is recorded.

At the next full minute, the reading process is begun by pressing the “start” button and typing the mass deficit measurement from the scale into the computer (thus documenting the mass of the LiF powder being read). Once activated, the reader will steadily heat the LiF to 318°C and will measure the integrated charge generated by the stimulation of photomultiplier tubes as light is emitted from the TLD-100 material (specifically in glow peaks IV and V (26)). This charge and mass are recorded on the technician's worksheet, and when the reader temperature has cooled to 110°C the planchette is reopened and the read TLD-100 material is removed by vacuum. The process of reading one TLD capsule should take a total of 2 minutes, and the TLD reading process continues with the next TLD in a series. A typical TLD reading session begins with 3 standards being read, then 3 controls, then 6-8 sets of 3 measurement TLDs, then 2 controls, then 6-8 sets of 3 measurements, then 2 controls, then 6-8 sets of 3 measurements. The reading session ends with 3 controls and 3 standards being read; and a typical reading session lasts approximately 3 hours and includes 6 standard TLDs, 10 control TLDs, and 54-72 measurement TLDs.

Once the charge and mass readings have been obtained for each of the TLDs, the following correction factors are determined based on the properties of the TLD-100 batch and the irradiation parameters: sensitivity (K_S), fading (K_F), linearity (K_L), energy dependence (K_E), and f-factor (or absorbed dose to the medium as opposed to the absorbed dose to the TLD material). Finally, the TLD dose is calculated by multiplying the measured average charge per mass by all of the correction factors. As the effective atomic mass of TLD-100 is similar to that of tissue, the estimated dose to tissue is easily calculated

by applying an f-factor (if necessary). As standard protocol, the RPC provides their radiation dose measurements to their customers as absorbed dose to muscle (with the f-factor already factored into the sensitivity correction factor).

1.2.4 TLD Correction Factors

1.2.4.1 Fading Correction Factor

The TLD fading correction factor accounts for the fact that some electrons will gain sufficient energy at room temperature to escape from their traps, thus resulting in loss of signal and potential uncertainties in dose measurements. For TLD-100 material, this value is relatively small (5-10% per year) (21, 26, 27) and is most unpredictable within the first 14 days. Therefore, the RPC recommends performing TLD readout 14 or more days after irradiation to reduce uncertainty. Per RPC protocols, TLD fading (K_F) is calculated by (36):

$$K_F = \frac{N}{\left(a \cdot e^{(-b \cdot X)} + c \cdot e^{(-d \cdot X)}\right)} \quad (1-1)$$

where N, a, b, c, d are values established when a TLD-100 batch is commissioned and X is the number of days since the TLD material being read was irradiated.

1.2.4.2 Linearity Correction Factor

The TLD linearity correction factor corrects for TLD material response to dose, since dose response is measured by the increase (or decrease) in the light per mass emitted during readout as dose to the material increases (or decreases). For TLD-100 material, this value is typically linear (with variations existing between batches) from approximately 200 mGy to 6 Gy (for the RPC's B09 TLD-100 batch). Radiation dosimetry measurements

performed for doses outside this range will require additional characterization to assess the supralinearity characteristics of this batch and determine appropriate batch linearity correction factors (K_L) for the dose range being investigated. Per RPC protocols, K_L is calculated for doses within a commissioned dose range by (36):

$$K_L = m \cdot d_{raw} + b \quad (1-2)$$

where m and b are values established when a TLD-100 batch is commissioned and d_{raw} is calculated from (36):

$$d_{raw} = \frac{Q}{mg} \cdot K_S \cdot K_F \quad (1-3)$$

with Q being the integrated charge read by the TLD reader (in μC), mg being the mass of the irradiated TLD-100 material (in mg), K_S being the system sensitivity correction factor, and K_F being the fading correction factor.

1.2.4.3 Sensitivity Correction Factor

The TLD sensitivity correction factor (K_S) is calculated by dividing the decay-corrected expected dose delivered to the standards by the cobalt machine by the product of the average of the standard measurements, the fading correction factor for the standards (which may be different from that of the TLDs being read), and the linearity correction for the standards (using the decay-corrected expected dose as the raw dose value) as shown by (36):

$$d_{\text{exp}} = d_{\text{cal}} \cdot e^{-\left(\ln(2)/T_{1/2}\right) \cdot t} \quad (1-4)$$

$$K_s = \frac{d_{\text{exp}}}{(K_F)_{\text{Std}} \cdot (K_L)_{\text{Std}} \cdot \left(\left(\frac{Q}{mg}\right)_{\text{Std}}\right)_{\text{Avg}}} \quad (1-5)$$

$$(K_L)_{\text{Std}} = m \cdot d_{\text{exp}} + b \quad (1-6)$$

where d_{exp} is the decay-corrected expected dose delivered to the standards TLDs by the cobalt machine, d_{cal} is the dose delivered by the cobalt source when it was calibrated, $T_{1/2}$ is the half-life of cobalt-60, t is the time elapsed between the calibration of the cobalt source and the irradiation of the standard TLDs, $(K_F)_{\text{Std}}$ is the fading correction factor for the standard TLDs, $(K_L)_{\text{Std}}$ is the linearity correction factor for the standard TLDs, and $((Q/mg)_{\text{Std}})_{\text{Avg}}$ is the average of the six standard TLD measurements.

1.2.4.4 Energy Correction Factor

The TLD energy correction factor corrects for TL material over-response (compared to tissue response) to the energy to which the TLD was irradiated, which can be as high as 40% in low energy (diagnostic) applications (31) and as high as 6.5% at cancer therapy energies (36). For TLD-100 material, this value is typically unity (with variations existing between batches) from approximately 1 MV to 4 MV (for the RPC's B09 TLD-100 batch as determined at batch commissioning). Radiation dosimetry measurements performed for energies outside this range require additional characterization to assess the energy response characteristics of a specific TLD-100 batch for the energy range being investigated.

1.2.4.5 f-Factor Utilization

As standard protocol, the RPC provides their radiation dose measurements to their customers as absorbed dose to muscle (with the appropriate f-factor already included in the sensitivity correction factor). There are applications where it is necessary to determine an additional factor to correct from dose to muscle to another medium reflecting the environment in which a TLD was placed when irradiated (for example, in air or in an acrylic phantom). In such situations, an additional f-factor (f) should be included in dose calculations considering TLD irradiation environment by (26, 37):

$$f = \left[\frac{(\mu_{en} / \rho)_{Environment}}{(\mu_{en} / \rho)_{Dosimeter}} \right] \quad (1-7)$$

where $(\mu_{en}/\rho)_{Environment}$ is the mass absorption coefficient of the environment in which the TLD was located (in cm²/mg), and $(\mu_{en}/\rho)_{Dosimeter}$ is the mass absorption coefficient to which the TLD dosimeter was calibrated (in cm²/mg). These mass absorption attenuation coefficient values can often be obtained from data published by the National Institute of Standards and Technology (NIST) (38).

1.2.5 TLD Dose Calculation

Finally, considering all of the correction factors presented above, the dose to a medium can be calculated from TLD light output and mass measurements by (26, 31):

$$\bar{D}_{Medium} = \frac{Q}{mg} \cdot K_S \cdot K_L \cdot K_E \cdot K_F \cdot f \quad (1-8)$$

where \bar{D}_{Medium} is the dose to a medium (in mGy), Q is the integrated charge measured from the TLD light output of a TLD-100 sample during the reading process (in μC), m is the mass of the irradiated TLD-100 material (in mg), K_S is the sensitivity correction factor (in $\text{mGy} \cdot \text{mg} / \mu\text{C}$), K_L is the linearity correction factor (unitless), K_E is the energy correction factor (unitless), K_F is the fading correction factor (unitless), and f is the f-factor correcting for the medium in which the TLD was irradiated (unitless).

1.3 CT Radiation Dose Measurements

1.3.1 Background of CT Dose Measurements

Although the radiation dose received by patients while undergoing CT scans has been the subject of recent high-profile media activity (8-12), the need to measure this entity was realized in the very early days of computed tomography. Perry and Bridges were the first to publish CT radiation exposure and dose measurements in 1973 using an ionization chamber pressed in wax between a polymethyl methacrylate (PMMA) cylinder and a water-filled soccer ball bladder taking point exposure measurements for single slice CT (39). TLD-100 was first used to measure single slice CT exposure in 1974 (40). Among the first to present a system for characterizing multi-slice CT dose was a group from the US Food and Drug Administration (FDA) lead by Shope in 1981 when he introduced the concept of CT Dose Index (CTDI) and the corresponding phantoms (41), which has evolved with technological advances and continues to be the clinical standard for characterizing CT scanner x-ray beam output.

1.3.2 CT Dose Index (CTDI)

CTDI provides a convenient technique used to estimate the average absorbed dose delivered from multiple contiguous CT irradiations (including scatter tail dose pile-up) by subjecting the standard PMMA CTDI phantom to one axial scan; or (42):

$$CTDI = \frac{1}{N \cdot T} \int_{-\infty}^{\infty} D(z) dz \quad (1-9)$$

where N is the number of data channels, T is the detector width sampled by each channel (and the product N*T is therefore the total nominal x-ray beam width during the scan (37)), and D(z) is the radiation dose profile along the z-axis (the axis parallel to the CT table). Practically, this expression is simplified to an entity that can be realistically measured with a commercially available 100 mm pencil ionization chamber (42):

$$CTDI_{100} = \frac{1}{N \cdot T} \int_{-50mm}^{50mm} D(z) dz \quad (1-10)$$

Since the pencil ionization chamber effectively measures the integrated exposure along its active length, this expression can be simplified to (37):

$$CTDI_{100} = \frac{(f \cdot C \cdot E \cdot L)}{N \cdot T} \quad (1-11)$$

where f is the f-factor that converts in-air exposures to dose in air (0.87 rad/R or 8.7 mGy/R), C is the electrometer calibration factor, E is the reading provided by the electrometer after one axial scan in the center of the CTDI phantom (in R or mR), L is the

active length of the pencil ionization chamber (100 mm), and the product N*T is the total nominal x-ray beam width during the scan.

However, since the dose distribution within an object (the CTDI phantom in this case) is not uniform throughout (with increased dose being deposited superficially), the CTDI-weighted index ($CTDI_w$) was also created. This is obtained by taking $CTDI_{100}$ measurements at the center of the CTDI phantom ($CTDI_{100}^{center}$) and by averaging $CTDI_{100}$ measurements taken 1 cm below the surface at the 12, 3, 6, and 9 o'clock positions ($CTDI_{100}^{periphery}$), or (37):

$$CTDI_w = \frac{1}{3}(CTDI_{100}^{center}) + \frac{2}{3}(CTDI_{100}^{periphery}) \quad (1-12)$$

It has been estimated that $CTDI_{100}^{center}$ and $CTDI_{100}^{periphery}$ tend to underestimate the equilibrium dose (i.e. the true “saturation” dose at $z=0$, including the dose scatter tails as the measured medium length approaches infinity (43)) by a factor of 0.6 and 0.8, respectfully (42).

In order to account for the changes in dose deposition related to variable x-ray beam distribution (such as with gaps or overlaps in beam coverage), the CTDI-volume index ($CTDI_{vol}$) is calculated from this $CTDI_w$ value as (37):

$$CTDI_{vol} = CTDI_w \cdot \frac{(N \cdot T)}{I} \quad (1-13)$$

where I is the table movement per rotation of the x-ray tube. For helical scans, this expression becomes (37):

$$CTDI_{vol} = CTDI_w / pitch \quad (1-14)$$

where pitch is the table distance traveled in one complete revolution of the x-ray tube divided by the nominal beam width, or (37):

$$pitch = I / (N \cdot T) \quad (1-15)$$

$CTDI_{vol}$ provides a useful estimate of the average radiation dose (in mGy) within a scanned volume of PMMA for a specific scan protocol (42). These estimates are only intended to be applied for CTDI phantoms of similar attenuation and size undergoing an identical CT scan technique; and can only be reliably used in such circumstances. This does not typically include human imaging since patient anatomy is heterogeneous and exhibits varying attenuation and size properties.

A noticeable shortcoming of the $CTDI_{vol}$ measurement is that it does not account for the length an object is scanned ($length_{scan}$) (in cm). In other words, regardless of whether an object is scanned for 20, 50, or 100 cm, the $CTDI_{vol}$ dose estimate remains the same (42). Therefore, the dose length product (DLP) is calculated (in units of mGy-cm) by the following equation (37):

$$DLP = CTDI_{vol} \cdot length_{scan} \quad (1-16)$$

It has been estimated that DLP underestimates the total energy imparted by 30% for all scan lengths (42). Further, the units for this entity are not intuitive and therefore not very helpful in a clinical setting to determine the dose (or perhaps more appropriately, the risk) a

patient receives as a result of a CT scan. Fortunately, DLP can be used to estimate the biological effect or detriment to an individual undergoing a CT scan based on the body region irradiated to yield an effective dose (E) (in mSv). This is calculated by (42):

$$E \approx k \cdot DLP \quad (1-17)$$

where k is a coefficient (in mSv/(mGy*cm)) published in AAPM Report 96 (shown in Table 1-3) that is specific to a patient's age and the region of body scanned.

Table 1-3: k values published in AAPM Report 96 (42) to convert 16 cm or 32 cm diameter head CTDI phantom-based DLP estimates to effective dose estimates. Adult head, neck, head and neck, and pediatric patient k values were based on the 16 cm diameter phantom; while the remaining k values were based on the 32 cm diameter phantom.

Region of Body	k (mSv/(mGy*cm))				
	0 Years Old	1 Year Old	5 Years Old	10 Years Old	Adult
Head and Neck	0.013	0.0085	0.0057	0.0042	0.0031
Head	0.011	0.0067	0.004	0.0032	0.0021
Neck	0.017	0.012	0.011	0.0079	0.0059
Chest	0.039	0.026	0.018	0.013	0.014
Abdomen and/or Pelvis	0.049	0.03	0.02	0.015	0.015
Trunk	0.044	0.028	0.019	0.014	0.015

The k coefficients provided in Table 1-3 were determined by Monte Carlo simulations on the Medical Internal Radiation Dose (MIRD) Committee's MIRD V anthropomorphic mathematical phantom (42, 44, 45); which has also been incorporated into the CT dose research performed by the United Kingdom's formerly named National Radiological Protection Board (NRPB) (now known as Radiation Protection Division of the

Health Protection Agency), the Imaging and Performance Assessment of CT (ImPACT) group's CT dose models (46-48), the Monte Carlo simulation program created by McNitt-Gray's group at the University of California at Los Angeles (UCLA), and many others. Although this phantom is based on reference data published in ICRP Publication 23 (49) and is considered among the best such models in existence (as evidenced by the fact that it is among the most common of the mathematical phantoms used for estimating patient dose), this phantom is based on the radiological response to only three generalized tissues (bone, lung, and soft tissue) in 27 radiosensitive organs modeled after geometric shapes; and therefore is limited in its ability to predict patient dose for the wide variety of patient sizes and shapes that undergo VC.

Further, while CTDI is a good measure of CT scanner output, it is not intended to represent the dose for patients—who present in widely varying sizes, shapes, and attenuation (50). Since a standard CTDI phantom is only 15 cm long in the axial direction, and a pencil ionization chamber is only 10 cm long, CTDI techniques will naturally underestimate scatter doses experienced in typical adult anatomy by not considering the “tails” of the z-axis dose profile (51). Additionally, CTDI is technically expressed in terms of dose-to-air (not dose to tissue) based on its f-factor of 0.87 rad/R (or 8.7 mGy/R); so such estimates are technically a step away from tissue dosimetry (50). The appropriate f-factor correlating dose in a material to dose in air for a CTDI phantom has been demonstrated by Monte Carlo modeling to vary by location within the phantom, the presence or absence of a bowtie filter, the kVp setting, the length of the pencil ionization chamber, and by the diameter of the CTDI phantom (51).

CTDI is so ubiquitous in CT imaging that modern CT scanners provide $CTDI_{vol}$ and DLP value estimates to users, and DICOM structure reports at MD Anderson Cancer Center additionally provide a dose report for clinicians for those scans performed since January 2010. The term “dose report”, however, as labeled in ClinicStation is something of

a misnomer and reported CTDI_{vol} and DLP values are misleading because of these limitations. Although effective dose can be calculated from these CTDI_{vol} values and is commonly used to quantify risk, with anthropomorphic phantom experiments showing good agreement between cumulative organ dose measurements and these CTDI-based effective dose values (52), during a VC scan only the abdomen and pelvis are irradiated. Additionally, VC protocols at MD Anderson Cancer Center utilize a static CT technique regardless of the size of the patient, which will result in more centrally located organs (like the rectum) receiving lower doses on larger patients than on thinner patients. Since the number of organs irradiated is low and the potential inter-patient organ dose variance may be high, using CTDI-based effective dose estimates may under- or overestimate true patient risk. Therefore specific organ doses are more appropriate to quantify patient risk in such instances (20).

1.3.3 Monte Carlo Method

Monte Carlo modeling, when validated by independent phantom or in-vivo measurements, is considered the gold standard for calculating dose to an organ from irradiation. Monte Carlo modeling is a computationally intensive technique developed through the 1930's and 1940's that has been used to study complex systems (including those in the physical sciences, engineering, applied statistics, business, telecommunications, and gaming fields) that have many coupled degrees of freedom, significant uncertainty of input parameters, and complicated boundary conditions (53). As the term "Monte Carlo" was coined in honor of the famed casino of the same name in Monaco (54), this method relies on repeated sampling of random events (via random or pseudo-random numbers) and probability statistics to investigate problems; thus allowing for the examination of more complex systems than can be investigated by more deterministic means (55). For example, calculating the interaction of a single x-ray photon

with one or two atoms of a single tissue type within the body can be solved fairly simply; however, solving the system of interactions for the many tissues within the body for the relatively large number of photons emitted during a VC exam is impractical by any other means besides Monte Carlo modeling.

For CT, this simulation procedure requires development of the CT scanner model (as the source of the x-rays), the patient model (using the acquired images), and the x-ray beam path (in this case, a helical geometry). ImPACT's CTdosimetry software is probably the most used research tool for estimating organ doses and is based on CTDI and Monte Carlo data in a single-size patient geometry MIRD V mathematical phantom (56), but makes several assumptions in its methodology that may result in uncertainties in dose estimates (44). The Monte Carlo process created by McNitt-Gray's group at the University of California at Los Angeles (UCLA) is a well-documented and validated methodology (44, 57-62) created specifically for MDCT; but this methodology is also limited in that since it uses patient images as the basis for its calculations, the results yielded by such simulations are very patient specific and therefore limited in terms of patient size and organ distribution. This Monte Carlo process is valuable, though, in that it can provide organ dose estimates for true patient geometries. True (i.e. direct) CT point dose measurements would be ideal to validate or benchmark such a Monte Carlo modeling procedure.

1.3.4 CT Point Dose Measurements

Direct CT dosimetry measurements using TLDs, Farmer (aka thimble) ionization chambers, metal-oxide semiconductor field-effect transistors (MOSFET), film, diodes, plastic scintillators, or optically stimulated luminescent dosimeters (OSLDs) (23) are often performed in research to validate other indirect means of determining radiation dose (e.g. CTDI, surface exposure, mathematical models, or Monte Carlo simulations). Ideally, direct methods are preferred for radiation dose measurement (63) because they provide true

measurements of radiation interactions in a medium. Unfortunately, these measurements are rarely realized because they are typically considered invasive and often unsafe for use in a patient. Therefore, various phantoms have been developed to mimic a true patient using standard reference organ sizes and locations and by using materials that are approximately tissue equivalent in the CT energy and dose range.

When validating an indirect dosimetry assessment tool like a mathematical (64) or Monte Carlo (58, 63, 65, 66) model (for example) , or when estimating the dose to an organ during a procedure (40, 64, 67-71), TLDs are typically placed on the surface of and/or inserted into the organs of anthropomorphic phantoms and in-air exposure or organ dose measurements are made using the CT protocol modeled. Since indirect methods/models are typically based on approximations from (often similar) reference patient and organ sizes, comparison results between indirect dosimetry methods (for example, between Monte Carlo simulations and anthropomorphic phantom measurements) are often reported to be favorably consistent with one another (65, 66) (with anthropomorphic testing being used to benchmark and/or validate Monte Carlo modeling results). While agreement between model and phantom measurement results is a testament to the ability of such a model to represent the physics scenario within a given situation, such models may not in reality provide an accurate understanding of the absorbed doses received by a patient; as has been observed in a study comparing anthropomorphic phantom dose to cadaver dose from identical CT protocols (72).

Non-agreement between cadaver and phantom measurements or Monte Carlo models may be due to the fact that both simulations and phantoms are fundamentally based on approximations to patient size, shape, and radiation response; and additionally to the possibility that radiation dose response within a cadaver may differ from that in living tissue or in a phantom. Therefore, although phantom measurements are valuable from practical and risk-reward perspectives, they may not provide accurate patient organ

absorbed dose measurements as they are based on approximations to true patient size and in-vivo radiation dose response; and the accuracy of a Monte Carlo model that is benchmarked against a phantom (which is inherently based on approximations) can be questioned. Thus, in-vivo organ absorbed dose measurements are necessary to benchmark and validate existing indirect measurement models such as phantoms or Monte Carlo simulations.

1.3.5 MD Anderson VC Rectal Dose Estimates

VC offers an opportunity to obtain in-vivo organ dose measurements without additional duress to a patient because a rectal catheter (to which TLDs can be affixed) is inserted into a patient as a routine aspect of the procedure. Additionally, the centrality of the rectum within a patient's body decreases the likelihood that surface dose variations that are characteristic of CT scans (61) will result in TLD point dose measurement inconsistencies and/or errors. To date, direct in-vivo organ dose measurements have never been performed for internal organs during VC scans or even during MDCT scans in general; thus, the accuracy of any indirect dose estimates is currently unknown (17-19, 73). Further, although the average VC patient effective dose is estimated to be 7 mSv at MD Anderson, such effective dose estimates are based on calculations from reference patients and uniform phantoms; therefore uncertainty exists with such risk estimates (20).

Previous in-vivo CT measurements have been conducted for cone beam CT (CBCT) by Walter, et al and Jeng, et al. Walter used a 7 mm diameter ionization chamber inserted into patients' rectums (74) (that was connected to an electrometer requiring input potentials of up to ± 400 V). Jeng used TLDs attached to a rectal catheter that was inserted into the rectum (75). Using rectal dose measurements from these studies to estimate VC rectal dose provides questionably correlated results because CBCT, not MDCT, was used

to acquire these in-vivo dose measurements; but these studies do lend credence to this general approach of obtaining in-vivo measurements within the rectum.

CBCT is an imaging modality typically used in dental applications and in on-board imaging of modern linear accelerators (linacs) for image guided radiation therapy (IGRT) (which was the application for both Walter's and Jeng's research). Although imaging on CBCT devices is faster than MDCT, the image quality provided by CBCT devices is generally inferior to that of MDCT devices. The differences between the MDCT and CBCT modalities (and therefore opportunities for errors in dose estimation) are many, including: VC protocols at MD Anderson requires the use of a beam width of 40 mm and many rotations of the x-ray tube on the MDCT to obtain image data where CBCT imaging is accomplished in one rotation of the x-ray tube and with a beam width of 450 mm. In fact, Kim, et al. compared the modalities and concluded that under as similar technique constraints as possible, the CTDI measurements for CBCT were 49% lower than those of MDCT (76)—which underscores the fact that the beam dose distribution characteristics of the two modalities are considerably different.

Since the only previous direct in-vivo rectal CT dose measurements that have been obtained do not apply to VC or even MDCT, any VC dose predictions based on these CBCT data are prone to error. In spite of these limitations in accuracy, by assuming CBCT and MDCT both demonstrate a linear relationship between mAs and absorbed dose, and by assuming the linear relationship of the two modalities are correlated, the rectal dose received by a patient undergoing VC can be approximated from the in-vivo data published by Walter (74) and Jeng (75) for the population of patient sizes represented in each study. Doing so, the CT technique used in VC at MD Anderson Cancer Center yield approximate mean rectal doses of 5.2 mGy and 4.4 mGy for each respective population of patient habitus (patient anthropomorphic measurements were not provided by Walter (74); and ranged in Jeng's study (75) from 33.80 cm to 39.22 cm in patient width and from 18.70 cm

to 23.92 cm in patient thickness). Again, these dose estimates were based on several assumptions and therefore are prone to error.

DeMarco, et al performed Monte Carlo modeling using the UCLA code described above on six simulated patients of varying size to determine colonic dose based on whole body MDCT scans; obtaining colonic dose estimates ranging from 11 to 18 mGy (with an average of 13.8 mGy) across the varying sizes at the mAs used in the MD Anderson Cancer Center VC protocol (59). However, this estimate also has limited applicability to the rectal dose received by patients undergoing VC at MD Anderson because the CT scanner x-ray source model used in these calculations was based on a different scanner manufacturer, with a different beam width, for a whole body scan (which will provide more scatter dose to the rectum than VC), and pertained to the dose received by the entire colon (versus just the rectum). For these reasons, the rectal dose received by patients at MD Anderson will likely be less than this value.

Confirmation of this suspected lower rectal VC dose was obtained by simulating the MD Anderson VC protocol using the ImPACT CT dose calculation program. Using this protocol, an equivalent dose of 6.3 mSv is yielded for the lower large intestine of the MIRD V mathematical phantom on which this software is based (with equivalent dose being defined as the organ absorbed dose multiplied by the radiation quality factor, which is 1 for photons (14), thus implying a predicted absorbed dose of 6.3 mGy). A previous study showed that the UCLA Monte Carlo code demonstrated good agreement with ImPACT dose estimates when applied to the same MIRD V mathematical phantom (44), therefore the rectal dose received by patients at MD Anderson is predicted to be less than the 11 to 18 mGy range published by DeMarco (59).

Using Farmer ionization chamber measurements within the center bore of a homogeneous CTDI body phantom exposed using the MD Anderson Cancer Center CT technique for VC, a preliminary rectal dose estimate of 6.1 mGy was achieved. By

mathematically subtracting 6 cm from the CTDI body phantom and applying that thickness to the Lambert-Beer equation (Equation 3-2), an upper limit of a rectal dose estimate of 11.2 mGy was attained (for a theoretical approximate smallest diameter VC patient). An estimated lower rectal dose limit of 0.5 mGy for a very large patient was assumed for a patient undergoing VC at MD Anderson Cancer Center.

This 0.5-11.2 mGy dose estimate is limited, however, since a patient's irradiated volume during VC consists of heterogeneous tissues and since patients of different habitus will have different proportions of self-shielding (via adipose layers, soft and hard tissues, etc), this estimate is also subject to error. Conducting similar measurements in an anthropomorphic phantom would likely eliminate some (but not all) of these phantom homogeneity errors because such measurements would reflect dose to a reference patient, but would not be able to account for random variations in organ size and position that exist between people. Also, the largest source of variation in actual organ dose measurements is likely that introduced by the varying sizes and shapes of patients that undergo VC. Jeng and DeMarco published organ dose variances (resulting from differences in subject body composition) from the mean organ dose of each study population of up to 16.2% (75) and 22.9% (59), respectfully.

In spite of all of the limitations of each of these methods for estimating the patient rectal dose received at MD Anderson as a result of VC, all of these rectal dose estimates are within a consistent range (0.7-14 mGy). Therefore the rectal dose received by patients undergoing VC can reasonably be predicted to also fall within this range; but only actual direct measurements can verify any understanding of the radiation dose administered in such circumstances. This described difficulty in estimating the rectal dose range to be encountered by patients while undergoing VC at MD Anderson underscores the need for in-vivo organ dose measurements.

1.4 Hypothesis and Specific Aims

1.4.1 Hypothesis

Rectal dose measurements obtained in-vivo during virtual colonoscopy will have a rectal dose coefficient of variation that will be greater than 50%; and the anthropomorphic phantom dose measurements, CTDI_{vol}-based dose estimates, and Farmer chamber measurements in a CTDI body phantom will estimate rectal doses outside a 95% confidence interval of the in-vivo patient dose measurements.

1.4.2 Specific Aims

Various options currently exist that can provide estimates of patient organ dose received during virtual colonoscopy (VC). However, all of these techniques incorporate indirect methods that are based on estimates from reference anatomical geometry and may not reflect the actual organ dose received by any individual patient. Such is the case not only for VC, but for all organ absorbed dose measurements for multi-detector computed tomography (MDCT) examinations, where in-vivo measurements have never been feasible to validate indirect dose measurements and estimates. Currently, most MDCT dose estimates are based on measurements in a uniform phantom (which does not accurately represent patient anatomy) either in the form of CTDI_{vol} (which is based on integral dose measurements) or point (Farmer ionization chamber) measurements. Therefore the purpose of this research is to develop a method for obtaining in-vivo rectum dose measurements during VC and to compare these measurements to dose estimates obtained using the same CT scan protocols in an anthropomorphic phantom and a homogeneous acrylic phantom that is ubiquitously used to assess CT scanner radiation output.

1.4.2.1 Specific Aim 1: Establish TLD Linearity Correction Factors for VC Scan Parameters on a MDCT

Using thermoluminescent dosimeters (TLDs) obtained from the National Cancer Institute-funded Radiologic Physics Center (RPC) at MD Anderson Cancer Center, dose linearity correction factors will be obtained at 120 kVp specific to the polyenergetic spectrum produced by a MDCT in VC. These values will be determined by inserting one TLD per scan in an acrylic insert rod (with a custom-made tight TLD seat) and placing the insert rod into the center of an acrylic CTDI phantom. This phantom set-up will be used to irradiate several TLDs using helical scans irradiating the entire length of the CTDI phantom at varying mAs settings. This acquired absorbed dose data (in mGy) will be compiled, compared to point dose data (in mGy) obtained via Farmer ionization chamber, and used to calculate the TLD linearity correction factors for the conditions encountered by variously sized patients undergoing VC at MD Anderson Cancer Center.

1.4.2.2 Specific Aim 2: Obtain Rectal Dose Measurements in an Anthropomorphic Phantom and In-Vivo in Patients Undergoing VC with TLDs

An anthropomorphic phantom will be modified to approximate conditions during VC in three sizes of patients; and two double chambered TLDs will be inserted into the phantom in three iterations to assess VC rectal dose for those patients represented by each respective phantom configuration. Additionally, in-vivo rectal dose measurements will be acquired by affixing two TLDs to the inner lumen of 6 rectal catheters for use in 6 patient VC studies. During a VC procedure, when a catheter is inserted into a patient's rectum, these affixed TLDs will acquire four measurements of the absorbed radiation dose delivered to that patient's rectum using the standard MD Anderson VC MDCT scan technique. 12 rectal dose measurements (in mGy) will be obtained for each of the three phantom iterations and four rectal dose measurements will be obtained within each of the 6 patients

using the dose linearity correction factors established for 120 kVp in Specific Aim 1; along with the charge per mass readings, fading correction factor, and sensitivity correction factor provided by the RPC.

1.4.2.3 Specific Aim 3: Compare In-Vivo Rectal Dose Measurements to Anthropomorphic Phantom Measurements, CTDI-Based Dose Estimates and Point Dose Measurements from a Uniform Phantom

The rectal dose measurements of the three phantom configurations and in-vivo rectal dose measurements from 6 patients will be tabulated along with patient geometry measurements. These dose measurements will be compared to CTDI_{vol}-based dose estimates and point dose measurements (all in mGy) obtained from a 32 cm diameter CTDI body phantom while irradiated with the same technique. Coefficients of variation and 95% confidence intervals will be constructed for phantom, patient rectal dose measurements. This data will be used to test whether the between-patient rectal dose coefficients of variation are greater than 50% and if the anthropomorphic phantom dose measurements, CTDI_{vol}-based dose estimates, and the Farmer chamber dose measurement in a CTDI body phantom are outside the 95% confidence interval of the patient dose measurements.

CHAPTER 2.0: MATERIALS

2.1 Introduction

In order to accomplish the specific aims of this project, several items were required; including: a GE LightSpeed VCT scanner, a CIRS ATOM adult anthropomorphic phantom, a uniform polymethyl methacrylate (PMMA) 32 cm diameter CTDI body phantom (with accompanying insert rods), 79 double chambered thermoluminescent dosimeter (TLD) capsules, a custom-made PMMA CTDI insert rod with a tight TLD capsule seat, two ionization chambers (a Radcal model 9060/10x5-0.6 Farmer chamber and a Radcal model 9060/10X5-3CT CT pencil chamber), a Radcal model 9010 electrometer, and 10 E-Z-EM Super XL double contrast enema delivery systems.

2.2 GE LightSpeed VCT Scanner

Standard virtual colonoscopy (VC) at MD Anderson Cancer Center requires the use of a GE LightSpeed VCT scanner (GE Healthcare, Waukesha, WI) (see Figure 2-1) operating under the scanning protocol described in Table 1-1. This MDCT scanner model was first introduced by GE in 2004, with VCT standing for “volume computed tomography”. At the time of its introduction, this model was a significant upgrade from other MDCTs available in imaging speed capabilities (advertising the capability of imaging a stationary organ in as little as one second and a moving organ like the heart in as little as five seconds (77)). These imaging speeds are accomplished by incorporating more data channels than what was previously available (the GE LightSpeed VCT scanner utilized 64 data channels; while its primary competition at the time used a maximum of either 16, 32, or 40 data channels) and by using a very powerful x-ray tube that provided a beam width capable of irradiating detector lengths of 40 mm (versus the more standard 20 mm detector lengths) at fast rotation speeds (<400 ms) (78). Additionally, regardless of specified scanner

parameter setting, this scanner always collects data at the level of the smallest detector size (0.625 mm), which allows for the retrospective creation of CT images at varying thicknesses. With these developments, the GE Lightspeed VCT scanner was able to provide 73% more coverage per second (when at maximum pitch) than its CT predecessors (78). Although several MDCT scanners have been developed between the launch of this scanner and this writing, this scanner remains a very capable resource for accomplishing VC.



Figure 2-1. GE LightSpeed VCT Scanner (MD Anderson Cancer Center “CT9”).

The GE LightSpeed VCT scanner has the capability to receive image data acquired from its 0.625 mm detectors from 64 channels, and has a 70 cm bore diameter. It has six axial nominal beam widths available (1.25 mm, 2.5 mm, 5.0 mm, 10 mm, 20 mm, and 40

mm). Three pitch values are available for the 40 mm effective beam width used in VC (0.516, 0.984, and 1.375). The table can move through the gantry at speeds up to 137.5 mm/sec during imaging. Additionally, the GE LightSpeed VCT scanner has dual focal spot capabilities, where the scanner chooses the focal spot size based on the selected tube current and voltage to balance spatial resolution (which is better with the smaller focal spot size of 0.9 mm x 0.7 mm) and x-ray tube target heat capability (which is better with the larger focal spot size of 1.2 mm x 1.2 mm) (79). With the capabilities provided by the GE LightSpeed VCT scanner, a single VC prone or supine scan can be accomplished in 2.5-10 seconds (depending on the size of the patient) using standard MD Anderson VC protocols.

At the time of this writing, the Radiologic Physics section of the Department of Imaging Physics at MD Anderson Cancer Center supported four GE LightSpeed VCT scanners; most VC procedures at MD Anderson Cancer Center were performed on MDCT scanner “CT9”, but were also performed on “CT5” and “CT12” as necessary for procedure scheduling purposes. All TLD measurements used to accomplish Specific Aim 1 were performed on “CT9” scanner and VC rectal dose measurements were performed in this study on all three of these VCT scanners. It is not believed that the use of multiple MDCT scanners negatively affected the accuracy of the rectal dose measurements as all four MDCT scanners supported by the Radiologic Physics section demonstrating reasonable consistency in computed tomography dose index (CTDI) measurements in a 32 cm CTDI body phantom in their most recent annual surveys (with percent coefficients of variation of 2.3% for $(CTDI_{100})_{center}$, 2.2% for $(CTDI_{100})_{periphery}$, and 2.1% for $CTDI_w$).

2.3 CTDI Body Phantom

The Computed Tomography Dose Index (CTDI) body phantom used for this protocol was manufactured by the MD Anderson Cancer Center Machine Shop (Houston, TX) according to standardized dimensions. The original design for this phantom was first

published by Shope, et al in 1981 (41) as being a “cylindrical Plexiglas phantom 32 cm in diameter with arrays of LiF thermoluminescent dosimeters inside the phantom”. Since the CTDI technique pioneered by Shope has become the clinical standard for CT dose characterization, the basic design of this phantom has changed little since it was first introduced. The modern design for this phantom contains a bore in the center of the phantom that is sufficiently large (1.3 cm in diameter) to insert a pencil or Farmer ionization chamber; and at least four additional peripheral 1.3 cm diameter bores located at 90 degrees from one another at a depth of 1.0 cm from center of each bore to the phantom surface.

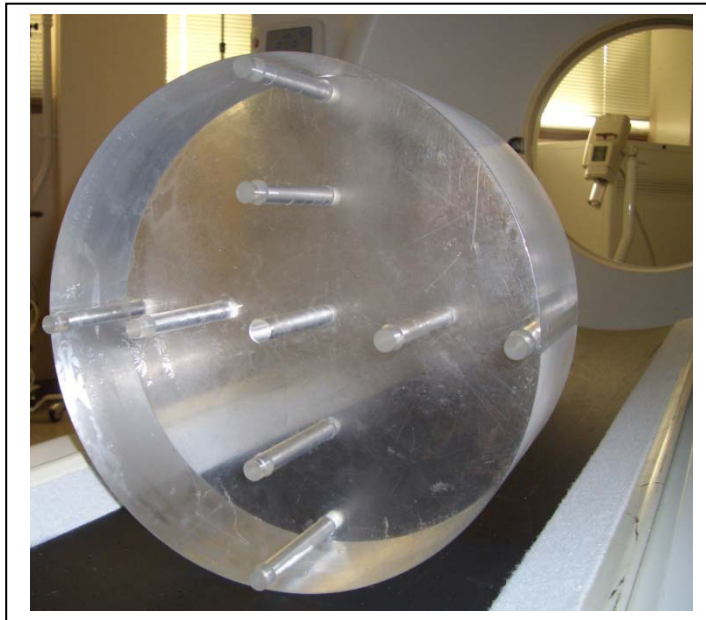


Figure 2-2. 32 cm CTDI body phantom with insert rods.

The CTDI body phantom (see Figure 2-2) contains the five aforementioned bores, along with four additional bores of the same diameter located equidistantly between each of the peripheral bores and the center bore. These additional bores were included into the phantom design to provide dose measurement capabilities that approximate for organ or

fetal locations. The phantom utilizes 8 acrylic insert rods that slide into each bore that is not being used to take measurements (i.e. the remaining bores that do not contain a measurement device) with minimal air gap. Additionally, the CTDI body phantom is uniformly composed of polymethyl methacrylate (PMMA), is fashioned as a 32 cm diameter cylinder that is 15 cm thick, and weighs approximately 13.2 kg (29 lbs). Commercial manufacturers provide CTDI body phantoms with additional features, such as an all-in-one 32 cm CTDI body, 16 cm CTDI adult head, and 10 cm CTDI pediatric head phantom. However, such features were not necessary for this project.

2.4 CIRS ATOM Adult Anthropomorphic Phantom

In addition to the CTDI body phantom, an ATOM adult male model 701 anthropomorphic dosimetry phantom (Computerized Imaging Reference Systems, Inc (CIRS), Norfolk, VA) (see Figure 2-3) was used to estimate the rectal dose received by patients undergoing VC at MD Anderson Cancer Center. The ATOM phantom line was originally developed and manufactured by ATOM Ltd (Riga, Latvia) beginning in 1985, and CIRS assumed exclusive manufacturing privileges of this phantom in 1999 (80). The standard ATOM model 701 adult male phantom consists of an anthropomorphic head, torso, pelvis, and upper femurs modeled in the representation of the “standard” man as published in ICRP 23 (49) from epoxy resins with tissue equivalent properties of adult bone (a composition of average age-based mineral densities and known trabecular and cortical ratios), soft tissue, lung (during held inspiration), spinal cord, cartilage (spinal discs), and brain (81, 82). The epoxy resins representing the bone and soft tissue in this phantom have linear attenuation coefficients that are within 1% of actual bone and water, respectively, from 50 keV to 25 MeV; and the material representing lung tissue during inspiration has a linear attenuation coefficient within 3% of actual lung tissue in this same energy range (81).

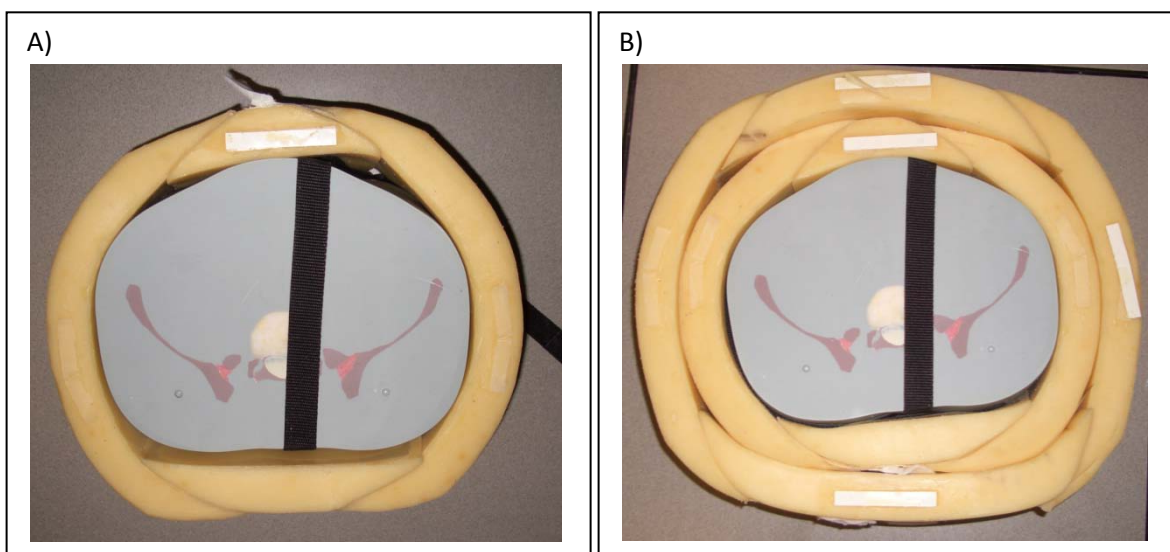


Figure 2-3. CIRS model 701 ATOM adult male phantom.

In addition to these tissue equivalent materials, adipose tissue equivalent fat layers can be purchased from CIRS for application onto the ATOM model 701 adult male phantom in order to accomplish dosimetry studies for larger, more realistic patients (see Figures 2-4 and 2-5). This set of fat layers consists of 10 slabs (4 cm thick by 20 cm in length) of proprietary soft gel material (providing adipose tissue equivalence within 1% for therapy and diagnostic energy photon beams) that has been reinforced with nylon/Lycra mesh and hook-and-latch pads for assembly (83). The 10 fat slabs are of varying lengths and are applied to the outer surface of the phantom abdomen in either one or two layers of four slabs (with two additional larger slabs available to accommodate adding fat to phantom dimensions larger than the abdomen, such as the thorax or pelvis).



Figure 2-4. CIRS model 701 ATOM adult male phantom simulated adipose tissue kit.



**Figure 2-5. A) ATOM phantom pelvis with first layer of simulated adipose tissue assembled;
B) ATOM pelvis with second layer of simulated adipose tissue assembled.**

The adult male ATOM phantom is divided into 39 cross-sectional blocks, with each section measuring 25 mm in thickness. The entire ATOM phantom line can be purchased

with five millimeter diameter bores (revealed after removing custom fitted plugs) strategically placed within 21 radiosensitive internal organs that are capable of housing TLD capsules. Additional customized plugs are available for purchase to house other dosimetry measurement devices such as TLD rods, chips, optically stimulated luminescent dosimeters (OSLD), or metal oxide semiconductor field effect transistors (MOSFET). Film can also be utilized for dosimetry by inserting appropriately sized film between phantom sections and by taping the adjoining sections together with dark tape to prevent light penetration (81).

Overall, the adult male ATOM phantom (including the legs) measures 173 cm in stature (5 ft, 8 in), weighs 73 kg (161 lbs), and has a thorax measuring approximately 32 cm by 23 cm (80-82, 84-86). The standardized anthropometry, access to internal organs, and photon beam tissue equivalence provided by the ATOM phantom have made this phantom a popular choice for experimentation regarding image quality and radiation dose assessment (82). Thus, the ATOM adult male phantom was a useful tool to approximate the rectal doses received by patients undergoing VC at MD Anderson Cancer Center.

2.5 PeopleSize Software

Although the ATOM phantom provided a valuable dosimetric tool with substantial tissue equivalence and the standardized anthropometry established in ICRP 23 (49), it was limited in that with the additional fat slabs this phantom could only represent those patients with one of three available pelvic circumferences. Since the VC technique utilized by MD Anderson Cancer Center is a uniform technique that is not adjusted for patients of varying sizes, the amount of absorbed dose received by the rectum is therefore directly related to that patient's habitus and body composition. Since any phantom experiment can only provide data representative of a limited number of patient sizes, it was important to determine which percentiles of the patient population (generalized in this study to be adults, aged 18-64, residing in the United States) were represented by the phantom data in each

configuration. Additionally, the fat slabs only extended 20 cm along the phantom pelvis; where the appropriate VC scan and scatter length of a patient represented by the phantom (and the average VC patient at MD Anderson Cancer Center) extends much further. Therefore, additional target population anthropomorphic data was needed; specifically regarding circumference measurements in the pelvis, abdomen and chest of a typical patient represented by the phantom with the fat slabs attached, such that additional attenuating material could be attached to the phantom surface in a proportionally appropriate manner. These anthropomorphic data were acquired from PeopleSize 2008 Professional software, version 1.1, developed by Open Ergonomics Ltd (Leicestershire, UK).

PeopleSize 2008 Pro software utilizes a simple user interface to provide customers with data regarding anthropomorphic dimension measurements and percentiles for a desired target population. PeopleSize 2008 provides percentiles and measurements for up to 289 individual anatomical locations for nine nationalities (US, UK, German, Australian, Belgian, French, Japanese, Chinese, Swedish) in up to nine adult age groups (18-64, 18-25, 18-39, 25-50, 40-64, 65+, 65-74, 75+, 85+) as well as pediatric data for every year from 2-17 years and infant data for subjects under 2 years of age (87). Due to limited data availability, complete data sets are not provided for some of these demographics in PeopleSize 2008. At the time of this writing, this software had been incorporated into research conducted by many industries that require ergonomic information; including healthcare, clothing, motor vehicle, and consumer products.

The anthropomorphic data provided by PeopleSize 2008 is based on existing older anthropomorphic survey data (acquired in dates ranging from the 1950's to the 1990's) that have been scaled by size and weight to estimate modern dimensions (with bony dimensions changing over time by a small magnitude and fatty dimensions changing over time by a larger magnitude). The modern dimensions calculated by this software have

been verified by comparing the predicted measurements to government-conducted surveys (including the US Government's most recent National Health and Nutrition Examination Survey (NHANES), conducted from 2003-2006). Such comparisons have found that at the most difficult dimensions to estimate (dimensions where fat is more likely to accumulate), the software demonstrated an overall average error of 0.0% in the 5th percentile and -0.1% in the 95th percentile; with individual landmark dimensions falling within approximately a $\pm 3\%$ margin (87). Thus, the PeopleSize 2008 software provided a dependable means to determine the necessary anthropomorphic dimensions for the target patient population represented by the respective ATOM phantom configurations used to measure simulated VC rectal dose with thermoluminescent dosimeters (TLDs) at MD Anderson Cancer Center.

2.6 Thermoluminescent Dosimeter (TLD) Capsules

As described in Chapter 1.4.2.1, TLDs were used to acquire all in-vivo VC rectal dose measurements. TLDs provide many benefits to users, including the capability of being ground into powder and conformed to the geometry of its container (which provides the added benefit of eliminating directional dependence from dose measurements). Advantages of the TLD-100 (LiF:Mg,Ti) powder used in our measurements also include (26, 31): a wide useful linear dose range (from 50 μ Gy-1000 Gy), performance independent of dose rate, small size, excellent uniformity within a batch (if appropriately prepared), quick and convenient readout, very good precision (as low as 0.22%), low uncertainty (usually around 2-5%, with the uncertainty published by the RPC being 2.5% for their standard set-up at therapeutic doses (35)), commercial availability, and substantial tissue equivalence for most applications.

TLD-100 material has several inherent disadvantages as well, but most of these disadvantages can be overcome with sufficient effort. Examples of such disadvantages include (26, 31): careful calibrations at low doses and energies (diagnostic range) due to

supralinearity of TLD-100 response compared to tissue, the need for specific calibrations for each batch because of batch-to-batch inconsistencies, loss of TLDs due to small size, inconvenience associated with delayed dosimeter reading (a minimum of 14 days is typically desirable), inconvenience and cost associated with readings performed by an outside entity, spurious luminescence effects (which are mostly eliminated with N₂ gas and by using uniform TLD-100 powder grain size), sensitivity that is altered after large doses or repeated doses (which is mostly eliminated with proper annealing techniques or by not reusing material), and reader instability (which can be improved with well-trained technicians and by control TLDs to track changes in charge measurements at uniform doses). Ultimately, the advantages of TLD-100 were determined to outweigh these stated disadvantages, and TLD capsules were determined to be the best method available for measuring patient rectal dose from VC.

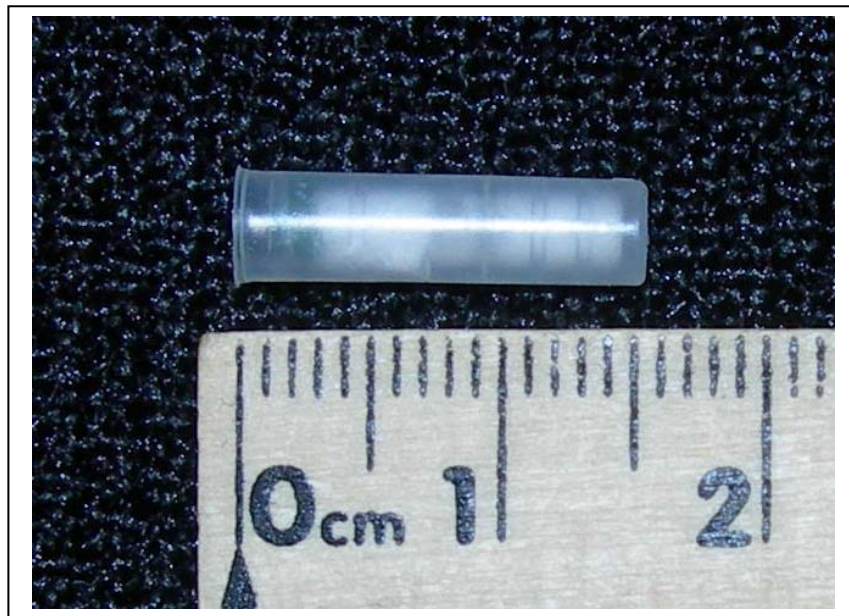


Figure 2-6. Double chamber TLD capsule obtained from the RPC.

The TLDs used in this experiment were obtained from and read by the NCI-funded Radiologic Physics Center (RPC) at MD Anderson Cancer Center (Houston, TX). The TLDs consisted of plastic capsules containing two approximately 22 mg aliquots of ground TLD-100 powder in a double chamber plastic capsule with a wax plug. As mentioned in Chapter 1, the TLD-100 material was grown by Thermo Scientific (Waltham, MA); and was ground, mixed, and packaged into plastic cylindrical capsules (4.0-4.2 mm in tapered diameter by 15.6 mm in length) (see Figure 2-6) by Quantaflux, LLC (Dayton, OH).

When the RPC receives their order of TLDs from Quantaflux, the RPC quantifies the fading, energy, and linearity correction factors for the batch of TLD-100 material (as described above in Chapter 1.2.4). Once the material's radiation response characteristics have been sufficiently quantified, they then provide these TLDs to customers for therapy beam quality assurance purposes. When the TLDs are returned to the RPC from their customers, they wait at least 14 days after irradiation to reduce the uncertainty effects of drift on the TLD charge measurement results. During readout, the mass of an aliquot of TLD-100 powder is determined from a Mettler AT261 DeltaRange analytical balance (Mettler-Toledo International Inc, Griefensee, Switzerland). This mass of TLD-100 material is then placed on the planchette of a Harshaw QS 3500 TLD reader (ThermoFisher Scientific Corporation, Santa Fe, NM) where it is heated at a constant rate to 318 degrees Celsius. The light emitted from the TLD-100 material stimulates the reader's photomultiplier tubes, which is converted to a charge measurement and reported to the RPC's TLD technologist.

The RPC calculates a sensitivity correction factor (K_S) from measurements of Cobalt-60 irradiated standard and control TLDs. This K_S value (in cGy/ μ C/mg) allows one to determine the radiation dose to muscle tissue from the obtained charge and mass readings. The RPC also calculates factors that correct for: fading (K_F) using Equation 1-1:

$$K_F = \frac{N}{\left(a \cdot e^{(-b \cdot X)} + c \cdot e^{(-d \cdot X)}\right)} \quad (1-1)$$

(with coefficient values determined at commissioning of this batch of TLD-100 material to be $a=1.2815$, $b=0.00010885$, $c=0.067810$, $d=0.071908$, $N=1.3493$, and X representing the number of days between irradiation and readout); linearity (K_L) (defined for doses between 200 mGy and 6000 mGy by Equation 1-2, with $m=-0.00028943$, $b=1.08683$, and d_{raw} being defined by Equation 1-3):

$$K_L = m \cdot d_{raw} + b \quad (1-2)$$

$$d_{raw} = \frac{Q}{mg} \cdot K_S \cdot K_F \quad (1-3)$$

and energy (K_E) (defined from energies ranging from Cobalt-60 ($K_E=1.000$) to ≥ 17 MV ($K_E=1.065$)). However, as both the rectal doses and energies encountered by patients undergoing VC are less than the ranges for which the respective correction factors provided by the RPC are valid, Specific Aim 1 was necessary to quantify TLD performance by defining K_L at 120 kVp ($K_{L,120}$) for the range of doses encountered in VC.

2.7 Custom-Made PMMA CTDI Insert Rod

In order to accomplish Specific Aim 1 and define $K_{L,120}$ for the range of doses encountered in VC, it was necessary to provide appropriately varying doses to TLDs under controlled conditions. Since the rectal dose and energy spectrum experienced by a patient undergoing VC at MD Anderson Cancer Center is a function of the size of the patient and the spectrum of the output of the MDCT scanner x-ray tube, it was determined that the easiest way to approximate such conditions would be in a common CTDI body phantom

(which roughly approximates the size and attenuation of a large reference patient). This phantom was determined to be a reasonable and reproducible approximation of the beam hardening and attenuation produced by a patient.

In order to create TLD irradiation conditions as reproducible as possible, such that TLD placement at each irradiation condition was as consistent as possible and the MDCT beam attenuation uniformly approximated the scatter observed in the rectum of a patient undergoing VC, a PMMA insert rod of approximately identical external geometry as that of the insert rods that fill the bores of the CTDI phantoms during standard CTDI phantom use (1.27 cm diameter x 17 cm long cylinder) was designed and created by the MD Anderson Cancer Center Machine Shop (Houston, TX) (see Figure 2-7A). This custom-made insert rod differed from the standard CTDI insert rod in that it could be disassembled (via a tight fitting 0.95 cm diameter x 0.32 cm deep male/female mating). Once disassembled (see Figure 2-7B), a single TLD capsule could be inserted into a tapered 0.45 – 0.46 cm diameter by a 0.80 cm cylindrical seat (see Figure 2-7C). Tape was attached to one side of the insert rod (as seen in Figure 2-7) to ensure the TLD-loaded insert rod was consistently inserted into the CTDI body phantom with the TLD located in the geometric center of the phantom. An additional view of a TLD seated within the female side of the custom-made insert rod is provided in Figure 2-8.

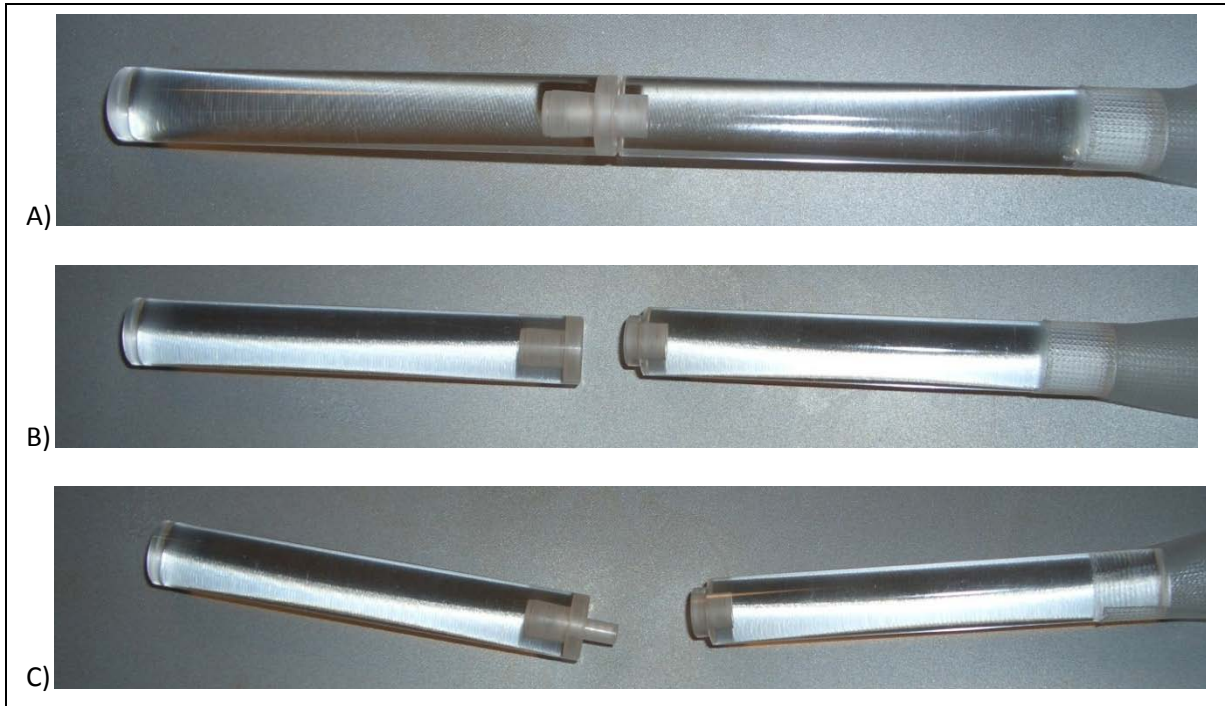


Figure 2-7. A) Assembled custom-made PMMA CTDI insert rod with TLD seat; B) Disassembled custom-made insert rod; C) Disassembled custom-made insert rod with TLD in seating.



Figure 2-8. Female side of disassembled custom-made insert rod with TLD capsule placed in seating.

2.8 Ionization Chambers

To accomplish Specific Aim 1 and define $K_{L,120}$ for the range of doses encountered in VC, independent dose measurements were additionally required to which TLD dose measurements could be compared. Further, in order to identify any potential measurement discrepancies in the event of a change in the x-ray tube within a MDCT scanner between the time the $K_{L,120}$ correction coefficients were determined and when actual anthropomorphic phantom and in-vivo patient VC measurements were acquired, several x-ray beam quality factors were evaluated. These beam quality factors included the beam half-value layer (HVL), quarter-value layer (QVL), CTDI in-air ($(CTDI_{100})_{air}$) (88), and weighted CTDI ($CTDI_w$). Volume CTDI ($CTDI_{vol}$) was calculated from this $CTDI_w$ value, and these measurements were compared to the $CTDI_{vol}$ value displayed on the scanner console. Each of these measurements was obtained using an electrometer and one of two varieties of ionization chambers.

Ionization chambers operate by exploiting and measuring the effects that result when an ionized particle moves through a gas. In their most basic form, ionization chambers are composed of a direct current (DC) voltage source connected to positive and negative electrodes separated by a gas (usually atmospheric air). Significant insulation (often with measures such as a guard ring) is additionally required to protect the integrity of the voltage bias established between the electrodes (89). When ionizing radiation (for example a photon) enters the active volume of the ionization chamber, it interacts with the gas within the active volume and produces an ion pair (a positive ion and a free electron) by either the photoelectric effect, Compton scattering, or pair (or triplet) production; depending on stochastic events and the energy of the incident photon. Secondary photons, electrons, positrons or delta rays created by these interactions result in other ionizations occurring within the chamber as well; and the interactions occurring within the chamber should mirror

those occurring outside the chamber (as long as the chamber walls are sufficiently thick to achieve electronic equilibrium) (89).

The average energy deposited by an incident photon into an active volume is primarily a function of the binding energies of the gas within which it is interacting (90). The number of ion pairs created by interactions initiated by an incident photon can therefore be estimated by dividing the energy of the incident photon by the experimentally-determined average values of energy dissipation per ion pair (also known as W-values) for a type of incident radiation and for a species of gas. When an incident photon creates fast electrons within the active volume of an ionization chamber filled with air (or air equivalent material), the W-value is 33.8 eV/ion pair (89). Therefore, if a 1 MeV incident photon becomes fully stopped within the active volume of an ionization chamber, approximately 33,000 ion pairs will be created.

Under normal conditions in a volume of gas, these newly generated ion pairs will quickly recombine and no net charge will result. Ionization chambers, when connected to an electrometer, utilize a large voltage bias (± 200 V to ± 500 V) surrounding the active volume to minimize or prevent such ion pair recombination. As the recombination of the ion pairs is prevented, the respective ions migrate to the attracting electrode; and the result is a decrease in the bias voltage. An electrometer measures and amplifies this change in the DC voltage bias (ΔV) across a series resistor (R_s) (typically between 10^9 - 10^{12} ohms), and determines the saturated ion current (I_s) by Equation 2-1.

$$I_s = \Delta V / R_s \quad (2-1)$$

The exposure (R) in charge per unit mass (C/kg) is calculated from the saturated ion current provided in Equation 2-1 and time of exposure as shown in Equation 2-2:

$$R = \frac{I_s}{M} \cdot t \quad (2-2)$$

$$M = 1.293 \frac{\text{kg}}{\text{m}^3} \cdot V \cdot \frac{P}{P_0} \cdot \frac{T_0}{T} \quad (2-3)$$

where M is the mass of air in the active volume calculated from Equation 2-3, V is the volume of the ionization chamber active volume (in m³), P is the air pressure in the chamber (in mmHg), P₀ is the standard air pressure (760 mmHg), T is the air temperature in the chamber (in Kelvin (K)), T₀ is the standard temperature (273.15 K), and t is the time of exposure (in sec). Although C/kg is the SI unit for exposure, the more commonly used value for exposure is the Roentgen (R); which is additionally calculated by the conversion: 1 R = 2.58 x 10⁻⁴ C/kg.

As an example to provide insight to the order of magnitude of the measurements required to utilize this technology, if an ionization chamber with an active volume of 1000 cm³ is exposed at a rate of 1x10⁻³ R/hr at standard temperature and pressure, a saturated ionization current of 9.27x10⁻¹⁴ amperes (A) would result. Such low currents underscore the need for the above mentioned significant insulation and guard rings (to prevent leakage of current from the respective electrodes), and for quality electrometer instrumentation. Several models of quality ionization chambers and electrometers are commercially available that have been designed for specific measurement purposes; including the thimble (or Farmer) style ionization chamber, the pencil ionization chamber, and the electrometer described below. These entities were used in Specific Aim 1 to measure beam quality and to establish TLD response correction factors to the MDCT x-ray spectrum experienced by patients undergoing VC at MD Anderson Cancer Center.

2.8.1 Farmer Ionization Chamber

The first fast-responding thimble ionization chamber (cylindrical ionization chambers incorporating two electrodes separated by insulation and a chamber of gas surrounded by air-equivalent material and connected by wire to a feed-back amplifying electrometer) was first introduced by Frank Farmer in 1946 (91). Before his work, ionization chambers were both much slower and much more bulky. In honor of his work developing this detection technology, such thimble chambers are commonly referred to Farmer chambers. Over the years, Farmer ionization chambers have proven to be very valuable tools to medical physicists operating in both therapy and diagnostic disciplines; and they were used in our accomplishment of Specific Aim 1 by providing standard point exposure measurements used to determine the $K_{L,120}$ values for the TLD-100 material for the energy and to estimate the rectal dose range received by patients undergoing VC during survey and CT imaging.

The Farmer ionization chamber used to acquire the baseline values for our TLD exposure measurements was the Radcal model 9060/10x5-0.6 (S/N 16563) (Radcal Corporation, Monrovia, CA). This chamber (shown in Figure 2-9A) has an active volume of 0.6 cm^3 , utilizes C552 air-equivalent conductive plastic walls and electrode, has an active volume of air that is unsealed from the environment, has a 12 m low-noise triax cable, weighs 0.28 kg, and comes with a polyacetal build-up cap (see Figure 2-9B) (92). In order to reduce air gap within a CTDI phantom when this chamber is in place and to provide as uniform a phantom environment as possible, the MD Anderson Cancer Center Machine Shop (Houston, TX) created an acrylic insert rod with a cut along the length of the cylinder to house the triax cord (see Figure 2-9C).

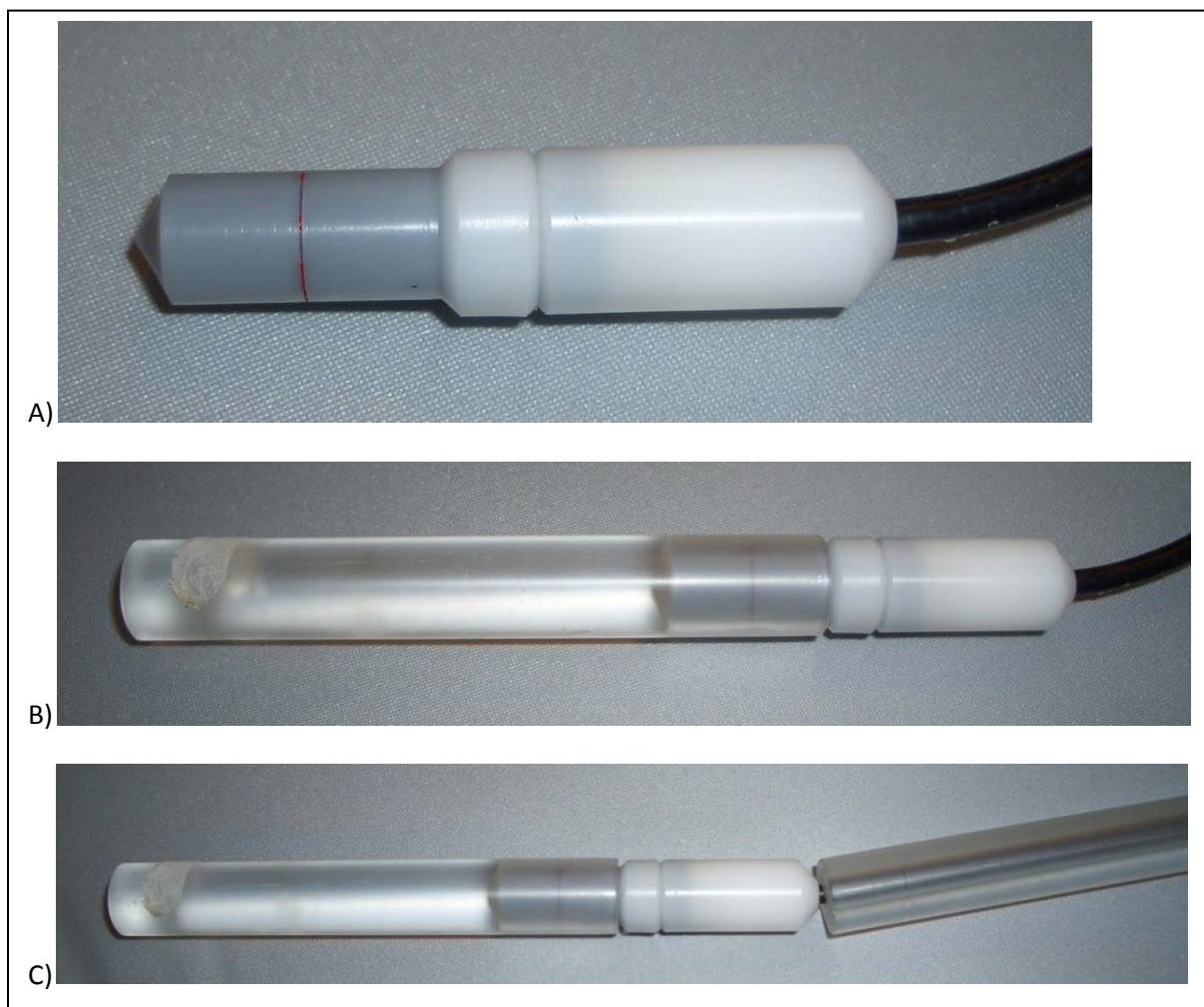


Figure 2-9. A) Radcal 0.6 cm³ 9060/10x5-0.6 Farmer-style ionization chamber; B) Radcal Farmer ionization chamber with build-up cap attached; C) Radcal Farmer ionization chamber with build-up cap and custom-made triax cord insert rod attached.

The active volume of the chamber is 9 mm in diameter and 21 mm in length. The total length of the chamber is 54 mm, and the total diameter is 12 mm. The triax cord is 3 mm in diameter. This chamber can be operated in one of six modes: dose rate (recording air kerma rates ranging from 1 mGy/min to 74 Gy/min), dose (recording total accumulated air kerma ranging from 0.1 mGy to 6 kGy), maximum dose rate (providing the peak air kerma in an exposure from 1 mGy/min to 74 Gy/min), auto dose (for repeated hands-off

measurements where respective measurement parameters (exceeding a 0.6 R/min threshold) don't change between measurements, last dose (for determining total accumulated air kerma at any time during a continuous exposure from 0.1 mGy to 6 kGy), and cine mode (used for machines, like fluoroscopy, that produce exposures in pulses greater than 0.01 mGy/pulse). The resolution provided by this ionization chamber is 1 mGy/min or 0.1 mGy. The energy dependence falls within $\pm 5\%$ for beams of energy between 40 keV and 1.33 MeV when a build-up cap is incorporated; and the exposure rate dependence operates within $\pm 2\%$ between the 6 mGy/min and 6 kGy/min (92). The calibration accuracy provided by this chamber is $\pm 4\%$ after temperature and pressure condition correction when using Co-60 as the calibration source. MD Anderson Cancer Center sends all Farmer ionization chambers for calibration on a biennial basis and cross-calibration checks between similar chambers on an annual basis.

2.8.2 CTDI Pencil Ionization Chamber

In 1978, Suzuki and Suzuki from Capintec, Inc (Montvale, NJ) introduced an expanded, pencil-shaped version of the Farmer-style ionization chamber that was capable of measuring an integrated exposure over a distance (compared to Farmer's chamber that measured exposure at a point) (93). This pencil ionization chamber was created for the expressed purpose of measuring exposures from CT scans, and this tool has found considerable usefulness with the development of computed tomography dose index (CTDI) as a ubiquitous method for measuring CT exposure characteristics. A pencil ionization chamber was used to quantify several CT beam characteristics in the accomplishment of Specific Aim 1 (including half-value layer (HVL), quarter-value layer (QVL), CTDI in-air ($(\text{CTDI}_{100})_{\text{air}}$) (88), weighted CTDI (CTDI_w), and volume CTDI (CTDI_{vol}).



Figure 2-10. Radcal model 9060/10X5-3CT 3 cm³ pencil chamber.

The pencil ionization chamber used to quantify the MDCT beam quality was a Radcal model 9060/10X5-3CT (S/N 8696) (Radcal Corporation, Monrovia, CA). This chamber (shown in Figure 2-10) has an active volume of 3 cm³, utilizes C552 air-equivalent conductive plastic to compose the walls and electrode, has an active volume of air that is unsealed from the environment, has a 2 m low-noise triax cable, weighs 0.11 kg, and comes with a polyacetal build-up cap to create a fit with the CTDI phantom with minimal air gap (92).

The active volume of the chamber is 3 cm³, measuring 9 mm in diameter and 100 mm in length. With the build-up cap, the diameter of the chamber becomes 12 mm and the length is 127 mm. The total length of the chamber with the cap in place is 165 mm, and the total diameter remains 12 mm. The triax cord is 3 mm in diameter. This chamber can be operated in the same six modes as the Farmer chamber within the following air kerma limits: dose rate (1 mGy/min to 15Gy/min), dose (0.01 mGy to 1.2 kGy), maximum dose

rate (1 mGy/min to 15Gy/min), auto dose (1200 mR/min threshold), last dose (0.01 mGy to 1.2 kGy), and cine mode (greater than 1 nGy/pulse). The resolution provided by this ionization chamber is 0.1 mGy/min or 0.01 mGy. The energy dependence operates within $\pm 5\%$ with beams of mean hardness ranging from 3 to 20 mm Al HVL; and the exposure rate dependence operates within $\pm 2\%$ between dose rates of 0.2 mGy/s and 300 mGy/min (92). The calibration accuracy provided by this chamber is $\pm 4\%$ after temperature and pressure conditions when moderately filtered x-rays at 150 kVp and 10.2 mm Al HVL hardness are used as the calibration source. As with the Farmer ionization chamber, calibration of all pencil ionization chambers are performed on a biennial basis and cross-calibration checks are performed on an annual basis.

2.8.3 Electrometer

As mentioned in the descriptions above, neither the Farmer nor the pencil ionization chamber operates unless attached to an electrometer to provide a bias voltage to the chamber, to receive voltage change information, to amplify and process the data, and to provide exposure measurements to the user. A Radcal model 9010 Radiation Monitor Controller electrometer (S/N 90-2261) (Radcal Corporation, Monrovia, CA) was used in Specific Aim 1 to determine the exposures in each irradiation condition as detected by the respective ionization chambers. In order to interchange ionization chambers, this electrometer was connected in series to a Radcal 9060 converter unit (S/N 90-2292), a Radcal 90C5-6 extension cable, and finally the ionization chamber as shown in Figure 2-11. This converter unit allows the Radcal 9010 electrometer to be used with any Radcal 10-series interchangeable ionization chamber (92).

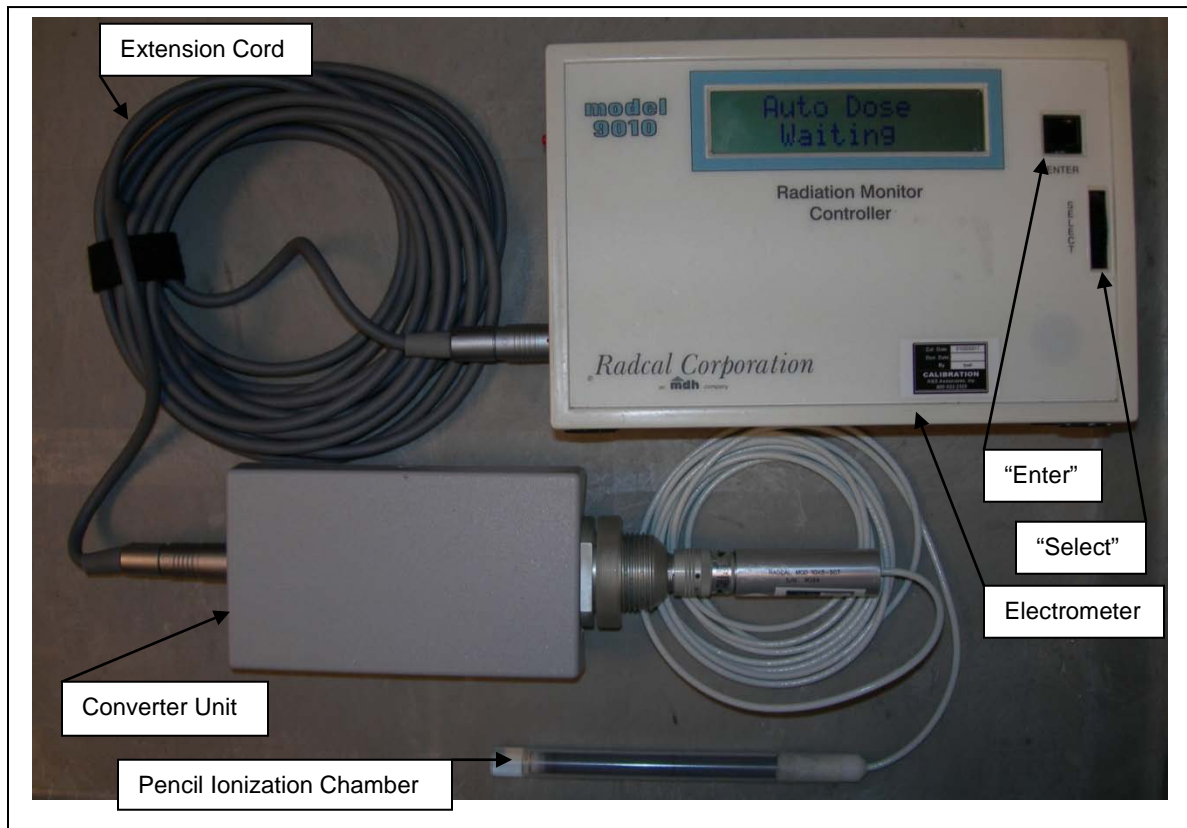


Figure 2-11. Radcal 9010 Radiation Monitor Controller electrometer, Radcal 90C5-6 extension cable, Radcal 9060 converter unit, and Radcal model 10X5-3CT pencil chamber attached in series.

The Radcal 9010 electrometer shown in Figure 2-11 provides measurement displays and menu selections on a two-line liquid-crystal display with 16 characters per line. Menu selections are browsed by turning the “Select” dial and by pressing the “Enter” button when a desired setting is displayed. This electrometer operates in the modes described above for the specific ionization chambers (dose rate, dose, maximum dose rate, auto dose, last dose, and cine mode). The energy response and resolution for each of these modes depend on the ionization chamber utilized.

This electrometer is powered by three 9V batteries, which provide approximately 40 hours of normal use. A “Replace Battery” message is displayed when appropriate. This

electrometer applies a ± 260 V bias to the connected ionization chamber, which requires up to 60 seconds to stabilize when the electrometer is first turned on. As per normal start-up procedures, this electrometer additionally performs room temperature and pressure checks; and displays the necessary ionization chamber correction factor that has been automatically applied to the measurement values displayed. The Radcal 9010 electrometer boasts a measurement repeatability of $\pm 1\%$, and a measurement accuracy of $\pm 4\%$ (92). As with the ionization chambers described above, calibration of all electrometers are performed on a biennial basis and cross-calibration checks are performed on an annual basis.

2.9 Double Contrast Enema Delivery System

As mentioned in Chapter 1, standard procedure for VC at MD Anderson Cancer Center requires the insertion of a rectal catheter into a patient for gas insufflation of the colon and for iodinated contrast agent administration and retention. The rectal catheter and enema system routinely used by MD Anderson Cancer Center during VC procedures is the E-Z-EM Model 8925 Super XL Double Contrast Enema Delivery System (Bracco Diagnostics Incorporated, Princeton, NJ). All contents of this enema delivery system are shown in Figure 1-2 and include: a 2500 cm³ contrast agent bag, 152 cm of 12.7 mm lumen plastic tubing, two plastic tubing clamps, a blue insufflation tube, a blue insufflation bulb (which is not used during VC at MD Anderson Cancer Center), a retention cuff (balloon) inflation bag (containing approximately 100 cm³ of air), 51 cm of 1.6 mm diameter lumen plastic inflation bag tubing, and a flexible Miller™ Enema Air Tip with silicone elastomer inflatable retention cuff (balloon) (94). All contents of this enema delivery system are latex-free, and are used clinically as described in Chapter 1.

The Miller™ Enema Air Tip (see Figure 2-12) is the portion of the enema that is inserted into a patient's rectum while undergoing VC (i.e. the rectal catheter) at MD

Anderson Cancer Center. This is also the portion of the enema delivery system to which TLDs were attached in order to accomplish Specific Aim 2 and obtain in-vivo rectal dose measurements in patients undergoing VC. As can be seen in Figure 2-12, the blue insufflation tube, the large clear contrast agent tube, and the small clear balloon inflation tube converge into the rectal catheter.

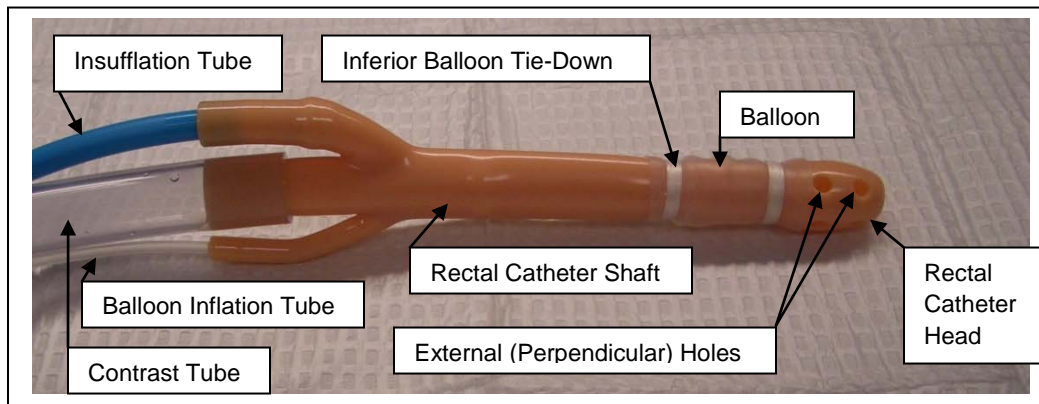


Figure 2-12. Close up view of Miller™ Enema Air Tip rectal catheter contained in the E-Z-EM Model 8925 Super XL Double Contrast Enema Delivery System.

The entire rectal catheter wall thickness is approximately 1.8 mm. Within the interior of the catheter (seen in Figure 2-13), the majority of the shaft volume (approximately 50%) accommodates contrast agent flow into the patient, with the rest of the shaft volume containing extrusions where tubes have been molded into the interior wall of the catheter to accommodate insufflation gas flow and balloon inflation (approximately 25% for each of the two tubes). The balloon inflation tube terminates within the shaft of the rectal catheter into the balloon portion of the shaft just superior to the inferior balloon tie-down. The gas insufflation tube terminates just inferior to the exterior holes on the head of the rectal catheter (perpendicular to the central axis) and contains a port into the central contrast agent volume to expel insufflation gas into a patient's colon.

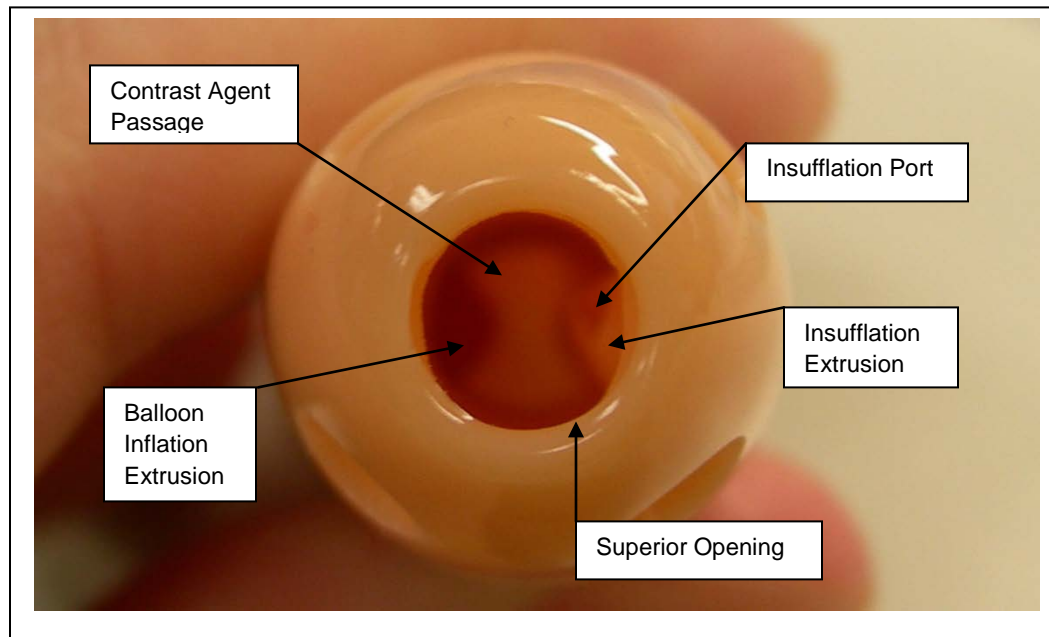


Figure 2-13. Interior view of Miller™ Enema Air Tip rectal catheter.

Superior to the shaft (which measures 9.5 mm across the largest lumen diameter (i.e. where the contrast agent flows)), the diameter opens to a maximum diameter of 13.5 mm in the head of the rectal catheter and narrows to 6.2 mm at the superior opening. Besides the superior opening, the rectal catheter has eight exterior elliptically-shaped holes aligned perpendicularly to the central axis; each providing a port for insufflation gas and contrast agent administration into the rectum and colon that is 3.0 mm in the narrow diameter and 3.9 mm in the large diameter. Each of these internal features of the rectal catheter (the superior hole, the exterior holes, the enlarged diameter head, the shaft with the two extrusions, and the internal insufflation gas port) must be navigated when inserting and affixing TLDs into the head of the rectal catheter as described in Chapter 3 (and illustrated in Figure 3-25).

CHAPTER 3.0: METHODS

3.1 Introduction

The methods used to estimate patient rectal dose during virtual colonoscopy (VC) are described in this chapter in order of the specific aims outlined earlier. First, in accordance with Specific Aim 1, thermoluminescent dosimeter (TLD) linearity correction factors were established for a range of doses at 120 kVp for a multi-detector computed tomography (MDCT) scanner using VC scan parameters in a 32 cm CT dose index (CTDI) body phantom. Next, in accordance with Specific Aim 2, rectal dose measurements using TLDs were obtained in VC simulations within an anthropomorphic phantom and in-vivo within patients undergoing VC. Finally, in accordance with Specific Aim 3, in-vivo rectal dose measurements were compared to anthropomorphic phantom dose measurements, CTDI_{vol}-based dose estimates, and point dose measurements taken in a CTDI body phantom. These specific aims were accomplished in order to test our hypotheses: in-vivo rectal dose measurements obtained during virtual colonoscopy will have a rectal dose coefficient of variation that will be greater than 50%; and anthropomorphic phantom rectal dose measurements, CTDI_{vol}-based dose estimates, and Farmer chamber measurements in a CTDI body phantom will estimate rectal doses outside the 95% confidence interval of the mean patient dose measurements.

3.2 Specific Aim 1: Establish TLD Linearity Correction Factors for VC Scan

Parameters on a MDCT

Although the Radiologic Physics Center (RPC) (Houston, TX) typically provides energy and dose linearity correction coefficients to customers as a standard service, their established correction factors pertain to those doses and energies encountered in photon or electron cancer therapy by linear accelerator and are specifically defined for higher

energies (a minimum of 1 MV) and doses (a minimum of 200 mGy) than those obtained by MDCT dose to a patient's rectum. Therefore Specific Aim 1 was deemed necessary for this project, which provided correction factors relevant for MDCT at the energy and in the dose range encountered in VC. Guidance, TLDs, and TLD readout for the establishment of these coefficients were provided by staff at the RPC (under the direction of Dr. David Followill).

3.2.1 MDCT Beam Characterization

In order to identify any discrepancies in TLD readings and actual dose measurements in the event of a change in the MDCT x-ray tube between TLD irradiation and anthropomorphic phantom or in-vivo patient VC measurements, several x-ray beam quality factors were measured. These measurements were conducted in the same CT sessions as when the TLDs were irradiated to establish the dose linearity correction factors for VC conditions, and upon completion of all in-vivo dose measurements. Doing so provided the additional advantage of producing data that may reduce the variability or uncertainty between the TLD patient dose readings and future Monte Carlo rectal dose calculations because the equivalent source model of some Monte Carlo codes relies on this beam data to develop the virtual CT scanner that delivers the dose to the patient in the simulation (60). These measured beam factors included the half-value layer (HVL), quarter-value layer (QVL), CTDI in-air measured with a 100 mm pencil chamber ($(CTDI_{100})_{air}$) (88), weighted CTDI ($CTDI_w$), and volume CTDI ($CTDI_{vol}$) for the MD Anderson Cancer Center VC technique on the institution's "CT9" GE LightSpeed VCT scanner; as well as HVL and QVL measurements on the "CT5" and "CT12" GE LightSpeed VCT scanners to demonstrate consistency in x-ray tube output between the three MDCT scanners utilized for VC.

3.2.1.1 HVL and QVL Measurement

The HVL and QVL measurements were made using the method described by Mathieu, et al (95) incorporating the Lambert W function (the multivalued inverse of Equation 3-1) as a more generalized form of the Lambert-Beer equation (Equation 3-2) such that it becomes appropriate for the polyenergetic spectrums encountered in CT:

$$z = W(z) \cdot e^{W(z)} \quad (3-1)$$

$$I = I_0 \cdot e^{-\mu \cdot x} \quad (3-2)$$

where z is a complex number (96), I is the intensity of the filtered photon beam (measured as exposure in mR), I_0 is the intensity of the unfiltered photon beam (mR), μ is the linear attenuation of the filtering material (in mm^{-1}), and x is the thickness of the attenuating material (in mm). Mathieu used these equations, along with an empirical model for a mean linear attenuation coefficient ($\bar{\mu}$) for the polyenergetic photon spectrum in narrow-beam geometry (Equation 3-3) as the basis to derive Equation 3-4 and Equation 3-5 to interpolate the HVL and QVL, respectively:

$$\bar{\mu} = \mu_0 + \lambda \cdot \left(\frac{I}{I_0} \right) \quad (3-3)$$

$$HVL = \frac{\ln 2}{\bar{\mu}} = \frac{\ln 2}{\mu_0 + \lambda \cdot \left(\frac{1}{2} \right)} \quad (3-4)$$

$$QVL = \frac{\ln 4}{\bar{\mu}} = \frac{\ln 4}{\mu_0 + \lambda \cdot \left(\frac{1}{4} \right)} \quad (3-5)$$

where $\bar{\mu}$ represents the mean attenuation coefficient of the polyenergetic photon beam, and λ and μ_0 are unknown coefficients whose values are simplified to Equation 3-6 and Equation 3-7, respectively, by Lambert W interpolation.

$$\lambda = \frac{x_2 \cdot \ln\left(\frac{I_1}{I_0}\right) - x_1 \cdot \ln\left(\frac{I_2}{I_0}\right)}{x_1 \cdot x_2 \cdot \left(\left(\frac{I_2}{I_0}\right) - \left(\frac{I_1}{I_0}\right)\right)} \quad (3-6)$$

$$\mu_0 = \frac{x_1 \cdot \left(\frac{I_1}{I_0}\right) \cdot \ln\left(\frac{I_2}{I_0}\right) - x_2 \cdot \left(\frac{I_2}{I_0}\right) \cdot \ln\left(\frac{I_1}{I_0}\right)}{x_1 \cdot x_2 \cdot \left(\left(\frac{I_2}{I_0}\right) - \left(\frac{I_1}{I_0}\right)\right)} \quad (3-7)$$

Equations 3-6 and 3-7 are based on attenuated exposure measurements $\left(x_1, \frac{I_1}{I_0}\right)$ and

$\left(x_2, \frac{I_2}{I_0}\right)$; where x_1 and x_2 are two thickness of aluminum 1100 alloy (in mm), and $\frac{I_1}{I_0}$ and

$\frac{I_2}{I_0}$ each represent the respective ratios of the exposure measurements made using x_1 and

x_2 thickness of Al 1100 alloy filtration to the exposure measurements made with no filtration.

The value of the technique proposed by Mathieu is its demonstrated ability to accurately interpolate x-ray beam hardness values (such a HVL or QVL, which describe the thickness in millimeters of aluminum 1100 alloy (mm Al) necessary to reduce the intensity of an attenuated beam to one half or one quarter of its unattenuated value, respectively) using only one unfiltered and two filtered beam intensity measurements (each of which are acquired with different thicknesses of aluminum alloy filtration). This technique is contrasted with the more traditional technique, where HVL and QVL have been measured

taking several measurements with increasing aluminum thicknesses until the radiation intensity measurements were less than half of the unattenuated intensity; and the HVL was interpolated (using either linear or semi-logarithmic interpolation methods) between the two thicknesses that yielded slightly less and slightly more than half exposure value filtration. Thus, to measure both HVL and QVL required a minimum of five (and typically many more) exposure measurements traditionally and only three with Lambert W interpolation. Mathieu showed that by attempting to obtain both HVL and QVL with only three total exposure measurements with a pencil ionization chamber on a CT scanner at 120 kVp, the interpolated HVL and QVL values will only be within 5% of the nearest measurable HVL thickness 22% and 23% of the time, respectively, when using linear interpolation; and 76% and 84% of the time, respectively, when using semi-logarithmic interpolation. Under the same conditions, the Lambert W interpolation method yielded HVL and QVL values within 5% of the nearest measureable thickness in 100% of the measurements (95).

To obtain the HVL and QVL measurements, two thicknesses of aluminum 1100 alloy were measured with electronic calipers, and the average of eight measurements at different points on each of the aluminum plates was determined to be the average thickness of each Al 1100 plate. Next, the Radcal pencil ionization chamber described in Chapter 2 was secured inside the center bore of a CTDI head phantom using paper towels to prevent chamber movement within the phantom resulting from CT scanner table movement during chamber alignment to the scanner isocenter, and the CTDI phantom was set onto the head-holder attachment and was affixed to the GE LightSpeed VCT scanner table. The pencil chamber was positioned within the center bore of the CTDI head phantom such that in-air measurements could be acquired. The Radcal pencil ionization chamber was connected to the Radcal electrometer by triaxial cable, and the electrometer was set to acquire measurements in auto dose mode (in units of mR). After the ionization chamber/phantom assembly was secured to the scanner head-holder attachment with tape, the table was

moved such that the center of the active volume of the pencil chamber was located at isocenter. The CT scanner was then set to the zero position ((0,0,0) in the frontal, sagittal, and axial planes) (see Figure 3-1).



Figure 3-1. Using a CTDI head phantom on the head-holder attachment to place the pencil ionization chamber at isocenter of the CT scanner bore for in-air measurements.

With the pencil ionization chamber in-air at isocenter, the CT scanner was placed in service mode, and the x-ray tube was set to remain stationary through a scan (i.e. such that it did not rotate when the tube was on) at the bottom position of the gantry (in the 180 degree position) (see Figure 3-2). The scanner was otherwise set such that the x-ray tube irradiated the ionization chamber to the same technique as that used by MD Anderson

Cancer Center for VC described in Table 1-1: 120 kVp, 100 mA, the default trigger rate of 984 Hz, large (body) bowtie filter, small focal spot, effective beam width of 40 mm, and the default calibration vector setting of “full”. Exposure times of one second were used for these exposures to achieve a total of 100 mAs as opposed to the 0.5 second rotation head time described in Table 1-1 (yielding 50 mAs) because VC at MD Anderson Cancer Center utilizes two CT scans (one each with the patient in a prone and in a supine position). Since each scan provides 50 mAs of exposure to the patient, and since dose is linearly related to mAs (37), these two exposures were combined into one 100 mAs exposure for the purpose of these beam quality measurements.

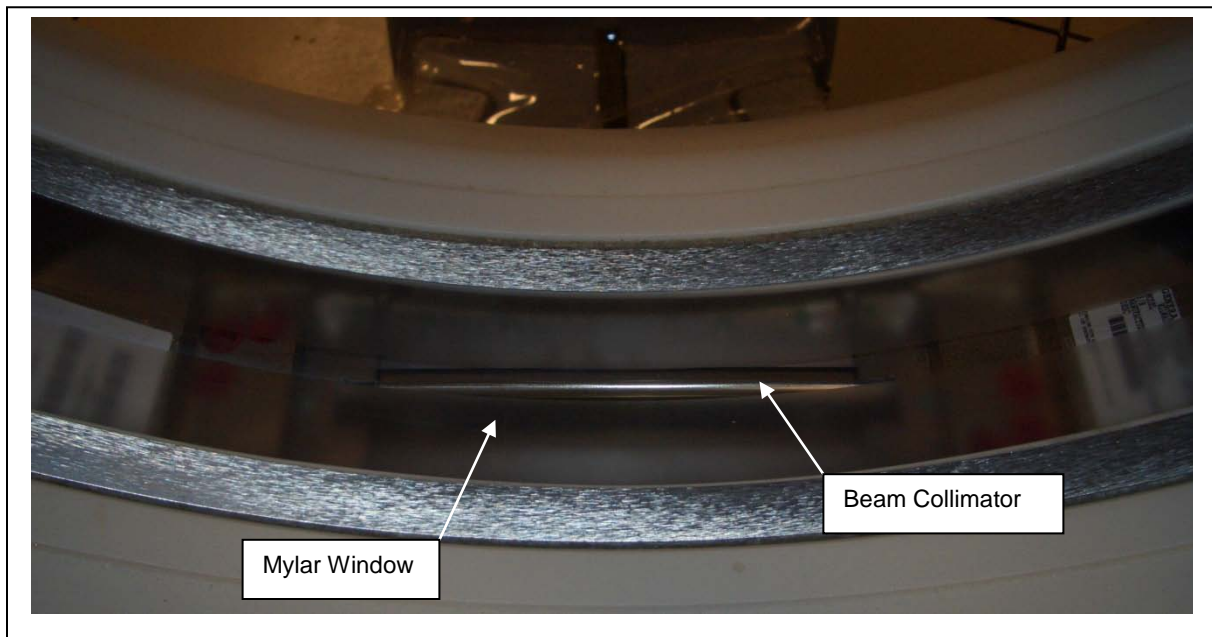


Figure 3-2. X-ray tube held stationary at the 180 degree (bottom) position of the CT scanner.

Exposure measurements were acquired for three separate scans, and the average of the three exposures (in mR) was determined to be the I_0 value (see Figure 3-3). One of the measured sheets of Al 1100 alloy ($x_1 = 6.36$ mm thick) was then set on the gantry over the Mylar window and exposure measurements were again acquired for three scans (with

the average being considered the I_1 value). Finally, a second 13.48 mm thick sheet of Al 1100 alloy was added to the beam filtering, providing a total filter thickness of $x_2 = 19.84$ mm. Exposure measurements were acquired for three scans in this third configuration (see Figure 3-4), and the average of these measurements was determined to be the I_2 value. With all of the measurements complete, the HVL and QVL values of the MDCT scanner were determined for 120 kVp using the VC protocol using Equations 3-4, 3-5, 3-6 and 3-7.



Figure 3-3. Configuration used to measure the unattenuated exposure (I_0).



Figure 3-4. Configuration used to measure the x_1 and x_2 attenuated exposures (I_1 and I_2).

3.2.1.2 $(CTDI_{100})_{air}$, $CTDI_w$, and $CTDI_{vol}$ Determination

With the CT scanner in normal image acquisition mode (i.e. such that the x-ray tube rotated when on), and the pencil ionization chamber located in air at isocenter (as was the case for the HVL and QVL measurements displayed in Figure 3-1 above), the CT scanner was set to the following technique to approximate (for CTDI measurement purposes) irradiation conditions experienced in VC at MD Anderson Cancer Center: axial scan, 0.5 sec per rotation of the x-ray tube, an effective beam width of 40 mm, 120 kVp, 200 mA, standard reconstruction algorithm, large (body) bowtie filter, large body scan field of view (SFOV) and 50 cm display field of view (DFOV). In a manner similar to the scan technique utilized in the beam HVL and QVL measurements, 100 mAs was used to acquire these CTDI measurements to simulate the combined dose received by patients undergoing VC from the prone and supine CT scans. Exposure measurements were acquired (in mR) for

three scans using this technique, the average of these exposure measurements was calculated, and the $(CTDI_{100})_{air}$ was calculated using Equation 1-11:

$$CTDI_{100,air} = \frac{(f \cdot C \cdot E \cdot L)}{(N \cdot T)} \quad (1-11)$$

where $f = 0.0087$ mGy/mR, $C = 1$ (the actual temperature and pressure correction factor of 0.99 was factored into the exposure reading provided by the electrometer, therefore $C=1$ was used), E was the average of the three exposure measurements (in mR), L was the length of the pencil chamber ($L = 100$ mm), N was the number of data channels, T was the detector width sampled by each channel, and the product $N \cdot T$ was the nominal beam width ($N \cdot T = 40$ mm). In order to establish the linearity of the MDCT scanner output with mAs, $(CTDI_{100})_{air}$ measurements were acquired using this technique in 10 mAs increments from 20 mAs (40 mA) to 170 mAs (340 mA). The results of these linearity measurements gave us confidence these measurements would also be linear within the center bore of a CTDI body phantom.

The final step of characterizing the beam quality was to determine the $CTDI_w$ in the 32 cm CTDI body phantom with the MD Anderson Cancer Center VC protocol. To do this, the CT table padding was peeled back, and the head-holder attachment was removed. Next, the phantom was placed on the unpadded MDCT scanner table and positioned by laser alignment such that the gantry isocenter was located at the phantom's center bore and such that the other bores were located at the 12, 3, 6, and 9 o'clock positions. The scanner was zeroed (0,0,0) to the center (in the frontal, sagittal, and axial planes) of the phantom according to the laser alignments, and the phantom was secured in place with tape. The standard acrylic insert rods were inserted into the 8 peripheral bores of the CTDI body phantom and the pencil chamber was inserted into the center bore such that the

marked center of the ionization chamber corresponded with the center of the phantom (and the scanner landmark (zero) point) (see Figure 3-5).

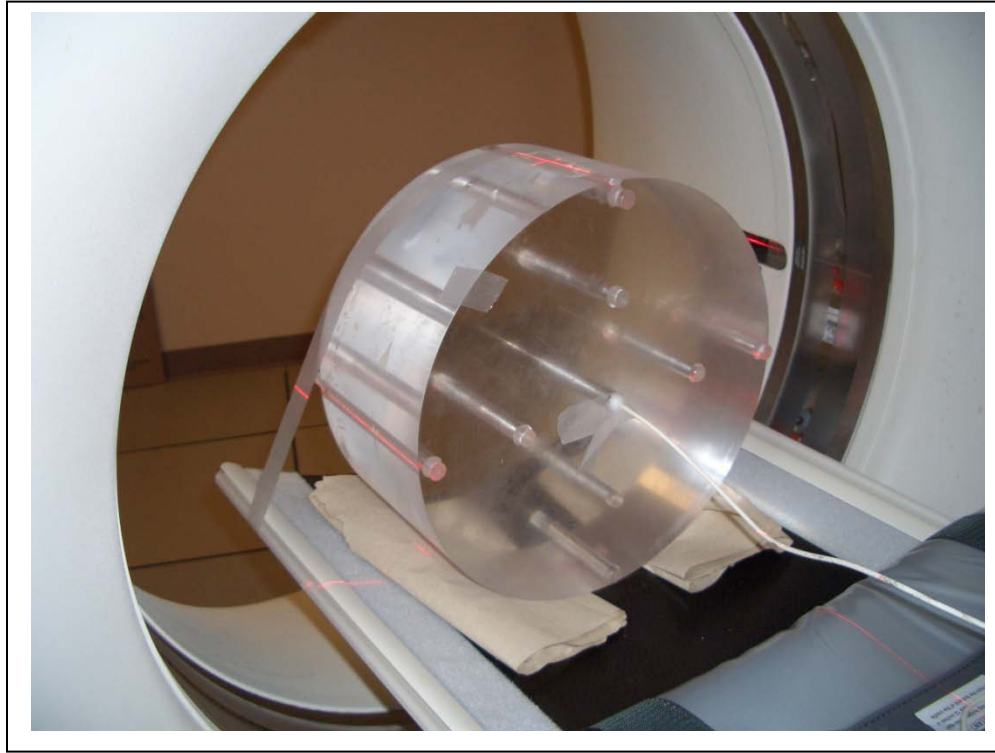


Figure 3-5. Configuration used to measure the exposure in the center bore of the CTDI body phantom, which was used to calculate $(CTDI_{100})_c$.

The electrometer was used in the auto dose measurement mode (in mR) and the scanner was set to the following technique to represent VC conditions at MD Anderson Cancer Center (axial scan, 0.5 sec per rotation of the x-ray tube, nominal beam width of 40 mm, 120 kVp, 200 mA (totaling 100 mAs to represent combined patient dose from the prone and supine CT scans), standard reconstruction, large (body) bowtie filter, large body SFOV, and 50 cm DFOV. Exposure measurements were acquired (in mR) for three scans. The average of these measurements was calculated and this average exposure value was used to calculate the $CTDI_{100}$ value for the center bore ($(CTDI_{100})_c$) using Equation 1-11 and

the same values for f , C , L , and $N \cdot T$ as those previously used to calculate the $CTDI_{100,air}$ values.

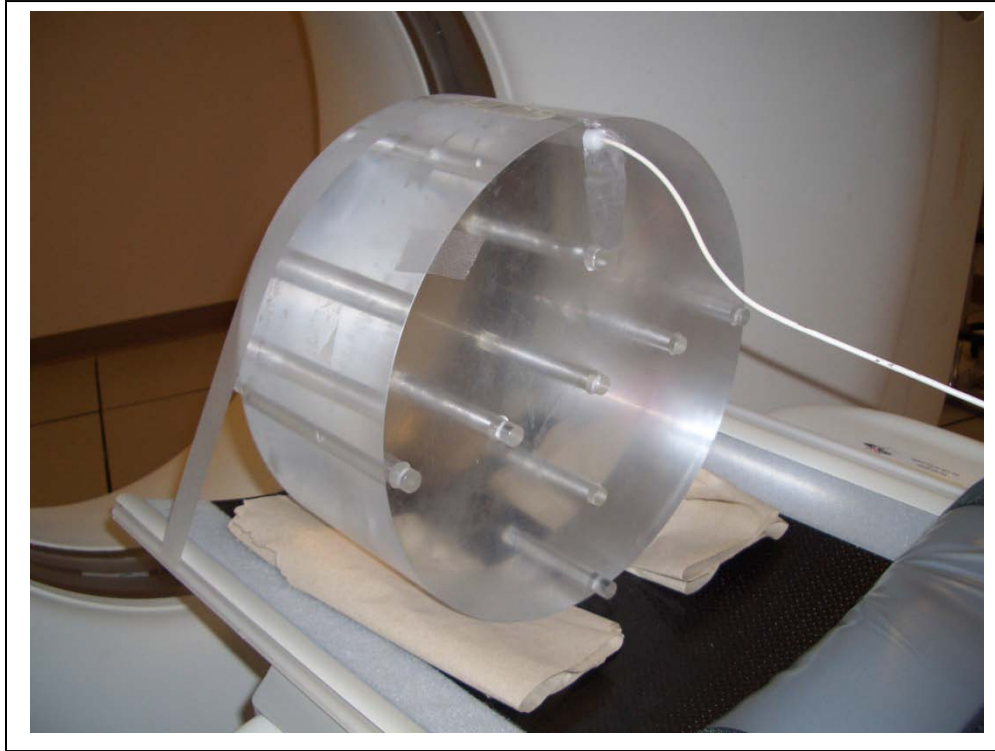


Figure 3-6. Configuration used to measure the exposure in the 12 o'clock bore of the CTDI body phantom, which was used to calculate $(CTDI_{100})_{12}$. A similar configuration was used to measure the respective exposures in the determination of $(CTDI_{100})_3$, $(CTDI_{100})_6$, and $(CTDI_{100})_9$.

Next, the pencil ionization chamber was removed from the center bore and placed in the peripheral bore in the 12:00 position of the phantom (and the insert rod that formerly occupied that bore was placed in the center bore) (see Figure 3-6). The process used to measure the three exposure measurements with the pencil ionization chamber in the determination of $(CTDI_{100})_c$ was repeated, yielding the $CTDI_{100}$ value for the 12 o'clock bore position ($(CTDI_{100})_{12}$). Similarly, the process was repeated for the peripheral bores located in the 3, 6, and 9 o'clock positions, and the CTDI values for these positions were also

determined ((CTDI₁₀₀)₃, (CTDI₁₀₀)₆, and (CTDI₁₀₀)₉, respectively). These four peripheral CTDI₁₀₀ values were averaged to obtain the (CTDI₁₀₀)_{periphery} value used in Equation 1-12 to calculate CTDI_w. Volume CTDI (CTDI_{vol}) was calculated from this CTDI_w value using Equation 1-14, and this measurement was compared to the CTDI_{vol} value displayed on the scanner console to verify consistency.

$$CTDI_w = \frac{1}{3}(CTDI_{100})_{center} + \frac{2}{3}(CTDI_{100})_{periphery} \quad (1-12)$$

$$CTDI_{vol} = CTDI_w / pitch \quad (1-14)$$

3.2.2 Determination of TLD Dose Linearity Correction Coefficients for Virtual Colonoscopy

3.2.2.1 TLD Irradiation at Exposures Received by Patients Undergoing Virtual Colonoscopy

The Farmer style ionization chamber was attached to the electrometer and was placed in the phantom's center bore (with the standard PMMA insert rods placed in the 8 remaining peripheral bores) (see Figure 3-7). The build-up caps were attached to the proximal (wired) end and to the distal (active volume) end of the Farmer chamber (as shown in Figure 2-9) such that the entire bore volume was occupied with minimal air gap. The CTDI body phantom was positioned at isocenter in the "CT9" GE LightSpeed VCT scanner table. The Farmer ionization chamber was aligned within the center bore such that the active volume was at the center (0,0,0 coordinate) of the phantom as shown in Figure 3-7.

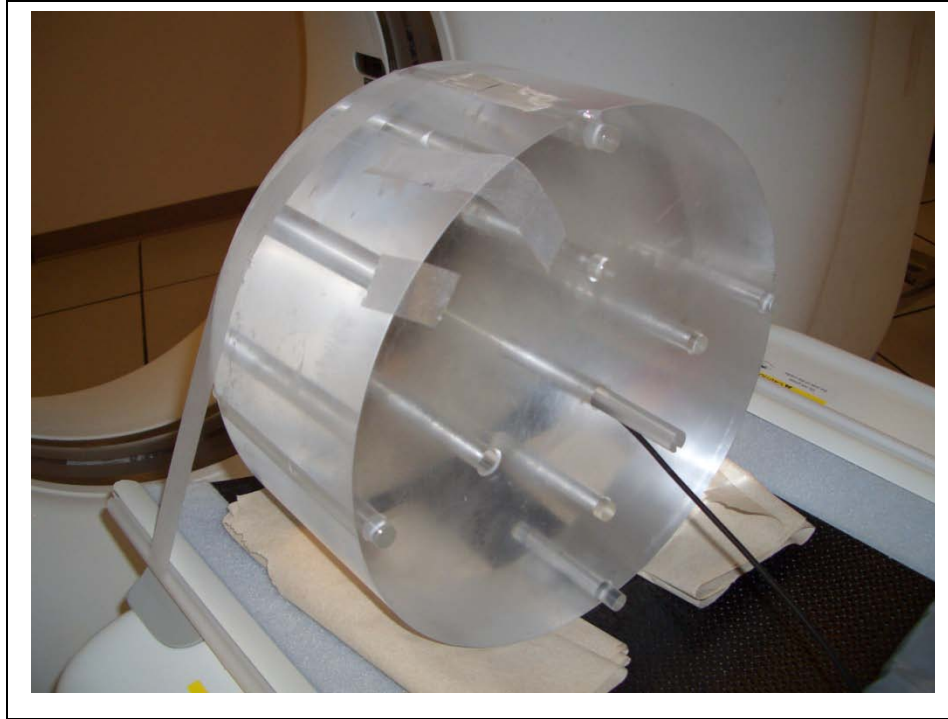


Figure 3-7. Configuration used to measure the exposure in the center bore of the CTDI body phantom with the Farmer ionization chamber.

A posterior-anterior (PA) survey (i.e. scout) image was obtained of the phantom assembly at 120 kVp and 10 mA. A helical scan was specified to be conducted from 75 mm superior to 75.4 mm inferior to the landmarked (0,0,0) coordinate (i.e. through the length of the CTDI phantom). The CT scanner was set to standard MD Anderson VC protocols: full helical scan mode with 0.5 sec rotation time, 1.25 mm image thickness, 39.37 mm/rotation table speed, 0.984 pitch, 0.8 mm interval, 120 kVp, 100 mA, 0 sec delay, and standard reconstruction algorithm.

The ionization chamber exposure was measured and recorded for two scans under the specified CT technique for a total photon output of 100 mAs per x-ray tube rotation (representing the cumulated exposure acquired from both the prone and supine 50 mAs scans in VC). In addition to exposure, the scan time (in sec), the scanner estimate of

CTDI_{vol} (in mGy), and the scanner estimate of dose length product (DLP) (in mGy*cm) were recorded for each scan for reference purposes. This process was repeated three times, and the average of the three iterations of two summed exposure measurements was determined to be the exposure value used for comparison with the TLD doses. The exposures from the PA scout scans were not measured or documented as this dose is known to be small, is often considered negligible compared to that provided by the actual CT scan (15), and is not displayed on the scanner console (thus no benchmark for comparison is available). The dose contributions to each patient from the PA and lateral scout scans was estimated as described in Chapter 3.3.2.7.

Next, one double-chambered TLD capsule was inserted into the seating cut in the center of the custom-designed insert rod (fabricated by the MD Anderson Cancer Center Machine Shop and shown in Figures 2-7 and 2-8). The Farmer ionization chamber was replaced within the CTDI body phantom with the TLD-loaded insert rod, and the TLD was placed in the center (in the frontal, sagittal, and axial planes) of the CTDI body phantom (with the CT scanner still landmarked to this location as (0,0,0)) (see Figure 3-8). The phantom was then irradiated with the TLD embedded within its center using the same CT technique settings as those previously used to irradiate the Farmer ionization chamber (including the use of two helical scans in each measurement). After a TLD was irradiated, the TLD-loaded insert rod was removed from the phantom and the irradiated TLD capsule was taped to a piece of paper and the paper was carefully labeled to document the study number assigned to that TLD and the conditions under which each TLD was irradiated.

After the two CT scans representative of the two supine and prone scans received by a patient undergoing VC had been accomplished, the TLD-loaded insert rod was loaded with a second unirradiated TLD capsule within the customized insert rod. The newly assembled TLD-loaded insert rod was identically placed back within the CTDI body phantom, and the second TLD was irradiated in the same manner as the Farmer ionization

chamber and the first TLD. TLD readout results from the RPC were provided on the same sheet of paper as that on which the irradiated TLDs were labeled to minimize opportunities for incorrect results to be reported for a specific scan technique.

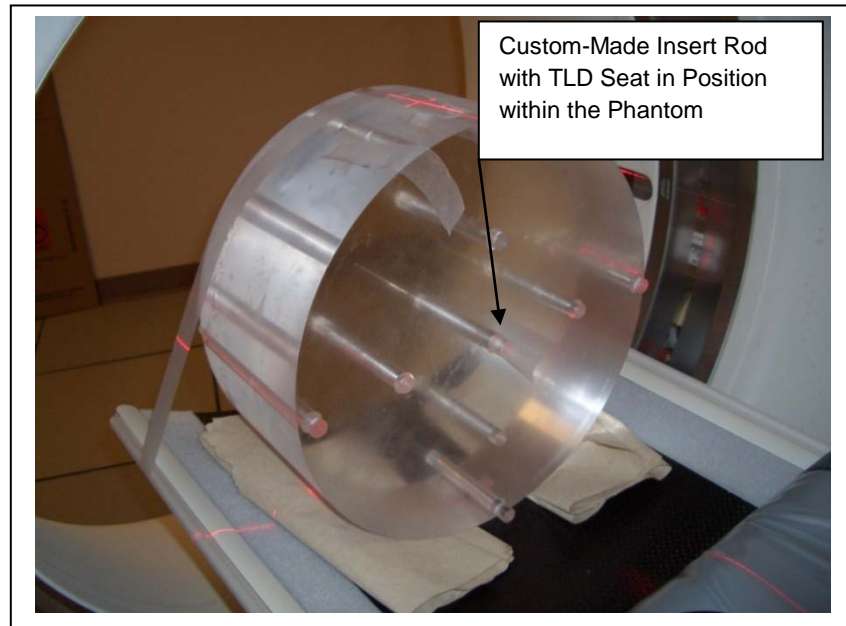


Figure 3-8. Configuration used to measure the dose in the center bore of the CTDI body phantom with a TLD inserted into the custom-made insert rod.

In order to obtain the TLD dose linearity response for the spectrum of rectal doses expected to be encountered in the range of sizes of VC patients, this technique was repeated at approximately 0.5 mGy increments from the lowest expected dose to the highest expected dose. Since it is well-known that dose is linearly proportional to mAs (37), the scan technique was increased in 10 mAs increments from the estimated lowest rectal dose (described in Chapter 1.3.5) of 0.5 mGy (0.7 mGy was measured at 20 mAs) to the estimated upper rectal dose of 11.2 (10.8 mGy at 170 mAs) to achieve the approximate 0.5 mGy dose increments desired. For the lowest dose levels, where the Farmer chamber could not detect exposure in the center of the CTDI body phantom, exposure values were

extrapolated based on the linearity of the CTDI values at the mid- and upper range dose levels. These extrapolations were based on the principle of x-ray tube linearity observed in the $CTDI_{100,air}$ measurements.

In order to ensure $K_{L,120}$ values pertaining to the lowest doses were sufficiently quantified, four TLDs (each with two aliquots of TLD-100 powder) were used to measure doses at 20, 30, 40, and 50 mAs. The doses administered at the mid- and upper-range tube currents (in 10 mAs increments from 60 mAs to 170 mAs) were each measured with two TLDs (each also containing two aliquots of TLD-100 powder). Thus, a total of 16 doses were measured (along with 5 background TLDs) for a total of 45 TLDs being used to determine the $K_{L,120}$ values for this TLD batch under VC conditions. As each TLD capsule contained two separate chambers filled with TLD-100 material, either eight or four total TLD measurements were therefore obtained at the low and mid/high-dose ranges, respectively. The TLDs were read by the RPC a minimum of 14 days after irradiation in order to reduce uncertainties caused by fading and drift.

3.2.2.2 TLD Readout and Dose Linearity Correction Factor Calculation

The RPC conducted the TLD read-out process as described in Chapters 1.2.3 and 2.4, and provided the following data for each TLD: charge reading (Q) (in μC), aliquot TLD mass (mg) (in mg), sensitivity (K_S) (i.e. dose to muscle in $cGy/\mu C/mg$, which was converted to $mGy/\mu C/mg$ for the order of magnitude of rectal doses received by patients undergoing VC) (see Equation 1-5 for details on K_S determination), and fading correction factor (K_F) (unitless) (see Equation 1-1). In order to calculate the dose to the acrylic phantom using the method outlined in Equation 1-8, the f-factor for acrylic ($f_{Acrylic} = 0.78 \text{ rad/R}$) was divided by the f-factor for muscle/soft tissue ($f_{Muscle} = 0.94 \text{ rad/R}$) (42) in a manner similar to that described by Equation 1-7. Thus, TLD dose to the CTDI body phantom was calculated by Equation 3-8:

$$D_{Medium} = \frac{Q}{mg} \cdot K_S \cdot K_{L,120} \cdot K_F \cdot \frac{f_{Acrylic}}{f_{Muscle}} \quad (3-8)$$

where $K_{L,120}$ is the dose linearity correction factor for the GE LightSpeed VCT spectrum at 120 kVp (unitless). TLD response may not be linear at diagnostic energies or in the dose range experienced by patients undergoing VC (25, 26), therefore the two correction coefficients cannot be determined independently without additional information being available regarding TLD-100 batch response to this energy or dose range. Therefore, the dose linearity correction factor could only be defined for the desired range of doses for each desired energy spectrum. However, it was only necessary for this protocol to define the dose linearity correction factor at 120 kVp because that is the only energy specified by MD Anderson Cancer Center VC protocols. Defining K_L at additional energies was therefore determined to be outside the scope of this project.

In order to calculate values of $K_{L,120}$ appropriate for VC, the exposure measurements obtained by the Farmer ionization chamber (in mR) had to be converted to dose in the acrylic CTDI body phantom (in mGy). These calculations were made using the appropriate conversion factors (100 rad = 1 Gy, 1000 mGy = 1 Gy, 1000 mR = 1R) and an f-factor of $f_{Acrylic} = 0.78 \text{ rad/R}$ (42). The Farmer ionization chamber measurement represented an accumulated dose to the center point within the CTDI body phantom as a result of the direct photon beam and from scatter through the phantom. The average dose of the three Farmer ionization chamber exposure measurements for each mAs setting was calculated and estimated to be the true dose within the medium (D_{Medium}) for that specific protocol. Using this value as a standard by which to compare the dose response within the TLDs, $K_{L,120}$ was calculated by rearranging Equation 3-8 into Equation 3-9:

$$K_{L,120} = \frac{D_{Medium}}{\frac{Q}{mg} \cdot K_S \cdot K_F \cdot \frac{f_{Acrylic}}{f_{Muscle}}} \quad (3-9)$$

where Q is the TLD charge reading (in μC), mg is the aliquot TLD mass (in mg), K_S is the TLD sensitivity correction factor (in $\text{mGy}/\mu\text{C}/\text{mg}$), K_F is the fading correction factor (unitless), $f_{Muscle} = 0.94 \text{ rad/R}$, and $f_{Acrylic} = 0.78 \text{ rad/R}$. These resultant $K_{L,120}$ values were used to establish a third-order polynomial regression curve using Excel software (Microsoft Corporation, Redmond, WA) based on apparent TLD dose measurements (i.e. TLD dose measurements not corrected by $K_{L,120}$ values). This regression equation was used to calculate anthropomorphic phantom and in-vivo patient rectal dose from apparent TLD dose measurements in VC at MD Anderson Cancer Center in Specific Aim 2.

3.3 Specific Aim 2: Obtain Rectal Dose Measurements in an Anthropomorphic Phantom and In-Vivo in Patients Undergoing VC with TLDs

With Specific Aim 1 accomplished, both the MDCT beam quality and the TLD response had been established for the dose range and energy spectrum received by a patient's rectum when undergoing virtual colonoscopy (VC). Before obtaining in-vivo rectal dose measurements in patients undergoing VC at MD Anderson Cancer Center, rectal dose measurements were acquired with thermoluminescent dosimeters (TLDs) (provided by the Radiologic Physics Center (RPC), Houston, TX) within an anthropomorphic phantom. Performing these measurements allowed for the identification of any potential problems in in-vivo measurements through "practice" measurements and allowed for an assessment of the accuracy of measurements acquired in a phantom compared to in-vivo measurements. MD Anderson Cancer Center Institutional Review Board (IRB) approval was obtained to perform in-vivo rectal radiation dose measurements for patients undergoing VC. IRB

approval was granted for this study to affix two TLDs to the inner diameter of the standard rectal catheters used in 10 patient VC studies at MD Anderson Cancer Center, but data for only 6 of these patients were available at the time of the writing.

3.3.1 Rectal Dose Measurement Simulation in an Anthropomorphic Phantom

In order to conduct simulated VC measurements in an anthropomorphic phantom, an ATOM model 701 adult male phantom (Computerized Imaging Reference Systems, Inc (CIRS), Norfolk, VA) was modified by placing a circular cut into the pelvis of the phantom to simulate an insufflated rectum during VC. This simulation also included modification of a rectal catheter tip that is used in VC and creation of a plug to lift the rectal catheter tip away from the posterior wall of the simulated insufflated rectum within the phantom. In order to increase the relevance of the results obtained from measurements within this phantom that was designed according to standardized geometric dimensions (that may not reflect the anatomy of many actual patients), additional simulations were performed with layers of simulated adipose tissue added to the surface of the anthropomorphic phantom such that rectal dose determination could be made to simulate patients of larger habitus.

3.3.1.1 Modifications to the Anthropomorphic Phantom

Measurement of the Miller™ rectal catheter contained within the E-Z-EM model 8925 Super XL Enema System (Bracco Diagnostics Incorporated, Princeton, NJ) revealed that the tip of the rectal catheter (where the TLDs were placed in this experiment) was approximately 25 mm in length. This length correlated well with the 25 mm length of each section of the ATOM phantom. Therefore it was determined that although rectal and colonic insufflation during VC extends for the entire length of these organs, irradiation conditions where these point measurements would be taken with the TLDs could be adequately replicated by only cutting a bore representative of an insufflated rectum into one

25 mm section of the ATOM phantom. Doing so also minimized potential damage to the ATOM phantom that may have been detrimental to future dosimetric or imaging experiments.

Selection of the phantom section to be cut was determined through analysis of supine CT images obtained from 29 randomly selected VC exams previously performed at MD Anderson Cancer Center from 9/22/2009 to 9/10/2010. In each of these supine CT image sets, the images containing the superior, center, and inferior portions of each rectal catheter head were evaluated with respect to reference anatomical bony landmarks (femoral heads, femurs, acetabulum, coccyx, pubic bone, ischia). These same bony landmarks were observed on the ATOM phantom, and the section of the phantom that most closely corresponded to the average location of the rectal catheter head (and therefore the average location of the TLDs) was determined. Among the 29 exams evaluated, the TLDs would have been placed in the anatomical location approximately corresponding to ATOM phantom section 33 in 9 patients, in section 34 in 15 patients, and in section 35 in 5 patients (see Figure 3-9). As the mean, median, and mode of this distribution all equaled or rounded to section 34, this ATOM phantom section was determined to contain the average location of the rectal catheter head during VC at MD Anderson Cancer Center.



Figure 3-9. Representative images of patients with a mean TLD location corresponding to section 33, section 34, and section 35, respectively, of the ATOM phantom

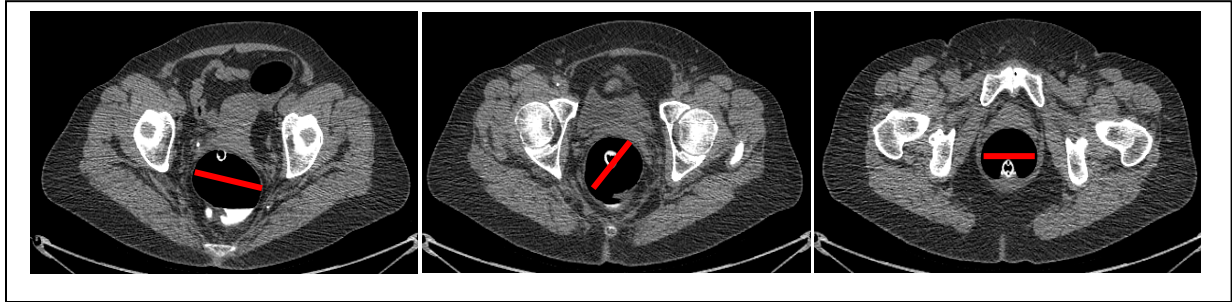


Figure 3-10. Illustration of maximum rectal diameter measurements at the superior, central, and inferior TLD locations

Determination was also made regarding the size of the insufflated rectum at the location corresponding to the placement of the TLDs in this study. This measurement was important in order to resolve the size of the cut to make within section 34 of the ATOM phantom. This estimation was made using two different methods. The first method for determining the size of the insufflated rectum incorporated measurements of the largest diameter of the rectum in the supine scan image that corresponded to the superior, central, and inferior borders where the TLDs would be located within a patient (see Figure 3-10). These measurements were made using the tools available in Philips iSite Enterprise patient archiving and communication system (PACS) (Philips Healthcare, Andover, MA). The largest rectal diameter in an exam was chosen to be the reference measurement obtained because it was the easiest dimension to determine in each rectum (which varied widely in size and shape of insufflation within the population of VC patients analyzed). The average maximum rectal diameter measurement at the superior portion of the TLDs was 59.6 mm, the average of the diameter measurements at the center of the TLDs was 69.3 mm, and the average of the diameter measurements at the inferior portion of the TLDs was 59.4 mm. The average of these three diameters was 62.8 mm, which represented the average insufflated rectal diameter as concluded by our first method.

The second approach for determining the size of rectal insufflation involved estimating the average diameter of the rectum after insufflation while accounting for potential differences in these measurements based on rectal catheter head placement within the surrounding anatomy and based on the size of the patient. Of the 15 patients that had their respective rectal catheter heads placed in the anatomical position that corresponded to section 34 of the ATOM phantom, six of these patients were approximately the same size as the ATOM phantom. This was based on estimating the cross sectional shape of each patient and the phantom to be an oval (at the approximate center image where TLDs would be located), by measuring the short and long radii (r_{short} and r_{long} , respectively) of each patient, and by calculating the estimated cross sectional area (Area) of each of the 15 patients (see Figure 3-11) using Equation 3-10:

$$Area = \pi \cdot r_{\text{short}} \cdot r_{\text{long}} \quad (3-10)$$

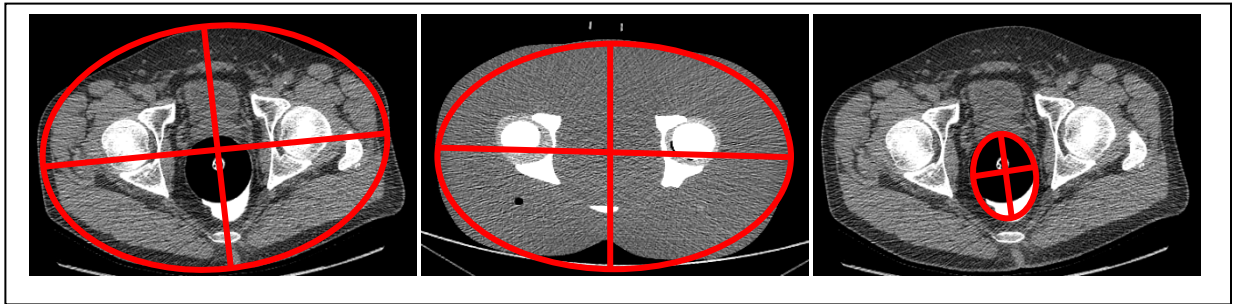


Figure 3-11. Illustration of the approximation of the cross-sectional area of a patient, the ATOM phantom, and the cross-sectional area of the patient's insufflated rectum, respectively, at the mean TLD location

Using this method, the cross sectional area of the ATOM phantom was estimated to be 550 cm², and the average cross sectional area of the six patients was estimated to be 554 cm² (within 1%). Next, the area of the insufflated rectum of each of these six patients

was also estimated to be an oval and the area of each insufflated rectum was also approximated using Equation 3-10. The six rectal cross sectional areas were averaged to obtain a cross sectional area of 33.5 cm^2 . Normalizing this area by the difference between the average patient cross sectional area and the phantom cross sectional area, an average insufflated rectal cross sectional area was calculated to be 33.2 cm^2 for a patient of approximately equal cross sectional size to the ATOM phantom. This area was determined to be equivalent to a circle 65.0 mm in diameter, which showed good agreement with the 62.8 mm average diameter estimate obtained from the first measurement technique. Averaging these two diameters yielded a circle of approximately 64 mm in diameter, which was determined to be the most appropriate diameter for the circular cut that was placed in the phantom to represent an insufflated rectum around the TLDs.

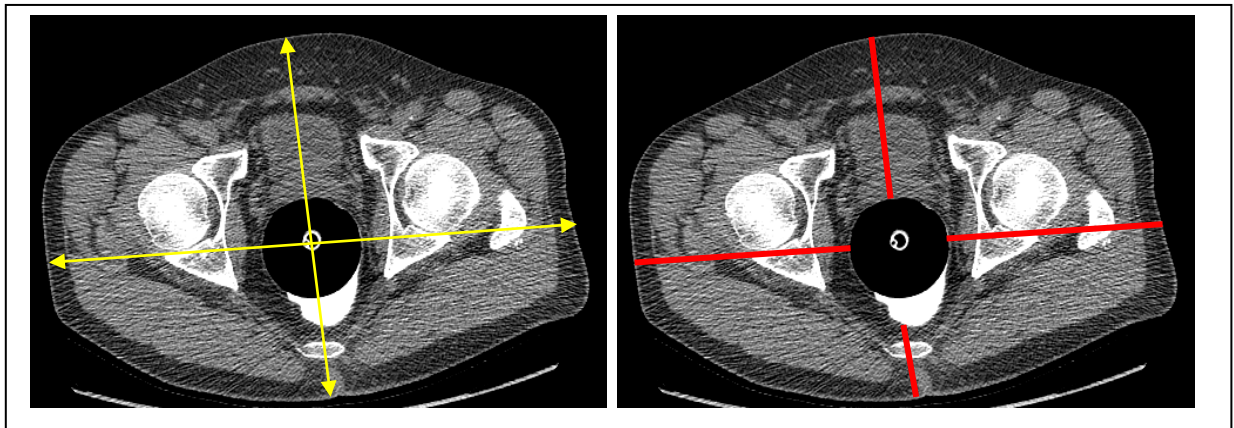


Figure 3-12. Illustration of the determination of the location of an insufflated rectum within the axial plane of a patient by establishing reference coordinate axes and acquiring rectum-to-surface distance measurements along the reference coordinate axes, respectively

With the ATOM phantom section selected and the size of the simulated insufflated rectum calculated, it was appropriate to determine proper placement of the cut within the phantom slice. This was accomplished by measuring the distance of the insufflated rectum

to the surface of each patient in both the x and y directions. In these measurements, the reference x- and y- coordinate systems were established with respect to the locations of the femoral heads in each patient (because not all patients' femoral heads were lying parallel to the CT scanner table and were therefore slightly tilted within the scan) such that the reference x-coordinate in each patient was parallel to an imaginary axis through the femoral heads. The center of each reference coordinate axes was established to be the approximate center of the insufflated rectum, and the distance measurements from the rectal wall to a patient's skin were taken along this reference coordinate axis. This measurement process is illustrated in Figure 3-12.

These rectal wall measurements within the six patients that most closely were represented by the ATOM phantom showed that the average insufflated rectum lied slightly to a patient's left by an average of 6.6 mm, and towards a patient's posterior surface by an average of 57.5 mm. Transposing the anticipated 64 mm diameter circular cut onto the phantom using these dimensions proved problematic, however, because such a cut within the phantom would have cut through the phantom's coccyx; which would not be a realistic scenario for VC gas insufflation. Therefore, the location of the 64 mm diameter circular cut within section 34 of the ATOM phantom was modified to be the approximate center in the lateral direction, and 5 mm anterior to the coccyx (which provided a representative posterior rectum positioning similar to that demonstrated in the actual patient measurements) (see Figure 3-13).

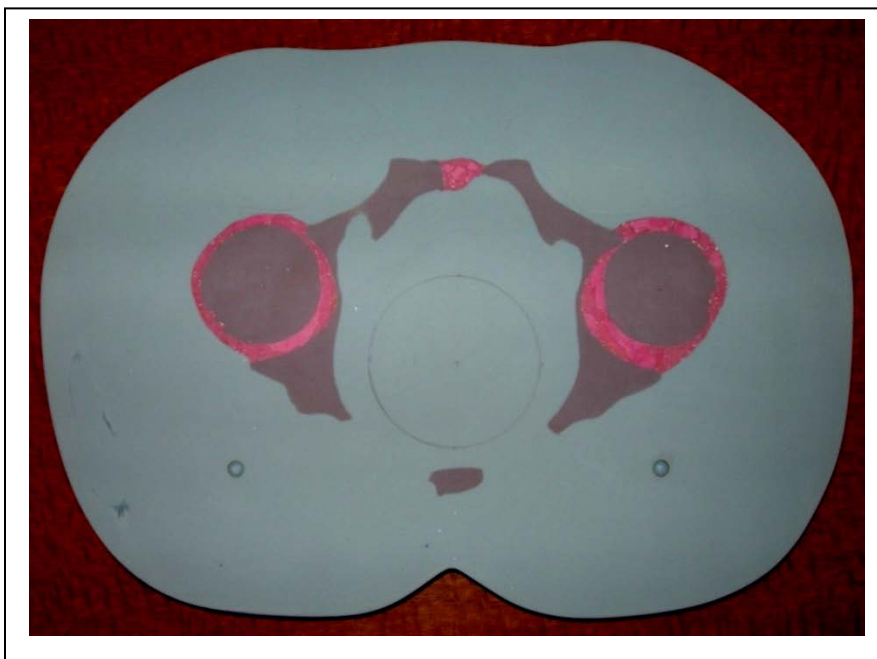


Figure 3-13. ATOM 701 adult male phantom section 34 before modification to include simulated insufflated rectum.

The circular cut into section 34 of the ATOM phantom that simulated the insufflated patient rectum was made by the MD Anderson Cancer Center Machine Shop (Houston, TX). The cut was designed to be circular to make the cutting process easier. Much of the removed phantom plug was spared such that it could be reinserted into the bore to accommodate future dosimetric and imaging studies. Where some phantom material was lost during the cutting process (based on the width of the cutting tool), the plug was supplemented with a sleeve composed of solid water material to reestablish a functionally tight fit when the plug was inserted into the phantom. Figure 3-14 shows section 34 of the ATOM phantom both with the simulated insufflated rectum and with the plug in place.

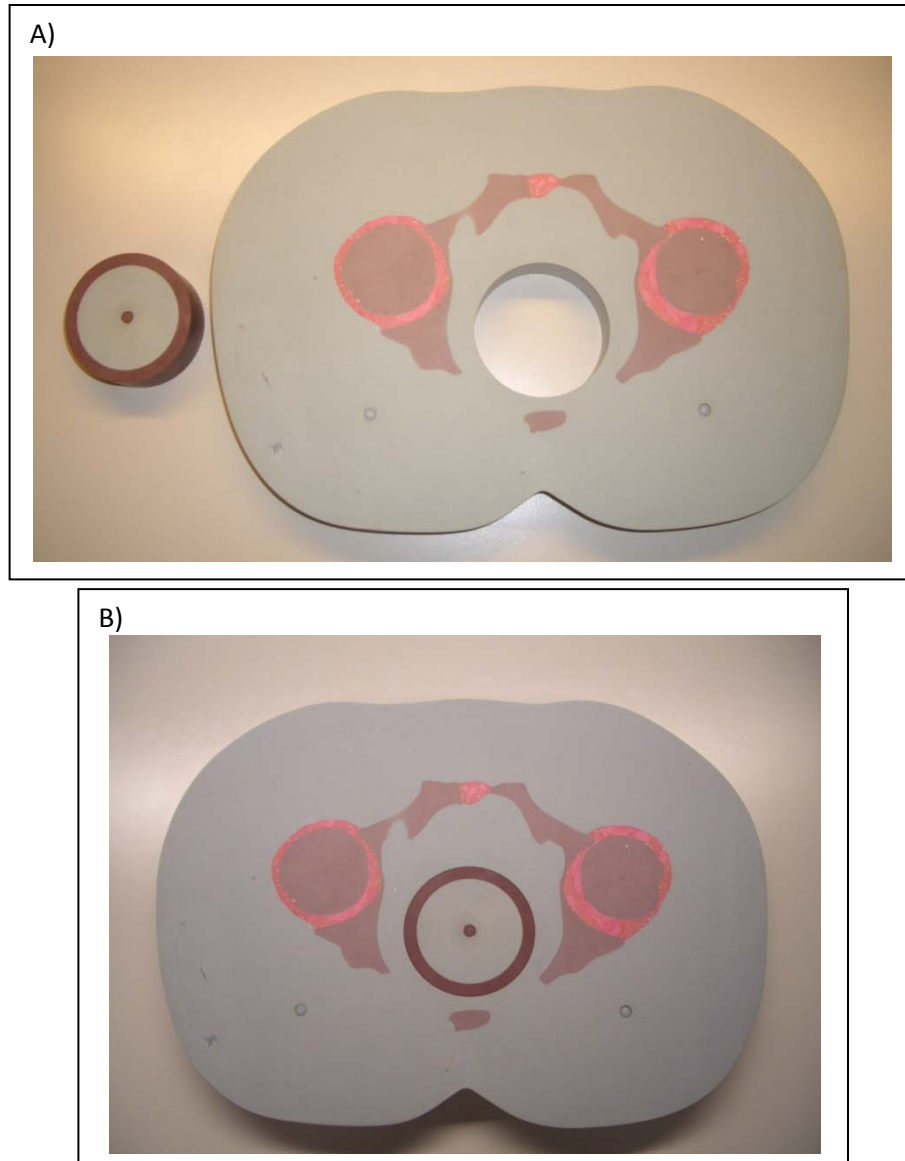


Figure 3-14. A) ATOM 701 adult male phantom section 34 after modification to include simulated insufflated rectum; B) ATOM phantom section 34 with plug for non-VC studies.

3.3.1.2 Modifications to the Rectal Catheter

With the ATOM phantom appropriately configured to accommodate simulations of rectal dose measurements during VC at MD Anderson Cancer Center, it was necessary to modify a rectal catheter such that it could be placed within the assembled ATOM phantom.

This was accomplished by simply excising the superior 24 mm of a rectal catheter head from the rest of the rectal catheter as shown in Figure 3-15. Since a review of the 29 previous supine VC scans revealed that the rectal catheter rests at various locations within the insufflated rectum and rarely against the posterior portion of the rectum (as would be the case if the catheter tip was simply placed into the insufflated rectal cavity shown in Figure 3-14A), a low-density Styrofoam plug was fabricated to lift the modified rectal catheter tip away from the simulated rectal catheter wall to more closely represent VC conditions (shown in Figure 3-16).

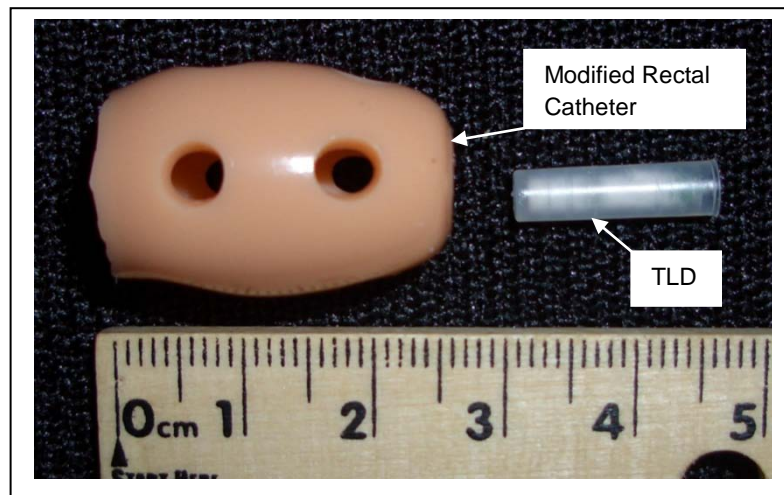


Figure 3-15. Miller™ Enema Air Tip rectal catheter modified for insertion into ATOM phantom section 34 for simulated VC.

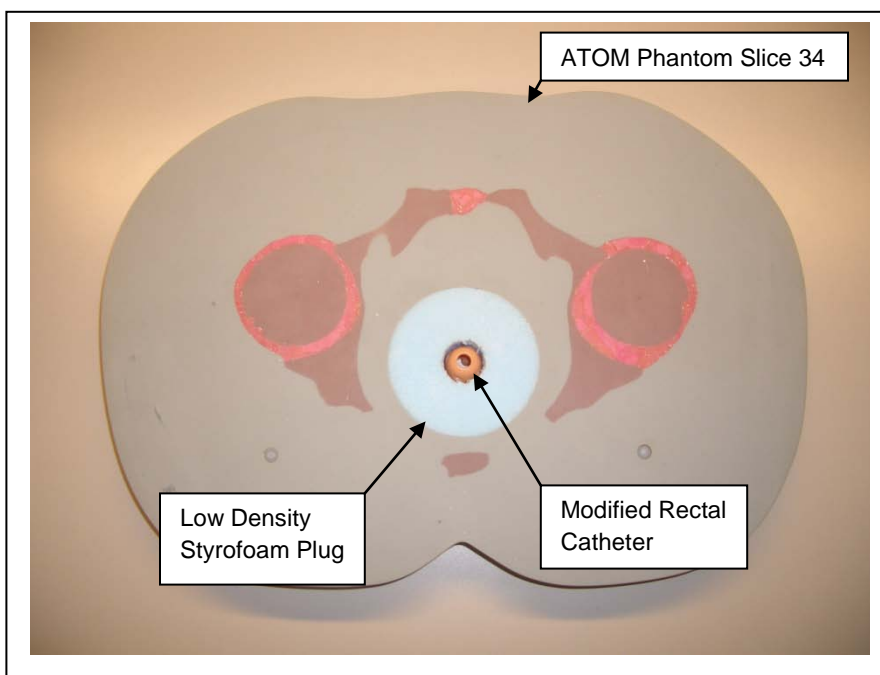


Figure 3-16. Low density Styrofoam plug designed for insertion into the phantom simulated insufflated rectum to lift the rectal catheter tip away from the phantom posterior rectal wall during simulated VC.

3.3.1.3 Anthropomorphic Phantom Assembly

Once the ATOM phantom had been modified to represent VC conditions at MD Anderson Cancer Center, the phantom was assembled such that the sections were properly aligned and ordered from section 1 at the top of the phantom head descending to section 39 at the upper thigh. For convenience during phantom irradiation, the phantom was assembled such that several sections were attached to each other by tape and/or nylon straps according to anatomical grouping: the shoulders/thorax/abdomen (sections 10-29), the pelvis (sections 30-37), and the upper legs (sections 38-39). The phantom head (sections 1-9) was not utilized because its presence would have only contributed minimally to the rectal scatter dose and because of the difficulties associated in positioning this portion of the phantom to adjoin to the rest of the phantom torso when the adipose

tissue layers were attached. Since the ATOM phantom legs were not available to simulate the additional scatter dose that would be present in a real patient, the CTDI body phantom and an additional anthropomorphic abdomen and pelvis phantom designed for imaging studies (manufacturer unknown) was attached to sections 38-39 as shown in Figure 3-18 below to approximate such scatter dose contribution to the rectum from a patient's legs.

3.3.1.4 Phantom Measurements and Determination of Population Percentages Represented

With the phantom assembled, anthropomorphic measurements were acquired to determine the percentage of the population represented by the phantom. A limitation of any anthropomorphic phantom is the fact that, although they are designed and fabricated to represent a standardized “typical” human in composition and dimension (in accordance with ICRP 23 (49) in the case of the ATOM phantom (81, 82)), they are limited in that the results rendered from dose measurements obtained in these phantoms only can be considered accurate for patients of approximately equal size and body composition as the phantom. Therefore, it was important to determine the percentage of the population that was represented by the ATOM phantom.

A limit to the validity of anthropomorphic phantom geometry measurements in their correlation to measurements obtained in actual patients undergoing VC exists in that the phantom is constructed of rigid epoxy resin materials fashioned after a standing patient, and actual patients are composed of materials that shift depending on whether that patient is lying either on their dorsal or ventral surfaces during VC. True patient dimensions demonstrate depth measurements that decrease and breadth measurements that increase, compared to when standing erect, when a patient is laying on their dorsal or ventral surfaces. Therefore, measurements that quantified dimensions involving patient breadth or depth were determined to be inappropriate for comparison between patient and phantom

dimensions. Patient circumference measurements can also vary based on patient position (specifically regarding whether a patient is standing or lying), especially in the buttocks region on most patients (as well as in other regions in obese patients) where folds in the skin can make true circumference measurements difficult to achieve and where the distribution of excess weight can shift along the axial direction of a large patient. The changes in patient circumference with patient position, however, are not as significant as changes in patient breadth or depth; therefore circumference measurements were determined to be most appropriate for comparison between true patient measurements and phantom measurements.

PeopleSize 2008 Professional software (version 1.1) (Open Ergonomics Ltd, Leicestershire, UK) was used to determine the percentage of US adults (aged 18-64) represented by the ATOM phantom. This software provided anthropomorphic data for six trunk circumferential measurements, including: chest circumference at the armpits (axillae), waist circumference at the midpoint, abdominal waist circumference, mid-hip circumference, hip circumference around the buttocks, and maximum hip circumference. The locations on the ATOM phantom corresponding to each of these locations are shown in Figure 3-17. The results of these measurements, and the percentile of the US adults aged 18-64 represented by these measurements, are shown in Table 3-1.

In order to expand the applicability of measurements obtained in the anthropomorphic phantom to patients of different habitus, CIRS has manufactured additional layers of adipose tissue-equivalent material in order to conduct dosimetry studies for obese patients using the ATOM phantom. These “fat slabs” were designed to be applied to the outer surface of the phantom in up to two layers as described in Chapter 2. These fat slabs provided the capability to perform dosimetry studies with the ATOM phantom for patients of three sizes.

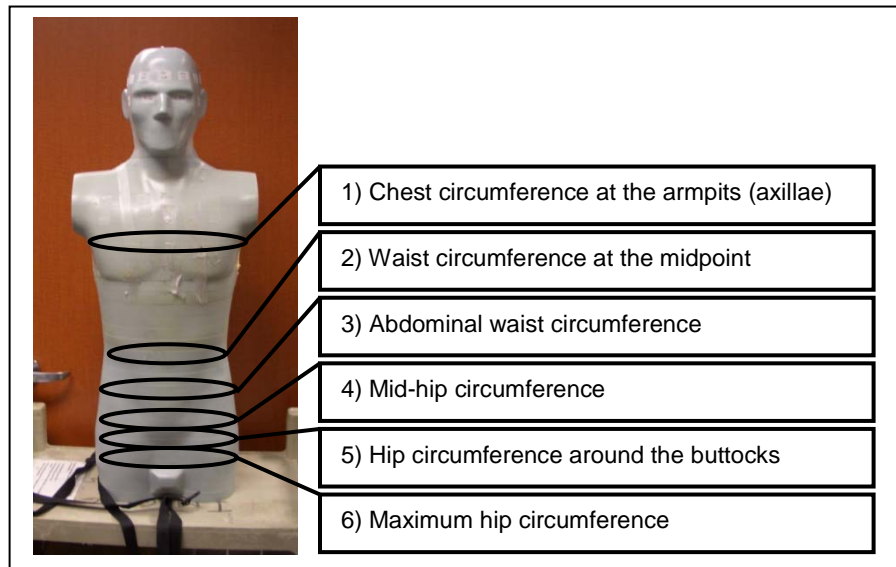


Figure 3-17. Locations of circumference measurements on the ATOM phantom, including: 1) chest circumference at the armpits (axillae), 2) waist circumference at the midpoint, 3) abdominal waist circumference, 4) mid-hip circumference, 5) hip circumference around the buttocks, and 6) maximum hip circumference.

Table 3-1. CIRS ATOM phantom circumference measurements and corresponding percentage of US adults aged 18-64 represented.

Measurement	ATOM Circumference (mm)	Percentile of US Adults (18-64 Years) (%)
Chest circumference at armpits (axillae)	940	20
Waist circumference, at the mid point	815	23
Waist circumference, abdominal	850	27
Mid-hip circumference	890	9
Hip circumference, around buttocks	890	4
Hip circumference, maximum	920	5
<i>Average</i>	<i>884</i>	<i>15</i>

The adipose tissue-equivalent phantom fat slabs were positioned onto the ATOM phantom pelvis in a manner similar to that shown in Figure 2-5A such that the fat slabs attenuated the primary CT beam before being measured by the TLDs within the modified rectal catheter placed in the phantom's rectum. The fat slabs were assembled onto the

ATOM phantom by first attaching the hook and latch ends of the large “1B” and “1D” slabs such that the labels were facing the same direction. Next, these attached slabs were slid over the lateral portions of the previously assembled ATOM pelvis (sections 30-37) with slab “1B” being placed over the phantom’s left side. Slab “1A” was then slid under the hook and latch assembly against the posterior side of the phantom such that the widest surface was in contact with the phantom. The first layer of fat slabs was complete when slab “1E” was similarly slid under the hook and latch assembly on the anterior side of the phantom. Anthropomorphic measurements were then performed on the fatter ATOM phantom to determine the percentage of US adults aged 18-64 that were represented by this habitus.

Table 3-2. Circumference measurements of the first layer of CIRS adipose tissue slabs after attachment to the ATOM phantom pelvis and the corresponding percentage of US adults aged 18-64 represented.

Measurement	Fat Layer 1 + ATOM Circumference (mm)	Percentile of US Adults (18-64 Years) (%)
Mid-hip circumference	1170	92
Hip circumference, around buttocks	1175	87
Hip circumference, maximum	1180	81
<i>Average</i>	<i>1175</i>	<i>87</i>

As mentioned in Chapter 2, these fat slabs only provide 20 cm of phantom surface coverage. Therefore only three of the six circumference measurements acquired for the ATOM phantom torso were able to be acquired for the two additional phantom configurations, including: mid-hip circumference, hip circumference around the buttocks, and maximum hip circumference. The results of these measurements and the percentiles of US adults aged 18-64 represented by these dimensions are provided in Table 3-2. Averaging the percentiles of US adults aged 18-64 represented by these three

circumference measurements yielded an approximation that the 87th percentile was represented by the phantom configuration with the first layer of fat slabs attached to the pelvis.

Table 3-3. Circumference and thickness of supplemental fat material to add to anthropomorphic regions of the ATOM phantom corresponding to the 87th percentile of US adults aged 18-64.

Anthropomorphic Region	87th Percentile of US Adults (18-64 yr) Circumference (mm)	Supplemental Circumference to be Added to Phantom (mm)	Supplemental Thickness to be Added to Phantom (mm)
Chest circumference at armpits (axillae)	1155	215	34
Waist circumference, at the mid point	1135	320	51
Waist circumference, abdominal	1135	285	45
<i>Average</i>	<i>1142</i>	<i>273</i>	<i>44</i>

Using this phantom configuration to approximate the rectal dose received by a patient undergoing VC at MD Anderson Cancer Center was problematic because where the fat slabs only extended 20 cm along the phantom's pelvis, an appropriate VC scan of a person whose torso length equaled that of the phantom would have been much longer. Therefore, in order to appropriately represent the conditions experienced by a patient undergoing VC, additional application of adipose tissue-equivalent material to the external surface of the ATOM phantom was necessary. The amount of additional fat material necessary to represent a patient in the 87th percentile of US adults aged 18-64 was determined by calculating the 87th percentile measurements of the three additional circumferences measured for the ATOM phantom without the fat slabs in place (but which were not measureable due to the short length of the fat slabs). These three additional circumferences included: chest circumference at armpits (axillae), waist circumference at

the midpoint, and abdominal waist circumference. The results of these circumference values provided by PeopleSize 2008 Pro, the amount of fat circumference required to be added, and the amount of additional fat required to be added to the ATOM phantom to achieve these circumferences are provided in Table 3-3.

Upon completion of the analysis required for the ATOM phantom with the first fat layer attached, the second fat layer was added to the exterior of the first fat layer in a manner similar to that shown in Figure 2-5B. This was accomplished by first attaching the hook and latch pads located at the ends of the large “2B” and “2D” slabs such that the labels were facing the same direction. Next, these attached slabs were slid over the lateral portions of the previously assembled 87th percentile ATOM pelvis (sections 30-37) with slab “2B” being placed over the phantom’s left side. Slab “2A” was then slid under the hook and latch assembly on the posterior side of the phantom such that the widest surface was in contact with the first fat layer. The second layer of fat slabs was complete when slab “2E” was similarly slid under the hook and latch assembly on the anterior side of the phantom. The same three pelvis circumference measurements as were performed on the first layer of fat slabs when attached to the ATOM phantom were then performed on the phantom with the second fat layer attached to determine in PeopleSize 2008 Pro software the percentage of US adults aged 18-64 this third habitus represented. These measurements and percentiles are provided in Table 3-4, and the average of these measurements was approximated to be representative of the 99th percentile of US adults aged 18-64 years.

Table 3-4. Circumference measurements of the second layer of CIRS adipose tissue slabs after attachment to the ATOM phantom pelvis, and the corresponding percentage of US adults aged 18-64 represented by this phantom configuration.

Measurement	Fat Layer 2 + ATOM Circumference (mm)	Percentile of US Adults (18-64 Years) (%)
Mid-hip circumference	1410	99.9
Hip circumference, around buttocks	1435	99.5
Hip circumference, maximum	1465	99.99
<i>Average</i>	<i>1437</i>	<i>≈99</i>

In a manner similar to that performed for the first fat layer, the average amount of additional fat material was determined with PeopleSize 2008 Pro that was required to be added to: the phantom chest circumference at the armpits (axillae), the waist circumference at the midpoint, and the abdominal waist circumference; such that the phantom configuration represented the 99th percentile of US adults aged 18-64. These 99th percentile circumferences, the amount of additional circumference, and the amount of additional thickness to add to the built-up phantom (with the first fat layer and supplemental fat material) are provided in Table 3-5. Obtaining 99th percentile patient measurements was useful for this study because such measurements should represent minimum rectal dose limits (due to maximum attenuation by surrounding fatty tissue), which insured that the lower limits of administered rectal doses would be detectable with the TLDs in this study. We did not expect to perform many (if any) in-vivo measurements in patients large enough to be considered within the 99th percentile of US adults aged 18-64.

Table 3-5. Circumference and thickness of supplemental fat material to add to anthropomorphic regions of the CIRS ATOM phantom (with the first layer of supplemental fat already in place), corresponding to the 99th percentile of US adults aged 18-64.

Anthropomorphic Region	99th Percentile of US Adults (18-64 yr) Circumference (mm)	Supplemental Circumference to be Added to Phantom (mm)	Supplemental Thickness to be Added to Phantom (mm)
Chest circumference at armpits (axillae)	1352	197	31
Waist circumference, at the mid point	1481	346	55
Waist circumference, abdominal	1469	334	53
<i>Average</i>	<i>1434</i>	<i>292</i>	<i>47</i>

With the amount of supplemental fat material to be added to the chest circumference at the phantom's armpits (axillae), to the phantom's waist circumference at the midpoint, and to the phantom's abdominal waist circumference calculated for the two larger phantom configurations, the issue of appropriate selection of supplemental fat material to utilize became a relevant decision. It was determined that the most practical, workable, and cost effective material that could be implemented to create a realistic scatter medium was pig adipose material in the form of lard. Therefore 207 pounds of lard were purchased and repackaged into 8 space-saver plastic luggage bags (ITW Space Bag®, San Diego, CA) and two zipper-style resealable two-gallon bags that could be molded into shape and sealed after forcing air out of the bags. As an added precaution against soiling the CT scanner or phantom with this adipose material, a plastic sheet was placed between the CT scanner table and the phantom assembly. Each two-gallon bag was filled with 2-3 pounds of lard material, each medium-sized plastic luggage bag was filled with 15-18 pounds, and each large-sized luggage bag was filled with 30-35 pounds such that the appropriate thickness of fat material (shown in Tables 3-3 and 3-5) could be added to the exterior of the ATOM phantom at the appropriate locations both superior and inferior to the

CIRS fat tissue layers (over the thorax/abdomen and leg regions of the phantom). During the simulated VC procedures with the ATOM phantom, the bags of adipose tissue were secured in place around the appropriate phantom circumferences with duct tape.

3.3.1.5 Virtual Colonoscopy Simulation in an Anthropomorphic Phantom

Before acquiring any TLD measurements during simulated VC in the ATOM phantom, the “CT9” GE VCT scanner at MD Anderson Cancer Center was evaluated to determine the beam half-value layer (HVL), quarter-value layer (QVL), weighted computed tomography dose index ($CTDI_w$), volume CTDI ($CTDI_{vol}$), and 100 cm in-air CTDI ($CTDI_{100,air}$) as described in Chapter 3.2.1. These beam quality measurements were obtained for comparison purposes with those beam quality measurements that were acquired when the TLDs were irradiated during the calibration procedure (Specific Aim 1). HVL and QVL measurements were also performed upon the completion of in-vivo dose measurements on all three GE VCT scanners upon which measurements were performed to verify the consistency of the beam output of the x-ray tubes. Once the x-ray tube beam quality had been initially characterized by each of these entities on the “CT9” scanner, the ATOM phantom was prepared for simulated rectal dose measurements during VC.

Before placing the ATOM phantom onto the CT scanner, a plastic sheet was placed onto the table to reduce the risk of the simulated adipose material soiling the scanner. Next, each of the previously established ATOM phantom regions were placed onto the scanner table and assembled such that the respective regions (i.e. thorax and abdomen, pelvis, upper legs/leg simulation medium) abutted to one another. The 15th percentile configuration phantom was placed on the scanner table such that it was lying in a supine position and no additional fat slabs were attached (see Figure 3-18). The MDCT scanner was then landmarked to the (0,0,0) coordinate at the center of the phantom in the coronal plane (which had previously been marked on the phantom with tape), in the approximate

center of the phantom in the sagittal plane, and in the center of phantom section 34 in the axial plane (87.5 mm from the inferior edge of the phantom pelvis region). A piece of tape was placed on the scanner table in the axial direction at section 34 and a mark was placed on the tape along the laser marking the axial plane for consistency in alignment between the phantom and the CT scanner in the repeated scans. A posterior-anterior (PA) scout image of the assembled phantom was acquired at 120 kVp and 10 mA to determine the superior and inferior borders of the VC scan, which corresponded superiorly with section 18 at the base of the lungs and inferiorly at section 36 at the ischium. This scan length was based on the same landmarks used to determine scan length of actual patients undergoing VC at MD Anderson Cancer Center.

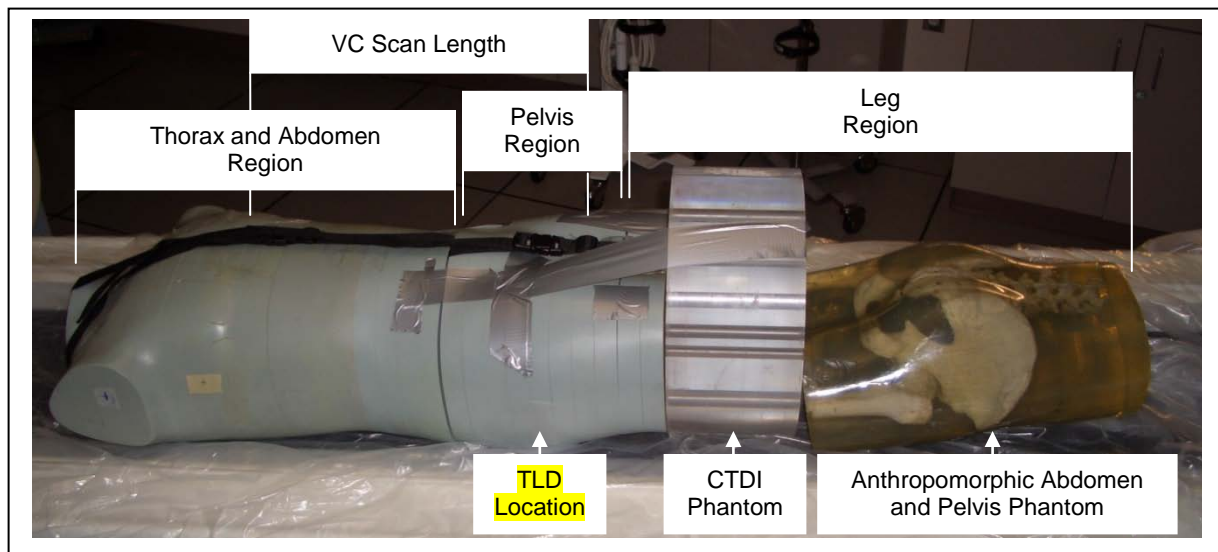


Figure 3-18. Phantom assembly utilized in simulated VC rectal dose assessment.

With the scan length established, the strap connecting the pelvic region of the phantom was disconnected, and section 34 was removed from the rest of the pelvis assembly. The custom-cut insufflated rectum plug was then removed from the phantom section and the Styrofoam plug was inserted into the bore. The modified rectal catheter tip

was then inserted into the Styrofoam plug, and two double-chambered TLDs (obtained from the RPC) were inserted into the modified rectal catheter tip. The TLDs were not attached to the rectal catheter wall or subjected to extensive quality assurance (QA) measures to ensure patient safety (as would be the case for in-vivo measurements) because such steps were unnecessary within the inanimate phantom.

When the two TLDs had been inserted into the modified rectal catheter, the ATOM phantom pelvis was reassembled, the strap holding the region together was refastened, and the entire ATOM phantom was carefully reassembled by aligning the marks on the scanner table and section 34 such that the phantom was in the same position as during the acquisition of the scout image. The MDCT scanner was then set to MD Anderson Cancer Center VC scan protocols: full helical scan mode with 0.5 sec rotation time, 1.25 mm image thickness, 39.37 mm/rotation table speed, 0.984 pitch, 0.8 mm image interval, 120 kVp, 100 mA, 0 sec delay, and standard reconstruction algorithm. The phantom was then irradiated in the supine position using this CT scan technique. Since CT dose is well known to be linearly proportional to mAs (37), and since this experiment was not concerned with obtaining the diagnostic benefits described in Chapter 1.1.2 that are associated with acquiring both supine and prone CT scans in VC, the ATOM phantom was not rolled over to a prone position but rather simply irradiated a second time with the same technique to simulate the prone scan.

Once the two double chambered TLDs had been irradiated with both supine VC scans, the pelvic region of the phantom was again disassembled and section 34 was removed. The two TLDs were then extracted from this phantom section and were taped to a sheet of paper that was carefully labeled with TLD identification information and the irradiation conditions of the TLDs. Next, a second set of two double chambered TLDs were inserted into the modified rectal catheter and the phantom was reassembled. The phantom was identically placed on the MDCT scanner using the alignment lasers and marks placed

on both the table and the phantom (see Figure 3-19); and the phantom was irradiated using the same MD Anderson Cancer Center method used to irradiate the previous TLDs. When the second set of TLDs had been irradiated, they were replaced with a third set of two double chambered TLDs within the ATOM phantom.

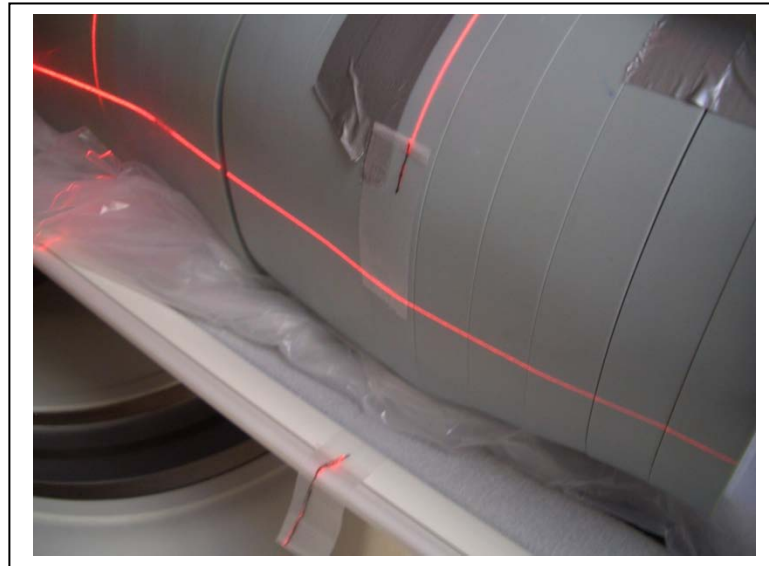


Figure 3-19. Placement of the anthropomorphic phantom on the MDCT scanner such that a mark designating the location of the TLDs within the phantom align via laser with a mark placed on the scanner table

After a total of three sets of two double chambered TLDs had been irradiated within the initial (15th percentile) ATOM phantom configuration (i.e. without the additional fat slabs and supplemental fat material), a fourth set of TLDs were inserted into the phantom and the first fat layer was added to the external circumference of the pelvis. For alignment purposes, a mark was placed on the surface of the fat slab that was 87.5 mm from the inferior edge of the phantom pelvis region to correspond to the center of phantom section 34. Next, a medium-sized space-saving bag containing lard was placed on the CT scanner table abutting to both the inferior and superior ends of the pelvis fat slabs (see Figure 3-

20A). The superior and inferior portions of the phantom were then placed on top of the bags filled with lard and were each covered with a second medium-sized bag. The two lard-filled bags were abutted around the respective lateral portions of the phantom and were attached at that end with two pieces of duct tape (see Figure 3-20B). The bags of adipose tissue were then wrapped around the respective portions of the phantom and were connected by two more pieces of duct tape on the opposite lateral portion of the phantom (see Figure 3-20D). On the phantom thorax and abdomen, the two bags were too short to connect on the opposite side; so an additional zipper-style two-gallon bag containing 2-3 additional pounds of adipose tissue was placed between the respective space-saver bags (see Figure 3-20C).

With the superior and inferior portions of the lard wrapped around the phantom, significant efforts were made to ensure the connecting regions of the phantom correctly abutted to one another. At times, this required placing towels and pillows under portions of the adipose material to correctly position the phantom. Once the regions of the phantom were adequately adjoined, the adipose tissue within the bags surrounding the phantom were then manipulated by hand such that the lard within the combined bags was approximately 51 mm thick at the abdomen and tapered down to approximately 34 mm thick at the abdomen in accordance with Table 3-3.

The adipose material attached to the leg region of the phantom was manipulated by hand to be an approximately uniform 40 mm throughout because this thickness equaled that of the fat slabs manufactured by CIRS (and anthropometric data for upper leg circumference was not available in PeopleSize 2008 Pro software). It should be noted, though, that manipulation of the fat to desired thickness was inexact and even after extensive efforts, certain portions remained thicker than others (for example, the central portions of the lard-filled bags supporting the phantom weight were unavoidably thinner than the lateral portions of those bags due to the effects of gravity).

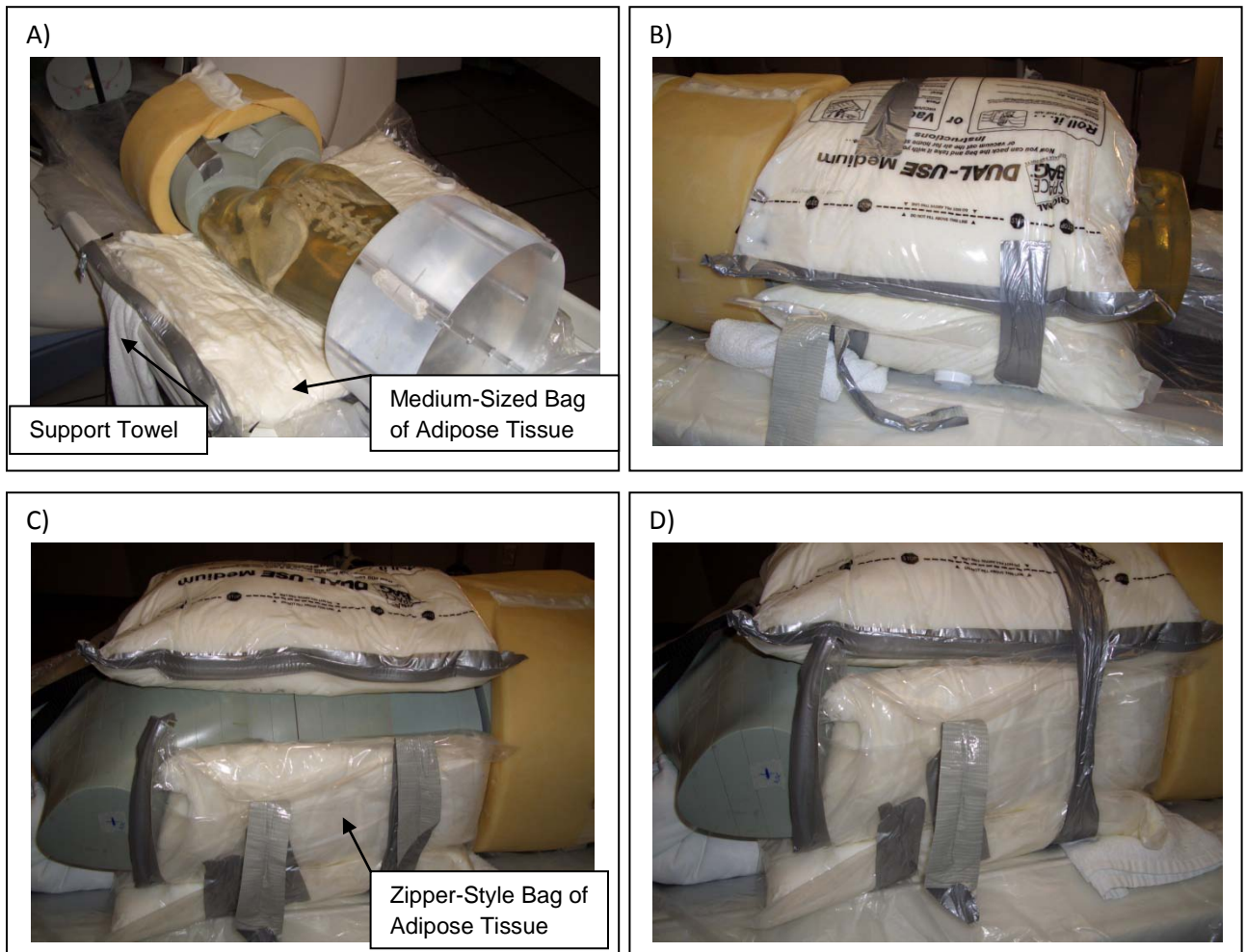


Figure 3-20. A) Placement of the phantom onto a medium-sized bag filled with adipose tissue to represent the 87th percentile of US adults aged 18-64; B) Attachment of two abutting adipose tissue-filled bags with duct tape at the lateral portion of phantom; C) The use of a zipper-style two-gallon bag filled with adipose tissue to connect opposing bags surrounding the phantom thorax and abdomen; D) Attachment of the abutting adipose tissue-filled bags with duct tape at the opposite lateral portion of phantom after pulling the bags tightly around the phantom.



Figure 3-21. ATOM phantom assembled to represent the 87th percentile of US adults aged 18-64 for simulated VC.

When the respective regions had been supplemented with sufficient adipose material to represent the 87th percentile of US adults aged 18-64 (the percentile corresponding to the pelvic circumference attained when the first fat layer was added to the ATOM phantom pelvis), the phantom was reassembled (see Figure 3-21) onto the MDCT scanner such that the mark placed on the pelvic fat slab at phantom section 34 aligned with the mark placed on the scanner table. This phantom configuration was then irradiated twice (both times with the phantom in the supine position) using the MD Anderson Cancer Center CT scan technique for VC provided above. The pelvis region of the phantom was

then rolled away from the rest of the phantom assembly, disassembled, the TLDs within section 34 were replaced with two more double chambered TLDs, the phantom configuration was reassembled, and the process was repeated such that a total of three measurement sets of two double chambered TLDs were acquired in the 87th percentile phantom configuration.

Upon the completion of measurements acquired to represent the rectal dose received by the 87th percentile of US adults aged 18-64 while undergoing VC, the phantom was modified to accommodate for measurements representing the dose received by the 99th percentile (the percentile corresponding to the pelvic circumference attained when the second fat layer was additionally added to the ATOM phantom pelvis) during VC. This was accomplished by disassembling the entire phantom used to represent the 87th percentile and by placing two double chambered TLDs into the ATOM phantom pelvis. Next, the second fat layer was added to the ATOM phantom pelvis and the pelvis assembly was placed on the CT scanner table.

In order to ensure consistency in phantom placement between iterations and configurations, a piece of tape was placed on the external surface of the second pelvic fat slab and a line was placed on the tape 87.5 mm from the inferior surface of the pelvic region. This line represented the location of the center of ATOM phantom section 34 and the location of the TLDs, and the pelvis assembly was adjusted on the scanner table such that this line was in alignment to the line previously placed on the scanner table. A large-sized bag of lard was then placed onto the CT scanner table both superiorly and inferiorly to the phantom pelvis such that both bags abutted to the second fat slab layer encompassing the phantom pelvis. A medium-sized bag of lard was additionally placed on top of each large-sized bag, and the 87th percentile phantom configuration was assembled using these medium-sized bags on top of the large-sized adipose tissue bags.

Once the 87th percentile phantom configuration had been reassembled, a second large-sized bag of adipose tissue was placed on top of the superior and inferior regions of the 87th percentile phantom configuration, and the two large-sized bags were attached at one lateral portion of each region of the phantom by two pieces of duct tape. In a manner similar to that used to assemble the 87th percentile configuration, the large-sized bags were then pulled tightly around the phantom and secured at the opposite lateral side of the phantom by two additional pieces of duct tape (incorporating an additional zipper-style two-gallon bag of adipose tissue to connect the large-sized bags on the thorax/abdomen portion of the phantom). In a manner also similar to that incorporated to assemble the 87th percentile phantom configuration, considerable care was taken to ensure the adjoining portions of the ATOM phantom were correctly mated to one another by using additional towels and pillows to prop up portions of the phantom as appropriate.

When the ATOM phantom was correctly aligned, the bags of adipose tissue were adjusted to ensure they abutted to the pelvic fat slabs, and then the lard within the large-sized bags were manipulated by hand such that the abdominal thickness of lard was approximately 54 mm thick and tapered to approximately 31 mm thick at the chest (in accordance with Table 3-5). As with the 87th percentile phantom configuration, the large-sized bags of lard surrounding the leg portion of the phantom assembly were additionally manipulated to be approximately 40 mm thick throughout. Such hand manipulation of the adipose tissue within the bags was inexact, and portions of the respective bags unavoidably accumulated more lard (i.e. the lateral portions of the bags) than other portions (i.e. the portion of the bags supporting the weight of the phantom).



Figure 3-22. ATOM phantom assembled to represent the 99th percentile of US adults aged 18-64 for simulated VC.

Figure 3-22 shows the final phantom assembly used to represent the body habitus of the 99th percentile of US adults aged 18-64. In order to acquire multiple measurements within a phantom configuration, the pelvic region of the phantom was rolled away from the rest of the phantom assembly (see Figure 3-23), disassembled, irradiated TLDs were harvested and replaced with unirradiated TLDs within the ATOM phantom pelvis, and the entire phantom was reassembled for each measurement set. This process became very time consuming and required patience. As was the case with the two previous phantom configurations simulating VC using the MD Anderson Cancer Center protocol, the three measurement sets of two double chambered TLD measurements were acquired for the phantom configuration simulating the rectal dose received by the 99th percentile of US adults aged 18-64 undergoing VC.



Figure 3-23. Disassembly of 99th percentile phantom configuration for repeated TLD measurements during simulated VC; with the two layers of CIRS simulated phantom fat disattached from the ATOM phantom pelvis region (held in-tact during simulated VC by the black nylon strap shown).

Simulation of in-vivo rectal dose measurements in an ATOM phantom was completed after the three sets of two double chambered TLDs were irradiated within the phantom configuration simulating the 99th percentile of US adults aged 18-64. In total, three sets of two double chambered TLD measurements were accomplished for three phantom configurations equaling 12 TLD dose measurements per habitus for a total of 36 TLD measurements with the ATOM phantom. The RPC conducted the TLD read-out process a minimum of 14 days after irradiation as described in Chapters 1.2.3 and 2.4.

3.3.1.6 Simulated Virtual Colonoscopy Data Analysis

The results provided by the RPC included the following data for each TLD: charge reading (Q) (in μC), aliquot TLD mass (m) (in mg), sensitivity (K_S) (i.e. dose to muscle in $\text{cGy}/\mu\text{C}/\text{mg}$, which was converted to $\text{mGy}/\mu\text{C}/\text{mg}$ for the order of magnitude of rectal doses received by patients undergoing VC) (using Equation 1-5), and fading correction factor (K_F) (unitless) which was adjusted according to Equation 1-1 to account for the time delay between TLD irradiation and readout. The linearity and energy correction factors ($K_{L,120}$) used to calculate dose for these measurements were those established in Specific Aim 1. These dose measurements were used to fit a regression model estimating rectal dose based on a patient's effective diameter; and 95% confidence intervals and an R^2 goodness of fit coefficient were calculated for this regression analysis. The average of the 12 dose measurements at each simulated habitus was determined to be the dose received by a specific patient habitus, and these average dose values were used to accomplish Specific Aim 3 in comparing the TLD dose measurements to CTDI_{vol} -based size specific dose estimate (SSDE) and Farmer chamber dose measurements taken in a uniform CTDI body phantom.

3.3.2 In-Vivo Rectal Dose Measurements during Virtual Colonoscopy

MD Anderson Cancer Center Institutional Review Board (IRB) approval was obtained to perform in-vivo rectal radiation dose measurements for patients undergoing VC. IRB approval was granted for this study to affix two TLDs to the inner diameter of the standard rectal catheters used in 10 patient VC studies at MD Anderson Cancer Center. At the time of this writing, however, data was only available for six VC patient measurements, and therefore data will only be presented in this work for those six patients. As mentioned above, each of the TLDs used in this study contained two measurement chambers; and therefore four total rectal radiation dose measurements were obtained for each patient. Per standard VC procedure, the rectal catheters were not used for more than one patient (which

significantly reduced the opportunity for infection in patients as a result of participation in this study); therefore 6 different rectal catheters were used in this study.

The only deviation from the standard MD Anderson Cancer Center protocol for VC (described in Chapter 1.1.2) introduced by this study was the measurement of the radiation dose received by the rectum by affixing the two small TLDs inside the same rectal catheter used as a part of the standard VC procedure. Four measurements were obtained per patient of the accumulated dose administered to that patient's rectum from four scout images and both prone and supine CT scans. In order to reduce the chances of TLD-100 material coming in direct contact with patients, of TLDs becoming dislodged from the rectal catheter, or of patients or researchers receiving an infection as a result of participation in this study, a quality assurance (QA) system was established covering five stages of quality control (QC). These QC steps were implemented into the TLD/catheter assembly and VC processes.

3.3.2.1 QC Step 1: Testing TLD Capsules for Leakage

The first stage of QC was designed to ensure that the plastic encapsulating the TLDs remained watertight while in a patient. These measures were important because although LiF toxicity data shows that initial GI symptoms may appear with quantities of LiF ingestion as low as 120 mg (97) (and this amount is greater than the total amount of LiF used per patient in this study), irritation of the mucosal cells of the rectum and large intestine may result from contact with LiF (97-99). However, as the tissues of the rectum and distal portions of the large intestine only permit trace amounts of most materials to be absorbed (98), it was determined that there was little risk of notable side effects in the very unlikely event that LiF escaped encapsulation.

In order to ensure the integrity of the TLD encapsulation, the following steps were accomplished for each TLD/rectal catheter assembly:

1. Two double chamber TLDs obtained from the Radiologic Physics Center (RPC) were visually inspected with a magnifying glass to ensure there were no cracks in the plastic capsule and that the wax plug was firmly in place.
2. The TLDs were submersed in a tap water bath within a small container for a period no less than 24 hours (see Figure 3-24).
3. After at least 24 hours had passed, LiF powder within the TLD capsule was carefully examined for any condensation or nonuniformities. As LiF is hygroscopic (97), it readily absorbs water within its environment and should provide visually obvious signs of any such water intake. The appearance of the TLD capsule was compared to that of a control TLD that had not been submerged.
4. Any TLD that would have absorbed water would be deemed to have an insufficient seal for this project and therefore returned to the RPC.



Figure 3-24. QA test #1: Place TLDs in a water bath for 24 hours.

3.3.2.2 Attaching TLDs to the Rectal Catheter

Once the integrity of the TLD plastic encapsulation was established, two double-chambered TLDs were inserted into the inner lumen of the rectal catheter and secured by Silicone II (General Electric Corporation, Huntersville, NC) silicone glue and suture string (Tyco Healthcare, Norwalk, CT). Both of these agents had previously established a history of being bio-inert in other applications at MD Anderson Cancer Center (with this silicone glue used in the assembly of eye plaques treating ocular melanomas with brachytherapy and the suture being used surgically). These TLDs were secured inside this rectal catheter tip as illustrated in Figure 3-25 using the method described below. Although the placement of the TLDs within the catheter decreased its inner diameter, care was taken to ensure the function of the device was not substantially altered.

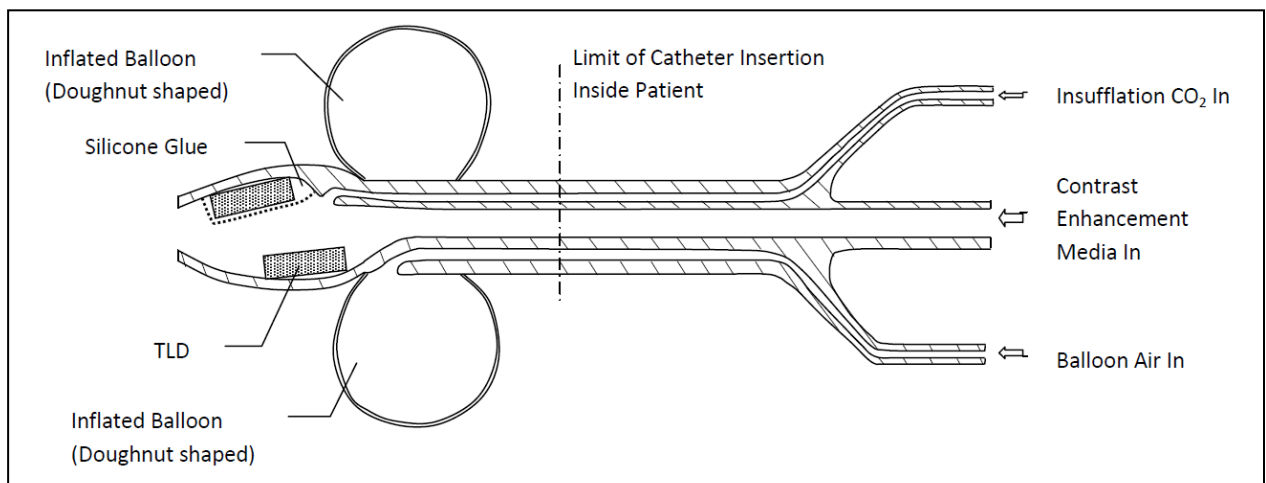


Figure 3-25. Cross section diagram of TLD placement within the rectal catheter

The following steps were accomplished to assemble the two TLDs to the inner lumen of the rectal catheter:

1. One end of the bag in which the E-Z-EM Super XL Enema Delivery System (Model 8925) was packaged was carefully cut using scissors (see contents of the bag in Figure

- 1-2). Although the catheter assembly was not a sterile device, care was taken when handling the device to minimize contamination and protect the components.
2. A pea-sized amount of silicone glue was placed onto the tip of an unfolded paperclip and this glue was dabbed onto the inner lumen of the rectal catheter tip (see Figure 3-26) through the superior opening just proximal to (and on the same axis as) the balloon inflation extrusion (as labeled in Figure 2-13). This application of glue was repeated with several pea-sized applications of silicone glue applied to the same area such that the interior of the catheter head was similar in appearance to Figure 3-27.
 3. Two 10 cm lengths of 2-0 (0.3 mm diameter) polypropylene suture string (Tyco Healthcare, Norwalk, CT) were weaved through the external ports of the rectal catheter such that they bridged the bed of silicone glue (without becoming embedded into the bed of glue) and the two ends were loosely tied with the first throw of a surgeon's knot (the right end of the suture was tied over the left end twice yielding a double overhand knot) as shown in Figure 3-28.
 4. One TLD was then inserted into the superior opening of the rectal catheter and carefully navigated to the applied glue bed (under the suture bridge) using an unfolded paperclip fed through the superior and exterior bores of the rectal catheter. When the TLD was in position along the inner surface of the rectal catheter tip abutting to the superior lip of the rectal catheter lumen (adjacent to the superior opening), the TLD was pressed into the glue using the paper clip and the double overhand knots were drawn taught. The Surgeon's knots were then completed with the second throw such that the TLD was secured into position. With the TLD secure, most of the excess suture was removed, and the knots were rotated into the interior of the rectal catheter as shown in Figure 3-29.

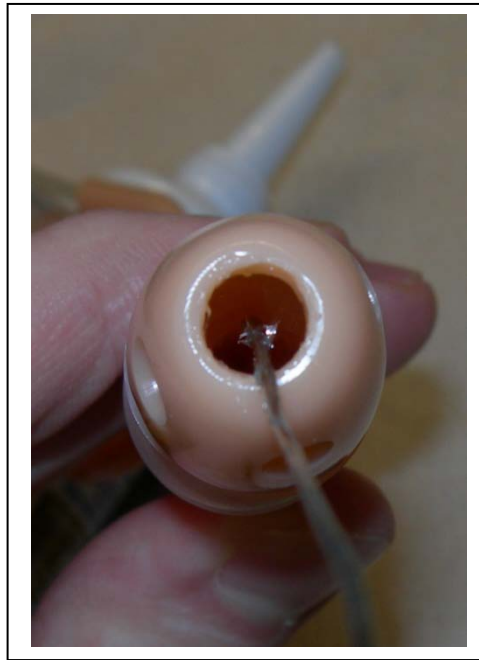


Figure 3-26. Application of a pea-sized amount of silicone glue to the interior of the rectal catheter.

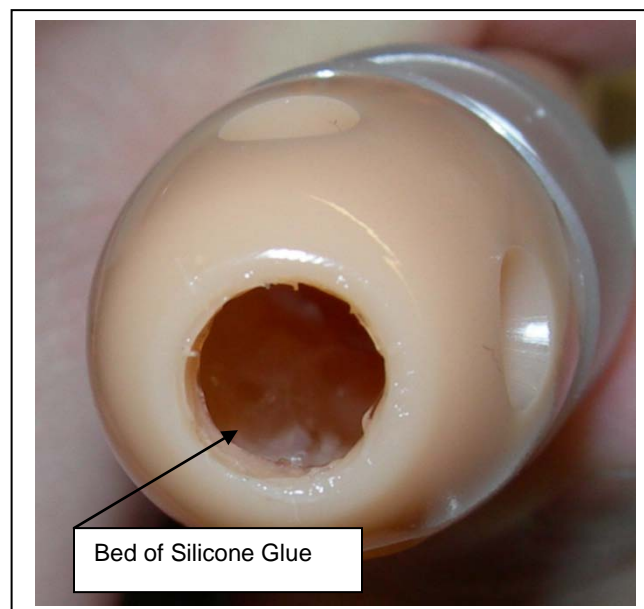


Figure 3-27. Proper amount of silicone glue applied to the inner lumen of the rectal catheter tip.

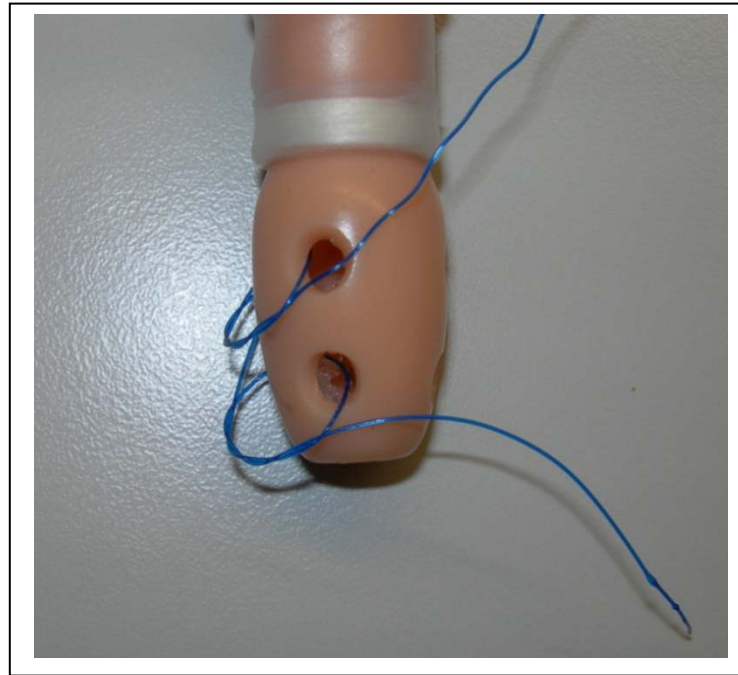


Figure 3-28. Two 10 cm lengths of suture string tied in the first throws of surgeon's knots.

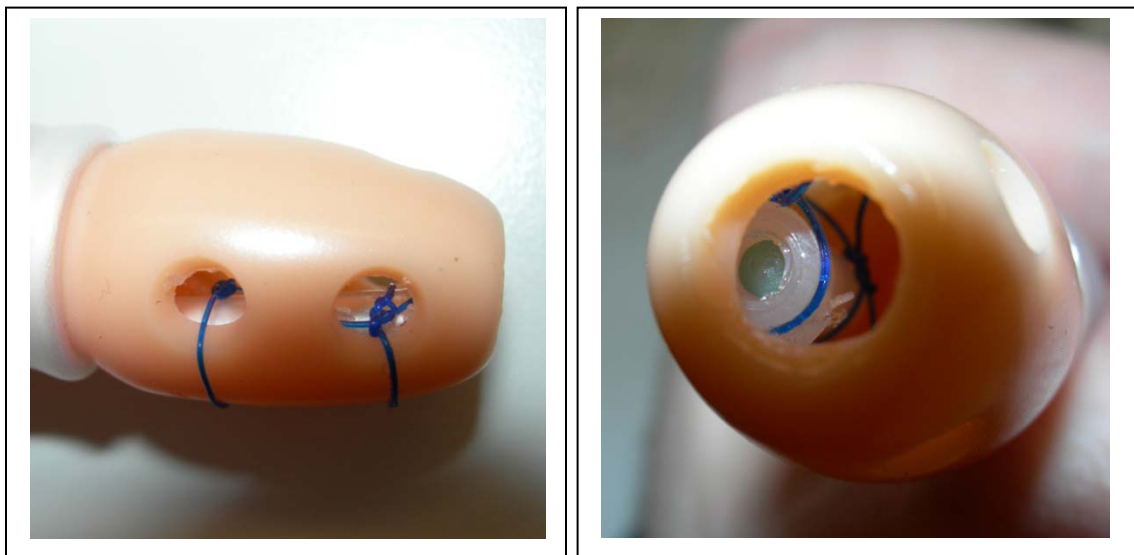


Figure 3-29. Proper placement of the first TLD to the inner lumen of the rectal catheter tip.

5. The excess glue within the rectal catheter was smoothed over using a paperclip to ensure that no more than one of the external holes on the rectal catheter head was

occluded (to ensure that the functionality required of the rectal catheter was maintained).

6. While slightly pinching the tip of the rectal catheter such that the superior bore assumed an oval shape, the second TLD was inserted into the rectal catheter head such that the end of the TLD that contained the wax plug was the last portion of the TLD to enter the rectal catheter (see Figure 3-30). Inserting the TLD in this manner ensured that the TLD was placed with minimal effort and that the TLD would remain within the rectal catheter during the VC procedure due to the tapered geometry of the TLD capsule (with the plugged end of the TLD having the largest diameter). This TLD was not secured with silicone glue or suture because the partial occlusion of the superior opening of the catheter by the secured TLD prevented the escape of the unglued TLD.

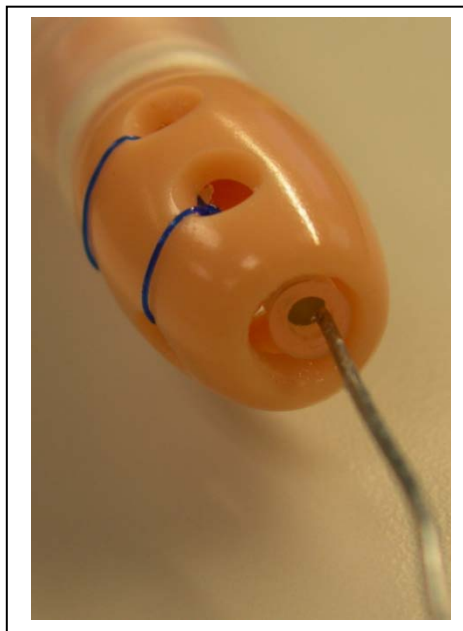


Figure 3-30. Proper insertion of the second TLD into the rectal catheter head.

7. Excess glue was wiped from the exterior of the rectal catheter tip.

8. The rectal catheter/TLD assembly was placed in a warm and dry environment, and the silicone glue was permitted to dry for a minimum of 24 hours.
9. After at least 24 hours had passed, the assemblies were visually inspected to verify the placement of the TLD within the rectal catheter head and to verify that the TLDs and glue did not occlude more than one external hole on the rectal catheter head. The final TLD/rectal catheter assembly is shown in Figure 3-31.
10. As a final check of the functionality of the rectal catheter assembly, air was forced through the open end of the blue insufflation tube to verify that the gas insufflation port within the rectal catheter was not accidentally occluded with silicone glue. If it was discovered that this hole was occluded, a hole was punctured and reamed out in the silicone glue at the gas insufflation port (shown in Figure 2-13) to reestablish gas insufflation capability.

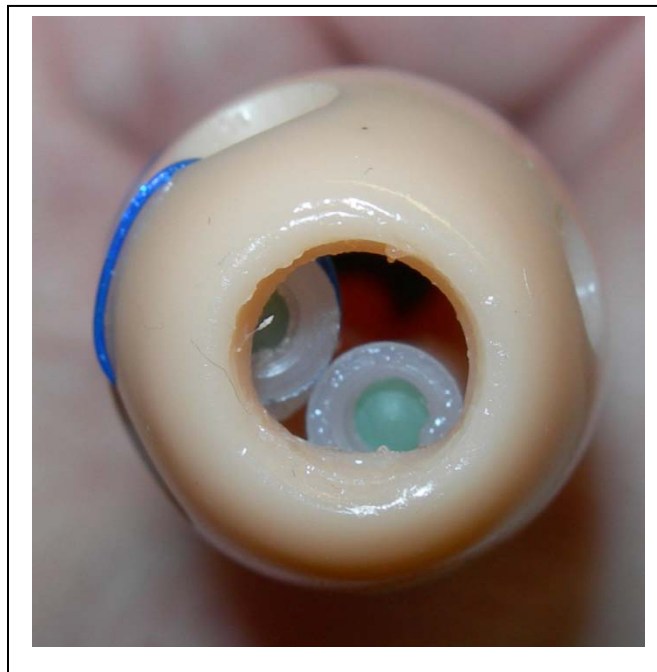


Figure 3-31. Proper final placement of two TLDs within the rectal catheter.

3.3.2.3 QC Step 2: *Testing for Secure TLD Attachment to the Rectal Catheter*

The second stage of QC was designed to ensure that the TLDs would remain attached to the rectal catheter at all times while in a patient. This was accomplished by applying compression and flexion conditions to the exterior surface of the rectal catheter with forces exceeding those encountered in the rectal environment; and by water flow testing the apparatus with pressures exceeding those encountered in the contrast administration process. The second stage of QC was not executed until the glue had been permitted to dry for at least 24 hours, and execution of this QC stage was conducted with the following steps:

1. Observing the TLDs through the superior opening of the catheter, the rectal catheter head was physically compressed several times by hand force such that the two TLDs came into contact with one another. During compression, the secured TLD was observed for movement away from the catheter wall as the tension within the tip of the rectal catheter was applied and relieved. If little or no TLD movement from the catheter lumen wall was observed, additional compression forces were applied to the catheter head such that the TLDs both came in contact with the opposite catheter wall (completely collapsing the catheter tip). Again, the secured TLD was observed for movement away from the wall to which it was glued.
2. If little or no TLD movement was observed, the catheter head was again compressed such that the TLDs came in contact with the respective opposite walls, and the assembly was then rolled/flexed three or four times by hand force such that the TLDs were leveraged against each other and forced to peel the secured TLD away from the rectal catheter wall. While doing this, the secured TLD was observed for movement away from the catheter wall to which it was attached.
3. If little or no TLD movement was observed, tap water was poured into the contrast agent bag and the cap on the bag was closed. The rectal catheter tip was directed into

a sink and the contrast bag was held several feet higher than the rectal catheter tip.

The contrast bag containing the tap water was then squeezed such that water was forced through the rectal catheter at pressures greater than those encountered by hydrostatic means (i.e. at pressures greater than those experienced during VC).

4. If the TLDs remained within the rectal catheter, the catheter assembly was determined to have passed the second QC step. If, however, a catheter assembly failed any of these tests, the assemblies were immediately dried and the TLDs were reapplied using the same process described above (Section 3.3.2.2). No TLD/catheter assembly was be used clinically unless it passed each of these tests.

3.3.2.4 QC Step 3: Disinfection of Rectal Catheter Assembly

The third stage of QC was implemented to ensure patients did not receive an infection as a result of participation in this study. In spite of the fact that VC is a clean procedure (and not a sterile procedure), the TLD/rectal catheter assemblies underwent disinfection after successfully completing the first two stages of QC (and before being inserted into patients). Careful handling ensured disinfection was maintained until the catheter came in contact with a patient. To conduct this QC procedure, the following steps were accomplished:

1. 70% isopropyl alcohol solution (Target Corporation, Minneapolis, MN) was poured into an appropriately sized container to 10 cm of depth.
2. The contrast agent bag, tubes and rectal catheter were coiled into a circle approximately 25 cm in diameter, similarly to the configuration in which it was packaged by the manufacturer.
3. The contrast agent tubing was grasped, exposing the rectal catheter (the portion that was to be inserted into the rectum), and the rectal catheter was submerged 9 cm into

the 70% isopropyl alcohol (up to the bulge on the shaft). The catheter assembly remained in the alcohol solution for at least 10 seconds.

4. After the alcohol bath was completed, the catheter tip was removed from the alcohol solution and excess alcohol was gently shaken from the rectal catheter back into the container.
5. With the assembly still coiled, the disinfected assembly was returned to the original E-Z-EM Double Contrast Enema Delivery System packaging in a similar manner as originally packaged for storage until used clinically. Careful handling ensured disinfection was maintained until the catheter came into contact with a patient. The enema packaging was secured with packing tape to ensure the contents of the bag remained secure while in storage.
6. The disinfected rectal catheter assemblies were stored in a dark location that was secure from outside radiation sources.

3.3.2.5 Irradiating TLDs during VC and QC Step 4: Maintenance of Control of TLDs at All Times

Once the TLD/rectal catheter assemblies, preparatory QA steps, and disinfection were completed, 6 patients were recruited for the study in accordance with the conditions established for IRB approval. This study was limited to those patients whom were already approved for VC by their primary physician and their insurance. Patient recruitment, informed consent, and evaluation were conducted by one of two board certified radiologists experienced in VC interpretation (Drs. David Vining and Priya Bhosale). The process of obtaining informed consent for this protocol was overseen by the Office of Translational and Clinical Research within the Division of Diagnostic Imaging at MD Anderson Cancer Center.

The criteria for inclusion in this study included: those patients scheduled for VC as part of routine standard-of-care (including both screening and diagnostic VC exams), an

ability to provide informed consent, and an ability to read and speak English (because the team was unable to conduct the informed consent process in any other language). Criteria for exclusion from this study included: women of childbearing age (unless a negative urine or serum pregnancy test was obtained within 48 hours prior to participating in the study), a history of allergic reaction to iodinated-contrast agents, and patients under the age of 18. Eligible participants were asked to participate in this research study between one and 30 days before the VC CT scan was conducted. Participants were made aware that if for any reason during the procedure the participant wished to cease their involvement with the study, their desires would be adhered to without prejudice and that their VC examination would be conducted in the usual manner.

Once a patient had agreed to participate in this study and provided informed consent, a disinfected and sealed rectal catheter/TLD assembly was removed from storage for the scheduled VC appointment and provided to the radiologist at the MDCT scanner. Although the typical VC protocol at MD Anderson Cancer Center does not require a physician to administer the rectal catheter, appropriately trained radiologists conducted all enema tip administration and removals for this study. The fourth stage of QC was incorporated to ensure that the radiologist maintained control of the TLDs at all times. This was accomplished by adhering to the following procedures:

1. The bag was opened, but not disposed of, using standard infection control personal protective equipment (PPE) (gloves).
2. When beginning the procedure, the catheter assembly was carefully removed from the bag and the inner lumen of the rectal catheter visually inspected through the superior opening to verify that two TLDs could be visualized within the catheter (verifying an appearance similar to that shown in Figure 3-31). The VC procedure was not to proceed unless both TLDs were present.

3. Upon verification of the presence of two TLDs within the catheter tip, the contrast bag was clamped at the tubing and filled with the iodinated contrast agent by the CT technologist. Additionally, the gas insufflation pump was connected to the blue tube by the technologist and the rectal catheter was inserted into the patient by the radiologist for the VC procedure (see Figure 1-4).
4. Upon completion of the CT scan, the catheter was removed from the patient's rectum and the radiologist immediately verified that two TLDs were present within the catheter. If both TLDs were discovered to not be present within the catheter, it would be up to the discretion of the radiologist to determine whether active retrieval actions should be taken (i.e. Fleet's enema). If such an event were to occur, active retrieval actions would not typically be necessary after VC as all contents of the rectum and bowel are discharged from the patient into a toilet almost immediately upon the completion of the exam.
5. In the very unlikely event that one or both TLDs became dislodged from the rectal catheter during a VC procedure, only the TLD that remained (if any) was to be used for data acquisition purposes. If the situation were to arise, any dislodged TLDs were not to be pursued due to infection control reasons.
6. Upon the completion of the VC procedure and verification of the presence of both TLDs within the catheter, the radiologist held the rectal catheter such that it could be cut with scissors and separated from the rest of the enema delivery system. The enema delivery system was disposed as medical biohazardous waste. The rectal catheter was closed within a zipper-style bag and this bag was enclosed into an additional bag for infection control purposes. A folded piece of paper was placed between the two bags containing the patient's medical record number, the date of the exam, and the patient's study number (1-10).

The CT scans were performed in accordance with the standard MD Anderson Cancer Center VC procedure outlined in Chapter 1.1.2, with each patient receiving CT scans in both a supine and prone position using a standard technique. As discussed above, the two scans are necessary during VC to evaluate segments of the colon that may be collapsed during one of the scans, as well as to shift residual feces/water that may mask or simulate colonic lesions. During each VC procedure, the two affixed TLDs acquired a total of four measurements of the accumulated absorbed radiation dose delivered to that patient's rectum during the two PA scout scans, the two lateral scout scans, and the two CT scans.

3.3.2.6 TLD Retrieval and QC Step 5: Disinfection of Rectal Catheter Assembly and TLD Capsules

The fifth stage of QC was incorporated to ensure the investigators and RPC staff did not receive an infection as a result of participation in this study. This step involved a thorough disinfection of the TLD/rectal catheter assembly, the harvesting of irradiated TLDs from the rectal catheters, and an additional thorough disinfection of these TLD capsules.

To do so, the following procedures were conducted:

1. A suitable work environment was established with a deep sink and running water. Anti-microbial soap, disinfection wipes (containing bleach), 70% isopropyl alcohol in a container, and appropriate personal protective equipment (PPE) (non-latex gloves, eye protection, and disposable coat/covering) were collected.
2. With PPE donned, the bag containing the used rectal catheter was opened and the paper containing patient identity information was also removed from the bag.
3. The exterior of the rectal catheter was then scrubbed for 30 seconds (with PPE donned) with anti-microbial soap, disinfection wipes and copious warm tap water.

4. The sutures holding the superior TLD to the rectal catheter were then cut, and the TLDs were squeezed from the rectal catheter with hand pressure into the container containing the 70% isopropyl alcohol solution; where they remained for several minutes.
5. When the TLDs had been retrieved from a catheter, that catheter was inserted back into the zipper-style plastic bags and discarded as standard waste.
6. Upon completion of the TLD disinfection within the isopropyl alcohol, the TLDs were dried with paper towels, securely attached to a sheet of paper labeled only with the patient's study number (1-6) and the date of the VC scan, and stored as appropriate (i.e. in a dark place away from outside radiation sources) for at least 14 days before being delivered to the RPC for reading.
7. Upon completion of these TLD resection and disinfection steps, the workspace and sink were thoroughly disinfected with disinfection wipes. When workspace disinfection was completed, the PPE were disposed as standard waste (except the eye protection, which was disinfected as appropriate).
8. When clean-up and disinfection were accomplished, the patient study number (1-6) was listed along with the patient medical record number and the date of the exam in a password-protected study data collection Excel spreadsheet (Microsoft Corporation, Redmond, WA) located on a secure computer at MD Anderson Cancer Center that was password protected and located in a locked room. The spreadsheet columns containing the patient identifiers were additionally hidden when not in use (to prevent unnecessary personnel from incidentally viewing this information). When the necessary information was recorded, those papers containing the patient identifiers that were placed in the bags immediately after the VC scans had occurred were shredded. Medical record numbers were only used when necessary to preserve data integrity, and all involved research staff that had access to these records completed training for

maintaining confidentiality of health information. Complete confidentiality was maintained during this study and during manuscript preparation.

3.3.2.7 Patient Rectal Dose Determination

Once at least 14 days had passed from a VC procedure and TLD readout had been accomplished, the RPC provided the following information for the purpose of calculating patient rectal dose: TLD aliquot charge reading (in μC), aliquot TLD mass (in mg), sensitivity correction factor (in $\text{cGy}/\mu\text{C}/\text{mg}$) and fading correction factor (unitless). These values, along with the regression model for the dose linearity correction factor at 120 kVp ($K_{L,120}$) established in Specific Aim 1, were used to calculate the four rectal dose measurements (in mGy) obtained for each of the 6 VC patients using Equation 3-8. Since each of these TLD measurements included the rectal dose administered by the four to five scout scans and two CT scans administered in each VC, additional efforts were made to estimate the contribution of the scout scans to the measured doses.

Estimation of rectal dose from scout scans was performed in a similar manner as that published by O'Daniel, et.al. in (15). First, patient lateral and PA TLD-to-surface distance measurements were obtained from patient DICOM images, and the average distance of the TLDs from the table during the in-vivo measurements were recorded for both the prone and supine scans. Next, a Farmer style ionization chamber was placed on a block on the CT scanner table such that the active volume of the chamber was at the measured average supine TLD distance above the CT table. Lateral and PA scout scan lengths were then established such that the active volume of the Farmer style ionization chamber was placed in the center of each scout image. In-air exposure measurements were then acquired using the same techniques as those to which the patients were exposed (120 kVp, 10 mA). This process was repeated for the average distance from the CT table to the TLDs when patients were placed in a prone position and for the scout

technique used for the prone scout scans (120 kVp and 80 mA). Using the inverse square law and patient lateral and PA TLD-to-surface distance measurements obtained from patient DICOM images, each patient's entrance skin exposure was then estimated for both the PA and lateral scout scans in both the supine and prone positions. By assuming an effective keV of 60 from the scout image technique of 120 kVp, a mass attenuation coefficient of $\mu/p=0.2025 \text{ cm}^2/\text{g}$ (100), and density of 1.04 g/cm^3 (90) for soft tissue, the attenuated exposure to the rectum for each scout scan was estimated using the Lambert-Beer equation (Equation 3-2). These attenuated exposure estimates were added and were converted to dose estimates using the f-factor for muscle ($f_{\text{Muscle}}=0.94 \text{ rad/R}$), thus yielding a total rectal dose estimate from the scout scans. These total scout scan dose estimates were subtracted from the four TLD rectal dose measurements obtained in each patient to calculate CT rectal dose measurements for each patient. The average of these four CT dose measurements was determined to be the rectal dose to a specific patient from the CT scans administered in VC, and these average dose values were used to accomplish Specific Aim 3 in comparing the TLD dose measurements to anthropomorphic phantom measurements, CTDI_{vol}-based dose estimates (including the size specific dose estimates (SSDE)) and Farmer chamber dose measurements obtained in a uniform CTDI body phantom.

3.4 Specific Aim 3: Compare In-Vivo Rectal Dose Measurements to Anthropomorphic Phantom Measurements, CTDI-Based Dose Estimates and Point Dose Measurements from a Uniform Phantom

3.4.1 Introduction

When the TLD measurement results were received from the RPC and absorbed dose measurements were calculated for every in-vivo dose measurement patient (along

with the average rectal dose for each phantom configuration and patient) in Specific Aim 2, these average dose measurements were compared to anthropomorphic phantom measurements, CTDI_{vol}-based size specific dose estimates (SSDE) estimates and a Farmer chamber dose measurement taken in a uniform CTDI body phantom. To do so, the following values were tabulated by phantom configuration and patient in a password-protected Excel spreadsheet (Microsoft Corporation, Redmond, WA) to protect patient identity in accordance with IRB and HIPAA requirements: phantom configuration (P0-P2) or patient identifier (a number 1-6), patient medical record number and VC scan date (with these columns hidden and password protected for additional patient identity protection), patient thickness measurements obtained using Philips iSite Enterprise PACS software (Philips Healthcare, Andover, MA) from a supine CT image that was determine to be the median location of the TLDs (posterior-anterior (PA), lateral, and circumference measurements, along with effective diameter), percentile of US adults aged 18-64 the patient represents, the image number that was used to measure patient thickness, the number of scout scans in the VC procedure, the number of CT scans in the VC procedure (because a prone or supine scan occasionally must be repeated; such as in cases where a scan shows that the bowel was not insufflated sufficiently), all rectal doses from TLD measurements, average phantom or patient TLD rectal dose measurements, CTDI_{vol} based rectal dose estimates, Farmer chamber measurements performed in a uniform CTDI body phantom, and SSDE dose estimates (described below). Mean square errors were calculated to compare these dose estimates to the in-vivo dose measurements for each patient. 95% confidence intervals (CI) were also established for the in-vivo TLD dose measurements, as was the percent coefficient of variation (%CoV) for each patient and for the population of patients that participated in this study. This between-patient %CoV value was calculated based on the average rectal dose measurement of each patient as was used as an indirect assessment of the size range of patients receiving VC at MD Anderson

Cancer Center. It was hypothesized in chapter 1.4.1 that this between-patient %CoV would be greater than 50%.

3.4.2 Size Specific Dose Estimate (SSDE)

Size specific dose estimate (SSDE) is a dose estimate introduced in AAPM Report 204 (101) that incorporates a correction factor to account for underestimation or overestimation of $CTDI_{vol}$ dose estimates resulting from patient size (with large patient dose being overestimated and small patient dose being underestimated by $CTDI_{vol}$) (42, 101). SSDE does not address other problems with CTDI measurements such as CTDI's lack of ability to measure extended scatter dose tails (43). The SSDE technique includes several options for determining patient size. The approach utilized in this work is that of the effective diameter, where AP and lateral measurement are acquired from one cross-sectional CT image (at the average location of the TLDs within the rectal catheter), multiplied together and the square root is taken of this product. Tables in AAPM Report 204 provide a specific correction factor based on the phantom used to determine the $CTDI_{vol}$ estimate and a specific patient's size measurement ($f_{Patient}^{Phantom}$) (101). For example, if a patient's AP and lateral dimensions summed to 22.2 cm such that an effective diameter of 10.7 cm is calculated (a small patient), and the $CTDI_{vol}$ estimate (in mGy) provided by the scanner was based on the 32 cm CTDI body phantom, the physicist would reference Table 1A in AAPM Report 204 to obtain a correction factor of $f_{22.2}^{32S} = 2.5$ (unitless) (101). This correction factor would be used to calculate the SSDE (in mGy) using Equation 3-11:

$$SSDE = CTDI_{vol} \cdot f_{Patient}^{Phantom} \quad (3-11)$$

The importance of this technique to correct CTDI_{vol} dose estimates is underscored in this example, where the correction factor of $f_{22.2}^{32S} = 2.5$ implies that the CTDI_{vol} estimate provided by the scanner underestimated the actual patient dose by 250% (due to the small size of the patient).

The $f_{\text{Patient}}^{\text{Phantom}}$ values published in AAPM Report 204 show an exponential relationship between the normalized dose correction coefficient and patient dimension measurements. Additionally, the $f_{\text{Patient}}^{\text{Phantom}}$ values were independently verified by four different laboratories (two involving Monte Carlo calculations and two involving physical measurements in phantoms), with the results showing considerable agreement (101). As SSDE provides users with an estimate of patient dose based on patient size and MDCT scanner output, this technique theoretically provides a better estimate of the average patient dose than standard CTDI_{vol} dose estimates.

3.4.3 Outlier Analysis

In order to explain potential differences between patient rectal dose measurements and anthropomorphic phantom dose measurements due to insurmountable differences that may arise during in-vivo sampling (such as differences in TLD placement, amount of iodine contrast, and body composition), several additional Hounsfield Unit (HU) measurements were performed on the axial images for each patient. Relative bone density measurements were obtained by averaging six HU measurements acquired in supine images of the ATOM phantom and in each patient's femoral heads as illustrated in Figure 3-32. These measurements were acquired in the femoral heads of each patient regardless of the location of the TLDs within the rectum in order to provide a consistent assessment of each patient's bone density, and the average HU measurements were plotted in a bar chart (in Chapter 4) for comparison purposes.



Figure 3-32. Illustration of the assessment of patient relative bone density via HU measurements in six ROI measurements encompassing the femoral heads.

The combined effects of differences in iodine contrast present, bone density, and TLD placement were assessed through histograms of the supine and prone CT images (see Figure 3-33). The images analyzed for each patient and the ATOM phantom were chosen on the basis of being the average location of the two TLDs in each scan series. Since iodine and bone provided the highest HU numbers in each VC image, the histogram of each of these images were thresholded to those values greater than 200 HU, and that number of pixels was divided by the total number of pixels in an image ($512 \times 512 = 262,144$ pixels). For comparison purposes between patients, each of these percentages were then normalized to a display field of view (DFOV) of 50 cm (such that the pixel areas were equal in each image) by multiplying the ratio of the pixel area in an image by the pixel area at 50 cm DFOV (0.0095 cm^2). Such quantification of highly attenuating material provided insight into the effects of such factors as TLD placement, iodine contrast, and bone density on the TLD rectal dose measurements.

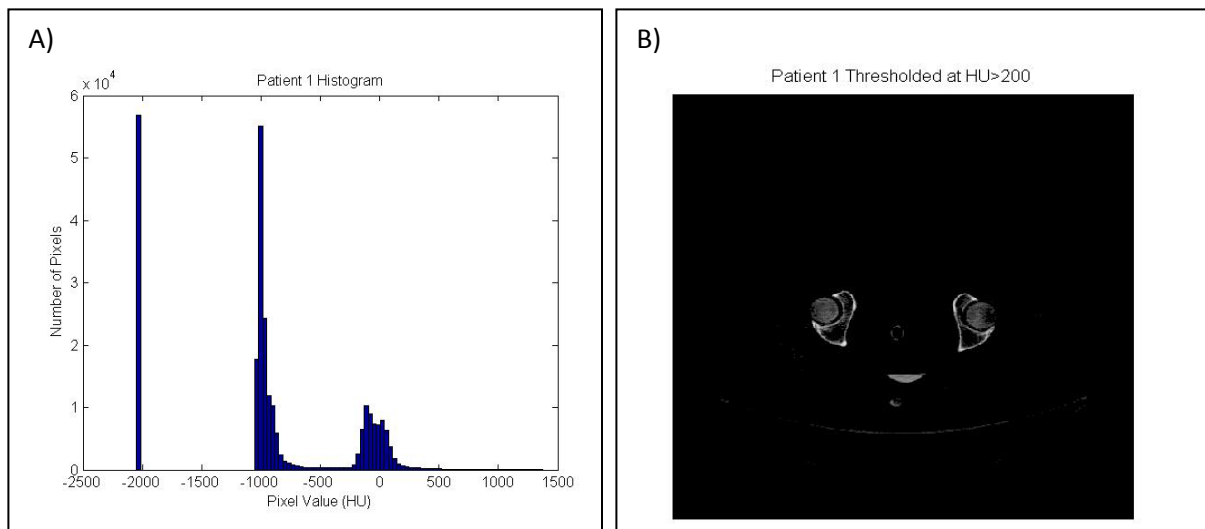


Figure 3-33. A) Histogram of a supine VC image of a patient. B) Patient supine VC image after being thresholded to include only those voxels with HU values greater than 200.

3.4.4 Statistical Analysis

Regression analysis was used to establish a rectal dose predictive model from anthropomorphic phantom measurements. A multiple-order polynomial regression equation and R^2 goodness of fit coefficient were also established for this anthropomorphic phantom regression analysis. These predictive rectal dose values were compared to the in-vivo patient rectal dose measurements obtained in Specific Aim 2.

Understanding the size of patients undergoing VC at MD Anderson Cancer Center was determined to be important based on the fact that the dose delivered to a patient's rectum using this fixed CT technique will be a function of the size of that patient. As an indirect assessment of the size distribution of VC patients participating in this study, a between-patient percent coefficient of variation (%CoV) value was determined by dividing the standard deviation of the average rectal dose measurements from the six patients by

the average measured rectal dose for the study population. This %CoV value was assessed to determine whether it exceeded 50%, as stated in the hypothesis.

Mean square error (MSE) calculations were performed to compare the in-vivo rectal dose measurements to anthropomorphic phantom measurements, SSDE dose estimates, and uniform CTDI phantom-based dose estimates (including Farmer chamber dose measurements, measured $CTDI_{vol}$ for the beam output received by patients undergoing VC, and $CTDI_{vol,center}$ (providing a CTDI dose estimate that did not consider the peripheral pencil chamber measurements)). Calculations were also performed to determine if the differences between the mean TLD rectal dose measurements, the anthropomorphic phantom, the SSDE estimates, the $CTDI_{vol}$ -based estimates, and the Farmer chamber measurements in a CTDI body phantom were outside the 95% confidence interval (as stated in the hypothesis). The results of these analyses are provided in Chapter 4.

CHAPTER 4.0: RESULTS

4.1 Introduction

The results from the phantom and patient virtual colonoscopy (VC) rectal dose measurements are reported in the order presented in Chapter 3 and arranged according to the specific aims outlined in Chapter 1. First, in accordance with Specific Aim 1, thermoluminescent dosimeter (TLD) linearity correction factors were established for a range of doses at 120 kVp for a multi-detector computed tomography (MDCT) scanner using VC scan parameters in a 32 cm CT dose index (CTDI) body phantom. Next, in accordance with Specific Aim 2, rectal dose measurements using TLDs were obtained in VC simulations within an anthropomorphic phantom and in-vivo within patients undergoing VC. Finally, in accordance with Specific Aim 3, in-vivo rectal dose measurements were compared to anthropomorphic phantom measurements, CTDI_{vol}-based dose estimates, and point dose measurements obtained in a CTDI body phantom. These specific aims were accomplished in order to test our hypotheses: In-vivo rectal dose measurements obtained during virtual colonoscopy will have a rectal dose coefficient of variation that will be greater than 50%, and the differences between the anthropomorphic phantom measurements, CTDI_{vol}-based dose estimates, and Farmer chamber measurements in a CTDI body phantom will exceed the 95% confidence interval of in-vivo rectal dose measurements.

4.2 Specific Aim 1: Establish TLD Linearity Correction Factors for VC Scan

Parameters on a MDCT

As stated earlier, although the Radiologic Physics Center (RPC) (Houston, TX) typically provides energy and dose linearity correction coefficients to customers as a standard service, their established correction factors pertain to those doses and energies encountered in photon or electron cancer therapy by linear accelerator and are specifically

defined for higher energies (a minimum of 1 MV) and doses (a minimum of 200 mGy) than those obtained by MDCT dose to a patient's rectum during a VC exam. Therefore Specific Aim 1 characterized baseline x-ray beam performance and provided correction factors relevant for MDCT at the energy and dose range encountered in VC.

4.2.1 MDCT Beam Characterization

In order to identify any discrepancies in TLD readings and actual dose measurements between MDCT scanners used for VC or in the event of a change in the MDCT x-ray tube between TLD irradiation and anthropomorphic phantom or in-vivo patient VC measurements, several x-ray beam quality factors were measured. These measurements were conducted in the same CT sessions as when the TLDs were irradiated to establish the dose linearity correction factors for VC conditions, and upon completion of in-vivo patient dose measurements. These measured beam factors included: the half-value layer (HVL), quarter-value layer (QVL), CTDI in-air measured with a 100 mm pencil chamber ($(CTDI_{100})_{air}$), weighted CTDI ($CTDI_w$), and volume CTDI ($CTDI_{vol}$) for the MD Anderson Cancer Center VC technique.

4.2.1.1 HVL and QVL Measurement

The HVL and QVL measurements were made using the method described by Mathieu, et al (95) incorporating the Lambert W function described in Chapter 3.2.1.1 for the polyenergetic spectrums encountered in CT. These HVL and QVL measurements were obtained on the two scanning occasions where the TLD dose linearity correction factors were established for a 120 kVp MDCT photon beam. This technique required the acquisition of in-air exposure measurements using a 100 mm pencil ionization chamber of unattenuated and attenuated stationary (i.e. non-rotating) beams specified to approximate conditions used in VC at MD Anderson Cancer Center (120 kVp, 100 mA, 1 sec exposure

time, large body filter, small focal spot, 40 mm nominal beam). The total beam quanta output per rotation of 100 mAs was used to simulate the combined beam output from both the prone and supine scans used in VC. The results of the three exposure measurements obtained with each amount of beam filtration on each testing date (in mR); the average, standard deviation, and percent coefficient of variation (%CoV) of those exposure measurements; the values for λ and μ_0 calculated from Equations 3-6 and 3-7, respectively; and the HVL and QVL (both in mm Al) values calculated from Equations 3-4 and 3-5, respectively, are provided in Table 4-1.

These results demonstrated excellent measurement precision, with all exposure measurements at a given filtration having a %CoV less than 0.1% and with the HVL and QVL values demonstrating consistent x-ray tube quality on different days five months apart and across 3 MDCT scanners. The HVL values also corresponded well with the HVL measured during acceptance testing of the scanner (7.96 mm Al). This 2% difference may be the result of a small drift in tube output, or may be caused by inherent uncertainties in the measurement of the filtration thickness or of the ionization chamber measurements. No standards currently exist stating an amount of allowable change in HVL measurements a tube may experience before requiring replacement. The effect of these differences in x-ray tube output between the respective dates and scanners likely had a minimal impact on the TLD doses calculated based on the linearity correction factors determined at 120 kVp on the “CT9” MDCT at MD Anderson Cancer Center, regardless of the CT scanner used to accomplish a VC.

Table 4-1. Results of HVL and QVL measurements obtained on the MDCT scanners at MD Anderson Cancer Center used for VC procedures under VC simulation conditions; where Date is the date the measurements were obtained (corresponding to the dates used to determine the TLD correction factors), CT is the MD Anderson Cancer Center nomenclature for the MDCT scanner on which the exposure measurements were performed, Filtration is the thickness of aluminum 1100 alloy used to attenuate the primary beam, Exp represents the respective exposure measurements obtained at each thickness, Avg Exp is the average of the exposure measurements, St Dev is the standard deviation of the exposure measurements, %CoV is the percent coefficient of variation of the exposure measurements, λ and μ_0 are coefficients utilized by Lambert W interpolation, HVL is the half-value-layer, and QVL is the quarter-value-layer.

Date	CT	Filtration (mm Al)	Exp #1 (mR)	Exp #2 (mR)	Exp #3 (mR)	Avg Exp (mR)	St Dev (mR)	%CoV (%)	λ	μ_0	HVL (mm Al)	QVL (mm Al)
1/17/11	CT9	0	1263	1263	1264	1263	0.577	0.05	0.0412	0.0683	7.79	17.63
		6.36	706.6	705.9	706.4	706.3	0.361	0.05				
		19.84	272.7	273.1	272.9	272.9	0.200	0.07				
4/2/11	CT9	0	1269	1271	1269	1270	1.155	0.09	0.0411	0.0685	7.78	17.60
		6.36	709.1	710.0	709.8	709.6	0.473	0.07				
		19.84	273.4	273.3	273.7	273.6	0.173	0.06				
6/18/11	CT9*	0	1306	1305	1305	1305	0.577	0.04	0.0420	0.0685	7.75	17.56
		6.36	727.7	727.8	727.6	727.7	0.100	0.01				
		19.84	280.6	280.4	280.8	280.6	0.200	0.07				
6/18/11	CT12	0	1303	1302	1303	1303	0.577	0.04	0.0429	0.0692	7.65	17.35
		6.36	721.3	721.3	721.4	721.3	0.058	0.01				
		19.84	275.8	275.6	276.0	275.8	0.200	0.07				
6/18/11	CT5	0	1277	1277	1276	1277	0.577	0.05	0.0419	0.0686	7.74	17.52
		6.36	711.5	711.4	710.9	711.3	0.321	0.05				
		19.84	273.8	273.7	273.8	273.8	0.058	0.02				

*The x-ray tube on this scanner was replaced between the time the last in-vivo VC was performed and before the final HVL and QVL measurements could be acquired.

4.2.1.2 $(CTDI_{100})_{air}$, $CTDI_w$, and $CTDI_{vol}$ Determination

$(CTDI_{100})_{air}$ measurements were acquired using the same pencil ionization chamber configuration as that used to determine the HVL and QVL. $(CTDI_{100})_{air}$ required slightly different scan settings, however, as the scans were performed in axial mode (as opposed to the tube remaining stationary while the beam was on). In order to replicate beam conditions during VC at MD Anderson Cancer Center, the CT scan settings used to

determine $(CTDI_{100})_{air}$ via Equation 1-11 were: axial scan, 0.5 sec per rotation of the x-ray tube, a nominal beam width of 40 mm, 120 kVp, 200 mA, standard reconstruction algorithm, large (body) bowtie filter, large body scan field of view (SFOV) and 50 cm display field of view (DFOV). In a manner similar to the scan technique utilized in the beam HVL and QVL measurements, 100 mAs was used to acquire these CTDI measurements to simulate the combined dose received by patients undergoing VC from the prone and supine CT scans. The results of the exposure measurements (in mR), the average and standard deviation of those exposures (in mR), the percent coefficient of variation (in %), and the calculated $(CTDI_{100})_{air}$ values (in mGy) for the two scanning sessions that determined the TLD correction factors specific to MDCT are provided in Table 4-2.

Table 4-2. Results of in-air exposure measurements and corresponding $(CTDI_{100})_{air}$ calculations obtained on MD Anderson Cancer Center “CT9” MDCT under conditions simulating VC at MD Anderson Cancer Center; where Date is the date the measurements were obtained (corresponding to the dates used to determine the TLD correction factors and completion of in-vivo measurements), Exp represents the respective exposure measurement iteration obtained in each day, Avg Exp is the average of the exposure measurements, St Dev is the standard deviation of the exposure measurements, %CoV is the percent coefficient of variation, and $(CTDI_{100})_{air}$ is the corresponding in-air $CTDI_{100}$ value.

Date	Exp #1 (mR)	Exp #2 (mR)	Exp #3 (mR)	Avg Exp (mR)	St Dev (mR)	%CoV (%)	$(CTDI_{100})_{air}$ (mGy)
1/17/11	1032	1034	1034	1033	1.155	0.1	22.25
4/2/11	1028	1028	1028	1028	0	0	22.36
6/18/11*	1066	1069	1069	1068	1.732	0.2	23.23

*The x-ray tube on this scanner was replaced between the time the last in-vivo VC was performed and before the final HVL and QVL measurements could be acquired.

The results of these $(CTDI_{100})_{air}$ measurements also showed excellent precision with the %CoV being 0.2% or less, and good agreement between respective $(CTDI_{100})_{air}$ measurements on the different days and different x-ray tubes (which was replaced on the

“CT9” scanner in the three days between the last in-vivo patient measurement being acquired and the exposure tube measurements). The 0.5% difference between the $(CTDI_{100})_{air}$ measurements acquired on the same x-ray tube may be the result of inherent uncertainties in the measurement process and likely had a minimal impact on the TLD dose linearity correction factors determined at 120 kVp for the “CT9” MDCT at MD Anderson Cancer Center. The 4% difference between the $(CTDI_{100})_{air}$ measurements acquired on the different x-ray tubes was likely the combined result of changes in respective tube performance and inherent uncertainties in the measurement process, but these results still demonstrated good agreement between the outputs of several x-ray tubes and provided confidence in the uniformity of the in-vivo doses measured on multiple MDCT scanners during VC.

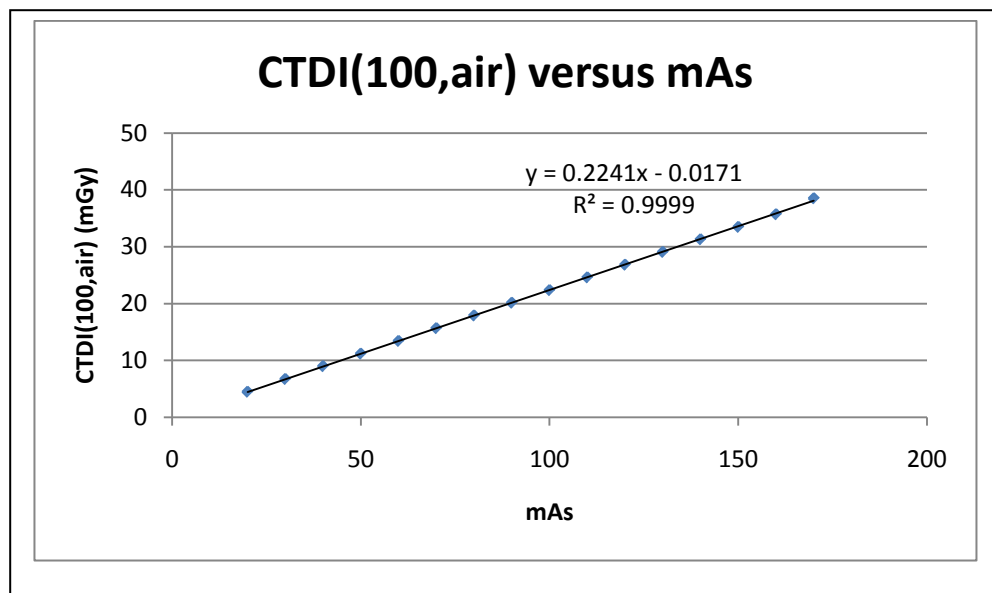


Figure 4-1. Linear relationship between MD Anderson Cancer Center “CT9” beam administered dose (measured in the form of $(CTDI_{100})_{air}$) and mAs.

In order to establish the linearity of the MDCT scanner dose output with mAs, $(CTDI_{100})_{air}$ measurements were acquired using this same scan technique in 10 mAs increments from 20 mAs (40 mA) to 170 mAs (340 mA),. These linearity measurements were helpful in extrapolating doses at the center of the CTDI body phantom that were sufficiently low as to be undetected with a Farmer ionization chamber (without this data, TLD dose linearity correction coefficients at 120 kVp could not be obtained for administered point doses less than 2.1 mGy). The linear relationship between these $(CTDI_{100})_{air}$ measurements and increasing mAs is demonstrated in Figure 4-1. The R^2 value of 0.999 demonstrates a very strong goodness of fit of the linear regression between the scanner mAs and the $(CTDI_{100})_{air}$ calculations.

In order to measure the weighted CTDI ($CTDI_w$) and volume CTDI ($CTDI_{vol}$), the pencil ionization chamber was placed within the CTDI body phantom and exposure measurements were acquired within the center bore and in the peripheral bores located in the 12, 3, 6, and 9 o'clock positions using the same scan technique as that used to determine $(CTDI_{100})_{air}$ at 100 mAs. These exposure measurements were used to calculate $CTDI_{100}$ values at each of these locations ($(CTDI_{100})_c$, $(CTDI_{100})_{12}$, $(CTDI_{100})_3$, $(CTDI_{100})_6$, and $(CTDI_{100})_9$, respectively). The peripheral CTDI values were averaged to calculate the $CTDI_{100}$ value at the periphery of the phantom ($(CTDI_{100})_{periphery}$), and this value was used with $(CTDI_{100})_c$ to calculate $CTDI_w$ via Equation 1-12. $CTDI_{vol}$ was calculated from $CTDI_w$ using Equation 1-14. Each of these CTDI values are provided in Table 4-3 for the two sessions used to determine the TLD dose linearity correction coefficients at 120 kVp and in a session that was conducted upon the conclusion of in-vivo dose measurements (where the "CT9" MDCT scanner contained a newly replaced x-ray tube).

Table 4-3. Results of exposure measurements within a CTDI body phantom and corresponding CTDI calculations obtained on the MD Anderson Cancer Center “CT9” MDCT scanner under conditions simulating VC at MD Anderson Cancer Center; where Date is the date the measurements were collected (corresponding to the dates used to determine the TLD correction factors), Pos is the position of the pencil chamber within the CTDI phantom, Exp represents the respective exposure measurements obtained at each position, Avg Exp is the average of the exposure measurements, St Dev is the standard deviation of the exposure measurements, %CoV is the percent coefficient of variation, $(CTDI_{100})_{pos}$ is the corresponding $CTDI_{100}$ value at that position, $CTDI_w$ is the weighted CTDI, $CTDI_{vol}$ is the measured volume CTDI, and Scanner $CTDI_{vol}$ is the volume CTDI value provided by the CT scanner console.

Date	Pos	Exp #1 (mR)	Exp #2 (mR)	Exp #3 (mR)	Avg Exp (mR)	St Dev Exp (mR)	%CoV Exp (%)	$(CTDI_{100})_{pos}$ (mGy)	$CTDI_w$ (mGy)	$CTDI_{vol}$ (mGy)	Scanner $CTDI_{vol}$ (mGy)
1/17/11	Center	217.6	216.8	216.8	217.1	0.462	0.21	4.72*	7.99	8.12	8.26
	12:00	447.9	465.0	461.1	458	8.96	1.96	9.96			
	3:00	451.0	457.4	450.5	453.0	3.85	0.85	9.85			
	6:00	406.5	407.4	408.5	407.5	1.00	0.25	8.86			
	9:00	452.3	451.6	451.8	451.9	0.361	0.08	9.83			
	Periph							9.63			
4/2/11	Center	215.5	216.0	215.9	215.8	0.265	0.12	4.69*	8.14	8.27	8.26
	12:00	459.3	461.5	461.6	460.8	1.30	0.28	10.02			
	3:00	480.5	479.6	475.9	478.7	2.44	0.51	10.41			
	6:00	431.3	427.1	424.6	427.7	3.39	0.79	9.30			
	9:00	447.0	447.3	447.0	447.1	0.173	0.04	9.72			
	Periph							9.86			
6/18/11 [†]	Center	223.2	222.3	222.8	222.8	0.451	0.20	4.85*	8.24	8.37	8.26
	12:00	473.5	482.0	478.5	478.0	4.27	0.89	10.40			
	3:00	464.8	463.4	461.1	463.1	1.87	0.40	10.07			
	6:00	415.7	415.5	421.3	417.5	3.29	0.79	9.08			
	9:00	468.7	467.9	469.0	468.5	0.569	0.12	10.19			
	Periph							9.94			

* Approximate position of the rectum within a patient

[†] Measurements were performed on the same MDCT scanner with a replaced x-ray tube

The results of these $CTDI_{100}$ measurements also demonstrated good precision, with the %CoV being 2% or less, and good agreement between the respective $CTDI_w$ and $CTDI_{vol}$ measurements. The 2% difference between the $CTDI_w$ and $CTDI_{vol}$ measurements obtained with the same x-ray tube may be the result of inherent uncertainties in the measurement procedures. The 2% difference between the average $CTDI_w$ and $CTDI_{vol}$ measurements obtained with different x-ray tubes may be the result of slight differences in

performance between the x-ray tubes and inherent uncertainties in the measurement equipment. These $CTDI_{vol}$ values also corresponded well with the $CTDI_{vol}$ value provided by the MDCT scanner for this scan technique ($CTDI_{vol}=8.26$ mGy), with an average percent difference of 0.08%. The effect of these differences in x-ray tube output between the respective dates and x-ray tubes likely had a minimal impact on the TLD dose linearity correction factors determined at 120 kVp for the “CT9” MDCT at MD Anderson Cancer Center, and provided confidence regarding the dose measurements obtained from different MDCT scanners of the same model.

4.2.2 Determination of TLD Dose Linearity Correction Coefficients for Virtual Colonoscopy

With the x-ray tube beam output well characterized at 120 kVp for the TLD irradiation sessions that would determine dose linearity response correction factors of the TLDs at 120 kVp ($K_{L,120}$), the pencil ionization chamber was replaced with a Farmer style ionization chamber in the center of the 32 cm CTDI body phantom. Using a scout image, the scan length was specified to be conducted from 75 mm superior to 75.4 mm inferior to the center of the CTDI body phantom. The CT scanner was set to standard MD Anderson VC protocols (also listed in Table 1-1 above): full helical scan mode with 0.5 sec rotation time, 1.25 mm image thickness, 39.37 mm/rotation table speed, 0.984 pitch, 1/64 channel setting, 0.8 mm interval, 120 kVp, 100 mA, 0 sec delay, and standard reconstruction algorithm. The ionization chamber exposure was measured and recorded for two scans under the specified CT technique for a total photon output of 100 mAs per x-ray tube rotation (representing the cumulated exposure acquired from both the prone and supine 50 mAs scans in VC).

The exposure measurements obtained by the Farmer ionization chamber (in mR) were converted to dose in the acrylic CTDI body phantom (in mGy) using an f-factor of $f_{Acrylic}= 0.78$ rad/R. This process was repeated three times and the average of these three

acrylic dose measurements was used to calculate the dose at the center of the CTDI body phantom at 100 mAs. This entire process was repeated for scanner photon outputs per rotation ranging from 20 mAs to 170 mAs in 10 mAs increments to administer doses to the center of the CTDI body phantom ranging from 0.6 mGy to 8.9 mGy (using the f-factor for acrylic), approximately reflecting the expected range of rectal doses administered in VC at MD Anderson Cancer Center as estimated in Chapter 1.3.5 (0.7-10.8 mGy when an f-factor appropriate for rectal dose is used, $f_{\text{Muscle}} = 0.94 \text{ rad/R}$). Doses were extrapolated based on the linear relationship between Farmer ionization chamber measured doses and mAs and assigned to those tube output values where doses were too low to be directly measured by the Farmer chamber (i.e. at 20 and 30 mAs). The principle of linearity between administered dose and mAs was demonstrated in Figure 4-1.

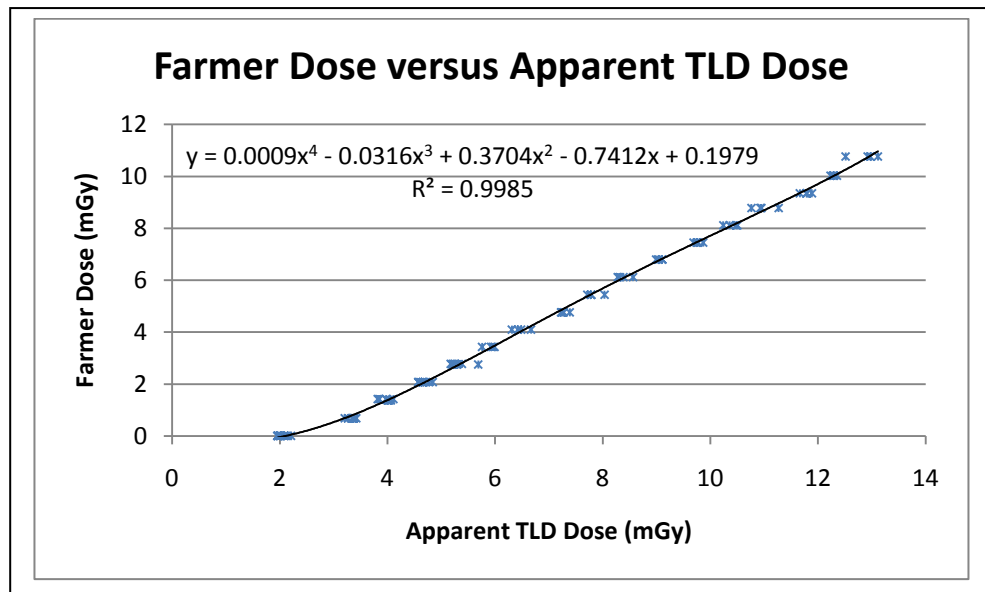


Figure 4-2. Fourth-order polynomial regression curve predicting Farmer ionization chamber response for the RPC's B09 TLD-100 batch from apparent TLD dose measurements (those uncorrected for dose linearity or energy) on MD Anderson Cancer Center "CT9" MDCT scanner.

After determining the average Farmer chamber dose at each respective mAs technique, double chambered TLDs were placed within the center of the CTDI body phantom (in a custom-designed insert rod), and the TLDs were irradiated under the same conditions as the Farmer ionization chamber. After TLD readout, the RPC provided the following information: measured TLD aliquot charge reading (Q) (in μC), TLD aliquot mass (m) (in mg), sensitivity (K_S) (which was converted to $\text{mGy}/\mu\text{C}/\text{mg}$ for the order of magnitude of rectal doses received by patients undergoing VC), and fading correction factor (K_F) (unitless). An f -factor for acrylic ($f_{\text{Acrylic}} = 0.78 \text{ rad/R}$) was divided by the f -factor for muscle/soft tissue ($f_{\text{Muscle}} = 0.94 \text{ rad/R}$), and the uncorrected TLD dose to the CTDI body phantom was calculated by Equation 3-8 for each TLD chamber. The results of the Farmer ionization chamber measurements are plotted with a fourth-order polynomial regression against the resultant apparent (i.e. uncorrected) TLD dose measurements in Figure 4-2.

$K_{L,120}$ values were calculated for every TLD chamber in this dose range by dividing the Farmer measured dose by the apparent TLD dose as demonstrated in Equation 3-9. The average $K_{L,120}$ value and the %CoV were determined for every mAs setting. These TLD charge and mass measurements, the K_S and K_F correction coefficients, the calculated TLD doses (not corrected for dose linearity or photon energy), the Farmer ionization chamber measured doses, the $K_{L,120}$ values and the average $K_{L,120}$ values at each mAs setting, and the %CoV for the $K_{L,120}$ values at each mAs setting are provided in Table 4-4.

Table 4-4. Results of Farmer ionization chamber determined dose measurements, TLD dose measurements, and TLD dose linearity correction factors at 120 kVp obtained in a 32 cm diameter CTDI body phantom under identical conditions simulating VC on MD Anderson Cancer Center “CT9” MDCT; where mAs represents the scanner setting used, Charge represents the measured reading, Mass is the mass of TLD aliquot read, K_S is the sensitivity correction factor, K_F is the fading correction factor, TLD Dose represents the apparent dose predicted by the TLD, Farmer Dose represents the dose measured by a Farmer chamber or extrapolated from data demonstrating dose linearity with mAs, $K_{L,120}$ represents the TLD dose linearity correction factor at 120 kVp, Avg $K_{L,120}$ is the average of the $K_{L,120}$ values at a mAs value, and %CoV is the percent coefficient of variation of the $K_{L,120}$ values.

mAs	Charge (μC)	Mass (mg)	K_S (cGy/ $\mu\text{C}/\text{mg}$)	K_F	TLD Dose (mGy)	Farmer Dose (mGy)	$K_{L,120}$	Avg $K_{L,120}$	%CoV $K_{L,120}$ (%)
20	0.07693	21.69	110.0	1.042	3.373	0.565	0.167	0.169	2.07
	0.07878	21.92	110.0	1.042	3.418	0.565	0.165		
	0.07465	21.22	110.0	1.042	3.346	0.565	0.169		
	0.07301	21.27	110.0	1.042	3.265	0.565	0.173		
	0.07430	22.03	110.0	1.042	3.208	0.565	0.176		
	0.07564	21.30	110.0	1.042	3.378	0.565	0.167		
	0.07758	21.98	110.0	1.042	3.357	0.565	0.168		
	0.07530	21.35	110.0	1.042	3.354	0.565	0.168		
30	0.08889	21.99	108.7	1.048	3.821	1.176	0.308	0.291	3.56
	0.09289	22.09	108.7	1.048	3.975	1.176	0.296		
	0.09111	22.37	108.7	1.048	3.850	1.176	0.305		
	0.09484	21.80	108.7	1.048	4.112	1.176	0.286		
	0.09250	21.99	110.0	1.042	4.001	1.143	0.286		
	0.09147	21.57	110.0	1.042	4.033	1.143	0.283		
	0.09337	22.14	110.0	1.042	4.011	1.143	0.285		
	0.09258	21.66	110.0	1.042	4.065	1.143	0.281		
40	0.1063	21.70	110.0	1.042	4.659	1.722	0.370	0.369	1.98
	0.1073	21.39	110.0	1.042	4.771	1.722	0.361		
	0.1068	21.82	110.0	1.042	4.655	1.722	0.370		
	0.1110	21.81	110.0	1.042	4.841	1.722	0.356		
	0.1045	21.72	110.0	1.042	4.576	1.722	0.376		
	0.1066	22.00	110.0	1.042	4.609	1.722	0.374		
	0.1050	21.83	110.0	1.042	4.575	1.722	0.376		
	0.1063	21.57	110.0	1.042	4.687	1.722	0.367		
50	0.1308	21.74	108.7	1.048	5.687	2.282	0.401	0.432	3.15
	0.1217	22.10	108.7	1.048	5.205	2.282	0.438		
	0.1198	21.40	108.7	1.048	5.292	2.282	0.431		
	0.1214	21.69	108.7	1.048	5.291	2.282	0.431		
	0.1192	21.76	110.0	1.042	5.210	2.300	0.441		
	0.1225	21.64	110.0	1.042	5.384	2.300	0.427		
	0.1222	22.46	110.0	1.042	5.175	2.300	0.444		
	0.1201	21.77	110.0	1.042	5.247	2.300	0.438		
60	0.1373	21.81	108.7	1.048	5.951	2.848	0.479	0.482	1.74
	0.1361	21.72	108.7	1.048	5.923	2.848	0.481		
	0.1347	22.11	108.7	1.048	5.759	2.848	0.494		

	0.1381	21.80	108.7	1.048	5.988	2.848	0.476		
70	0.1507	21.98	108.7	1.048	6.481	3.404	0.525	0.526	2.28
	0.1510	22.61	108.7	1.048	6.313	3.404	0.539		
	0.1499	22.06	108.7	1.048	6.423	3.404	0.530		
	0.1459	20.68	108.7	1.048	6.669	3.404	0.510		
80	0.1683	22.02	108.7	1.048	7.225	3.954	0.547	0.543	1.00
	0.1631	21.28	108.7	1.048	7.245	3.954	0.546		
	0.1661	21.25	108.7	1.048	7.389	3.954	0.535		
	0.1681	21.84	108.7	1.048	7.276	3.954	0.544		
90	0.1773	21.72	108.7	1.048	7.716	4.517	0.585	0.577	1.75
	0.1810	21.98	108.7	1.048	7.784	4.517	0.580		
	0.1888	22.22	108.7	1.048	8.032	4.517	0.562		
	0.1832	22.25	108.7	1.048	7.783	4.517	0.580		
100	0.1941	22.17	108.7	1.048	8.280	5.076	0.613	0.605	1.47
	0.1922	21.67	108.7	1.048	8.384	5.076	0.605		
	0.1918	21.80	108.7	1.048	8.317	5.076	0.610		
	0.1958	21.62	108.7	1.048	8.561	5.076	0.593		
110	0.2059	21.38	108.7	1.048	9.103	5.640	0.620	0.623	0.62
	0.2115	21.96	108.7	1.048	9.104	5.640	0.619		
	0.2090	21.88	108.7	1.048	9.029	5.640	0.625		
	0.2102	22.10	108.7	1.048	8.991	5.640	0.627		
120	0.2294	22.20	108.7	1.048	9.768	6.184	0.633	0.633	0.76
	0.2207	21.53	108.7	1.048	9.690	6.184	0.638		
	0.2278	21.82	108.7	1.048	9.869	6.184	0.627		
	0.2195	21.29	108.7	1.048	9.746	6.184	0.634		
130	0.2415	22.04	108.7	1.048	10.358	6.736	0.650	0.648	1.18
	0.2429	21.86	108.7	1.048	10.504	6.736	0.641		
	0.2307	21.30	108.7	1.048	10.238	6.736	0.658		
	0.2428	21.90	108.7	1.048	10.480	6.736	0.643		
140	0.2523	21.82	108.7	1.048	10.930	7.281	0.666	0.664	1.91
	0.2534	22.26	108.7	1.048	10.761	7.281	0.677		
	0.2508	21.66	108.7	1.048	10.945	7.281	0.665		
	0.2614	21.93	108.7	1.048	11.267	7.281	0.646		
150	0.2659	21.31	108.7	1.048	11.795	7.754	0.657	0.658	0.78
	0.2755	21.91	108.7	1.048	11.886	7.754	0.652		
	0.2671	21.65	108.7	1.048	11.662	7.754	0.665		
	0.2736	21.94	108.7	1.048	11.788	7.754	0.658		
160	0.2854	21.94	108.7	1.048	12.296	8.314	0.676	0.677	0.41
	0.2730	20.89	108.7	1.048	12.353	8.314	0.673		
	0.2893	22.36	108.7	1.048	12.230	8.314	0.680		
	0.2874	22.13	108.7	1.048	12.276	8.314	0.677		
170	0.3037	21.89	108.7	1.048	13.115	8.934	0.681	0.694	2.03
	0.2997	21.84	108.7	1.048	12.972	8.934	0.689		
	0.3049	22.30	108.7	1.048	12.924	8.934	0.691		
	0.2948	22.27	108.7	1.048	12.513	8.934	0.714		
Bkg	0.04755	22.30	104.7	1.059	1.962	0	0	0	4.39
	0.05089	21.78	104.7	1.059	2.150	0	0		
	0.04804	22.16	104.7	1.059	1.995	0	0		
	0.05071	22.32	104.7	1.059	2.090	0	0		
	0.04692	21.98	104.7	1.059	1.964	0	0		
	0.05224	21.79	104.7	1.059	2.206	0	0		
	0.04690	22.33	110.0	1.042	1.998	0	0		
	0.04664	21.99	110.0	1.042	2.017	0	0		
	0.04538	22.11	110.0	1.042	1.952	0	0		
	0.04963	22.23	110.0	1.042	2.123	0	0		

The $K_{L,120}$ values were used to establish a third-order polynomial regression curve based on apparent TLD dose measurements (i.e. TLD dose measurements not corrected by $K_{L,120}$ values). The results of this regression analysis are shown in Figure 4-3. Although Chapter 1 discussed several of the inherent difficulties involved with using TL-100 material to measure doses at diagnostic energies and doses, the TLDs demonstrated good reproducibility with all %CoV values for an administered mAs setting being 3.56% or less (with several %CoV values being less than 1%). The TLDs also demonstrate a general increase in %CoV values at lower administered doses. The R^2 value of 0.992 demonstrates a very strong goodness of fit of the third-order polynomial regression between the uncorrected TLD predicted doses and the $K_{L,120}$ calculations. This third-order polynomial regression equation was used to calculate anthropomorphic phantom and in-vivo patient rectal doses from apparent TLD dose measurements in VC at MD Anderson Cancer Center in Specific Aim 2.

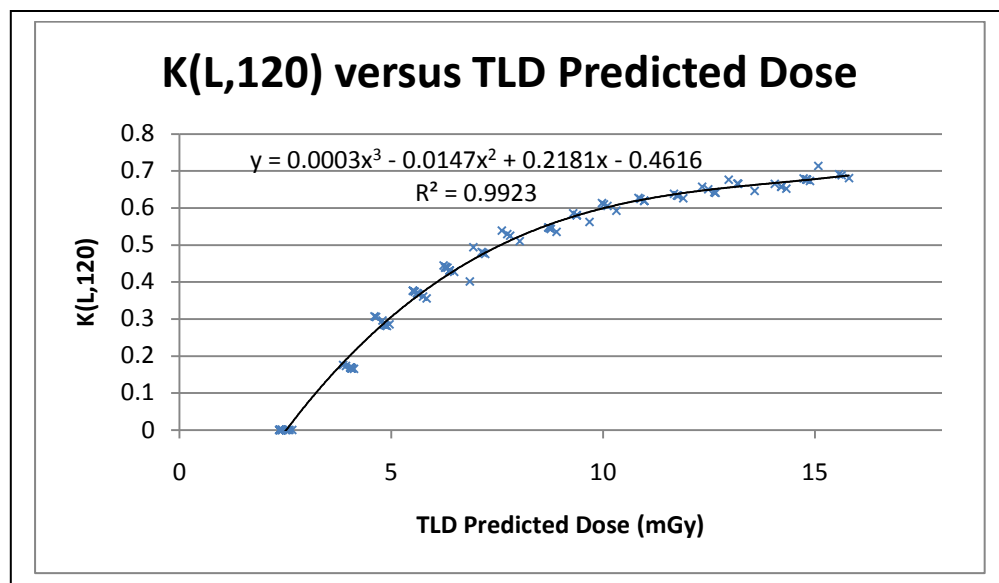


Figure 4-3. Third-order polynomial regression curve predicting $K_{L,120}$ values for the RPC's B09 TLD-100 batch from apparent TLD dose measurements (those uncorrected for dose linearity or energy) on MD Anderson Cancer Center "CT9" MDCT scanner.

From Table 4-3, by approximating that the rectum is located in the center of the phantom, the estimated dose to a patient's rectum from CTDI measurements is provided by the average $CTDI_{vol,center}$ measurements (the average $(CTDI_{100})_{center}$ measurements corrected for pitch), which yields a dose estimate of 4.78 mGy. Similarly, the dose to a patient's rectum estimated by the Farmer style ionization chamber measurements in the center of a CTDI body phantom is provided by the measurements displayed in Table 4-4 at 100 mAs, which average to be 6.12 mGy after applying the f-factor for dose to muscle ($f=0.94$ rad/R) to the exposure measurements. These uniform phantom-based dose estimates (summarized in Table 4-5) were compared in Specific Aim 3 to the dose estimates provided by the TLD measurements within the anthropomorphic phantom and within patients undergoing VC in Specific Aim 2 to assess whether the differences between the mean TLD rectal dose measurements, the $CTDI_{vol}$ -based SSDE estimates, and the ionization chamber measurements in a CTDI body phantom exceeded 10% of a 95% confidence interval (as stated in the hypothesis).

Table 4-5. Summary of rectal dose estimates obtained in a uniform CTDI body phantom, where $CTDI_{vol}$ is the volume CTDI value determined from pencil chamber measurements simulating the technique used in virtual colonoscopy, $CTDI_{vol,center}$ is the volume CTDI estimate only considering the center bore measurement in the $CTDI_w$ calculation, and Farmer is the dose measured by the Farmer chamber in the center bore.

$CTDI_{vol}$ (mGy)	$CTDI_{vol,center}$ (mGy)	Farmer (mGy)
8.3	4.8	6.1

4.3 Specific Aim 2: Obtain In-Vivo Rectal Dose Measurements in Patients

Undergoing VC with TLDs

With Specific Aim 1 accomplished, both the MDCT beam quality and the TLD response had been established for the dose range and energy spectrum received by a patient's rectum when undergoing virtual colonoscopy (VC). With this data, rectal dose measurements were obtained in an anthropomorphic phantom during simulated VC and in-vivo rectal dose measurements were obtained in actual patients undergoing VC at MD Anderson Cancer Center. All of these rectal dose measurements were acquired with thermoluminescent dosimeters (TLDs) (provided by the Radiologic Physics Center (RPC), Houston, TX).

4.3.1 Rectal Dose Measurement Simulation in an Anthropomorphic Phantom

Two double chamber TLDs were inserted within a rectal catheter that was placed in a simulated insufflated rectum within an anthropomorphic phantom. The 15th percentile phantom configuration was then placed on the MD Anderson "CT9" MDCT scanner in a supine position irradiated twice with the standard MD Anderson Cancer Center VC protocol to simulate patient scans in both a prone and a supine position: full helical scan mode with 0.5 sec rotation time, 1.25 mm image thickness, 39.37 mm/rotation table speed, 0.984 pitch, 0.8 mm image interval, 120 kVp, 100 mA, 0 sec delay, and standard reconstruction algorithm. The two irradiated TLDs were then replaced with a set of two un-irradiated TLDs within the phantom; and this process was repeated twice for a total of three sets of virtual colonoscopy rectal dose measurements.

Table 4-6. Results of TLD dose measurements during simulated VC in an anthropomorphic phantom configured to represent patients of three sizes of US adults aged 18-64 (15th percentile, 87th percentile, and 99th percentile); %ile represents the population percentile at the TLD location represented by the phantom configuration, Dim is the effective diameter of the phantom at the location of the TLDs, Charge represents the measured reading, Mass is the mass of TLD aliquot read, K_s is the sensitivity correction factor, K_F is the fading correction factor, Uncorr Dose represents the dose predicted by the TLD before corrections for dose linearity and energy were applied, K_{L,120} represents the TLD dose linearity correction factor at 120 kVp, TLD Dose represents the dose predicted by the TLD after corrections for dose linearity and energy were applied, Avg Dose is the average of the dose measurements for a phantom configuration, and %CoV is the percent coefficient of variation of the TLD dose measurements.

%ile	Dim (cm)	Charge (μC)	Mass (mg)	K _s (cGy/μC/mg)	K _F	Uncorr Dose (mGy)	K _{L,120}	TLD Dose (mGy)	Avg TLD Dose (mGy)	%CoV TLD Dose (%)
15	26.61	0.2532	21.82	110.0	1.042	13.301	0.677	9.011	8.804	1.92
		0.2515	21.83	110.0	1.042	13.205	0.676	8.928		
		0.2504	21.74	110.0	1.042	13.202	0.676	8.925		
		0.2432	21.64	110.0	1.042	12.882	0.672	8.653		
		0.2475	21.82	110.0	1.042	13.001	0.673	8.754		
		0.2509	21.66	110.0	1.042	13.277	0.677	8.990		
		0.2495	22.08	110.0	1.042	12.952	0.673	8.712		
		0.2278	20.50	110.0	1.042	12.737	0.670	8.533		
		0.2600	22.49	110.0	1.042	13.251	0.677	8.968		
		0.2397	21.55	110.0	1.042	12.749	0.670	8.543		
		0.2471	21.58	110.0	1.042	13.124	0.675	8.859		
		0.2381	20.96	110.0	1.042	13.021	0.674	8.770		
87	34.90	0.1786	22.11	110.0	1.042	9.259	0.622	5.758	5.743	2.53
		0.1783	21.49	110.0	1.042	9.510	0.627	5.966		
		0.1776	22.14	110.0	1.042	9.194	0.620	5.704		
		0.1784	21.35	110.0	1.042	9.578	0.629	6.021		
		0.1773	22.20	110.0	1.042	9.154	0.619	5.671		
		0.1746	21.81	110.0	1.042	9.176	0.620	5.689		
		0.1698	21.72	110.0	1.042	8.691	0.615	5.508		
		0.1688	21.05	110.0	1.042	9.191	0.620	5.702		
		0.1778	21.71	110.0	1.042	9.387	0.625	5.864		
		0.1770	22.08	110.0	1.042	9.188	0.620	5.699		
		0.1760	21.83	110.0	1.042	9.241	0.621	5.743		
		0.1695	21.44	110.0	1.042	9.062	0.617	5.593		
99	43.75	0.1269	22.16	110.0	1.042	6.564	0.515	3.383	3.475	4.33
		0.1278	21.43	110.0	1.042	6.835	0.531	3.631		
		0.1288	22.10	110.0	1.042	6.680	0.522	3.489		
		0.1329	21.99	110.0	1.042	6.927	0.536	3.714		
		0.1258	21.67	110.0	1.042	6.654	0.521	3.465		
		0.1288	21.62	110.0	1.042	6.828	0.531	3.624		

		0.1260	22.00	110.0	1.042	6.565	0.515	3.383		
		0.1247	21.70	110.0	1.042	6.587	0.517	3.404		
		0.1206	21.91	110.0	1.042	6.309	0.499	3.150		
		0.1248	21.47	110.0	1.042	6.663	0.521	3.473		
		0.1275	22.20	110.0	1.042	6.583	0.517	3.400		
		0.1301	21.99	110.0	1.042	6.781	0.528	3.581		

In order to use the phantom to represent sub-populations of patients of larger habitus than the 15th percentile of US adults aged 18-64, bags of simulated phantom adipose material were placed around the phantom pelvis and bags of pig adipose material (lard) were placed around the thorax, abdomen and legs to represent patients of the 87th and 99th percentile of US adults aged 18-64. The results of the TLD rectal dose measurements for each phantom configuration are provided in Table 4-6. The percent coefficients of variation (%CoV) of the 12 measurements obtained at each habitus demonstrate good precision (i.e. less than 5%) in the TLD measurements, and demonstrate the same trend observed in Specific Aim 1 that lower doses yield higher %CoV values.

Figure 4-4 plots the mean TLD organ dose, Farmer ionization chamber, SSDE, $CTDI_{vol}$, and $CTDI_{vol,center}$ measurements against patient size measurements (effective diameter). An exponential regression curve for the TLD measurements is also provided along with 95% confidence intervals of the regression and of the mean TLD measurements at each phantom habitus. The R^2 value of 0.993 demonstrates a very strong goodness of fit of the regression equation to the data. This regression additionally demonstrates the exponential relationship between dose and patient size predicted in other studies (101, 102).

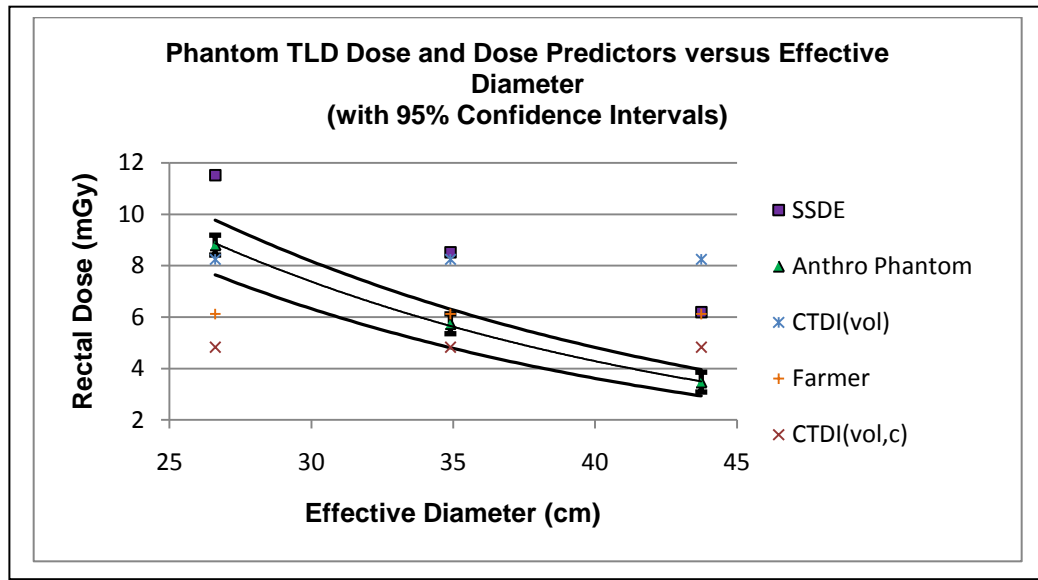


Figure 4-4. Anthropomorphic phantom mean TLD rectal dose measurements as a function of phantom effective diameter with an exponential regression curve (including 95% confidence intervals of both entities), as well as rectal dose estimates obtained from a uniform CTDI body phantom (all in mGy). CTDI_{vol} is the measured volume CTDI dose estimate, CTDI_{vol,center} is the CTDI₁₀₀ measurement acquired at the center of the CTDI body phantom and corrected for pitch, and SSDE is the size specific dose estimate.

4.3.2 In-Vivo Rectal Dose Measurements during Virtual Colonoscopy

Once MD Anderson Cancer Center Institutional Review Board (IRB) approval was granted for in-vivo rectal radiation absorbed dose measurements during VC, 6 patients previously approved by their respective insurances to receive the procedure that met all of the criteria outlined in Chapter 1.1.1 were approached for enrollment in the study. Patient rectal dose measurements were obtained from May – June 2011 at MD Anderson Cancer Center. Based on retrospective measurements from patient CT images, the average distance from the TLDs (within the rectum) to the table was calculated to be 10.5 cm for supine scans and 14.6 cm for prone scans. These distances were used to estimate the

rectal dose administered to each patient from the scout scans as described in Chapter 3.3.2.7. The results of these scout rectal dose estimates are provided in Table 4-7, with the scout scans accounting for 1.4%-2.2% of the total VC rectal doses measured in each patient.

Table 4-7. Results of dose estimates received from scout images during VC within 6 patients; where Pt # represents the study specific patient identification number, Supine mA is the tube current technique utilized to acquire the PA and lateral scout scans with the patient positioned in the supine position, Supine PA Dist is the distance from the TLDs to the patient's surface in the PA direction, Supine PA Dose is the estimated dose administered to the TLDs within the rectum from the supine PA scout, Supine Lat Dist is the distance from the TLDs to the patient's surface in the lateral direction, Supine Lat Dose is the estimated dose administered to the TLDs within the rectum from the supine lateral scout, Prone mA is the tube current technique utilized to acquire the AP and lateral scans with the patient positioned in the prone position, Prone AP Dist is the distance from the TLDs to the patient's surface in the AP direction, Prone AP Dose is the estimated dose administered to the TLDs within the rectum from the prone AP scout, Prone Lat Dist is the distance from the TLDs to the patient's surface in the lateral direction, Prone Lat Dose is the estimated dose administered to the TLDs within the rectum from the prone lateral scout.

Pt #	Supine mA	Supine PA Dist (cm)	Supine PA Dose (mGy)	Supine Lat Dist (cm)	Supine Lat Dose (mGy)	Prone mA	Prone AP Dist (cm)	Prone AP Dose (mGy)	Prone Lat Dist (cm)	Prone Lat Dose (mGy)	Total Scout Dose (mGy)
1	10	10.8	0.016	19.5	0.003	80	11.0	0.130	17.8	0.041	0.190
2	10	7.4	0.032	18.3	0.005	80	10.0	0.162	14.7	0.078	0.277
3	10	9.8	0.020	19.0	0.004	80	13.6	0.077	18.0	0.039	0.140
4	10	9.2	0.022	17.2	0.006	80	11.5	0.117	17.5	0.043	0.189
5	10	7.7	0.030*	19.0	0.004	80	13.0	0.086	17.6	0.043	0.193
6	10	8.6	0.025	19.3	0.004	80	11.2	0.124	20.2	0.025	0.178

*Patient received two supine AP scans

The results of the TLD rectal dose measurements for each patient are provided in Table 4-8. The percent coefficients of variation (%CoV) of the 4 TLD measurements

obtained within each patient demonstrate reasonable precision in the TLD measurements, but do not necessarily demonstrate the same trend observed in Specific Aim 1 that lower doses yield higher %CoV values. Figure 4-5 plots the in-vivo TLD rectal dose measurements as well as the anthropomorphic phantom measurements, SSDE dose estimates, and CTDI phantom based dose estimates against patient size measurements (effective diameter). A regression curve is provided for the anthropomorphic phantom measurements (as a faint, dotted line), which is the same regression curve provided in Figure 4-4. The in-vivo measurements appeared to include two outlier measurement points (Patients 4 and 5) that were not believed to represent standard VC conditions in Specific Aim 3, which will be explained in more detail below. Also provided in Figure 4-5 are the 95% confidence intervals of the in-vivo rectal dose measurements (which assumed a t-distribution of the TLD measurements at a patient habitus).

Table 4-8. Results of in-vivo TLD rectal dose measurements during VC within 6 patients;
where # represents the study specific patient identification number, Dim is the effective
diameter of the patient at the location of the TLDs, %ile is the percentile of US Adults
represented by the patient circumference at the location of the TLDs, Charge represents the
measured reading, Mass is the mass of TLD aliquot read, K_s is the sensitivity correction
factor, K_F is the fading correction factor, Uncorr Dose represents the dose predicted by the
TLD before corrections for dose linearity and energy were applied, $K_{L,120}$ represents the TLD
dose linearity correction factor at 120 kVp, TLD Dose represents the dose predicted by the
TLD after corrections for dose linearity and energy were applied, Scout Dose is the estimate
of patient rectal dose received, Avg Dose is the average of the CT dose measurements for a
patient (not including the scout scans), and %CoV is the percent coefficient of variation of the
TLD dose measurements.

#	Dim (cm)	%ile (%)	Charge (μ C)	Mass (mg)	K_s (cGy/ μ C/mg)	K_F	Uncorr Dose (mGy)	$K_{L,120}$	Scout Dose (mGy)	TLD Dose (mGy)	Avg TLD Dose (mGy)	%CoV TLD Dose (%)
1	30.3	27	0.2763	21.95	108.5	1.052	14.37	0.674	0.190	9.497	10.13	10.0
			0.2659	21.80	108.5	1.052	13.92	0.668		9.113		
			0.2963	21.67	108.5	1.052	15.61	0.689		10.57		
			0.2968	20.54	108.5	1.052	16.49	0.699		11.33		
2	26.2	7	0.3570	21.52	108.5	1.052	18.94	0.720	0.277	13.36	12.53	5.0
			0.3302	21.05	108.5	1.052	17.90	0.712		12.47		
			0.3475	22.16	108.5	1.052	17.90	0.712		12.46		
			0.3091	20.56	108.5	1.052	17.16	0.705		11.82		
3	30.5	31	0.2760	21.47	108.5	1.050	14.65	0.678	0.140	9.788	9.78	1.8
			0.2543	20.19	108.5	1.050	14.35	0.674		9.532		
			0.2833	21.85	108.5	1.050	14.77	0.679		9.896		
			0.2611	20.10	108.5	1.050	14.80	0.680		9.920		
4	26.9	11	0.2685	21.92	108.5	1.049	13.94	0.668	0.189	9.131	8.96	5.6
			0.2481	21.89	108.5	1.049	12.90	0.653		8.231		
			0.2587	21.23	108.5	1.049	13.87	0.667		9.068		
			0.2709	21.63	108.5	1.049	14.25	0.673		9.401		
5	28.4	31	0.3644	22.08	108.5	1.049	18.78	0.719	0.193	13.31	13.05	5.6
			0.3164	20.63	108.5	1.049	17.46	0.708		12.16		
			0.3716	21.73	108.5	1.049	19.46	0.724		13.90		
			0.3250	20.26	108.5	1.049	18.26	0.715		12.85		
6	28.0	35	0.3362	21.96	108.5	1.039	17.26	0.706	0.178	12.01	11.37	4.7
			0.3138	21.05	108.5	1.039	16.81	0.702		11.62		
			0.3046	21.53	108.5	1.039	15.95	0.693		10.88		
			0.3156	22.11	108.5	1.039	16.09	0.695		11.00		

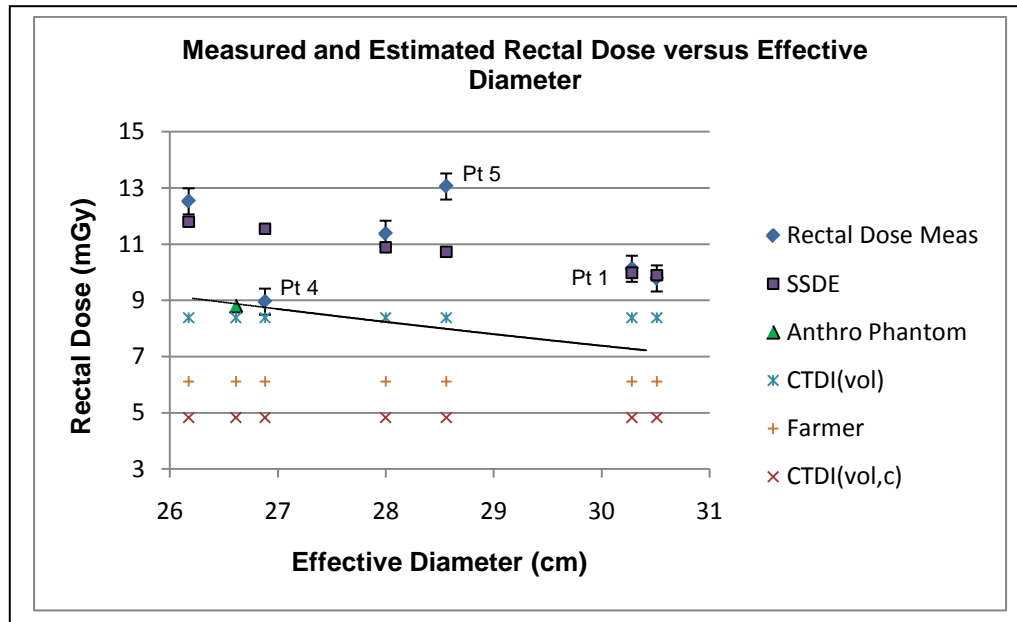


Figure 4-5. In-vivo mean TLD rectal dose measurements (with the 95% confidence intervals) as a function of patient effective diameter, as well as rectal dose estimates obtained from an anthropomorphic phantom and a uniform CTDI body phantom (all doses are provided in mGy). SSDE is the size specific dose estimate, Anthro Phantom is the anthropomorphic phantom TLD rectal dose measurement, $CTDI_{vol}$ is the measured volume CTDI dose estimate based on the x-ray tube output in VC, Farmer is the Farmer chamber measurements within the center bore of the uniform CTDI body phantom, $CTDI_{vol,c}$ is the $CTDI_{100}$ measurement acquired at the center of the CTDI body phantom and corrected for pitch. The data for Patients 1, 4, and 5 are specified for outlier analysis purposes as they represent those data measurements that were close to, below, and above, respectively, those dose prediction made by the SSDE technique. The faint dotted line is the regression of the anthropomorphic phantom dose measurements (also provided in Figure 4-4).

4.4 Specific Aim 3: Compare In-Vivo Rectal Dose Measurements to Anthropomorphic Phantom Measurements, CTDI-Based Dose Estimates and Point Dose Measurements from a Uniform Phantom

4.4.1 Introduction

Once all TLD measurement results were received from the RPC and absorbed dose measurements were calculated for every phantom configuration and patient (along with the average rectal dose for each phantom configuration and patient) in Specific Aim 2, the average in-vivo rectal dose measurements were compared to anthropomorphic phantom measurements, $CTDI_{vol}$ -based dose estimates (including the size specific dose estimates (SSDE)) and Farmer ionization chamber dose measurements obtained in a uniform CTDI body phantom. Figures 4-4 and 4-5 display the measurements within the anthropomorphic phantom at each phantom configuration and within each patient and compare these measurements with the CTDI-based and Farmer chamber measurements. Each of these values are additionally tabulated in Table 4-9 by phantom configuration and patient: phantom configuration percentile (a number P0, P1, P2) or patient identifier (a number 1-6), phantom or patient effective diameter measurements from a CT image that contained both TLDs, the percentile of US adults aged 18-64 represented by each phantom or patient circumference, the average phantom or patient TLD rectal dose measurements, the upper and lower 95% confidence intervals of the average measurements (based on a t-distribution assumption), Farmer chamber measurements in a CTDI body phantom, $CTDI_{vol,center}$ dose estimates, $CTDI_{vol}$ dose estimates, SSDE dose estimates, and the percent differences of each of these dose estimates from the confidence interval of the measured rectal dose estimates. As can be seen in Figures 4-4 and 4-5 and Table 4-9, SSDE is the only homogeneous phantom-based predictive model that varies with patient size; with the SSDE predictions appearing to run approximately parallel with the exponential regression line for the anthropomorphic phantom and concurrently with most of the in-vivo VC rectal dose measurements.

Table 4-9. Results of anthropomorphic phantom and in-vivo TLD dose measurements during VC within 3 phantom sizes and 6 patients; where # represents the study specific phantom or patient identification number, %ile represents the percentage of US adults aged 18-64 represented by the circumference of a specific phantom or patient, Dim is the effective diameter of the patient at the location of the TLDs, TLD Dose is the average of the dose measurements for a phantom configuration or patient, Low 95% CI is the lower 95% confidence interval of the mean dose measurement, Up 95% CI is the upper 95% confidence interval of the mean dose measurement, Farmer is the dose estimate obtained by Farmer chamber measurement in a CTDI body phantom, Farmer % Diff is the percent difference of the Farmer chamber measurement from the confidence interval of the mean TLD dose value, $CTDI_{vol,c}$ is the $(CTDI_{100})_{center}$ measurement corrected for pitch, $CTDI_{vol,c}$ % Diff is the percent difference of the $CTDI_{vol,center}$ measurement from the confidence interval of the mean TLD dose value, $CTDI_{vol}$ is the volume CTDI measurement (accounting for the tube output experienced by a patient in both the supine and prone scans), $CTDI_{vol}$ % Diff is the percent difference of the $CTDI_{vol}$ measurement from the confidence interval of the mean TLD dose value, SSDE is the size specific dose estimate, and SSDE % Diff is the percent difference of the SSDE estimate from the confidence interval of the mean TLD dose value. If a % Diff value is not provided (-), that value indicates that the dose estimate is within the 95% CI for the average TLD measurement.

#	%ile	Dim (cm)	Low 95% CI (mGy)	TLD Dose (mGy)	Up 95% CI (mGy)	Farmer (mGy)	$CTDI_{vol,c}$ (mGy)	$CTDI_{vol}$ (mGy)	SSDE (mGy)	Farmer % Diff (%)	$CTDI_{vol,c}$ % Diff (%)	$CTDI_{vol}$ % Diff (%)	SSDE % Diff (%)
P0	15	26.6	8.418	8.804	9.189	6.12	4.83	8.25	12	-27.3	-42.6	-2.0	25.4
P1	87	34.9	5.358	5.743	6.129	6.12	4.83	8.25	9	-	-9.8	34.6	39.1
P2	99	43.8	3.089	3.475	3.860	6.12	4.83	8.25	6	58.5	25.1	113.7	60.4
1	27	30.3	9.699	10.13	10.56	6.12	4.83	8.25	10	-35.2	-48.9	-12.7	-
2	7	26.2	12.10	12.53	12.96	6.12	4.83	8.25	12	-48.3	-59.2	-30.3	-0.4
3	31	30.5	9.355	9.784	10.21	6.12	4.83	8.25	10	-32.8	-46.9	-9.4	-
4	11	26.9	8.529	8.958	9.387	6.12	4.83	8.25	12	-26.1	-41.6	-0.3	19.8
5	31	28.4	12.63	13.05	13.48	6.12	4.83	8.25	11	-50.5	-61.0	-33.3	-13.3
6	35	28.0	10.94	11.37	11.80	6.12	4.83	8.25	11	-42.8	-54.8	-22.8	-

4.4.2 Percent Coefficient of Variation (%CoV)

The percent coefficient of variation (%CoV) was calculated to be 14.2% for the in-vivo TLD rectal dose measurements. This between-patient %CoV value was based on the mean TLD dose measurements of the six in-vivo patients, and was calculated to assess whether the between-patient rectal dose %CoV was greater than 50% (as stated in the hypothesis). The calculated %CoV value was much lower than expected, which is a reflection of the distribution of the sizes of patients that participated in this study. As can be seen in Figure 4-6, the distribution of patients that participated in this study was skewed toward the smaller percentiles of US adults aged 18-64; and more Gaussian distribution of patient sizes would likely have increased the between-patient %CoV. Therefore, the between-patient %CoV value of rectal dose measurements would likely increase with a larger sample population that would include patients of a larger habitus.

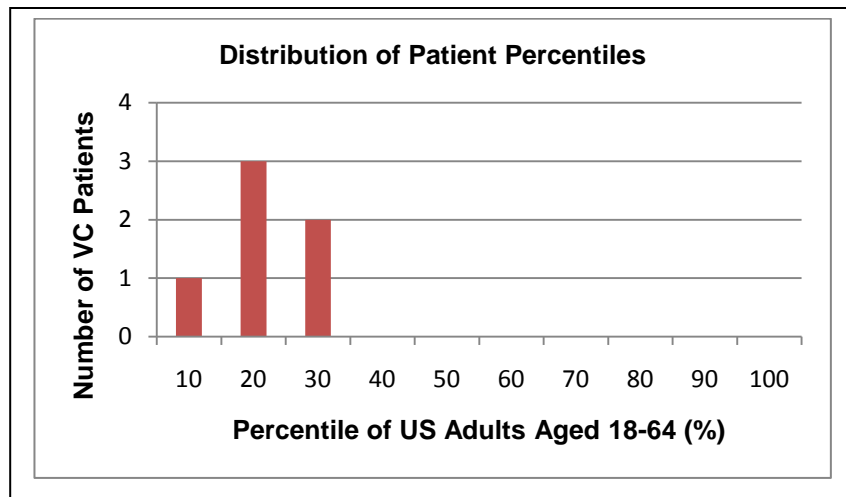


Figure 4-6. Distribution of VC patient percentiles participating in this study.

4.4.3 Outlier Analysis

The results of the relative bone density quantification via Hounsfield Unit (HU) numbers is provided in Figure 4-7. As can be seen from this figure, the anthropomorphic phantom demonstrates considerably higher bone density than any of the patients, with

Patients 4 and 5 demonstrating the highest relative bone density of the in-vivo measurement patients. This was not surprising considering the age and gender of Patient 4 (23 year old male), compared to that of the other patients who underwent VC in this study (ages ranging from 61 years to 78 years with an average age of 71.4 years among the four females and one male remaining); but was somewhat surprising for Patient 5 (78 year old female). It is likely that these differences in bone density impacted the in-vivo dose measurements provided in Figure 4-5, and Figure 4-7 perhaps only partially explains the outlier measurement point that appeared considerably lower than the rest of the in-vivo dose measurements (Patient 4). Further explanation regarding this outlier point is provided in Chapter 5.

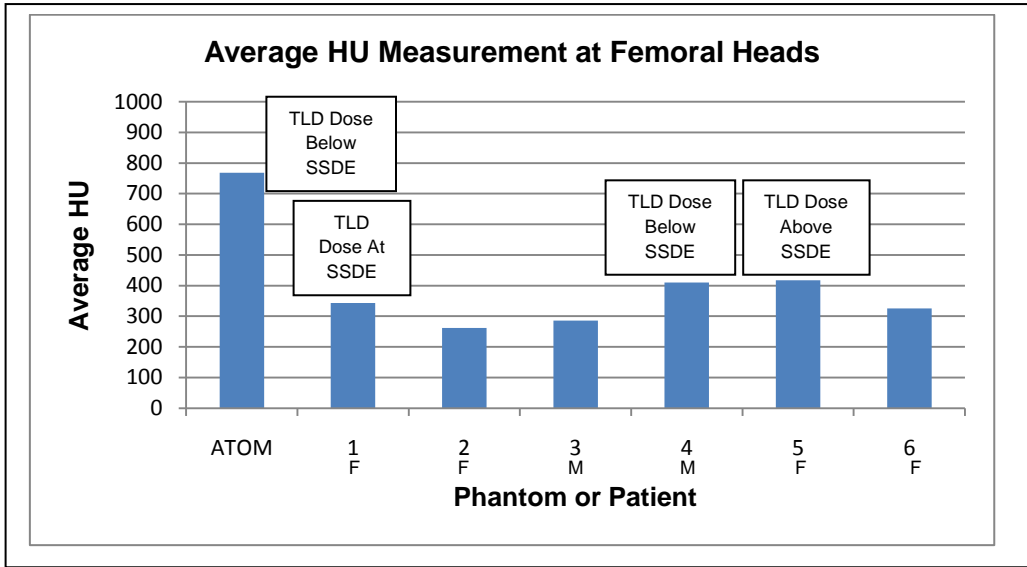


Figure 4-7. Patient and anthropomorphic phantom relative bone density quantified as the average HU values of six femoral head region of interest HU measurements within supine VC images. The gender of each patient is also provided.

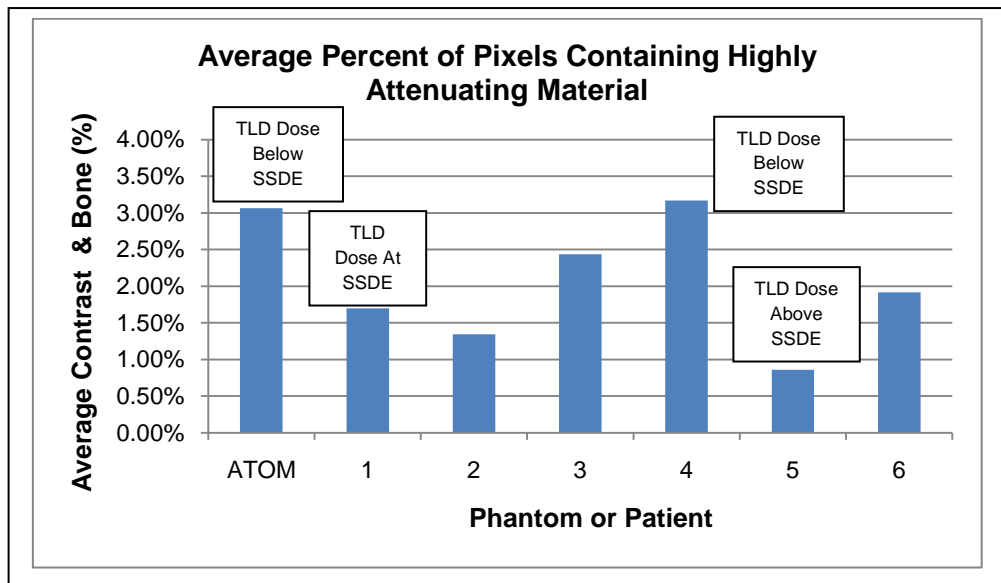


Figure 4-8. Average percent of pixels containing highly attenuating material as determined from histograms of the median location of the TLDs within the rectum in supine and prone VC scans. These measurements provided understanding regarding the effects of factors such as amount of iodine contrast agent present, bone density, and placement of TLDs with respect to surrounding anatomy have on in-vivo dose measurements.

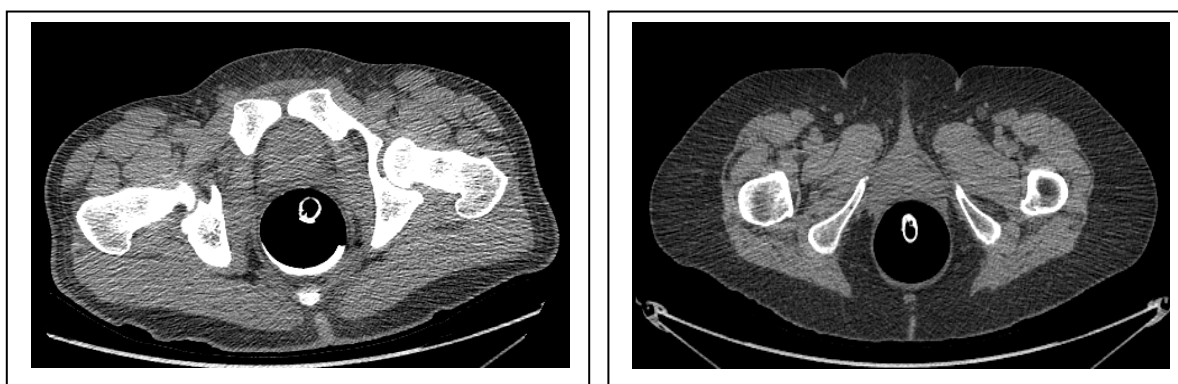


Figure 4-9. Visual comparison of CT images of Patients 4 and 5 at the mean TLD location; which represent the high and low extremes, respectively, of the amount of highly attenuating material at the mean TLD location present among the patients enrolled in this study.

The results of the determination of the percentage of highly attenuating material via histogram of supine and prone images containing the median TLD placement within the anthropomorphic phantom and each patient are provided in Figure 4-8. As can be seen from this figure, the anthropomorphic phantom and Patient 4 demonstrate considerably higher percentages of highly attenuating material than the rest of the patients. It can also be observed from this figure that Patient 5 (represented by the data point that considerably exceeded the rest of the in-vivo patient measurements) provided the lowest percentage of highly attenuating material of any of the patients at the level of the TLDs (somewhat inferior relative to the other patients). A visual comparison of the CT images at the average TLD location for Patients 4 and 5, which represent the high and low extremes of amount of highly attenuating material at the mean location of the TLDs, is provided in Figure 4-9. Although it is observed in Figure 4-7 that this Patient 5 did not have the lowest relative bone density, analysis of the VC scan images revealed that the TLDs were placed inferior within the rectum compared to the other patients such that the x-rays within the primary beam were only attenuated by the femurs and ischia (where the other patients' TLDs received more attenuation by the pelvis, as suggested by the higher percentages of highly attenuating material displayed in Figures 4-8 and 4-9). It additionally appears in Figure 4-9 that the ratio of soft tissue to fat within Patient 4 was greater at the TLD level than within Patient 5 (with soft tissue providing more beam attenuation than fat). As the anthropomorphic phantom and Patient 4 were of similar size (26.6 cm and 26.9 cm effective diameter, respectively) and percentage of highly attenuating material (3.06% and 3.17%, respectively), it was not surprising that the TLD dose measurements for the anthropomorphic phantom and Patient 4 were similar; and lower rectal doses were measured within these two entities than in the rest of the VC patients. Further, as the x-rays incident on the TLDs within Patient 5 underwent less attenuation from such highly attenuating materials as iodine contrast and pelvic bone, higher doses were measured in

this patient than in the rest of the VC patients. Further explanation regarding these outlier points is provided in Chapter 5.

4.4.4 Statistical Analysis

Mean Square Error (MSE) analysis was conducted to assess the quality of the rectal dose estimates provided by anthropomorphic phantom measurements, SSDE dose estimates, and uniform CTDI phantom based dose estimates (including Farmer chamber dose measurements, $CTDI_{vol}$, and $CTDI_{vol,center}$) to the in-vivo rectal dose measurements. The results of this analysis are provided in Table 4-10, with the best prediction model for each patient being highlighted. It can be seen from this table that the SSDE provided the best fit to the in-vivo dose measurements for all patients except one (the patient that was considerably younger than the rest of the population), where the anthropomorphic phantom regression provided the best dose estimate for that patient. As the Farmer chamber estimate, the $CTDI_{vol}$, and the $CTDI_{vol,center}$ dose estimates provided models that did not change with changing patient size, these models do not provide an adequate fit to rectal dose data for an entire population.

Calculations were also performed to determine whether the differences between the anthropomorphic phantom rectal dose measurements, the SSDE dose estimates, the $CTDI_{vol}$ -based estimates, and the Farmer chamber measurements in a CTDI body phantom was outside the 95% confidence interval of the in-vivo rectal dose measurements during VC (as stated in the hypothesis). This analysis (summarized in Table 4-9) determined that the rectal dose delivered to Patients 1, 3, and 6 during VC was predicted within the 95% CI by the SSDE model (with a 1.4%, 1.2%, and -4.3% difference from the mean TLD dose measurements, respectively) and not within the 95% confidence interval by any other method. Patient 2 exceeded the 95% CI by -0.4%. The rectal dose delivered to Patient 4 during VC was predicted within the 95% CI by the anthropomorphic phantom regression

model (2.0% from the mean TLD dose measurement), and the measured $CTDI_{vol}$ dose estimate at the VC beam output was -0.3% outside the 95%CI. The rectal dose delivered to Patient 5 was not predicted within the 95% CI by any dose estimation model, but was most closely estimated by the SSDE model (15.1% from the CI). Discussions regarding these results are provided in Chapter 5.

Table 4-10. Results of the mean square error (MSE) assessment of the quality of the predictions of patient rectal dose during VC provided by the anthropomorphic phantom measurement regression, the SSDE, and the uniform CTDI phantom-based dose estimate models compared with the in-vivo TLD dose measurements; where SSDE is the MSE of the size specific dose estimate model to the in-vivo dose measurements, Anth is the MSE of the anthropomorphic phantom measurement regression to the in-vivo dose measurements, Farmer is the MSE of the Farmer chamber measurement model to the in-vivo dose measurements, $CTDI_{vol,c}$ is the MSE of the $(CTDI_{100})_{center}$ measurement model (corrected for pitch) to the in-vivo dose measurements, $CTDI_{vol}$ is the MSE of the measured volume CTDI (based on beam output during VC) dose estimate model to the in-vivo dose measurements. The highlighted fields indicate the superior patient rectal dose prediction technique.

Patient	Mean Square Error (MSE) (in mGy)				
	Farmer	$CTDI_{vol,c}$	$CTDI_{vol}$	SSDE	Anth
1	2.00	2.65	0.94	0.07	1.41
2	3.20	3.85	2.14	0.36	1.73
3	1.83	2.48	0.77	0.06	1.30
4	1.42	2.06	0.35	1.30	0.09
5	3.47	4.11	2.40	1.16	2.52
6	2.63	3.27	1.56	0.24	1.57

CHAPTER 5.0: DISCUSSION

5.1 Introduction

Discussion of the results from the phantom and patient virtual colonoscopy (VC) rectal dose estimates, and the steps that led to the accomplishment of these measurements, are within this chapter and are reported in the order presented in Chapters 3 and 4. First, in accordance with Specific Aim 1, thermoluminescent dosimeter (TLD) linearity correction factors were established for a range of doses at 120 kVp for a multi-detector computed tomography (MDCT) scanner using VC scan parameters in a 32 cm CT dose index (CTDI) body phantom. Next, in accordance with Specific Aim 2, in-vivo rectal dose measurements using TLDs were obtained in VC simulations within an anthropomorphic phantom and in patients undergoing VC. Finally, in accordance with Specific Aim 3, rectal dose measurements were compared to $CTDI_{vol}$ -based dose estimates and point dose measurements obtained in a CTDI body phantom. This specific aim was accomplished in order to test our hypotheses: in-vivo rectal dose measurements obtained during virtual colonoscopy will have a rectal dose coefficient of variation that will be greater than 50%; and the differences between the anthropomorphic phantom measurements, the $CTDI_{vol}$ -based dose estimates, and Farmer chamber measurements in a CTDI body phantom will be outside the 95% confidence interval of in-vivo rectal dose measurements during VC.

5.2 Specific Aim 1: Establish TLD Linearity Correction Factors for VC Scan

Parameters on a MDCT

Specific Aim 1 was accomplished in two phases: CT beam characterization and TLD dose correction factor determination at 120 kVp ($K_{L,120}$) for the photon spectrum produced by GE LightSpeed VCT scanners at MD Anderson Cancer Center. The beam

characterization phase was accomplished in order to assess the reproducibility of this technique of determining the TLD $K_{L,120}$ values as time progressed (i.e. as the performance of the x-ray tube changed with time), to assess consistency of beam output on several MDCT scanners that may be used for VC, to help explain potential variations in TLD response, to assess potential effects of $K_{L,120}$ values in the event of a change in the x-ray tube as a part of scanner maintenance, and to better characterize the equivalent source model output for future Monte Carlo rectal dose calculations (60). The $K_{L,120}$ value determination phase was necessary because neither the dose linearity correction factor nor the energy correction factor were established by the Radiologic Physics Center (RPC) (Houston, TX) for the dose and energy ranges encountered during VC; and these data values could not reasonably be extrapolated from the correction factors established by the RPC due to the well-documented potential for non-linear response of TLD-100 material in this dose and energy range (25, 26, 28, 31).

5.2.1 MDCT Beam Characterization

As stated in Chapters 3 and 4, the beam quality measurements obtained within the first phase of Specific Aim 1 included: the half-value layer (HVL), quarter-value layer (QVL), CTDI in-air measured with a 100 mm pencil chamber ($(CTDI_{100})_{air}$), weighted CTDI ($CTDI_w$), and volume CTDI ($CTDI_{vol}$) for the MD Anderson Cancer Center VC technique on the institution's "CT9" GE LightSpeed VCT scanner. HVL and QVL measurements were also obtained upon the completion of the in-vivo measurements on "CT5", "CT9", and "CT12" scanners. As the x-ray tube was not replaced on any of the scanners until the completion of all in-vivo dose measurements, the value of these beam quality measurements were perhaps somewhat reduced. Reevaluation of HVL and QVL values with the replaced x-ray tube was conducted to investigate the differences between the hardness produced by a new x-ray tube and one at the end of its lifespan. The value of the beam output

measurements was increased in this study in the fact that the variability observed in the TLD measurements (and accordingly the $K_{L,120}$ values) was correctly assigned to the TLD process and not to the MDCT scanner output as the MDCT precision was characterized with these beam quality measurements. Additional value will result from these measurements if they are applied to the characterization of an equivalent source model in future Monte Carlo simulation. Ultimately, it was better to have an abundance of measurements that were not used than to desire such measurements retrospectively.

5.2.1.1 HVL and QVL Measurement

As mentioned in Chapter 4, the HVL and QVL measurements demonstrated good precision with all exposure measurements at a specific filtration on a specific day, with a percent coefficient of variation (%CoV) less than 0.1% being achieved. The HVL measurements between the three dates (approximately five months apart) and in the three MDCT scanners (with a total of four x-ray tubes) demonstrated a %CoV of 0.73% from one another, which was within the range of HVL measurement precision values for GE VCT scanners published by Mathieu et al (103) (0.20%-2.19% %CoV, with a mean of 0.42% for quarterly between-run precision measurements). Further, the QVL measurements between the two dates demonstrated a %CoV of 0.62% from one another, which was slightly greater than the range of QVL measurement precision values for GE VCT scanners published by Mathieu (103) (0.11%-0.50% %CoV, with a mean of 0.43% for quarterly between-run precision measurements).

During acceptance testing of the “CT9” MDCT scanner at MD Anderson Cancer Center in August 2008, the measured HVL with the large body bow-tie filter was 7.96 mm Al. The 2% difference observed between our HVL measurements and this measurement may be the result of differences in the methods used to obtain the HVL measurements, may be caused by inherent uncertainties in the measurement of the filtration thickness (using

several measurements with electronic calipers compared to the nominal thickness), or even of the ionization chamber measurements themselves (with a published uncertainty of $\pm 4\%$ after temperature and pressure condition corrections have been applied when using Co-60 as the calibration source). No standards currently exist stating an amount of allowable change in HVL measurements a tube may experience before requiring replacement. These results suggest that the effect of these observed differences in x-ray tube output between the respective dates and MDCT scanners likely had a minimal impact on the calculated TLD $K_{L,120}$ values or on the rectal dose measurements acquired during VC; and any variation observed in measured TLD dose between the MDCT scanner utilized in the VC scan, or between the phantom configuration and patients of equivalent size, are likely the result of uncertainties inherent within the TLDs' ability to measure dose at diagnostic-level doses and energies.

5.2.1.2 $(CTDI_{100})_{air}$, $CTDI_w$, and $CTDI_{vol}$ Determination

The exposure measurements used to calculate respective $(CTDI_{100})_{air}$ values on the two dates the $K_{L,120}$ values were determined (approximately 3 months apart) demonstrated a %CoV ranging from 0.00-0.20% from one another with a mean %CoV of 0.06%. This range of precision values for GE VCT scanners was slightly greater than that published by Mathieu et al (103) (0.04%-0.11% %CoV, with a mean of 0.05% for within-run precision measurements obtained within seconds of one another). As stated in Chapter 4, the results of the $(CTDI_{100})_{air}$ measurements also demonstrated very good agreement between respective $(CTDI_{100})_{air}$ measurements, with a %CoV of 0.08% between the $(CTDI_{100})_{air}$ measurements taken approximately 3 months apart. This precision was less than the quarterly between-run range of precision values for GE VCT scanners published by Mathieu (103) (a range of 0.47%-1.04% %CoV, with a mean of 0.58%).

The need to acquire $(CTDI_{100})_{air}$ measurements in order to verify the linearity of the MDCT scanner dose output with mAs became obvious retrospectively after the first scanning session designed to establish $K_{L,120}$ values. Ideally, this linearity would have been established during both irradiation sessions for the entire dose range in which the $K_{L,120}$ values were determined, but this was not accomplished. We are confident, however, that the x-ray tube output was linear during both irradiation sessions because of the well-documented linear relationship between dose and mAs (37) and the good precision between the irradiation sessions. Although these $(CTDI_{100})_{air}$ measurements established that the beam dose output was linear with mAs, the regression equation correlating the two entities for $(CTDI_{100})_{air}$ was not used to extrapolate the doses used to determine the $K_{L,120}$ values at 20 and 30 mAs. Rather, the linearity of the Farmer chamber measurements in the CTDI body phantom with mAs were used to extrapolate these lowest doses using the linear regression shown in Equation 5-1; where *FarmerDose* is the extrapolated point dose estimated in the center of the CTDI body phantom (in mGy), and mAs is the scan technique used.

$$FarmerDose = 0.0578 \cdot mAs - 0.5912 \quad (5-1)$$

As stated in Chapter 4, the results of the $CTDI_{100}$ measurements within the CTDI body phantom also demonstrated good precision, with the %CoV ranging from 0.04-1.96%. Further, the %CoV of the $CTDI_w$ values measured approximately three months from one another was 1.31%, which was within the range published by Mathieu (103) (a range of 0.61%-1.84% %CoV, with a mean of 0.84%). Good agreement was also observed between the respective $CTDI_w$ and $CTDI_{vol}$ measurements. The measured $CTDI_{vol}$ values corresponded well with the $CTDI_{vol}$ value provided by the MDCT scanner console for this scan technique ($CTDI_{vol}=8.26$ mGy), with a total %CoV of 1.03%.

The observed 0.5% difference between the respective $(CTDI_{100})_{air}$ measurements and the 2% difference between the respective $(CTDI_{100})_w$ and $(CTDI_{100})_{vol}$ measurements may have been the result of inherent uncertainties in the measurement device (with a published uncertainty of $\pm 4\%$ after temperature and pressure condition corrections have been applied when using Co-60 as the calibration source). These results further reinforce the belief that the effect of these observed differences in x-ray tube output between the respective dates likely had a minimal impact on the uncertainties observed in the calculated TLD $K_{L,120}$ values or on the TLD-measured rectal doses administered during VC, and any such uncertainties observed in the measured TLD doses obtained within a single phantom configuration or within patients are likely the result of uncertainties inherent within the use of TLD-100 powder as a measurement technique at diagnostic doses and energies.

5.2.2 Determination of TLD Dose Linearity Correction Coefficients for Virtual Colonoscopy

The results of the characterization of the RPC's B09 TLD-100 batch to diagnostic doses at the 120 kVp spectrum administered by MD Anderson Cancer Center's "CT9" scanner are provided in Figure 4-2 and Figure 4-3. With the determination of Figure 4-2, which directly converts the apparent TLD dose (uncorrected for energy or dose linearity) it was not technically necessary to determine the $K_{L,120}$ values for the dose range encountered in VC, since $K_{L,120}$ was calculated by dividing the Farmer chamber dose by the uncorrected TLD dose. However, in keeping with the traditional method of calculating TLD dose of multiplying the charge per mass reading by correction factors for sensitivity, fading, dose linearity and energy, $K_{L,120}$ values were determined for the dose range encountered in VC (shown in Figure 4-3).

It appears from the direct conversion of apparent (i.e. uncorrected) TLD dose to Farmer chamber dose displayed in Figure 4-2 that the TLD dose response at the 120 kVp spectrum is still within the linear region of the TLD-100 material's dose response for all

doses administered to the TLDs above background. In fact, if the background TLD measurements were to be omitted from the dataset, a linear regression equation is achieved that is characterized by a goodness of fit factor of $R^2=0.998$. This observed linearity is consistent with published lower dose limits of linearity for TLD-100 material, with the low-dose supralinearity region being published to approximately begin at doses less than or equal to 1 mGy (26).

The supralinearity observed in the regression line between the lowest dose measured by TLD and the background measurements necessitated that a non-linear regression line be created to completely characterize the relationship between the apparent TLD dose and the Farmer chamber measured dose. Therefore a fourth-order polynomial was used to characterize this relationship because it was found to be the minimally ordered regression that provided a goodness of fit factor ($R^2=0.999$) that was greater than that of the linear regression when the background apparent TLD doses were not considered. Without characterizing the background apparent TLD dose, a linear regression would certainly have been appropriate ($R^2=0.998$).

The observed linearity of the TLD dose response is not immediately apparent, however, by viewing the $K_{L,120}$ values provided in Figure 4-3. This figure demonstrates a third-order polynomial regression being necessary to describe the relationship between the apparent TLD dose and $K_{L,120}$ value that corrects the apparent TLD dose to the Farmer chamber dose (with a goodness of fit factor of $R^2=0.992$). This observed nonlinearity of the $K_{L,120}$ values is a mathematical consequence of the added complexity inherent within the $K_{L,120}$ value determination. $K_{L,120}$ is calculated by dividing the Farmer chamber dose measurement by the apparent TLD dose measurement. Establishing a regression equation where the dependent variable ($K_{L,120}$) is inherently a function of the independent variable (apparent TLD dose) is analogous to raising the order of the regression polynomial. In other words, if an embedded independent variable were to be removed from the dependent

variable of a linear regression by multiplication, the result would be a second-order polynomial regression. This mathematical reality was the reason the $K_{L,120}$ values did not display a linear trend with increasing apparent TLD dose.

Typically, under conditions where the RPC must determine the TLD dose linearity correction factor (K_L) for orthovoltage energies, they do so by first estimating the energy correction factor (K_E) based on data previously collected by the RPC that predicts appropriate K_E values based on photon beam hardness (half-value layer) and then by irradiating the TLDs to the dose range desired with Co-60 photons to determine K_L . This published data correlating orthovoltage K_E values to beam hardness describes the relationship as a non-linear function. Based on this data, an appropriate energy correction factor for the HVL measured in Specific Aim 1 would be approximately $K_E=0.7$. However, this estimate is not specific to the RPC's B09 batch of TLD-100 material and therefore subject to error. Since both the dose and energy dependence had not been previously characterized for the RPC's batch of B09 TLD-100 powder at the 120 kVp spectrum produced by MD Anderson Cancer Center's "CT9" scanner, it was impossible to separate the dose linearity correction from the energy correction to determine the proximity of the calculated energy correction to this predicted energy correction for this batch of TLD-100 powder.

Regarding the characterization of the TLD dose response at diagnostic-level energy doses, the goodness of fit factors of $R^2=0.992$ and 0.999 obtained for the $K_{L,120}$ correction factors and the direct conversion from apparent TLD dose to Farmer dose, respectively, provided confidence in the ability of the TLDs to determine the rectal doses delivered by VC. Additionally, although the TLDs perhaps introduced the primary source of error into our rectal dose measurements, the percent coefficient of variation values were determined to be 3.56% or less for all doses greater than background. This degree of precision provided additional confidence in the rectal dose measurements obtained in Specific Aim 2.

5.3 Specific Aim 2: Obtain Rectal Dose Measurements in an Anthropomorphic Phantom and In-Vivo in Patients Undergoing VC with TLDs

Specific Aim 2 was accomplished in two phases: measurement of rectal doses in an anthropomorphic phantom during simulated VC and in-vivo rectal dose measurements in patients undergoing actual VC procedures. The simulations within the anthropomorphic phantom were performed in order to provide dry runs for the in-vivo measurements (to ensure the process was well understood before any patients were subjected to the measurement process), to obtain additional rectal dose estimates, and to make preliminary determination regarding the legitimacy of using an anthropomorphic phantom to estimate patient organ dose (which is commonly done and is considered the benchmark for other indirect dose measurement techniques such as Monte Carlo simulation). Once doses had been measured within the anthropomorphic phantom during simulated VC and IRB approval had been obtained from MD Anderson Cancer Center, in-vivo rectal dose measurements were performed for 6 patients undergoing VC.

5.3.1 Rectal Dose Measurement Simulation in an Anthropomorphic Phantom

As mentioned in Chapter 1, anthropomorphic phantoms contain many inherent approximations; such as assuming all soft tissue organs interact with radiation in an equal manner, using “standardized” anatomical geometry that may or may not reflect a true patient’s anatomy, using proprietary materials that provide simulated bony tissue radiation interactions across a wide range of ages and for multiple types of bones, etc. Therefore the use of anthropomorphic phantoms to estimate patient doses is limited in many ways that are not yet fully understood. Therefore, in a similar manner in which Monte Carlo simulations are benchmarked against phantom measurements, one of the intents of this

study was to provide a first step toward benchmarking Monte Carlo estimates and phantom measurements against in-vivo measurements.

In order to accomplish this intent for phantoms within the parameters of this study where internal in-vivo measurements were to be acquired during VC, the anthropomorphic phantom had to be appropriately modified to represent patients undergoing VC. Since patients present in a variety of sizes, and because VC at MD Anderson Cancer Center is accomplished using a fixed technique, a patient's girth was assumed to be the primary determinate of the rectal dose received in VC. Therefore, efforts were made to utilize a single anthropomorphic phantom to simulate patients of several sizes. The rectal dose measurements obtained during the simulated VC were analyzed to ensure that the TLDs provided adequate precision for this study such that reliable rectal dose measurements during VC were accomplished, and a regression analysis was performed investigating the behavior of measured rectal doses with increasing patient habitus. This model, along with rectal dose predictions obtained from a uniform phantom, was compared to internal in-vivo measurements in an effort to assess the legitimacy of using a phantom to estimate true patient rectal dose during VC.

5.3.1.1 Modifications to the Anthropomorphic Phantom

The primary necessary modification to the anthropomorphic phantom was the creation of an insufflated rectum within the phantom. Many assumptions and approximations were requisite to determine an appropriately representative size, shape, and location of the insufflated rectum within the phantom. The fact that each of these approximations were based on generalizations regarding patient rectum size and shape after gas insufflation, the bony landmarks surrounding the location of the rectal catheter, and the focus on those patients whose size was approximately equal to that of the phantom introduced some of the same limitations that have always plagued the use of

anthropomorphic phantoms and therefore necessarily introduced potential rectal dose measurement differences from those obtained within actual patients.

Confidence is gained regarding the selected size and location of the insufflated rectum within the anthropomorphic phantom based on the population size and diverse techniques incorporated to determine these entities. The use of anatomical measurements from VC scans of 29 total patients when performing this analysis enabled anthropomorphic or positional irregularities observed in one or two patients to not greatly influence decision making (for example, a pelvis positioned in an asymmetric manner which would affect the determination of the location of the TLDs with respect to the body landmarks). Further, due to the fact that two separate methods were incorporated to determine the size and location of the insufflated rectum with respect to the surrounding bony landmarks, and that each of the two methods provided similar results, we are confident that the approximations made in creating the insufflated rectum within the phantom were appropriate for simulated VC at MD Anderson Cancer Center.

The decision to cut a 6.4 cm diameter bore into one section of this pricy phantom was not made lightly, and only done with the stipulation that efforts be made to salvage as much of the removed material as possible to plug the bore when not being used in simulated VC. The use of “solid water” plastic material to supplement the plastic plug where phantom material was unavoidably lost in the cutting process proved to be a good approximation to the proprietary soft-tissue equivalent material. CT scans of the phantom with the solid water/phantom plug in-place revealed that the solid water was sufficiently equivalent to the surrounding phantom material that no discernable difference in contrast was observed at any window width or level setting (see Figure 5-1). A comparison analysis of HU values between the solid water and the surrounding phantom material was not possible, however, because the thin size of the solid water material would not permit the creation of a sufficiently large ROI to attain stable consecutive HU measurements.

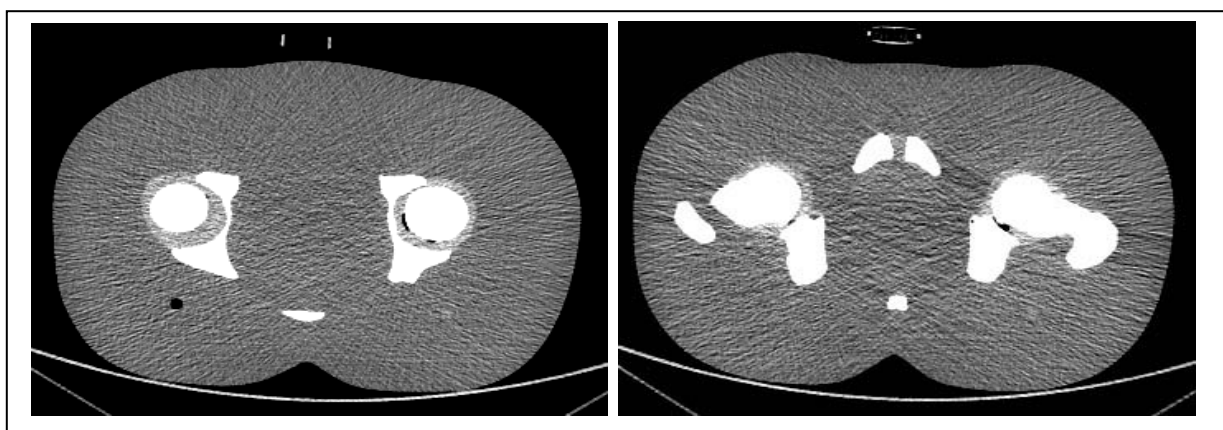


Figure 5-1. Visual comparison between ATOM phantom image without and with the rectal plug (including the solid water) in place, respectively.

As a preliminary assessment of the ability of the ATOM phantom to adequately represent a patient undergoing VC at MD Anderson Cancer Center, five ROI measurements of rectal tissues imaged in supine VC scans of 3 true MD Anderson Cancer Center patients (of approximately equal size to the ATOM phantom and who were chosen at random) yielded an average of 27.09 HU. Similarly, ATOM phantom soft tissue ROI measurements during simulated VC yielded an average measurement of 26.53 HU. This 2.06% difference in HU values represented a difference in linear attenuation coefficient of 0.05% between the actual VC patient rectal tissue and the phantom simulated soft tissue. Therefore, based on these measurements, the ATOM phantom appeared to provide an appropriate substitute for patient rectal tissue using the VC imaging technique.

An additional modification made to the anthropomorphic phantom involved the low-density Styrofoam plug that was inserted into the phantom to represent the carbon dioxide gas within the insufflated rectum while appropriately positioning the rectal catheter away from the posterior rectal wall. Although the location of the rectal catheter within the insufflated rectum was not consistent among the 29 patient VC scans analyzed, none of the

patients demonstrated rectal catheter placement against the posterior portion of the rectal wall. The simulated VC scans of the anthropomorphic phantom with the low-density Styrofoam plug inserted into the simulated rectum provided an average measurement of -931.66 HUs from five averaged ROIs within the insufflated rectum. This value compares well to true carbon dioxide ROI measurements obtained within insufflated rectums of 3 patients receiving VC scans at MD Anderson Cancer Center who were of approximately equal size to the ATOM phantom and who were chosen at random. The average of these measurements was -947.60 HU, which was only 1.68% larger than the HU value provided by the low-density Styrofoam plug. Therefore it was determined that the choice of the low-density Styrofoam plug to support the rectal catheter appeared to be a good choice of materials that only minimally attenuated the photons that were measured by the TLDs within the simulated rectum.

In order to use the ATOM phantom to obtain rectal dose estimates for patients of several sizes, fat substitutes were wrapped around the phantom in a manner that was consistent with population anthropomorphic data. The fat materials used included porcine adipose material (lard) and a simulated phantom fat kit manufactured by CIRS. The use of lard as a fat substitute during diagnostic imaging procedures was not a new scientific development (104-106). Many studies have been published that incorporated the use of lard in dual energy x-ray absorptiometry (DEXA) (107-117), ultrasound (118, 119) and in magnetic resonance imaging (MRI) (120-123). A literature review did not, however, reveal any previous research using this material for CT scans for the estimation of patient dose. Therefore, in addition to patient rectal dose measurements, a preliminary assessment of the use of lard as a low-cost scatter mechanism in anthropomorphic phantom VC dosimetry studies was conducted. Due to the novel nature of this approach, this material was only used as a scatter medium and did not attenuate the direct beam that was measured by the

TLDs. Therefore, speculation can be made that the use of lard in this study contributed to perhaps only 5% of each TLD reading.

An analysis of the scans that resulted from the simulated VC studies demonstrated that the lard provided photon attenuation that was similar to that of patient adipose tissue under VC conditions. Averaging five ROI measurements from the anthropomorphic phantom undergoing VC and 3 randomly selected patient VC scans at MD Anderson Cancer Center of similar size to the ATOM phantom yielded: a lard average measurement of -156.97 HU, a CIRS manufactured simulated phantom fat measurement of -79.54 HUs, and a true patient adipose tissue average measurement of -112.06 HUs. While these average ROI measurements yielded a 40.08% difference in HU number between the lard and the VC patient adipose tissue and a 29.02% difference in HU number between the CIRS phantom fat and the VC patient adipose tissue, the measured difference in HU numbers translated into a 5.06% difference between the linear attenuation coefficients of the lard and the patient adipose tissue, and a 3.66% difference between the CIRS phantom fat and the patient adipose tissue linear attenuation coefficients. This 3.66% difference between the CIRS fat and patient fat exceeded the 1% difference in tissue equivalence published by CIRS (83) for all diagnostic and therapeutic doses and energies.

These measurements suggest that the lard and the CIRS phantom fat provided similar deviations in linear attenuation coefficient from actual patient adipose tissue during VC. This fact, along with the simple advantage in cost that lard has over the CIRS phantom fat (around \$1 per lb of lard versus several thousand dollars for the CIRS simulated phantom fat system), suggest that lard could perhaps prove to be a reasonable substitute for patient fat in anthropomorphic phantom VC dosimetry studies. It should be stated, however, that the packaging and use of lard as a scatter medium was a labor intensive process. The value provided by the CIRS simulated fat material over lard was most apparent in the ease of use of the material (especially compared to the difficulties

encountered with the phantom set-up and packaging of the lard), the ability of the simulated fat material to support the weight of the phantom (where the lard was pushed laterally by the weight of the phantom), and the uniform coverage of the phantom fat material around the circumference of the phantom provided by the structure of the gelatinous phantom material and tapered design of the phantom fat. In contrast, the adjoining bags of lard were abutted by duct tape and included air gaps at the juncture. This design flaw of the lard system could be overcome with additional design efforts (such as tapering the lard within the bags and overlapping such bags when assembling them onto the phantom).

5.3.1.2 Anthropomorphic Phantom Assembly

During simulated VC with the anthropomorphic phantom, the most difficult and time consuming portion of the phantom irradiation process was the phantom set-up and tear-down between consecutive measurements at a single phantom habitus. The most complicated portion of this endeavor was aligning the respective sections of the phantom to one another. This process was made difficult by the design flaws inherent within the bags of lard as the semi-solid substance was forced laterally within the bags by the weight of the phantom. In order to adjoin the respective phantom portions as accurately as possible to create a uniform phantom scatter medium), supporting towels were frequently inserted between the table and the bags of lard; most notably in the lumbar and cervical areas of the phantom. Although the use of these towels slightly redistributed the lard within the bags, it is unlikely this redistribution had a significant effect on the measured rectal doses; also, the proper alignment of the respective ATOM phantom sections was considered a higher priority than ideal lard distribution.

Two additional approximations to true patient anatomy that were made regarding the ATOM phantom involved the phantom head and the phantom legs. The phantom head was not used during these simulated VC scans because this structure was difficult to

support (especially at the larger phantom sizes). It was believed that the phantom head would only minimally contribute to the scatter dose administered to the rectum, and therefore it is unlikely that the omission of this portion of the phantom had a significant impact on the doses measured by the TLDs within the rectum.

Regarding the legs of the anthropomorphic phantom, true ATOM phantom legs were not available for this study. Therefore this scatter medium was approximated by the use of two additional phantoms: an anthropomorphic torso phantom, and a CTDI body phantom. In order to achieve the best possible continuity in scatter material between the ATOM pelvis and the simulated legs in the 15th percentile configuration, the CTDI body phantom was abutted to the ATOM phantom and the anthropomorphic abdomen/pelvis phantom was placed inferior to the CTDI body phantom. This order of was reversed, however, when the layers of fat were applied such that the CTDI body phantom was placed inferior to the anthropomorphic abdomen/pelvis phantom. This change was made because the bags that were filled with lard were not large enough to wrap around the CTDI body phantom and because the anthropomorphic pelvis phantom could be elevated with towels to mate appropriately with the ATOM phantom pelvis once the bags of lard were wrapped around the simulated legs. As with the head of the ATOM phantom, it is believed that the specific geometry of the simulated phantom legs had a minimal impact on the rectal doses measured by the TLDs since they were not subjected to the primary beam at any time during the simulated VC (and they therefore acted solely as a scatter medium).

5.3.1.3 Phantom Measurements and Determination of Population Percentiles Represented

The determination of the percentile of US adults aged 18-64 represented by a phantom configuration was based on circumference measurements of the phantom and the population percentile data available in PeopleSize 2008 Pro software. The population of US adults considered in this study was limited to those between 18-64 years of age

because this demographic represented the population data that was most available within the software, and it represented a reasonable approximation to the actual population that receives VC at MD Anderson Cancer Center (which includes those older than 64 years of age). Additionally, the demographic used in this study was not a default population available in PeopleSize 2008 Pro software. This population was manually defined as 49% of US males aged 18-64 and 51% of US females aged 18-64, with a “mixed adults” correlation table. These manually defined settings were previously used in other studies assessing US adult sizes (124).

Circumference measurements were perhaps not the ideal technique to use for the determination of the population of US Adults represented by a phantom configuration, but it provided the best option available. Lateral and anterior-posterior (AP) dimensions are highly susceptible to shifts (especially in patients with a higher percentage of body fat) when a patient is lying down (e.g. while undergoing VC) versus when the patient is standing up (which was the posture for which data was available in PeopleSize 2008 Pro software). Realistically, circumference measurements are also subject to redistribution based on a patient’s posture (with dimensions shifting in a direction parallel to the CT scan table for patients with a higher body fat percentage); but of the options available, circumference presented the option with the least variation between the two postures and was therefore utilized in this study. Such potential redistribution in body fat based on position may have impacted this study’s regression analysis between measured rectal dose and effective diameter (especially if patients were to present in this study with larger habitus), but it is believed that any such impact was minimal and would be observed on a patient-by-patient basis (as no two people truly have the exact same body measurements and fat distribution).

A limitation of the data contained in PeopleSize 2008 Pro software is the lack of specific anatomical locations (i.e. anatomical landmarks) to which specific anthropometric measurements apply. While the user interface of the software provided helpful clues, more

specific anatomical landmarks would have made the measurement process more accurate. As stated above, though, due to the fact that no two people yield exactly identical anthropometric measurements at every anatomical location, this lack of specific information likely had a minimal effect on the rectal dose to effective diameter regression analyses contained within this study. These limitations likely had an impact, however, on the population percentiles provided for each patient participating in this study as there appeared to be some discrepancies between effective dose and percentiles for several patients in Table 4-8.

Although PeopleSize 2008 Pro software did not provide specific anatomical landmarks on which measurements should be based, the software did provide anthropometric measurement data resolution to the millimeter. This number of significant figures did not, however, improve the accuracy of the anthropometric measurements of the phantom; especially with regard to the measurements that encompassed the bagged lard. Although considerable efforts were undertaken to ensure that the lard within the bags was correctly distributed to match the distribution within a theoretical patient characterized by a percentile of US adults aged 18-64 (for example, ensuring that the thickness of the lard in the abdominal portion of the 87th percentile phantom configuration was 45 mm and was 34 mm at the armpits), it was ultimately unfeasible to go to the lengths necessary to ensure these exact measurements were obtained. Therefore, a ruler was simply used to obtain several measurements at each end of a bag to approximate that the lard was distributed in an appropriate manner. These measurements were complicated when the bags of lard were attached to the phantom during the simulated VC procedures as the weight of the phantom and the wrapping of the bags around the phantom unavoidably forced a lateral redistribution of the semi-solid lard within the bags. Although some of this fat redistribution realistically represented observed fat movement within patients when in a prone or supine position, obtaining and maintaining circumference measurements to the millimeter was

unfeasible in this study. Due to these factors in the lard redistribution, and due to the fact that a phantom population percentile was determined by averaging the circumference measurements at several anatomical locations, the population percentiles represented by each phantom configuration were susceptible to some error.

5.3.1.4 Virtual Colonoscopy Simulation in an Anthropomorphic Phantom

Besides the approximations inherent within the anthropomorphic phantom and within the population percentile represented by a phantom habitus configuration, an approximation to a true VC scan was made in the simulated VC in that two supine scans were performed on the anthropomorphic phantom (as opposed to a prone and a supine scan). This modification to actual VC procedure was utilized to minimize the difficulties associated with phantom set-up. Performing two supine CT scans was believed to be a reasonable approximation to a true VC exam where a prone and a supine scan are performed, but it also introduced opportunities for discrepancies between anthropomorphic phantom measurements and in-vivo measurements. Any discrepancies caused by this deviation from true VC protocol are believed to be minimal.

5.3.1.5 Simulated Virtual Colonoscopy Data Analysis

The trend of increasing %CoV observed in the phantom measurements with decreasing dose was also observed in Specific Aim 1 when the TLD dose and energy response was characterized. With the %CoV reaching 4.33% for the 99th percentile phantom configuration (likely the largest size of patient to undergo a VC), it was determined that TLD-100 material displays adequate precision to measure rectal doses during VC at MD Anderson Cancer Center. Additionally, a trend of patient CT dose decreasing in an exponential manner with an increase in patient size had been previously reported in other studies (101, 102). This trend was observed in our TLD dose measurements within the

anthropomorphic phantom and the calculated goodness of fit factor of $R^2=0.993$ of the exponential regression between the phantom effective diameter and the measured dose supported this finding.

The 95% confidence intervals (CI) for the mean phantom TLD measurements obtained at each patient size are admittedly difficult to observe in Figure 4-4. Although not displayed in Figure 4-4, a few measured dose values lied outside the 95% CI at each phantom effective diameter. This was likely due to the fact that the CIs displayed in Figure 4-4 were calculated based on a t-distribution. With only 12 data points available for each phantom habitus, it was very difficult to determine the distribution that was appropriate to model this data. Therefore, although some data lied outside this confidence interval range, it is unclear whether this data should (in reality) be considered outside the 95% confidence interval of the data.

The 95% CIs for the exponential regression equation modeling the measured rectal doses to the phantom effective diameter are admittedly large. Based on these confidence intervals, two patients' effective diameter could differ by up to 5 cm and still predict the same TLD dose within the 95% confidence interval. This large confidence interval was attributed to the fact that TLD measurements were only obtained at three effective diameters. If this analysis were expanded to include additional effective diameters, the coefficients within the exponential regression equation would likely experience small changes and the confidence intervals would likely narrow considerably toward the regression line.

The uniform phantom-based dose predictors were included in Figures 4-4 and 4-5 for illustrative purposes. With the data presented in this manner, the reader can easily see that all of the dose predictors, except the size specific dose estimate (SSDE), provided equal dose estimates regardless of the size of the patient; with the SSDE dose prediction being approximately parallel with the rectal dose regression developed by the TLD

measurements in the anthropomorphic phantom. Obviously, the dose estimates that do not change with patient size are not reliable prediction models of patient rectal dose as such models only predict patient dose for those patients of one size. The reason the SSDE dose prediction and the anthropomorphic phantom TLD measurements were not equal (and did not overlap) was believed to be due to the fact that the SSDE is based on an average dose distributed throughout the phantom (via the $CTDI_w$ component contained within SSDE) and the TLD measurements were point dose measurements obtained in a position slightly posterior to the center of a phantom. Therefore, because the dose within a phantom was higher at the phantom's surface than at the phantom's center, and since such higher dose measurements were included in the SSDE calculations and not in the TLD measurements, SSDE values should always be higher than dose measurements obtained near the center of a phantom.

For larger, more superficial organs in an anthropomorphic phantom that are completely within a scan volume, SSDE may be able to provide a reasonable first approximation to the dose administered to that phantom's organ. However, specific organ dose measurements would be required to verify this hypothesis. For organs not entirely within a CT scan volume or organs irradiated using dose modulation techniques (such as Smart mAs or automatic exposure control (AEC)), SSDE would not likely provide even reasonable first approximation estimates of the dose to that organ in an anthropomorphic phantom. In spite of these limitations, SSDE provides a useful adaptation to $CTDI_{vol}$ that accounts for patients of various sizes and provides general patient dose estimates within 10-20% of actual doses (101), and may even provide good approximations of dose administered to a point in the superior portion of the rectum within a typical VC patient.

5.3.2 In-Vivo Rectal Dose Measurements during Virtual Colonoscopy

The second phase of Specific Aim 2 included internal in-vivo rectal dose measurements in 6 patients undergoing VC at MD Anderson Cancer Center. Based on several literature reviews, it was believed that in-vivo dose measurements had never been performed inside patients undergoing virtual colonoscopy or even when undergoing MDCT scans in general. As such, significant efforts were made to define the scope of the project and to obtain IRB approval at MD Anderson Cancer Center. This approval was granted after the Food and Drug Administration (FDA) (Silver Spring, MD) determined that the study posed a non-significant risk to patients. One of the desired outcomes associated with this study is that more in-vivo CT dosimetric studies will be conducted in the future, not only within the rectum but also within other anatomical locations. Such studies would be important to validate patient or organ dose estimates produced by indirect means such as within phantoms, by Monte Carlo simulations, or by cadaveric studies.

5.3.2.1 Maintenance of Control of TLDs during VC Procedure

No TLDs became dislodged from the rectal catheter while performing in-vivo measurements during VC procedures. This TLD security was attributed to the fact that the TLDs were attached to the rectal catheter by both silicone glue and suture. Disinfection of the rectal catheter with 70% isopropyl alcohol may have negatively impacted the strength of the silicone glue. Although no substance is known to completely dissolve silicone glue, isopropyl alcohol is known to infiltrate the cells of silicone glue and expand them (rendering the bonds weaker). It is for this reason that the manufacturers of silicone glue recommend isopropyl alcohol when trying to remove the glue from surfaces. Therefore, incorporating the additional security of the suture provided sufficient adherence of the TLDs to the rectal catheters.

5.3.2.2 Patient Rectal Dose Determination

As demonstrated in Figure 4-7, Patient 4 had a higher relative bone density than the rest of patients receiving VC in this study due to the considerably younger age (and male gender) of this patient compared to the rest of the sample population. With this relatively high bone density, with a substantial amount of iodine contrast in the rectum, and with the TLDs located sufficiently superior within the rectum such that the primary x-ray beam was attenuated by the pelvis (as demonstrated in Figures 4-8 and 4-9), the measured readings and the 95% CI were lower than those of the rest of the patients. Conversely, although Patient 5 measured at a relatively high bone density as shown in Figure 4-7, the TLDs were placed more inferior within the rectum than in the rest of the patients such that the primary beam was not highly attenuated by the pelvis; but rather by the femurs and the ischia. This explains the low percentage of highly attenuating material in the axial plane of the TLDs observed in Figures 4-8 and 4-9. Since such relatively low amounts of highly attenuating material interacted with the primary beam on its path to the TLDs, the measured doses in this patient were understandably higher than in the rest of the study population.

Patient 4 had an effective diameter within 1% of that of the anthropomorphic phantom, at a comparable percentage of highly attenuating material in the images containing the median TLD location, and at similar measured rectal doses (within 1.7% of one another). Although it cannot be proven with just one young male patient with a seemingly typical amount of relative bone density, these in-vivo measurements suggest that x-ray attenuation in younger and relatively healthy adult populations are correctly represented by the ATOM anthropomorphic phantom; and conversely it may be implied that the ATOM phantom under-predicts doses in older patients with lower bone density. More patients would be required to definitively support these conclusions, however. It is noteworthy to mention that such younger and relatively healthy adult populations are not those typically receiving VCs, or even CT exams in general.

Although other studies (101, 102) (as well as the anthropomorphic phantom measurements in this study) predict a regression of patient CT dose decreasing exponentially with increasing effective diameter, the outliers within our in-vivo dose measurement results (Patients 4 and 5) rendered the calculation of any such regression a statistical problem for the in-vivo measurements (since the outliers account for 1/3rd of the total number of patients). Even though the driving factors behind these outlying measurements were believed to be known, it would take many more patients and perhaps even a mixed effects statistical model to create a regression of sufficient complexity to account for these factors and accurately predict patient rectal doses. Such endeavors would be important to undertake if adequate dose prediction models are to be developed.

It was observed in Chapter 5.3.1.5 that the simulated VC procedure within the anthropomorphic phantom provided rectal dose measurements that were considerably lower than those of the SSDE dose estimate. Although the two dose models decrease with increasing patient effective diameter in a nearly parallel nature, as stated above the differences between these dose models lies in the fact that SSDE is based on a weighted average dose throughout a phantom and the anthropomorphic phantom is solely based on point dose measurements in the approximate center of the phantom. It was interesting to observe that the higher rectal doses measured in the typical VC patients (due to a lack of relative bone density compared to the younger Patient 4 and the anthropomorphic phantom) almost exactly coincided with those higher dose estimates provided by the SSDE model. This coincidence is quantified by the mean square error analysis (MSE) provided in Table 4-10 that demonstrated that the SSDE model provided the best rectal dose estimate for 5 of 6 patients. Although the overlap of the values predicted in these models is somewhat coincidental, it appears that when assessing dose to the superior portion of the rectum in patients of approximately average bone density for the typical VC patient, SSDE provided dose estimates in this study within $\pm 5\%$ of actual measured rectal doses.

A close look at Table 4-9, in which in-vivo rectal dose measurements are compared to phantom dose estimates, may suggest some inconsistencies between the listed effective diameters and the provided percentiles of US adults aged 18-64 represented by each patient (as stated above in Chapter 5.3.1.3). One possible source for these apparent discrepancies is the fact that the percentiles were based on circumference measurements, where effective diameter (calculated by obtaining the square root of the product of the AP and lateral dimensions) was not. Secondly, while the PeopleSize software does provide a simple interface, it does not provide highly descriptive landmarks upon which anthropometric measurements should be based. The dimension within this software used to quantify the population percentile was described as “hip circumference, around buttocks”. It is possible that the circumference measurements acquired in this study do not completely reflect the anatomy intended in the PeopleSize software, and therefore some opportunity existed for error in the population percentiles provided in Tables 4-6, 4-8, and 4-9.

Additionally, the observed shifts in patient habitus mentioned in Chapter 3 yielded effective diameter measurements that were perhaps artificially inflated compared with analogous measurements performed on the uniform phantom and compared to the population percentiles provided. This suspicion of inflated effective diameters could perhaps also partially explain the apparent mismatch between patient effective diameters and population percentiles provided in Table 4-9. While it was expected that a patient’s adipose tissue would distribute laterally as they lay either prone or supine on the CT scanner table, the manner of this adipose tissue redistribution observed in patients provided a different shape than that of the anthropomorphic phantom; with the actual patients’ MDCT images yielding non-uniform lateral protrusions (where the phantom remained approximately oval shaped). Figure 5-2 displays a comparison of the distribution of the body mass during a simulated VC within the anthropomorphic phantom and in an actual VC within a patient.

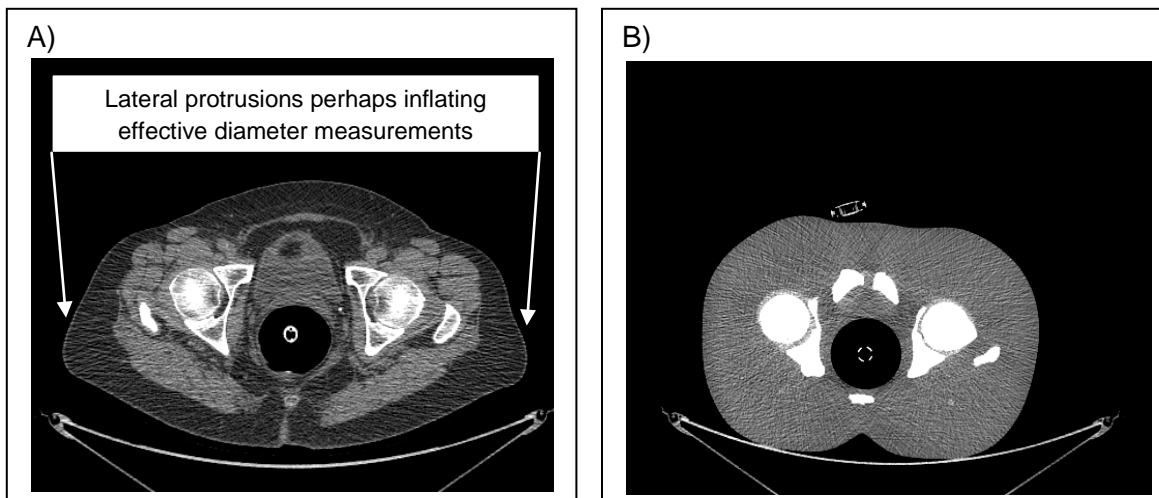


Figure 5-2. Visual comparison between A) non-uniform lateral adipose tissue distribution in patients, and B) anthropomorphic phantom.

In order to be consistent across all patients when performing patient size measurements, the lateral diameter measurements that were acquired to determine a patient's effective diameter were obtained at the maximum lateral distance; even when these protrusions were observed laterally. Therefore, the lateral diameter measurements obtained in this study were not indicative of an average lateral distance, but rather of the maximum lateral distance. Thus, it was possible that effective diameters assigned to those patients displaying this non-uniform distribution of adipose tissue were biased larger than appropriate; and such measurements provided an additional opportunity for disagreement between the data sets. It is possible that circumference measurements would have provided a better assessment of patient size than effective diameter in such cases when comparing anthropomorphic phantom measurement data to in-vivo patient data; however circumference is not readily assessed on CT scanners, and many interfaces do not offer tools to perform these measurements. Ultimately, effective diameter measurements were selected due to their utility in AAPM Report 204 (101), which describes SSDE as a function of effective diameter.

In order to accurately assess the dose delivered to the rectum as a result of the CT scans enlisted in the VC procedure, it was important to quantify the contribution to the TLD measured doses from the survey (aka scout) scans. Each patient, before undergoing both the supine and prone scan, received 2-3 scout scans (in both the PA and lateral directions) in order to ensure that the patient was appropriately positioned and that the CT scan covered all of the necessary anatomy. The results of the scout scan dose estimates are provided in Tables 4-7 and 4-8. While these administered doses were low (estimated to be between 0.140-0.277 mGy or 1.4-2.2% of the total VC rectal dose measurement), they introduced an opportunity for disagreement from the TLD measurements performed within the anthropomorphic phantom (which was not subjected to scout scans). These estimated scout doses were subtracted from the reported CT scan doses as shown in Figure 4-5 and Table 4-8, but as these doses are only estimates some disagreement may have been introduced between the anthropomorphic phantom and between the in-vivo measurements.

An exact comparison between the estimated scout scan entrance exposures calculated in this study and those results published by O'Daniel (15) is not possible; as O'Daniel did not provide entrance exposures for a GE VCT scanner (64 channels and a 40 mm beam), for 90° (lateral) scouts, for a tube current of 80 mA, or at an equivalent exposure measurement location (a VC patient thickness of 21.6 cm versus 22.5 cm thickness in O'Daniel). The closest comparison with data published in this paper would be based on a GE LightSpeed scanner (16 channels), at 10 mA and only for a 180° (PA) scout. Under these conditions, O'Daniel published an entrance skin exposure of 24.4 mR, while this study estimated an entrance exposure for a 180° scout at 10 mA to be 15.7 mR.

It should also be noted that the prone scout scans contributed considerably more dose to patients than the supine scout scans. This was due an oversight in the pre-set scanner settings that resulted in the prone scout scans being acquired at 80 mA compared to the 10 mA tube current used for the supine scout scans. While the scout image quality

was perhaps superior with the 80 mA technique, both imaging techniques provided images that were of sufficient quality to perform the functions required of the CT scout scan. Therefore, the prone scout technique could likely be decreased to 10 mA; which would have decreased the average scout dose administered to patients participating in this study by 59-85%.

Besides the dose contribution to the TLDs from the scout scans, additional consideration was required regarding measured TLD doses exceeding the maximum dose to which the TLD response was characterized. The initial estimates of rectal dose administered during VC that were discussed in Chapter 1.3.5 and Chapter 3 were based on Farmer chamber measurements as the midpoint dose, and 6 cm of acrylic material mathematically subtracted from the radius of the CTDI body phantom as the approximate upper dose limit and a simple estimate of 0.5 mGy as the lower dose limit. This initial rectal dose estimate was calculated to range from 0.5 mGy to 11.2 mGy. In calibrating the TLDs to this dose range, 0.7 mGy was administered at 20 mAs, and 10.8 mGy was administered at 170 mAs.

After calculation of the in-vivo TLD dose measurements, it was obvious that the doses administered at these mAs extremes did not completely encompass the range of doses encountered in the 6 patient measurements. The maximum dose characterized in Specific Aim 1 was 10.8 mGy (using an f-factor for dose to muscle), and 13 of 24 in-vivo TLD measurements exceeded this value. Patient 2 represented the minimum sized patient for which the TLD doses were measured in this study, and the maximum dose measured in the study was that within Patient 5. Based on the dose measurements from Patient 5, it can be estimated that the range of doses for which this batch of TLD-100 material should have been characterized in the diagnostic dose range by actual Farmer chamber and TLD measurement was 14.3 mGy (including the 95% confidence interval). This maximum dose, along with the measured dose range of 9.86 mGy to 13.05 mGy, suggests that although the

initial 11.2 mGy maximum dose estimate was not an entirely bad initial guess, the 11 mGy to 18 mGy dose range published by DeMarco (59) (for the entire colon) was more accurate for the rectum than initially expected. Based on the linearity of the administered doses to increasing mAs established in Specific Aim 1 with a very high goodness of fit factor (R^2), the TLD dose response extrapolations performed in this study to determine the rectal doses for those measurements exceeding the initial 11.2 mGy maximum rectal dose estimate were believed to be appropriate and robust.

It was also observed when accomplishing Specific Aim 1 and when TLD measurements were performed within the anthropomorphic phantom during simulated VC that the %CoV of the TLD measurements at a single dose increased with decreasing energy. This phenomena was not observed in the in-vivo measurements, however, as the %CoV appeared to maintain a value of approximately 5% for four out of six patients. The %CoV of these two outlier patients were 10% and 1.8% %CoV, even though the average dose readings from these two patients were within 0.5 mGy of one another. It is not known why the %CoV for these two patients varied from the others or each other, nor is it known why the %CoV for the in-vivo measurements averaged approximately 5% while the %CoV for the TLDs in the uniform phantom averaged 2% and the TLDs in the anthropometric phantom averaged 3%. This increase in %CoV was driven by increases in the standard deviations of the six patients compared to the phantom measurements, which was also reflected in larger 95% CIs than those observed in the respective phantom measurements. In spite of this decrease in %CoV and increase in CI, it is believed that the TLDs performed with adequate measurement precision in this study to reliably measure patient rectal doses during VC.

5.4 Specific Aim 3: Compare In-Vivo Rectal Dose Measurements to Anthropomorphic Phantom Measurements, CTDI-Based Dose Estimates and Point Dose Measurements from a Uniform Phantom

Since there are not yet many established methods to obtain organ dose measurements during CT scans, it is important to understand the accuracy of any such dose estimates provided by currently established methods. In an effort to preliminarily assess the accuracy of such methods, the in-vivo TLD rectal dose measurements were compared in Specific Aim 3 to dose estimates obtained from an anthropomorphic phantom, and a uniform CTDI body phantom using the same CT scan technique. These CTDI body phantom-based dose estimation techniques included: Farmer ionization chamber measurements within a CTDI body phantom, CTDI_{vol} measurements, $(\text{CTDI}_{100})_{\text{center}}$ measurements corrected for pitch (assigned the nomenclature “ $\text{CTDI}_{\text{vol,center}}$ ”), and SSDE dose estimates.

The Farmer chamber measurements used for comparison with the anthropomorphic phantom and in-vivo TLD measurements were based on the same exposure measurements used to determine the TLD $K_{L,120}$ values in Specific Aim 1. A difference existed, however, in the dose estimate used for comparison with anthropomorphic phantom and in-vivo measurements and those used to establish TLD response. The difference observed between these measurements was due to the fact that the f-factor that was multiplied by the measured Farmer chamber exposure, with the f-factor for muscle ($f=0.94$ rad/R) being used in Specific Aim 3 as opposed to the f-factor for acrylic ($f=0.78$ rad/R) that was used for the determination of the TLD $K_{L,120}$ values in Specific Aim 1.

It was necessary to use a common f-factor for both the apparent (uncorrected) TLD measurements and the Farmer chamber in Specific Aim 1 such that both f-factors cancelled out and were not erroneously factored into the $K_{L,120}$ determination. Since the CTDI body phantom is constructed of acrylic, this f-factor was utilized. However, TLD sensitivity (K_S) is

determined by the RPC in terms of absorbed dose to muscle. Therefore, in order to correctly compare the TLD measurement results to the Farmer chamber measurement dose estimate, the Farmer chamber exposure measurements were multiplied by the f-factor for muscle instead of that for acrylic.

The uniform CTDI phantom-based dose estimates were not found to provide dose estimates within 95% CI of the mean dose measurements within the anthropomorphic phantom. There were two uniform phantom measurements, however, that provided dose estimates with the 95% CI of the regression of the anthropomorphic phantom. Therefore, there may be some (limited) circumstances in which uniform CTDI phantom-based dose estimates may be useful in dose estimation.

Comparing the performance of the anthropomorphic and uniform phantom-based dose estimates to in-vivo measurements by MSE calculations showed that the SSDE model demonstrated the most consistent agreement to in-vivo measurements; providing the most accurate dose estimation for five of six patients, and predictions within the 95% CI for two of the patients. The remaining (younger) patient not conforming to the SSDE model was best predicted by the anthropomorphic phantom regression due to the fact that this patient more closely represented the phantom size and percentage of highly attenuating bone composition. Surprisingly, in spite of the fact that the $CTDI_{vol}$ dose estimate model does not change with changes in patient size, it did provide dose predictions for three patients with MSE values less than 1 mGy. However, with a larger and more uniformly distributed patient population, this percentage of relatively low MSE values will decrease because the $CTDI_{vol}$ model does not change with patient size; which makes the model generally unsuitable for dose predictions pertaining to a large population of individuals. Further, with a larger patient population that would include a representation of larger patients, all of the uniform dose predictions used in this study will predict doses for some range of patient sizes (as displayed in Figure 4-4).

Regarding our assessment of the variety of sizes of patients that undergo VC at MD Anderson Cancer Center, the percent coefficient of variation (%CoV) of the mean patient rectal doses was calculated to be 14.2%. This between-patient %CoV value was calculated to assess whether the between-patient rectal dose %CoV was greater than 50% (as stated in the hypothesis), which was an indirect assessment of the size distribution of patients receiving VC at MD Anderson Cancer Center. As can be seen in Figure 4-6, however, the distribution of patients that participated in this study was biased toward the smaller sizes of US adults. Due to the small sample size of this pilot study, it is unclear at this time whether this bias reflects a true bias in the population of adults receiving VC at MD Anderson Cancer Center; or whether this size distribution is simply a function of the small population of patients recruited for this study. If the size distribution of patients receiving VC at MD Anderson Cancer Center is truly smaller than that of the actual population of US adults aged 18-64, it could be a result of the fact that the typical patient receiving VC is greater than 50 years of age (and obese patients are less likely to survive to more advanced ages); or perhaps it could be a result of weight loss stemming from gastrointestinal issues that prompted a VC procedure. It is anticipated that this between-patient %CoV of rectal dose measurements would likely increase with a larger sample population.

The hypothesis of this study was: in-vivo rectal dose measurements obtained during virtual colonoscopy will have a rectal dose coefficient of variation that will be greater than 50%; and the differences between the anthropomorphic phantom dose measurements, the CTDI_{vol}-based dose estimates, and Farmer chamber measurements in a CTDI body phantom will be outside the 95% confidence interval for in-vivo patient VC dosimetry measurements. Based on the measurements obtained in this study, we have failed to prove the hypothesis prediction that the between-patient rectal dose coefficient of variation would exceed 50% based on our calculation yielding a coefficient of variation of 14.2%. Also, we have failed to prove the hypothesis prediction that the differences between the

anthropomorphic phantom dose measurements, the $CTDI_{vol}$ -based dose estimates, and Farmer chamber measurements in a CTDI body phantom would be outside the 95% confidence interval for in-vivo patient VC dosimetry measurements; as the SSDE and anthropomorphic phantom provided rectal dose estimates within the 95% confidence interval of mean patient dose measurements acquired in this study. Our data supports this hypothesis prediction, however, for the uniform $CTDI_{vol}$ dose models, the CTDI phantom-based $CTDI_{vol,center}$ and Farmer chamber rectal dose estimates.

5.5 Potential Future Work

In addition to the in-vivo measurements obtained for the 6 patients in this study, future work should concentrate on collecting in-vivo rectal dose measurements for a larger population of patients. Doing so would allow for a determination of the true distribution of rectal dose within a population of VC patients, which would allow for a better determination of the 95% confidence intervals than those provided in Figures 4-4 and 4-5. Future studies with a larger population of patients could also allow for an in-depth assessment of the validity of the rectal dose regression models developed within this study, even in those regression models such as the anthropomorphic phantom that were found to not predict typical VC patient dose with a high degree of accuracy, but were suggested to predict rectal doses in patients with higher relative bone density.

Future work related to this project should also focus on validating other indirect dose estimates to determine their accuracy compared to these direct TLD dose measurements. This could be accomplished by creating digital models of these same patients and performing VCs in Monte Carlo simulation to estimate rectal dose administered during the procedure. The groundwork to accomplish such dose comparisons has already been created, with the x-ray beam quality being adequately determined for the set-up of a Monte Carlo simulation equivalent source; and with 50 cm display field of view (DFOV)

reconstructions already available for each of the VC scans conducted in this study. Although it would be helpful in the development of such a Monte Carlo simulation equivalent source if ionization chamber exposure measurements were available at a modeled patient's surface, entrance surface exposures could be estimated with ionization chamber measurements at isocenter for the VC scan protocol by increasing the exposure measurements based on inverse square corrections for a patient's size; similarly to that which was done to estimate patient dose from the scout images (15). Ultimately, simulations could be performed based on the data already available without any such measurements. A new IRB approval would be required, however, for such a study as the IRB protocol for these measurements did not include exporting data to any other institutions where such modeling capabilities exist (such as McNitt-Gray's model at UCLA (44, 57-62, 102, 125)).

In addition to validating Monte Carlo models of dose administration, the techniques described in this study could be used to validate other indirect dose estimation techniques, such as other uniform or anthropomorphic phantom measurements or even cadaveric measurements. In order to more completely understand the accuracy provided by these (and Monte Carlo) dose estimates, however, dose measurements to additional organs would need to be acquired. Admittedly, the opportunities to acquire such measurements are primarily limited to those organs which contain accessible lumen structures (such as the digestive tract, the urinary tract, and perhaps the circulatory system). Measurements in each of these locations would present challenges and patient risks additional to those contained within this study. If a solid in-vivo benchmark could be established for these indirect measurement techniques, dose administered to many of the less accessible organs during CT scans could potentially be reliably estimated through refined modeling that considered patient size, anatomic composition and geometry, scan parameters, and other factors that contribute to patient dose.

Even if such models could be generated through a comprehensive series of direct organ dose measurements, the “bottom line” of such measurements is the determination of the risk to a patient. Ultimately, this determination may prove to be much more challenging than acquiring organ dose measurements at several sites and developing well-refined dosimetric understanding. A patient’s risk from radiation exposure is not simply a factor of the dose that patient receives, but also a factor of many other factors; to include (as an incomplete list): previous radiation exposure, tissues irradiated, genetic pre-disposition to cancer, cancer history, stochastic events, deterministic thresholds, etc. Such a thorough understanding of radiation biology does not currently exist to sufficiently determine the risk to a patient from CT scans, even with more comprehensive organ dose measurements. Therefore, while the performance of in-vivo organ dose measurements is a valuable step toward understanding patient risk from a diagnostic CT procedure such as VC, such measurements do not completely answer the fundamental question of patient risk.

Regarding the understanding of “ground truth” rectal organ dose from in-vivo rectal dose measurements, in order to completely correlate the TLD rectal dose measurements to actual patient rectal dose, consideration must be made regarding the amount of additional dose deposited to the rectum as a result of the presence of the iodinated contrast agent. Although the contrast agent acts as a highly attenuating material, photoelectric interactions likely occur within this material, which could deposit dose in surrounding tissues. Therefore, future work should also focus on modeling rectal dose as a function of the relative concentration of contrast agent within the rectum at the time of the VC scan. No such data is currently believed to be available; but a previous study (126) determined through a combination of liquid scintillation measurements of dose increase at various concentrations of iodinated contrast agent, HU measurements to determine the concentration of iodinated contrast agent in a medium, and Monte Carlo modeling of organ doses in an anthropomorphic phantom that dose to all five tissues analyzed increased with

the presence of an iodine contrast agent. The amount of organ dose increase was determined to be based on the concentration of the iodinated contrast agent present in the organ and the specific organs subjected to radiation. The study showed that in some tissues, when relatively high concentrations of iodinated contrast agents were present, the dose administered to the organ by the CT scan increased by as much as 74%. Therefore, an understanding of the dosimetric effects of the presence of the iodinated contrast agent within the rectum must be attained to fully quantify the radiation dose administered to the rectum during VC.

There are a few opportunities currently available to reduce the rectal dose resulting from VC procedures. Some institutions have incorporated the use of automatic exposure control (AEC) features such as GE's "Smart mAs" technology to modulate the dose to an appropriate level throughout the scan volume. Another potential method for reducing radiation dose to a patient would be to eliminate one of the two CT scans within the VC procedure. In order to eliminate one of the two CT scans (and still acquire a VC study of sufficient diagnostic quality), better computer aided detection (CAD) of polyps, better methods for insufflating the bowel, better methods for the removal of residual contrast agent while obtaining necessary contrast distribution, and improved ways to identify and see through fecal matter would have to be implemented. Although efforts have been applied to address each of these limitations, additional progress must be achieved to eliminate one of the two CT scans.

Radiation dose is eliminated completely when using optical colonoscopy (OC) or MRI technology as opposed to CT for VC (known as MR Colonography or MRC) (127-132). Although considered the "gold standard" by gastroenterologists, OC has many limitations; including: a relative inability to know exactly where in the colon the endoscope is at a given time, patient risks from sedation and bowel injury, and an insufficient number of qualified endoscopists to meet demands (screening, diagnosis, treatment, and surveillance). A

more wide-spread implementation of MRC could eliminate radiation dose. However, MRC requires longer scan times, which contributes to additional patient discomfort; and is not as widely accepted by clinicians as CT-based VC. Until acceptance for this modality increases and more radiologists are adequately trained to read MRC studies, CT-based VC remains a practical alternative to OC.

It theoretically may be possible to utilize the in-vivo dose measurements obtained in this study along with histograms of the CT images containing the median TLD location within the rectum to predict patient rectal dose. Based on a literature review, it is believed that such a dose prediction technique has not been attempted previously. Since the HU numbers upon which CT images are based is actually a measure of incident x-ray attenuation compared with that of water, and since CT irradiates patients from all angles, a histogram with a defined DFOV would provide data regarding the number and size of pixels providing the various amounts of x-ray beam attenuation during the CT scan. Since primary beam characteristics can be established with ionization chamber measurements at isocenter, fundamentally all of the information required to estimate patient rectal dose may be present. This technique would likely fail to accurately predict doses close to a patient's surface as these doses are known to vary with x-ray tube position.

5.6 Conclusions

A study was performed to acquire internal in-vivo measurements on patients undergoing virtual colonoscopy (VC) at MD Anderson Cancer Center. Such a study incorporating internal in-vivo measurements is not believed to have been performed previously for virtual colonoscopy or for multi-detector computed tomography (MDCT) scans in general. Such in-vivo measurements are important in order to benchmark the current indirect methods that are standard for determining patient dose from computed tomography (CT), including: measurements within a phantom, Monte Carlo simulation, and

cadaveric measurements. Our desire is that this study will pave the way for future internal in-vivo dose measurements in multiple organs to develop a better understanding of how current indirect dose estimates compare to actual measurements.

TLD response was characterized for the Radiologic Physics Center (RPC)'s B09 batch of thermoluminescent dosimeter (TLD) TLD-100 powder at the doses and energies encountered in VC at MD Anderson Cancer Center. Based on TLD measurements obtained within a computed tomography dose index (CTDI) body phantom, TLD dose linearity values were determined at 120 kVp ($K_{L,120}$) with a percent coefficient of variation (%CoV) less than 3.56% at all doses. A third-order polynomial regression with a goodness of fit factor of $R^2=0.992$ was constructed from this data, and this $K_{L,120}$ regression model was used to measure rectal doses administered to an anthropomorphic phantom and to patients during VC at MD Anderson Cancer Center.

Mean rectal dose measurements of 8.8 mGy, 5.7 mGy, and 3.5 mGy were acquired, respectively, during simulated VC (using the MD Anderson Cancer Center technique) within an anthropomorphic phantom that was configured to represent the 15th, 87th, and 99th percentile of US adult patients aged 18-64. The measured rectal doses decreased in an exponential manner with increasing phantom effective diameter. As observed in the measurements that were obtained to quantify the TLD response at diagnostic doses and energies, the %CoV increased with decreasing dose. The %CoV for the 99th percentile phantom configuration was calculated to be <5%, which implied that the TLDs were able to provide rectal dose measurements with reasonable precision for nearly all patients that are likely to undergo VC.

In-vivo rectal dose measurements were also acquired during VC using the MD Anderson Cancer Center protocol within 6 patients. The average rectal doses measured in the population of patients (of four TLD dose measurements per patient) ranged from 9.0 to 13.1 mGy. The measured rectal doses within a young adult male patient was favorably

predicted by the exponential regression model developed from the anthropomorphic phantom rectal dose measurements, while the typical VC patient population (older, mostly female adults) was favorably predicted by the size specific dose estimate (SSDE) dose model (as long as measurements were obtained sufficiently superior within the rectum). In contrast to what was observed in the previous TLD measurements, the TLD response at diagnostic doses and energies did not increase in %CoV with decreasing dose. The largest TLD measurement %CoV from the in-vivo data was 10.0%, which implied that the TLDs provided rectal dose measurements with reasonable precision for all patients in this study.

The between-patient percent coefficient of variation of the average TLD rectal dose measurements for each patient was calculated to be 14.2%. We therefore failed to prove our hypothesis that the between-patient percent coefficient of variation would exceed 50%. Further, we have failed to prove our hypothesis that the anthropomorphic phantom and uniform phantom-based rectal dose measurements would not provide dose estimates within the 95% confidence interval of the mean patient dose measurements as the SSDE dose model met this criteria for three patients and the anthropomorphic phantom met this criteria for the young adult patient who does not represent the typical VC population. Our results suggest that we may be able to accept our hypothesis for the CTDI volume ($CTDI_{vol}$) dose estimate, the $CTDI_{vol}$ dose estimate that disregarded the peripheral CTDI phantom exposure measurements ($CTDI_{vol,center}$) and the Farmer chamber dose estimates as each of these techniques yielded doses that were outside the 95% confidence interval of the mean for our initial patient population (n=6).

REFERENCES

1. Mitka, M. 2008. Colorectal cancer screening rates still fall far short of recommended levels. JAMA 299:622.
2. Vining, D. 2009. Evaluation and Mitigation of Potential Harms Associated with Virtual Colonoscopy for Colorectal Cancer Screening. CPRIT, MD Anderson Cancer Center, Houston TX. 10.
3. Vining, D., D. Gelfand, R. Bechtold, E. Scharling, E. Grishaw, and R. Shifrin. 1994. Technical feasibility of colon imaging with helical CT and virtual reality. AJR American Journal of Roentgenology 162 (Supplement).
4. McFarland, E. G., J. G. Fletcher, P. Pickhardt, A. Dachman, J. Yee, C. H. McCollough, M. Macari, P. Knechtges, M. Zalis, M. Barish, D. H. Kim, K. J. Keysor, and C. D. Johnson. 2009. ACR Colon Cancer Committee white paper: status of CT colonography 2009. J Am Coll Radiol 6:756-772 e754.
5. Johnson, C. D., M. H. Chen, A. Y. Toledano, J. P. Heiken, A. Dachman, M. D. Kuo, C. O. Menias, B. Siewert, J. I. Cheema, R. G. Obregon, J. L. Fidler, P. Zimmerman, K. M. Horton, K. Coakley, R. B. Iyer, A. K. Hara, R. A. Halvorsen, Jr., G. Casola, J. Yee, B. A. Herman, L. J. Burgart, and P. J. Limburg. 2008. Accuracy of CT colonography for detection of large adenomas and cancers. N Engl J Med 359:1207-1217.
6. Levin, B., D. A. Lieberman, B. McFarland, R. A. Smith, D. Brooks, K. S. Andrews, C. Dash, F. M. Giardiello, S. Glick, T. R. Levin, P. Pickhardt, D. K. Rex, A. Thorson, and S. J. Winawer. 2008. Screening and surveillance for the early detection of colorectal cancer and adenomatous polyps, 2008: a joint guideline from the American Cancer Society, the US Multi-Society Task Force on Colorectal Cancer, and the American College of Radiology. CA Cancer J Clin 58:130-160.

7. CMS. 2009. Decision Memo for Screening Computed Tomography Colonography (CTC) for Colorectal Cancer (CAG-00396N). U.S. Department of Health and Human Services Centers for Medicare and Medicaid Services (CMS).
8. Bogdanich, W. 2010. As Technology Surges, Radiation Safeguards Lag. In The New York Times, New York.
9. Bogdanich, W., and R. R. Ruiz. 2010. F.D.A. to Increase Oversight of Medical Radiation. In The New York Times, New York.
10. Harris, G. 2010. Scientists Say F.D.A Ignored Radiation Warnings. In The New York Times, New York.
11. Heuser, M. 2010. Scanning the scanners. In Los Angeles Times, Los Angeles.
12. Sternberg, S. 2007. Study: Unnecessary CT scans exposing patients to excessive radiation. In USA Today.
13. Brenner, D. J., and E. J. Hall. 2007. Computed tomography--an increasing source of radiation exposure. N Engl J Med 357:2277-2284.
14. ICRP. 1991. 1990 Recommendations of the International Commission of Radiological Protection. In ICRP Publication 60. International Commission of Radiological Protection.
15. O'Daniel, J. C., D. M. Stevens, and D. D. Cody. 2005. Reducing radiation exposure from survey CT scans. AJR Am J Roentgenol 185:509-515.
16. NCRP. 2009. Ionizing Radiation Exposure of the Population of the United States. In NCRP Publication 160. National Council on Radiation Protection and Measurements, Bethesda.
17. Brenner, D. J., and M. A. Georgsson. 2005. Mass screening with CT colonography: should the radiation exposure be of concern? Gastroenterology 129:328-337.

18. An, S., K. H. Lee, Y. H. Kim, S. H. Park, H. Y. Kim, S. H. Kim, and N. Kim. 2008. Screening CT colonography in an asymptomatic average-risk Asian population: a 2-year experience in a single institution. *AJR Am J Roentgenol* 191:W100-106.
19. Cohnen, M., C. Vogt, A. Beck, K. Andersen, W. Heinen, S. vom Dahl, V. Aurich, D. Haeussinger, and U. Moedder. 2004. Feasibility of MDCT Colonography in ultra-low-dose technique in the detection of colorectal lesions: comparison with high-resolution video colonoscopy. *AJR Am J Roentgenol* 183:1355-1359.
20. Martin, C. J. 2008. The application of effective dose to medical exposures. *Radiat Prot Dosimetry* 128:1-4.
21. Fowler, J., and H. Attix. 1966. Solid state integrating dosimeters. In *Radiation Dosimetry*. H. Attix, and W. Roesch, editors. Academic Press, New York. 241-290.
22. Wiedemann, E., and G. Schmidt. 1895. Uber luminescenz. *Ann der Physik und Chemie* 54:604.
23. Pradhan, A. S., J. I. Lee, and J. L. Kim. 2008. Recent developments of optically stimulated luminescence materials and techniques for radiation dosimetry and clinical applications. *J Med Phys* 33:85-99.
24. Daniels, F. 1950. Thermoluminescence and related properties of crystals. In *Rept. 4th Symp. Chem Phys. Radiation Dosimetry, 1950 Part 1*. Army Chem. Center, Edgewood, Maryland. 148.
25. Cameron, J. R., F. Daniels, N. Johnson, and G. Kenney. 1961. Radiation dosimeter utilizing the thermoluminescence of lithium fluoride. *Science* 134:333-334.
26. Kron, T. 1994. Thermoluminescence dosimetry and its applications in medicine - part 1: physics, materials and equipment. *Australasian Physical & Engineering Sciences in Medicine* 17:175-199.
27. Cameron, J. R., D. Zimmerman, G. Kenney, R. Buch, R. Bland, and R. Grant. 1964. Thermoluminescent Radiation Dosimetry Utilizing Lif. *Health Phys* 10:25-29.

28. Karzmark, C. J., J. White, and J. F. Fowler. 1964. Lithium Fluoride Thermoluminescence Dosimetry. *Phys Med Biol* 16:273-286.
29. Warton, R., and A. Holloway. 1966. Lithium Fluoride Thermoluminescent Dosimetry. *Radiology* 87:938-943.
30. Martensson, B. K. 1969. Thermoluminescence of LiF: a statistical analysis of the influence of pre-annealing on the precision of measurement. *Phys Med Biol* 14:119-130.
31. McKinlay, A. F. 1981. Medical Physics Handbooks 5: Thermoluminescence Dosimetry. Adam Hilger Ltd, Bristol.
32. Regulla, D. 1981. Operational aspects. In *Applied thermoluminescence dosimetry*. M. Oberhofer, and A. Scharmann, editors. Adam Hilger, Bristol. 123-141.
33. Horowitz, Y. 1990. The annealing characteristics of LiF:Mg,Ti. *Radiat Prot Dosimetry* 30:219-230.
34. Driscoll, C., J. Barthe, M. Oberhofer, G. Busuoli, and C. Hickman. 1986. Annealing procedures for commonly used radiothermoluminescent materials. *Radiat Prot Dosimetry* 14:17-32.
35. http://rpc.mdanderson.org/rpc/services/TLD_Services/TLD_Expected.htm. TLD Remote Monitoring Program - Expected Uncertainty. Radiologic Physics Center (RPC). University of Texas MD Anderson Cancer Center, Houston.
36. RPC. 2009. Radiologic Physics Center (RPC). Procedure for Calculating TLD Doses - Batch B09 (TG-51). University of Texas MD Anderson Center, Houston. 4.
37. McNitt-Gray, M. F. 2002. AAPM/RSNA Physics Tutorial for Residents: Topics in CT. Radiation dose in CT. *Radiographics* 22:1541-1553.
38. Seltzer, S. 2004. Tables of X-Ray Mass Attenuation Coefficients and Mass Energy-Absorption Coefficients. National Institute of Standards and Technology.

39. Perry, B. J., and C. Bridges. 1973. Computerized transverse axial scanning (tomography). 3. Radiation dose considerations. *Br J Radiol* 46:1048-1051.
40. McCullough, E. C., H. L. Baker, Jr., O. W. Houser, and D. F. Reese. 1974. An evaluation of the quantitative and radiation features of a scanning x-ray transverse axial tomograph: the EMI scanner. *Radiology* 111:709-715.
41. Shope, T. B., R. M. Gagne, and G. C. Johnson. 1981. A method for describing the doses delivered by transmission x-ray computed tomography. *Med Phys* 8:488-495.
42. AAPM. 2008. American Association of Physicists in Medicine (AAPM) Report 96. The Measurement, Reporting, and Management of Radiation Dose in CT. AAPM, New York.
43. Boone, J. M. 2007. The trouble with CTD100. *Med Phys* 34:1364-1371.
44. Jarry, G., J. J. DeMarco, U. Beifuss, C. H. Cagnon, and M. F. McNitt-Gray. 2003. A Monte Carlo-based method to estimate radiation dose from spiral CT: from phantom testing to patient-specific models. *Phys Med Biol* 48:2645-2663.
45. Lee, C., and J.-K. Lee. 2006. Computational Anthropomorphic Phantoms for Radiation Protection Dosimetry: Evolution and Prospects. *Nuclear Engineering and Technology* 38.
46. Jones, D. G., and P. C. Shrimpton. 1991. Survey of CT practice in the UK. Part 3: Normalised organ doses calculated using Monte Carlo techniques. National Radiation Protection Board (NRPB), Chilton.
47. Shrimpton, P. C., D. G. Jones, H. M. C., W. B. F., L. J. C., and F. K. 1991. Survey of CT practice in the UK. Part 2: Dosimetric aspects. In NRPB-R249. National Radiation Protection Board (NRPB), Chilton.
48. Shrimpton, P. C., M. C. Hillier, M. A. Lewis, and M. Dunn. 2006. National survey of doses from CT in the UK: 2003. *Br J Radiol* 79:968-980.

49. ICRP. 1975. Report on the Task Group on Reference Man, ICRP Publication 23. International Commission on Radiological Protection.
50. Bauhs, J. A., T. J. Vrieze, A. N. Primak, M. R. Bruesewitz, and C. H. McCollough. 2008. CT dosimetry: comparison of measurement techniques and devices. *Radiographics* 28:245-253.
51. Zhou, H., and J. M. Boone. 2008. Monte Carlo evaluation of CTD(infinity) in infinitely long cylinders of water, polyethylene and PMMA with diameters from 10 mm to 500 mm. *Med Phys* 35:2424-2431.
52. Cohnen, M., L. J. Poll, C. Puettmann, K. Ewen, A. Saleh, and U. Modder. 2003. Effective doses in standard protocols for multi-slice CT scanning. *Eur Radiol* 13:1148-1153.
53. http://en.wikipedia.org/wiki/Monte_Carlo_method. 2011. Monte Carlo Method. In Wikipedia. Wikimedia Foundation, San Francisco, CA.
54. Metropolis, N. 1987. The Beginning of the Monte Carlo Method. *Los Alamos Science Special Issue*:125-130.
55. Woller, J. 1996. The Basics of Monte Carlo Simulations. University of Nebraska-Lincoln, Lincoln.
56. <http://www.impactscan.org/ctdosimetry.htm>. 2010. CTDosimetry version 1.0.3. Imaging Performance Assessment of CT Scanners (ImPACT), London.
57. Angel, E., C. V. Wellnitz, M. M. Goodsitt, N. Yaghmai, J. J. DeMarco, C. H. Cagnon, J. W. Sayre, D. D. Cody, D. M. Stevens, A. N. Primak, C. H. McCollough, and M. F. McNitt-Gray. 2008. Radiation dose to the fetus for pregnant patients undergoing multidetector CT imaging: Monte Carlo simulations estimating fetal dose for a range of gestational age and patient size. *Radiology* 249:220-227.
58. DeMarco, J. J., C. H. Cagnon, D. D. Cody, D. M. Stevens, C. H. McCollough, J. O'Daniel, and M. F. McNitt-Gray. 2005. A Monte Carlo based method to estimate

- radiation dose from multidetector CT (MDCT): cylindrical and anthropomorphic phantoms. *Phys Med Biol* 50:3989-4004.
59. DeMarco, J. J., C. H. Cagnon, D. D. Cody, D. M. Stevens, C. H. McCollough, M. Zankl, E. Angel, and M. F. McNitt-Gray. 2007. Estimating radiation doses from multidetector CT using Monte Carlo simulations: effects of different size voxelized patient models on magnitudes of organ and effective dose. *Phys Med Biol* 52:2583-2597.
 60. Turner, A. C., D. Zhang, H. J. Kim, J. J. DeMarco, C. H. Cagnon, E. Angel, D. D. Cody, D. M. Stevens, A. N. Primak, C. H. McCollough, and M. F. McNitt-Gray. 2009. A method to generate equivalent energy spectra and filtration models based on measurement for multidetector CT Monte Carlo dosimetry simulations. *Med Phys* 36:2154-2164.
 61. Zhang, D., A. S. Savandi, J. J. Demarco, C. H. Cagnon, E. Angel, A. C. Turner, D. D. Cody, D. M. Stevens, A. N. Primak, C. H. McCollough, and M. F. McNitt-Gray. 2009. Variability of surface and center position radiation dose in MDCT: Monte Carlo simulations using CTDI and anthropomorphic phantoms. *Med Phys* 36:1025-1038.
 62. Zhang, D., M. Zankl, J. J. DeMarco, C. H. Cagnon, E. Angel, A. C. Turner, and M. F. McNitt-Gray. 2009. Reducing radiation dose to selected organs by selecting the tube start angle in MDCT helical scans: a Monte Carlo based study. *Med Phys* 36:5654-5664.
 63. Groves, A. M., K. E. Owen, H. M. Courtney, S. J. Yates, K. E. Goldstone, G. M. Blake, and A. K. Dixon. 2004. 16-detector multislice CT: dosimetry estimation by TLD measurement compared with Monte Carlo simulation. *Br J Radiol* 77:662-665.
 64. Lechel, U., C. Becker, G. Langenfeld-Jager, and G. Brix. 2009. Dose reduction by automatic exposure control in multidetector computed tomography: comparison between measurement and calculation. *Eur Radiol* 19:1027-1034.

65. Deak, P., M. van Straten, P. C. Shrimpton, M. Zankl, and W. A. Kalender. 2008. Validation of a Monte Carlo tool for patient-specific dose simulations in multi-slice computed tomography. *Eur Radiol* 18:759-772.
66. Wang, L., M. Lovelock, and C. S. Chui. 1999. Experimental verification of a CT-based Monte Carlo dose-calculation method in heterogeneous phantoms. *Med Phys* 26:2626-2634.
67. Nawfel, R. D., P. F. Judy, A. R. Schlepman, and S. G. Silverman. 2004. Patient radiation dose at CT urography and conventional urography. *Radiology* 232:126-132.
68. Parker, M. S., N. M. Kelleher, J. A. Hoots, J. K. Chung, P. P. Fatouros, and S. H. Benedict. 2008. Absorbed radiation dose of the female breast during diagnostic multidetector chest CT and dose reduction with a tungsten-antimony composite breast shield: preliminary results. *Clin Radiol* 63:278-288.
69. Perisinakis, K., M. Raissaki, N. Theocharopoulos, J. Damilakis, and N. Gourtsoyiannis. 2005. Reduction of eye lens radiation dose by orbital bismuth shielding in pediatric patients undergoing CT of the head: a Monte Carlo study. *Med Phys* 32:1024-1030.
70. Resten, A., F. Mausoleo, M. Valero, and D. Musset. 2003. Comparison of doses for pulmonary embolism detection with helical CT and pulmonary angiography. *Eur Radiol* 13:1515-1521.
71. Schenzle, J. C., W. H. Sommer, K. Neumaier, G. Michalski, U. Lechel, K. Nikolaou, C. R. Becker, M. F. Reiser, and T. R. Johnson. 2010. Dual energy CT of the chest: how about the dose? *Invest Radiol* 45:347-353.
72. Bou Serhal, C., R. Jacobs, F. Gijbels, H. Bosmans, R. Hermans, M. Quirynen, and D. van Steenberghe. 2001. Absorbed doses from spiral CT and conventional spiral tomography: a phantom vs. cadaver study. *Clin Oral Implants Res* 12:473-478.

73. Liedenbaum, M. H., H. W. Venema, and J. Stoker. 2008. Radiation dose in CT colonography--trends in time and differences between daily practice and screening protocols. *Eur Radiol* 18:2222-2230.
74. Walter, C., J. Boda-Heggemann, H. Wertz, I. Loeb, A. Rahn, F. Lohr, and F. Wenz. 2007. Phantom and in-vivo measurements of dose exposure by image-guided radiotherapy (IGRT): MV portal images vs. kV portal images vs. cone-beam CT. *Radiother Oncol* 85:418-423.
75. Jeng, S. C., C. L. Tsai, W. T. Chan, C. J. Tung, J. K. Wu, and J. C. Cheng. 2009. Mathematical estimation and in vivo dose measurement for cone-beam computed tomography on prostate cancer patients. *Radiother Oncol* 92:57-61.
76. Kim, S., T. T. Yoshizumi, G. Toncheva, S. Yoo, and F. F. Yin. 2008. Comparison of radiation doses between cone beam CT and multi detector CT: TLD measurements. *Radiat Prot Dosimetry* 132:339-345.
77. Fox, S. 2004. Dare to Dream. In *Volume CT*. G. Healthcare, editor. GE Healthcare, Waukesha, WI.
78. Schubert, S. 2004. What is Volume Computed Tomography? In *Volume CT*. G. Healthcare, editor. GE Healthcare, Waukesha, WI.
79. GE. 2006. *LightSpeed Series Technical Reference Manual*. GE Healthcare, Waukesha, WI.
80. CIRS. 2001. *ATOM Adult Male Phantom Model Number 701 Handling Instructions*. Computerized Imaging Reference Systems, Inc (CIRS), Norfolk, VA. 9.
81. CIRS. 2008. *ATOM Dosimetry Phantoms - A Family of Dosimetry Phantoms*. I. C. Computerized Imaging Reference Systems, editor, Norfolk, VA.
82. Hintenlang, D. E., W. E. Moloney, and J. Winslow. 2010. Physical Phantoms for Experimental Radiation Dosimetry. In *Handbook of Anatomical Models for Radiation*

- Dosimetry. X. G. Xu, and K. F. Eckerman, editors. Taylor and Francis Group, LLC, Boca Raton, FL. 389-409.
83. CIRS. 2006. Model 701 Abdominal/Thoracic Fat Layers, Custom Handling Instruction. Computed Imaging Reference Systems, Inc (CIRS), Norfolk, VA. 3.
 84. CIRS. 2005. Product Catalog. I. C. Computerized Imaging Reference Systems, editor, Norfolk, VA.
 85. CIRS. 2008. ATOM Dosimetry Verification Phantoms. I. C. Computerized Imaging Reference Systems, editor, Norfolk, VA.
 86. CIRS. 2008. ATOM Dosimetry Phantoms, Models 700-705. I. C. Computerized Imaging Reference Systems, editor, Norfolk, VA.
 87. <http://www.openerg.com/psz/index.html>. 2011. PeopleSize 2008 Visual Anthropometry Software. Open Ergonomics Ltd, Leicestershire, UK.
 88. European-Commission. 1999. European guidelines on quality criteria for computed tomography, EU Report No. EUR 16262. European Commission, Brussels, Belgium.
 89. Knoll, G. F. 1999. Radiation detection and measurement. John Wiley and Sons, Inc, Hoboken, NJ.
 90. Johns, H. E., and J. R. Cunningham. 1983. The Physics of Radiology. Thomas Books, Springfield, IL.
 91. Farmer, F. T. 1946. A feed-back amplifier for ionisation currents. Br J Radiol 19:27-30.
 92. Radcal. 2005. Model 9010 Radiation Monitor Controller Manual. Radcal Corporation, Monrovia, CA. 112.
 93. Suzuki, A., and M. N. Suzuki. 1978. Use of a pencil-shaped ionization chamber for measurement of exposure resulting from a computed tomography scan. Med Phys 5:536-539.

94. E-Z-EM. 2010. Model 8925 Super XL Enema System Instruction Manual. Bracco Diagnostics Inc, Princeton, NJ.
95. Mathieu, K. B., S. C. Kappadath, R. A. White, E. N. Atkinson, and D. D. Cody. 2011. An empirical model of diagnostic x-ray attenuation under narrow-beam geometry. In Press Med Phys, April 2011.
96. Corless, R. M., G. H. Gonnet, D. E. G. Hare, D. J. Jeffrey, and D. E. Knuth. 1996. On the Lambert W Function. Advances in Computational Mathematics 5:329-359.
97. <http://toxnet.nlm.nih.gov/cgi-bin/sis/search/r?dbs+hsdb:@rn+7789-24-4>. 2010. Lithium Fluoride, CASRN: 7789-24-4. U.S. National Library of Medicine, Bethesda. Toxnet Hazardous Substances Data Bank (HSDB).
98. Stevens, A., and J. S. Lowe. 2005. Human histology. Elsevier/Mosby ;, Philadelphia ;.
99. EMD. 2003. Material Safety Data Sheet (MSDS) for Lithium Fluoride. EMD Chemicals Inc, Gibbstown, NJ. 4.
100. ICRU. 1989. Tissue Substitutes in Radiation Dosimetry and Measurement, Report 44. International Commission on Radiation Units and Measurements, Bethesda, MD.
101. AAPM. 2011. American Association of Physicists in Medicine (AAPM) Report 204. Correction Factors for Patient Size in CT Dose Estimation. AAPM, New York.
102. Turner, A. C., D. Zhang, M. Khotonabadi, M. Zankl, J. J. DeMarco, C. H. Cagnon, D. D. Cody, D. M. Stevens, C. H. McCollough, and M. F. McNitt-Gray. 2011. The feasibility of patient size-corrected, scanner-independent organ dose estimates for abdominal CT exams. Med Phys 38.
103. Mathieu, K. B., M. F. McNitt-Gray, D. Zhang, H. J. Kim, and D. D. Cody. 2010. Precision of dosimetry-related measurements obtained on current multidetector computed tomography scanners. Med Phys 37:4102-4109.

104. Bohndiek, S. E., E. J. Cook, C. D. Arvanitis, A. Olivo, G. J. Royle, A. T. Clark, M. L. Prydderch, R. Turchetta, and R. D. Speller. 2008. A CMOS active pixel sensor system for laboratory- based x-ray diffraction studies of biological tissue. *Phys Med Biol* 53:655-672.
105. Ferreira, C. C., R. E. Ximenes, C. A. B. Garcia, J. W. Vieira, and A. F. Maia. 2010. Total mass attenuation coefficient evaluation of ten materials commonly used to simulate human tissue. In *International Conference on Defects in Insulating Materials. Journal of Physics: Conference Series*.
106. Sandison, G. A., M. P. Loye, J. C. Rewcastle, L. J. Hahn, J. C. Saliken, J. G. McKinnon, and B. J. Donnelly. 1998. X-ray CT monitoring of iceball growth and thermal distribution during cryosurgery. *Phys Med Biol* 43:3309-3324.
107. Chan, G. M. 1992. Performance of dual-energy x-ray absorptiometry in evaluating bone, lean body mass, and fat in pediatric subjects. *J Bone Miner Res* 7:369-374.
108. Gotfredsen, A., L. Baeksgaard, and J. Hilsted. 1997. Body composition analysis by DEXA by using dynamically changing samarium filtration. *J Appl Physiol* 82:1200-1209.
109. Gotfredsen, A., J. Podenphant, H. Norgaard, L. Nilas, V. A. Nielsen, and C. Christiansen. 1988. Accuracy of lumbar spine bone mineral content by dual photon absorptiometry. *J Nucl Med* 29:248-254.
110. Haderslev, K. V., P. H. Haderslev, and M. Staun. 2005. Accuracy of body composition measurements by dual energy x-ray absorptiometry in underweight patients with chronic intestinal disease and in lean subjects. *Dyn Med* 4:1.
111. Laskey, M. A., K. D. Lyttle, M. E. Flaxman, and R. W. Barber. 1992. The influence of tissue depth and composition on the performance of the Lunar dual-energy X-ray absorptiometer whole-body scanning mode. *Eur J Clin Nutr* 46:39-45.

112. Mazess, R. B., J. A. Trempe, J. P. Bisek, J. A. Hanson, and D. Hans. 1991. Calibration of dual-energy x-ray absorptiometry for bone density. *J Bone Miner Res* 6:799-806.
113. Pietrobelli, A., Z. Wang, C. Formica, and S. B. Heymsfield. 1998. Dual-energy X-ray absorptiometry: fat estimation errors due to variation in soft tissue hydration. *Am J Physiol* 274:E808-816.
114. Salamone, L. M., T. Fuerst, M. Visser, M. Kern, T. Lang, M. Dockrell, J. A. Cauley, M. Nevitt, F. Tyllavsky, and T. G. Lohman. 2000. Measurement of fat mass using DEXA: a validation study in elderly adults. *J Appl Physiol* 89:345-352.
115. Tothill, P., and W. J. Hannan. 2000. Comparisons between Hologic QDR 1000W, QDR 4500A, and Lunar Expert dual-energy X-ray absorptiometry scanners used for measuring total body bone and soft tissue. *Ann N Y Acad Sci* 904:63-71.
116. Tothill, P., W. J. Hannan, S. Cowen, and C. P. Freeman. 1997. Anomalies in the measurement of changes in total-body bone mineral by dual-energy X-ray absorptiometry during weight change. *J Bone Miner Res* 12:1908-1921.
117. Tothill, P., M. A. Laskey, C. I. Orphanidou, and M. van Wijk. 1999. Anomalies in dual energy X-ray absorptiometry measurements of total-body bone mineral during weight change using Lunar, Hologic and Norland instruments. *Br J Radiol* 72:661-669.
118. Browne, J. E., A. J. Watson, P. R. Hoskins, and A. T. Elliott. 2005. Investigation of the effect of subcutaneous fat on image quality performance of 2D conventional imaging and tissue harmonic imaging. *Ultrasound Med Biol* 31:957-964.
119. Kotzki, P. O., D. Buyck, D. Hans, E. Thomas, F. Bonnel, F. Favier, P. J. Meunier, and M. Rossi. 1994. Influence of fat on ultrasound measurements of the os calcis. *Calcif Tissue Int* 54:91-95.

120. Bash, C., M. Rothman, M. Hamet, D. Sorce, G. Zoarski, F. Mihara, and Y. Numaguchi. 1995. MRI of silicone vitreous ocular implants with phantom correlation. *Neuroradiology* 37:313-316.
121. Daniel, B. L., R. L. Birdwell, J. W. Black, D. M. Ikeda, G. H. Glover, and R. J. Herfkens. 1997. Interactive MR-guided, 14-gauge core-needle biopsy of enhancing lesions in a breast phantom mode. *Acad Radiol* 4:508-512.
122. Freed, M., J. A. de Zwart, J. T. Loud, R. H. El Khouli, K. J. Myers, M. H. Greene, J. H. Duyn, and A. Badano. An anthropomorphic phantom for quantitative evaluation of breast MRI. *Med Phys* 38:743-753.
123. Lagalla, R., L. Manfre, A. Caronia, F. Bencivinni, C. Duranti, and F. Ponte. 2000. Plain film, CT and MRI sensibility in the evaluation of intraorbital foreign bodies in an in vitro model of the orbit and in pig eyes. *Eur Radiol* 10:1338-1341.
124. Shah, C., A. K. Jones, and C. E. Willis. 2008. Consequences of modern anthropometric dimensions for radiographic techniques and patient radiation exposures. *Med Phys* 35:3616-3625.
125. Turner, A. C., M. Zankl, J. J. DeMarco, C. H. Cagnon, D. Zhang, E. Angel, D. D. Cody, D. M. Stevens, C. H. McCollough, and M. F. McNitt-Gray. 2010. The feasibility of a scanner-independent technique to estimate organ dose from MDCT scans: using CTDIvol to account for differences between scanners. *Med Phys* 37:1816-1825.
126. Amato, E., D. Lizio, N. Settineri, A. Di Pasquale, I. Salamone, and I. Pandolfo. 2010. A method to evaluate the dose increase in CT with iodinated contrast medium. *Med Phys* 37:4249-4256.
127. Achiam, M. P., E. Chabanova, V. Logager, H. S. Thomsen, and J. Rosenberg. 2007. Implementation of MR colonography. *Abdom Imaging* 32:457-462.

128. Achiam, M. P., V. Logager, E. Chabanova, H. S. Thomsen, and J. Rosenberg. Patient acceptance of MR colonography with improved fecal tagging versus conventional colonoscopy. *Eur J Radiol* 73:143-147.
129. Debatin, J. F., and T. C. Lauenstein. 2003. Virtual magnetic resonance colonography. *Gut* 52 Suppl 4:iv17-22.
130. Lauenstein, T. C. 2006. MR colonography: current status. *Eur Radiol* 16:1519-1526.
131. Luboldt, W., P. Bauerfeind, P. Steiner, M. Fried, G. P. Krestin, and J. F. Debatin. 1997. Preliminary assessment of three-dimensional magnetic resonance imaging for various colonic disorders. *Lancet* 349:1288-1291.
132. Luboldt, W., P. Steiner, P. Bauerfeind, P. Pelkonen, and J. F. Debatin. 1998. Detection of mass lesions with MR colonography: preliminary report. *Radiology* 207:59-65.

VITA

Jonathon W. Mueller was born in Campbellsville, KY on December 5, 1979 to Wayne A. Mueller and Patricia A. Mueller. Years after Patricia's passing in Jonathon's infancy, Wayne married Linda K. Mueller, whom jointly raised Jonathon and his two siblings. After graduating from Cloverleaf High School in Lodi, Ohio in 1998, Jonathon studied Biomedical Engineering at the University of Akron in Akron, Ohio; receiving his Bachelor of Science degree in May, 2003. Jonathon furthered his cooperative education experience at Moen Incorporated (North Olmstead, Ohio) as a contract engineer while undergoing the enrollment process into the United States Air Force. In January 2004, Jonathon was commissioned a Second Lieutenant in the Air Force Reserves and was assigned to the University of Akron in an educational assignment to obtain his Master of Science degree in Biomedical Engineering. After graduating in May 2006, he served three years in active duty as a Bioenvironmental Engineer at Altus Air Force Base, Oklahoma. In August 2009, he received an educational assignment to pursue a Specialized Master of Science in Medical Physics at The University of Texas Health Science Center at Houston Graduate School of Biomedical Sciences.

Permanent Address:

9 High Street

Seville, OH 44273